Planar Lensing Lithography: Enhancing the Optical Near Field.

by

David O. S. Melville

BE (*1st Class Hons.*)

A thesis presented for the degree of

Doctor of Philosophy

in

Electrical and Electronic Engineering

at the

University of Canterbury,

Christchurch, New Zealand.

1*st* of February, 2006

for my love Gemma

ABSTRACT

In 2000, a controversial paper by John Pendry surmised that a slab of negative index material could act as a perfect lens, projecting images with resolution detail beyond the limits of conventional lensing systems. A thin silver slab was his realistic suggestion for a practical near-field superlens – a 'poor-mans perfect lens'. The superlens relied on plasmonic resonances rather than negative refraction to provide imaging. This silver superlens concept was experimentally verified by the author using a novel near-field lithographic technique called Planar Lensing Lithography (PLL), an extension of a previously developed Evanescent Near-Field Optical Lithography (ENFOL) technique.

This thesis covers the computational and experimental efforts to test the performance of a silver superlens using PLL, and to compare it with the results produced by ENFOL.

The PLL process was developed by creating metal patterned conformable photomasks on glass coverslips and adapting them for use with an available optical exposure system. After sub-diffraction-limited ENFOL results were achieved with this system additional spacer and silver layers were deposited onto the masks to produce a near-field test platform for the silver superlens.

Imaging through a silver superlens was achieved in a near-field lithography environment for sub-micron, sub-wavelength, and sub-diffraction-limited features. The performance of PLL masks with 120-, 85-, 60-, and 50-nm thick silver layers was investigated. Features on periods down to 145-nm have been imaged through a 50-nm thick silver layer into a thin photoresist using a broadband mercury arc lamp. The quality of the imaging has been improved by using 365 nm narrowband exposures, however, resolution enhancement was not achieved.

Multiple layer silver superlensing has also been experimentally investigated for the first time; it was proposed that a multi-layered superlens could achieve better resolution than a single layer lens for the same total silver thickness. Using a PLL mask with two 30-nm thick silver layers gave 170-nm pitch sub-diffraction-limited resolution, while for a single layer mask with the same total thickness (60 nm) resolution was limited to a 350-nm pitch. The proposed resolution enhancement was verified, however pattern fidelity was reduced, the result of additional surface roughness.

Simulation and analytical techniques have been used to investigate and understand

the enhancements and limitations of the PLL technique. A Finite-Difference Time-Domain (FDTD) tool was written to produce full-vector numerical simulations and this provided both broad- and narrowband results, allowing image quality as a function of grating period to be investigated. An analytical T-matrix method was also derived to facilitate computationally efficient performance analysis for grating transmission through PLL stacks. Both methods showed that there is a performance advantage for PLL over conventional near-field optical lithography, however, the performance of the system varies greatly with grating period. The advantages of PLL are most prominent for multi-layer lenses.

The work of this thesis indicates that the utilisation of plasmonic resonances in PLL and related techniques can enhance the performance of near-field lithography.

PREFACE

This dissertation describes research undertaken in the Department of Electrical and Computer Engineering at the University of Canterbury between March 2003 and January 2006. I am grateful for the previous, and continuing, efforts of Dr Richard Blaikie, Dr Maan Alkaisi, and Dr Sharee McNab, who have provided the ground work for the development of near-field lithography techniques and the establishment of a rich array of equipment resources at the University of Canterbury.

Through the course of my study on the topic of near-field lithography I have learnt that there are major differences between a cynical and a discerning researcher. Both would suggest that near-field lithography is a difficult, time consuming process that is possibly not worth the effort. However, only the discerning researcher would find the motivation and courage to press on through countless attempts, happy in the knowledge that as a result of the research's conclusion more will be understood about the nature and usefulness of the near-field. I have spent time in both camps, but have thankfully found reward in the latter. I truly hope that through my efforts a better understanding of near-field lithography will be gained.

Aspects of the work described in this dissertation have been published and presented as follows:

Publications in Referred Journals

D. O. S. Melville and R. J. Blaikie. "Experimental comparison of resolution and pattern fidelity in single- and double-layer planar lens lithography". *J. Opt. Soc. Am. B*, 23(3): *in press*, 2006.

R. J. Blaikie and D. O. S. Melville. "Imaging through planar silver lenses in the optical near field". *J. Opt. A: Pure Appl. Opt.*, 7(2):S176-S183, 2005.

D. O. S. Melville and R. J. Blaikie. "Super-resolution imaging through a planar silver layer. *Opt. Express*, 13(6):2127-2134, 2005.

D. O. S. Melville and R. J. Blaikie. "Response to "Comment on 'Submicron Imaging with a Planar Silver Lens' "" [Appl. Phys. Lett. 86, 126101 (2005)]. *Appl. Phys. Lett.*, 86(12):126102, 2005.

D. O. S. Melville, R. J. Blaikie, and C. R. Wolf. "Submicron Imaging with a Planar Silver Lens". *Appl. Phys. Lett.*, 84(22):4403-4405, 2004.

Papers in Published in Referred Conference Proceedings

D. O. S. Melville, R. J. Blaikie, and M. M. Alkaisi, A Comparison of Near-Field Lithography and Planar Lens Lithography, 2nd International Conference on Advanced Materials and Nanotechnology (AMN-2), 6-11 February 2005, Queenstown, NZ. To be published in *Current Appl. Phys.* 2006

D. O. S. Melville and R. J. Blaikie. Improvement to silver superlens performance through narrowband exposure. SPIE Optics and Photonics '05, San Diego, USA, 1-5 September, 2005. *Proc. SPIE*, 5928:18-26, 2005.

D. O. S. Melville and R. J. Blaikie. "Near-field optical lithography using a planar silver lens", 48th Conference on Electron, Ion, Photon Beams and Nanotechnology (EIPBN04), 31 May 3 June 2004, San Diego, CA, USA. Published in *J. of Vac. Sci. & Tech. B*, 22 3470-3474, (2004). Selected for publication in the Virtual Journal of Nanoscience and Technology, vol 11 (no 1), 10 Jan 2005.

R. J. Blaikie, and D.O.S. Melville, Near-field imaging with a planar silver lens, *Proceedings of the 13th International Laser Physics Workshop* (LPHYS'04), p. 33. Trieste, Italy, 12-16 July 2004. Invited oral presentation performed by R. J. Blaikie.

R. J. Blaikie, M. M. Alkaisi, S. J. McNab, and D. O. S. Melville, Nanoscale optical patterning using evanescent fields and surface plasmons. Materials Research Society International Conference on Materials for Advanced Technologies (ICMAT), 7-12 Dec 2003, Singapore. Invited oral presentation performed by R. J. Blaikie. Published in *International Journal of Nanoscience* 3 (nos 4-5), 2004, 405-17.

Converence Talks (presenter in bold)

D. O. S. Melville, R. J. Blaikie, M. M. Alkaisi, "Near-field Plasmonic Lithography through a Silver Film", MacDiarmid Institute Student symposium, Wellington, New Zealand, 17-18 November, 2005. Winner 2nd best presentation.

D. O. S. Melville, R. J. Blaikie, M. M. Alkaisi, Super-Resolution through a Planar Lens , SPIE Optics and Photonics '05, San Diego, USA, 1-5 September, 2005.

D. O. S. Melville, R. J. Blaikie, M. M. Alkaisi, Projecting the Near-Field, 2nd International Conference on Advanced Materials and Nanotechnology (AMN-2), Queenstown, NZ, 6-11 Feburary, 2005.

Converence Poster Presentations (presenter in bold)

D. O. S. Melville, **M. M. Alkaisi**, and R. J. Blaikie, "Super-Resolution Near-Field Lithography using Planar Silver Lenses", 31st International Conference on Micro- and Nano-Engineering (MNE2005), 19-22 September 2005, Vienna, Austria. Winner 2nd prize in best poster award.

D. O. S. Melville, M. M. Alkaisi, and **R. J. Blaikie**, "Super-Resolution i-Line Proximity Lithography with a Silver Lens", 49th Conference on Electron, Ion, Photon Beams and Nanotechnology (EIPBN04), 31 May 3 June, 2005, Orlando, FL, USA.

D. O. S. Melville and R. J. Blaikie, "Near-field optical lithography using a planar silver lens", 48th Conference on Electron, Ion, Photon Beams and Nanotechnology (EIPBN04), 31 May 3 June 2004, San Diego, CA, USA.

Inivted talks and Seminars (presenter in bold)

D. O. S. Melville, M. M. Alkaisi, and R. J. Blaikie, "Near-field Plasmonic Lithography through a Silver Film", IBM Advanced Lithography Research Group, 5 September, 2005, IBM, Yorktown Heights, NY, USA.

D. O. S. Melville, M. M. Alkaisi, and R. J. Blaikie, "From Negative Refraction to Super-resolution" RLE group meeting, August 2005, Massachusetts Institute of Technology, MA, USA.

D. O. S. Melville, M. M. Alkaisi, and R. J. Blaikie, "From Negative Refraction to Super-resolution", Brongersma group meeting, August 2005, Stanford University, CA, USA.

D. O. S. Melville, M. M. Alkaisi, and R. J. Blaikie, "Super-Resolution through a Planar Silver Lens", Electrical and Computer Engineering Departmental seminar, 22 April, 2005, University of Canterbury, NZ.

D. O. S. Melville, M. M. Alkaisi, and R. J. Blaikie, "Pefect Lens Lithography: Imaging the Near Field", MacDiarmid Institute seminar, 16 April, 2004, University of Canterbury, NZ.

D. O. S. Melville, M. M. Alkaisi, and R. J. Blaikie, "Negative Refraction: Changing the Laws of Optics", EIPBN 2004 Raith users meeting, 2 June 2004, San Diego, CA, USA.

D. O. S. Melville, M. M. Alkaisi, and R. J. Blaikie, "Super-Resolution through a Planar Silver Lens", IEE/IEEE seminar, 6 May, 2004,University of Canterbury, NZ.

ACKNOWLEDGEMENTS

Without understatement the the credit for the ideas and work in thesis should be shared with my supervisor Dr Richard Blaikie. At the risk of embarrassing Richard, I see him as a mentor and a friend, who has guided me carefully and constructively through a project within which I have grown as both a researcher and a thinker under his tutelage. I will always remember the positive and personal influence he has had on my life.

This thesis also benefited immensely from Richard's policy to supply me with a stream of keen researchers to do my 'dirty work'. The first and most influential was Conrad Wolf; a cheerfully regimented German student who spent six months helping me develop the basic near-field process and encouraging me through the endless bug fixing that is associated with designing one's own simulation tool. I am very grateful for the work ethic Conrad instilled in me and the kick-start he provided. The next student in the line was Andrew Thompson; a motivated worker who become a good friend. I thank Andy for spending a summer helping me to optimise the important PMMA advanced planarisation step. The final help I received, which was over and above the call of duty was during the race to obtain features beyond the diffraction limit, when Alan Wright dedicated a month of his life into what eventually became a published success. I thank Alan for his efforts.

There are many other staff members that have made my life easier and in a few cases saved it. I would like to sincerely thank Dr Maan Alkaisi for being my co-supervisor and encouraging me to take up the challenge of this thesis. In the lab, the never ending dedication of Helen Devereux and Gary Turner is greatly appreciated. I am very thankful for Helen's ability to drop everything and immediately attend to your inconsequential problem, and for Gary's never say 'broken' attitude. In the final six months of the thesis, simulation and experimental discussions with Dr Matthew Arnold helped me to solidify a number of ideas and expanded the my thinking on others.

I would like to acknowledge the financial support from the University of Canterbury Brownlie Doctoral Scholarship and the financial backing and infrastructure provided by the MacDiarmid Institute and the Nanostructure Engineering Science and Technology (NEST) Group.

Other people that have helped me with technical aspects of my work and that

I would like to thanks are: Pablo Etchen for Ellipsometry, Mike Shurety, Dave van Leeuwen, Florin Predan, and Pieter Kikstra for database and computer issues, and Chito Kendrick for help with optical transmission measurements. I also wish my fellow students for countless moments of insight along the way.

One influence that I cannot forget is the distracting and time consuming influence of my co-PhD student James Muys. Without James encouraging me to spend time hatching hair-brain schemes and introducing me to the drug of caffeine, this thesis may never have been finished. On the other hand it may have been finished six months earlier, but I thank my friend James nonetheless.

Even through the intensive study required for a doctorate, it is family and friends that remain the major influence on your life. The need for time out from the stress of the work is best fulfilled through them. I especially want to thank my parents Sue and Don for all their support and for providing me with the platform that my life relies upon everyday.

Finally, I am eternally grateful for the depth of the unerring support from my beautiful wife Gemma. For encouragement, patience, inspiration, motivation, and above all for the laughter, I cannot thank you enough.

If people finish doctorates daily, then every day there is victory! I thank all those who fought in my victory.

TABLE OF CONTENTS

LIST OF FIGURES

LIST OF TABLES

ACRONYMS AND ABBREVIATIONS

ABC Absorbing Boundary Condition

AFM Atomic Force Microscope

BARC Bottom Anti-Reflection Coating

DC Direct-Current

Detak Surface Profilometer

DFT discrete-Fourier-transform

EBE Electron-beam Evaporation

EBL Electron Beam Lithography

ENFOL Evanescent Near-Field Optical Lithography

FDTD Finite-Difference Time-Domain

FEM Finite Element Method

FOM figure-of-merit

HMW high-molecular-weight

IC Integrated Circuit

IPA isopropyl alcohol

LMS Least-Mean-Square

MIBK methyl isobutyl ketone

MMP Multiple Multi-pole

MTF Modulation Transfer Function

NA Numerical Aperture

NOM Near-field Optical Microscope

OPC Optical Proximity Correction

PGMEA propylene glycol monomethyl ether acetate

PML Perfectly Matched Layer

PMMA poly(methyl methacrylate)

PLL Planar Lensing Lithography

RF Radio-Frequency

RIE Reactive Ion Etch

rms root-mean-square

SE Secondary Electron

SEM Scanning Electrical Microscope

SP Surface Plasmon

SPECL Surface Plasmon Enhanced Contact Lithography

SPW samples-per-wavelength

SRR split-ring resonators

TE Transverse Electric

TM Transverse Magnetic

TMAH tetra-methyl ammonium hydroxide

UV ultra-violet

VM Veselago Material

WEC wedge-error-correction

Chapter 1

INTRODUCTION

"It is as if light were writing with a thick pencil"

- John Pendry, IEE Talk (2002)

In our world we are surrounded by the constant hum of the computer revolution. Its effect on our lives is understated as rarely as it is disputed. This revolution has relied on the ongoing strength of the semiconductor industry and, as is the case with any technological revolution, it was made possible through the mastery of new materials. Like iron to the iron age, silicon is the material at the heart of the semiconductor industry that has pioneered the computer age. For the mastery of every technology, new tools are required. During the iron age it was not so much iron itself, but the development of tools and skills which enabled its properties to be harnessed. In the same way, the computer revolution should not necessarily be dedicated to silicon, but rather the not-so-famous tools that were utilised to exploit the material's properties. In this sense optical photolithography has been indispensable. Photolithography is the process which allows silicon to be patterned by transferring mask patterns into photo-sensitive material (photoresist), and it provides the ability to systematically reproduce micron and sub-micron scaled features at a low cost. It was this low-cost nature that enabled mass production of affordable integrated circuits. No other technique could have provided this, and without the favourable economics the revolution would have slowed to a crawl. As a tool, optical lithography has been just as fundamental to the revolution as silicon.

However, in future years photolithography's dominance in the semiconductor industry is at risk. Photolithography's fate is being driven by the continuing need for smaller and faster devices. This is a result of the belief in the resolution limits of optics; namely that light cannot be used to resolve objects smaller than the wavelength of the light. The semiconductor industry is now being forced to go to shorter wavelengths to produce smaller features. It has become extremely expensive and time consuming to make these moves to smaller wavelengths, and finding sources and optical elements for light manipulation has become arduous, and is only providing short-term answers.

The limiting factor for photolithography is diffraction. When light passes by an edge or goes through a narrow slit the light-rays are deflected, or diffracted. Figure 1.1 demonstrates the effect of diffraction when light passes through a slit which is narrow in dimensions compared to the wavelength of light. The diffracted wave fronts proceed to constructively and destructively interfere, producing high and low intensity fringes. The amount of diffraction is related to the width of the slit, and for small slits diffraction becomes so pronounced that at small distances away from the slit a representative image cannot be taken. This diffraction process not only limits lithography techniques, but also optical microscopy.

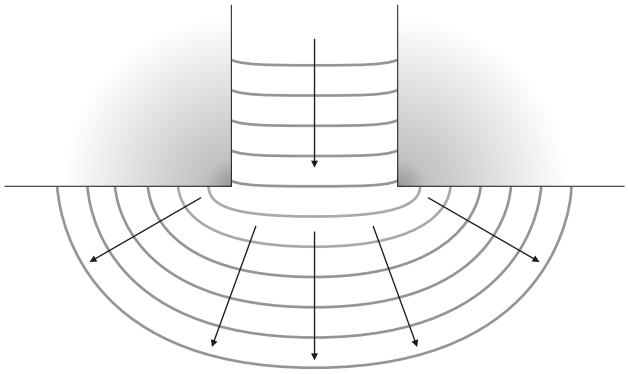

Fig. 1.1: The nature of diffraction: wavefronts diffract around the corners of the opening of a channel.

The imposed restrictions of diffraction on photolithography have been overcome through the utilisation of the electromagnetic near-field. The near-field holds all the electromagnetic information from a radiating object, but not all of it propagates. Instead, the parts of the near-field that contain information on sub-wavelength features decay away evanescently and consequently after a very small distance can no longer be sensed. This results in all structural information smaller than a wavelength being lost. The near-field has been employed previously to take the resolution of optical microscopy past the diffraction limit in the form of the Near-field Optical Microscope (NOM)[1]. Using the same premise, the field of photolithography achieved resolution unlimited by diffraction through the implementation of a new technique that utilised the near-field — this is know as Evanescent Near-Field Optical Lithography (ENFOL) [15–17].

ENFOL uses intimate contact between the lithography photomask and a thin layer of photoresist to ensure only a near-field exposure, and by doing so it has produced features sizes below conventional photolithography's limits. ENFOL was deemed to be promising but the development of new concepts to help enhance the near-field were needed to strengthen its performance. One particularly intriguing advancement was the concept of the 'perfect lens'.

In 2000, the exciting and controversial theory of the 'perfect lens' was proposed by

[1]The NOM is able to sense the near-field, by having an ultra fine tip very close to the source [13,14].

Pendry [18]. The idea generated huge interest in the area of metamaterials, and resulted in extensive theoretical, simulation, and experimental study [19, 20]. The key claim of Pendry's perfect lens theory was that the near-field of a source could be amplified and refocused by a slab of negative index material to reconstruct a sub-diffraction-limited image. This concept expanded on a 30-year-old theory surmising that propagating waves were also focused by such a slab [21]. Furthermore, Pendry suggested that a silver slab exposed under UV light could act as a near-field perfect lens, or a superlens. This gave solid direction for a surface-plasmon-mediated, sub-100nm, super-resolution imaging system.

This thesis covers the computational and experimental efforts to test the performance of a silver superlens by combining Pendry's concept with ENFOL to produce a new type of near-field optical lithography. This lithography is called Planar Lensing Lithography (PLL).

PLL attempts to provide higher intensity, and better contrast than ENFOL for sub-diffraction-limited features by using resonant high-spatial frequency plasmon waves on the surface of a silver superlens to expose photoresist. The performance is comparable to ENFOL at a separation from the lens [22], allowing the possibility of sub-diffraction-limited imaging without the need for resist-to-mask contact.

The work of this thesis details the initial work on PLL, showing that a silver slab could image the near-field features of a photolithography mask using a Mercury arc lamp [23]. This work is then followed by conclusive proof of sub-diffraction-limited imaging [24], confirming Pendry's controversial theory. The method used has also been extended to test double silver layers [25], after recent work suggested that dividing a silver slab into multiple layers could improve resolution [26]. Interest in the work has resulted in multiple mentions in general physics and optics literature [27–30], as has the work from a group at University of California, Berkeley, who have also demonstrated silver superlensing using an alternative technique [31].

The remainder of this thesis is structured as follows. A detailed exploration of the background for the topics important to the work is covered in Chapter 2, outlining the state of photolithography today and an in depth look into the debate that ensued after the 'perfect lens' proposal. Chapter 3 then details the Finite-Difference Time-Domain (FDTD) numerical technique that is used to simulate the PLL concept. The FDTD simulation code produced is validated against other techniques and the simulation's ability to test and visualise PLL is investigated.

The next chapter outlines the major experimental apparatus used during the work. Chapter 5 then details the use of these apparatus during the fabrication of near-field masks used for ENFOL and PLL. In Chapter 6, the exposure techniques are elaborated on before the first experiments using ENFOL and single layer PLL are described. In this chapter the first experimental evidence of sub-diffraction-limited imaging through

silver is presented. Chapter 7 outlines the results of the extended multi-layer PLL imaging technique, concluding the experimental result chapters.

Chapter 8 contains an in depth analysis of certain simulation work, where numerous FDTD simulations were performed to investigate the performance of the system for different PLL masks. An analytical technique is also covered, investigating the transmission performance of different superlens arrangements. Chapter 9 concludes the main points of this thesis and covers future work.

Chapter 2

BACKGROUND: OPTICAL LITHOGRAPHY AND THE 'PERFECT LENS'

"I'm sorry this letter is so long, but I did not have time to make it shorter."

- Mark Twain

The modern concept of lithography has its origins in the late 1700s when Alois Senefelder, an Austrian actor and playwright, formalised the principle of repeatable pattern transfer [32]. By exploiting the repellent nature of oil and water solutions, Senefelder was able to create contrasting areas on stone templates, or masks, that, when inked, would repel or attract an oil-based substance. This mask was then brought into contact with paper and a clear ink pattern was transferred.

This principle began what would become a highly economical pattern transfer process. In the mid 1800s, fully automatic presses had been developed which provided up to 10,000 prints per hour. The expensive printing plates could be made to reproduce patterns hundreds of thousands of times, making the time spent making them economical – the underlying strength of a lithography process. Figure 2.1 shows an example from 1902 of a map printed with a lithography process. The method was flexible enough to align multiple masks with a range of ink colours to produce elaborate images.

2.1 LITHOGRAPHY IN THE SEMICONDUCTOR INDUSTRY

In the twentieth century, lithography processes found new application in the realm of the semiconductor industry. When the semiconductor transistor was invented in Bell Labs in 1947, a solid-state alternative to the valve transistor was created seeding the modern computer age. The nature of the new transistor allowed planar fabrication that facilitated the sought after quality of device scaling. Scaling of the transistor initially saw tens of transistors incorporated into a single device producing the proof of concept for the Integrated Circuit (IC), which provided the basis of the hardware for the ensuing computer revolution. The IC was about to journey down a path of relentless

Fig. 2.1: A lithography print of the Western Governorships (of the Russian Empire) and Polish Kingdom in 1902. The map was printed in Warszawa, 1902 [1].

miniaturisation and density increases, however, in order to densely pack silicon transistors there needed to be a repeatable pattern transfer process to allow the IC to be produced economically. Optical photolithography soon became the accepted process for device manufacture.

Optical photolithography requires four elements to provide repeatable pattern transfer. These are: the layer to be patterned, a photosensitive pattern transfer layer (called photoresist), an optical light source, and a metal-patterned photomask. The process steps are shown in Fig. 2.2. The photoresist is exposed through a photomask before the exposed regions are developed away. A number of techniques are then used to transfer the photoresist pattern into, or onto, the substrate. It is the resolution, or size of the minimal feature in the optical lithography process, that is the focus of this thesis.

Improvements to the resolution of optical lithography have allowed the density and, through the reduction of signal path time, the speed of ICs to increase. The changes in the density, speed, and cost of ICs has closely followed the famous exponential prediction by Dr Gordon Moore that the complexity for minimum component cost would double every two years. A graph of the number of transistors shipped on each Intel^{TM} IC since 1971 is shown in Fig. 2.3 [3]. The figure also shows how closely the progress has followed Moore's prediction (dashed line), although it has become a self-fulfilling prophecy as it has motivated industry goals. Improvements have been made through many process refinements — finer detailed masks, better etching process, improved photoresists, and higher resolution optical patterning — with an ever increasing complexity making the process a far cry from the simple 19th century printing process. It is the optical transfer step that is seen as the major resolution obstacle for the lithography process.

The optical transfer step has three standard setups, which have a number of com-

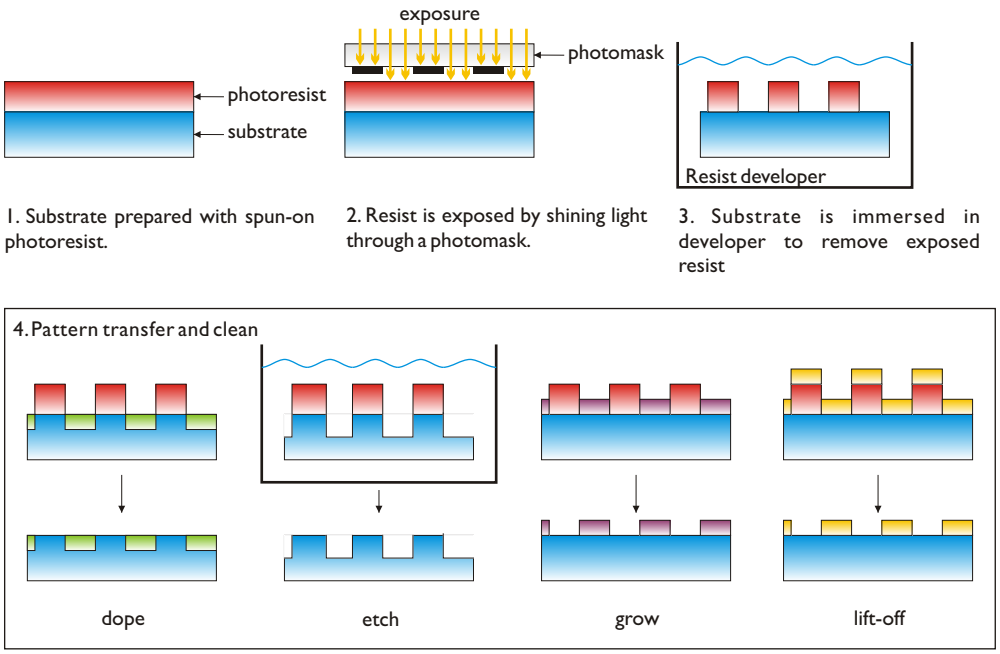

Fig. 2.2: Schematic of the standard optical lithography processing steps [2].

monalities, and which differ primarily in the positioning of the photomask. Schematics of these setups are shown in Fig. 2.4. The original technique was contact lithography (see Fig. 2.4(a)). This was the simplest approach as the resist and mask were brought into physical contact ensuring exact parallel positioning. However, this method was not considered viable in commercial processes because of contamination from the resist layer to the mask, which lead to low processing yields. To overcome this problem the industry introduced a gap between the mask and resist during the process. This is known as proximity lithography and the setup is shown in Fig 2.4(b). With the ever-pressing need for decreasing feature size, this method quickly ran into a major optical limitation [33]. This limiting factor was diffraction. Diffraction is caused when light meets an obstruction or passes by an edge, and results in the light waves being bent around the obstruction or edge. Small mask features cause the wavefronts to become circular, limiting a proximity system's ability to clearly image the feature into the resist.

With the development of extremely precise optical systems, enabling uniform large-area image projection, lensing systems were designed that could re-focus diffracted light and obtain maximum resolution from the propagating fields. This process, called projection lithography, is the currently the most common commercial process. Projection lithography systems position the mask at a separation from the substrate, and insert lenses in between the mask and substrate to focus light into the photoresist. Figure 2.4(c) shows the setup for optical projection lithography. The introduced lenses can have magnification properties to allow larger than one-to-one masks to be used. This al-

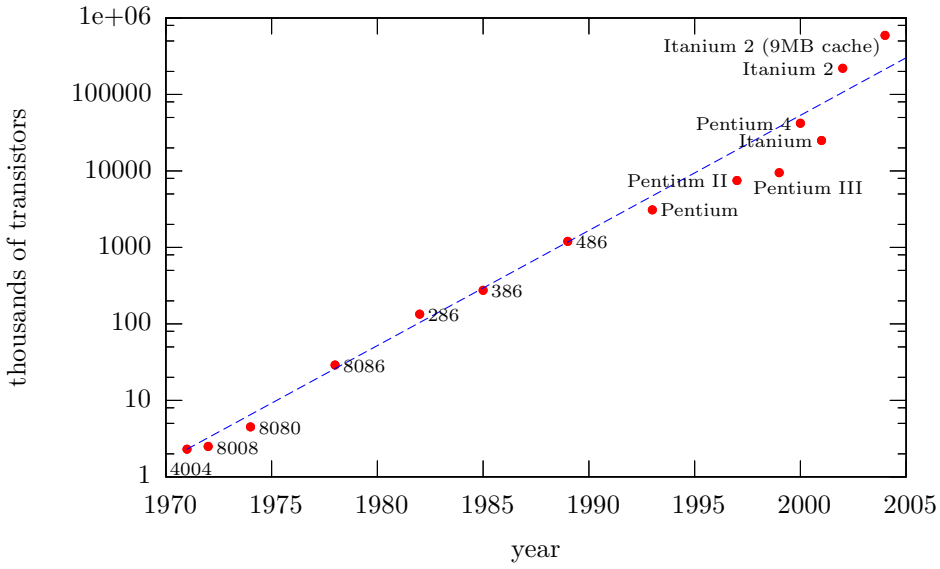

Fig. 2.3: Moore's law for the number of transistors on Intel's integrated circuits. The dashed line shows the path predicted by Dr Gordon Moore in 1965 [3].

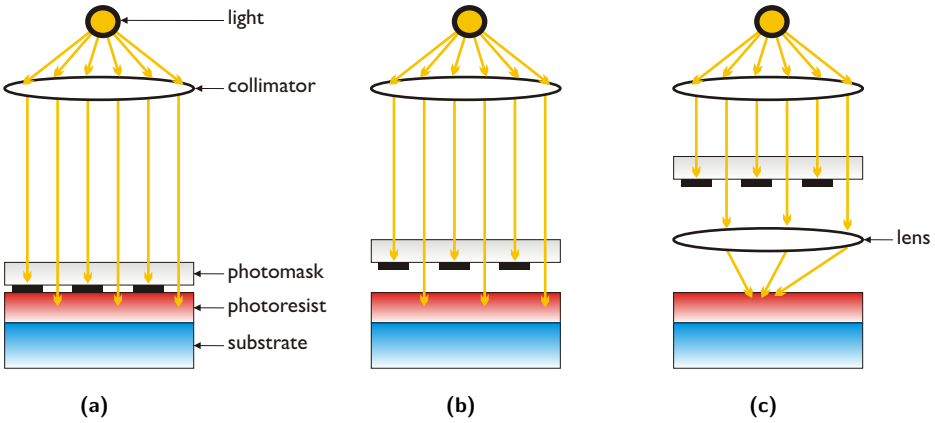

Fig. 2.4: Schematics of the setups for (a) optical contact lithography, (b) optical proximity lithography, and (c) optical projection lithography.

lows lower-resolution masks to be fabricated, reducing tolerances during mask making. The next section provides more detail about the effects of diffraction and calculations on resolution limits of optical lithography systems.

2.2 THE DIFFRACTION LIMIT

The diffraction limit imposes a resolution limit on conventional optical lithography systems as they rely on propagating light for exposure. It is the inherent wave-like nature of propagating light that causes diffraction at an edge boundary between media. In a lithography system, diffraction around mask patterns leds to diverging wave fronts that cause interference patterns and reduce the quality of an image.

The resolution limit of an optical system is usually found in one of three forms: isolated lines, isolated line pairs, or dense line gratings [34]. This is mostly due to the fact that it is relatively simple to calculate the diffraction limits of such patterns because of the symmetry involved. Once these resolution limits are found, a great deal can be said about the ultimate performance of the system.

The resolution limits of a proximity system are commonly found by employing Huygen's principle to describe the source generated from an aperture as a summation of spherical wavelets [35]. Solutions are then found which are consistent with the dimensions of the problem, leading to near-field and far-field resolution limitations [33]. The first solution uses the following assumption:

$$l^2 >> \lambda\sqrt{g^2 + r^2} \tag{2.1}$$

where l is the width of the feature, λ is the wavelength, g is the separation distance of mask and image, and r is the lateral distance from the centre of the diffraction point to the observation point. This result produces a near-field, or Fresnel diffraction pattern, which produces a blurring of the feature width by

$$\Delta l = l\frac{g}{D} \tag{2.2}$$

where D is the separation of the mask from the exposure source.

If the assumption of Equ. 2.1 is held then, for small separation (compared with distance from the exposure source), there is no fundamental limit to the feature size, since Δl tends to zero. This provides no resolution limit for contact lithography, however, this only holds for very small mask-image separation where the resist remains in the near-field.

As an example, if we take a λ of 365 nm[1], set $r = l/2$ (to give a 1:1 feature transfer ratio), and replace the much-greater-than with a lenient greater-than in the assumption of Equ. 2.1, we arrive at a near-field criterion for the maximum gap

$$g < \sqrt{\frac{l_{min}^4}{\lambda^2} - \frac{l_{min}^2}{4}} \tag{2.3}$$

where l_{min} denotes the minimum line feature of the system. For a 200-nm feature the gap must be less than 44 nm to place the image in the near-field. Hence, for near-field exposure the photoresist must be extremely close to the mask. Contact lithography systems don't often meet this criterion due to photoresist thickness. The criterion equation does concern itself with the interaction of propagating waves and higher resolution can be gained by near-field systems that couple energy through evanescent fields, as is the case for the Near-field Optical Microscope (NOM) [13, 14].

[1]The 365 nm, or i-line wavelength is a common UV exposure wavelength in university based lithography research.

For large gaps, a new formulation is used which uses far-field diffraction solutions or Fraunhofer diffraction. In this case, the required assumption is

$$l^2 << \lambda\sqrt{g^2 + r^2}. \tag{2.4}$$

In this regime, ray tracing and trigonometric assumptions lead to the common far-field proximity resolution limit [33]

$$l_{min} = \sqrt{\lambda g}. \tag{2.5}$$

A projection system's resolution limits differ from a proximity system by the inclusion of extra optical lensing components that amount to a Numerical Aperture (NA). The NA describes the ability of an optical lensing system to collect the diffracted orders produced by a mask and is defined by $\text{NA} = n \sin\theta$, where n is the refractive index of the surrounding media and θ is the maximum approach angle for light (as taken from the mask's surface normal).

Diffraction and the loss of the higher diffracted orders from a point source, caused by transmission through a lens with a particular NA, results in a far-field profile described by a $sinc^2$ function with a geometry controlled by the parameters of the optical system [36]. From this, resolution limits can be determined based on a number of criteria.

The minimum separation distance of an isolated line pair is a useful resolution limit as it indicates feature-proximity and size limits. The most common limit used is the Rayleigh criterion [36]. The Rayleigh criterion chooses the separation of the $sinc^2$ functions such that the central maximum of one coincides with the first minimum of the other. Figure 2.5(a) shows the positioning of the two $sinc^2$ functions and their combined intensity. The Rayleigh criterion sets a minimum separation distance at

$$l_{min} = 0.61\frac{\lambda}{NA}. \tag{2.6}$$

However, the small dip in the centre of the Rayleigh criterion intensity leaves room for further improvement, as a finely-tuned lithography process could still separate these two peaks. A tighter criterion for resolving focused line pairs in the far-field has been devised by Sparrow [36]. In Sparrow's criterion, two $sinc^2$ functions are super-imposed and brought together until there is no longer a dip in the middle of the resultant function. This is a good approximation for the resolution limit for line pairs in a lithography system as it is the point where no contrast is available to separate the two lines in the image. The Sparrow criterion gives a separation of

$$l_{min} = 0.47\frac{\lambda}{NA}. \tag{2.7}$$

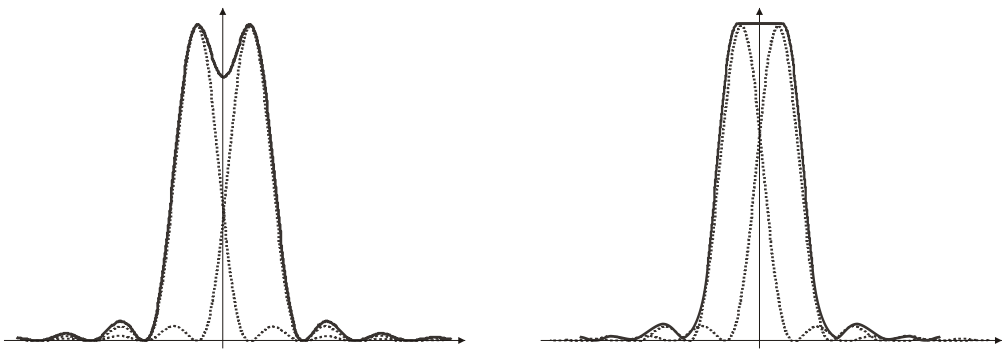

Fig. 2.5: Graphs showing the resolution criteria for two point sources for (a) Rayleigh and (b) Sparrow limits. The far-field intensity pattern generated by the point sources is shown by dashed lines, with the total fields drawn as solid lines.

For a projection lithography system, the isolated line pair criteria are often modified to

$$l_{min} = k\frac{\lambda}{NA} \tag{2.8}$$

where the k factor reflects the combined effects of all the process parameters in the system.

Another way to describe the resolution limits of a system is with dense gratings. This method is commonly used in this thesis. For dense gratings the orientation of exposing light effects the limit. For a projection lithography system with on-axis radiation the the limit is given by

$$p_{min} = \frac{\lambda}{NA} \tag{2.9}$$

where p_{min} is the smallest feature period resolvable, λ is the wavelength of the exposing light, and n is the refractive index of the media the light is traveling through. For off-axis radiation the minimum period reduces to

$$p_{min} = \frac{\lambda}{2NA}. \tag{2.10}$$

The off-axis radiation scheme performs better due to the removal of the vertical zeroth-order wave. For perfect collection of all propagating diffracted orders through the aperture this becomes

$$p_{min} = \frac{\lambda}{2n} \tag{2.11}$$

where n is the refractive index of the medium between the final lens and the photoresist.

Presently, integrated-circuit manufacturing processes are dominated by optical techniques. But the aforementioned limitations of optical systems led to well defined resolution restrictions that hinder the future development of nano-electronics. Much

work is currently being done to try to overcome these limitations. The next section details some of the techniques vying to become the next generation lithography.

2.3 BEATING THE DIFFRACTION LIMIT

A number of lithographic techniques that could take the semiconductor industry past the current projection lithography system limitations are being developed and all have their strengths and weaknesses [37–40]. Common techniques that are placed in the category of next generation lithographies (NGL's) include: nanoimprint lithography, immersion projection lithography, parallel electron beam lithography, X-ray lithography, and extreme UV lithography. A number of other low cost techniques are discussed in Ref. [2] including: interference lithography, spatial-phase-locked e-beam lithography, intimate-contact lithography, and a future generation "templated self-assembly" technique. All these processes provide resolution beyond projection lithography. Here the most promising concepts that provide arbitrary mask patterns are described, namely nanoimprint and immersion lithography.

2.3.1 Nanoimprint Lithography

The concept of using a stamping process for lithography has been around for many years, but in 1995 experimental demonstration of sub-25 nm patterning by using a SiO_2-on-silicon mold [41] showed that high-resolution stamp lithography was clearly possible and caused a surge of interest in the area of so-called nanoimprint lithography.

Figure 2.6 shows a schematic representation of the nanoimprint process. A rigid mold is brought into contact with a resist with an amount of pressure. The force exerted on the resist causes it to conform to the shape of the mold. The mold is then released, leaving a thickness modulation in the resist that can be transferred into the substrate by etching. The resist used historically is poly(methyl methacrylate) (PMMA), which is heated above its reflow temperature during imprinting to promote conformity. After development, the process was able produce 10-nm features [42, 43]. The practicality of the imprinting step has been improved further by using a process called 'Step-and-Flash' imprint, where a UV curable liquid is used as the resist [44, 45]. This enhancement allows alignment to still occur while the mold and substrate are in contact and before curing.

The two major limitations of nanoimprint are the high probability of mask damage and the requirement of a one-to-one mask. Mask damage is caused by the high pressures involved during imprinting and material transfer as a result of contact [46]. Work is currently underway to manage mask damage problems [47,48] and adhesion issues [42]. One-to-one mask fabrication for nanoscale features was one of the major limitations during the attempted commercialisation of X-ray lithography [49, 50]. Cost-effective

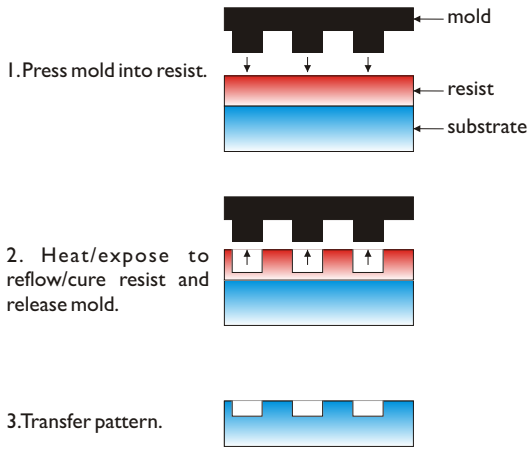

Fig. 2.6: Schematic of nanoimprint lithography processing steps.

mold creation and correction is and will continue to be a major obstacle for sub-50nm one-to-one mask fabrication.

Nanoimprint is a fast evolving technique, with a large amount of commercial interest. Additional work has been performed which enables the removal of the etching step by imprinting directly into the silicon [51], and roller nanoimprint lithography (RNIL) has been developed to enable better uniformity, less force, and the ability to repeat a mask continuously on a large substrate [52]. This technique will surely play a part in the future of the industry.

2.3.2 Immersion Projection Lithography

A strong contender to supersede current projection systems is immersion projection lithography. This technique simply explores the constraints of the resolution limit for a projection system, which includes the reciprocal relationship between the minimum feature size and the refractive index of the material between the final lens and imaging layer (Equ. 2.6). Increasing the refractive index of this material by using a fluid rather than air results in a reduction of the minimum feature size. Figure 2.7 shows how a standard projection setup is modified.

By the end of the nineteenth century, using numerical apertures greater than 1 was a common practice in optical microscopy, when oil immersion lenses were used to beat the diffraction limit. One hundred years later the same concept was used to increase lithography resolution [53, 54]. In this work, 200-nm features were patterned using an oil immersion lens of $NA = 1.25$ in a conventional single-layer resist.

Due to the lack of progress and the implementation expense of other techniques such as projection lithography at 157nm and 13.2nm (extreme UV), immersion lithogra-

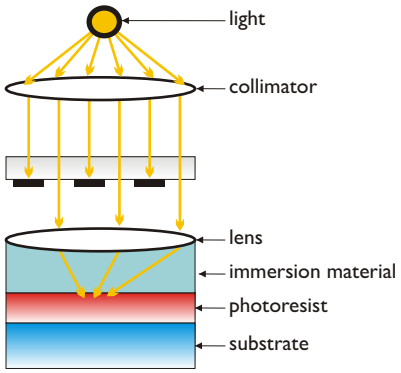

Fig. 2.7: Schematic of immersion projection lithography setup.

phy could provide the best choice for the next lithography solution with a 40% increase in resolution without the need for a completely new line of manufacturing equipment.

Recently, a number of low cost lithographic techniques have been developed based on intimate-contact lithography, which utilises the strength of optical patterning [55] and maximises resolution by using conformable membrane photomasks and resists that capture the photomask's near-field. The next section covers the developments of this lithography process.

2.4 EVANESCENT NEAR-FIELD OPTICAL LITHOGRAPHY

The resolution limits for proximity systems presented in Section 2.2 led us to the conclusion that, for small distances from the mask the quality of the image is still good for feature sizes that are diffraction-limited in projection systems. Unfortunately, the tolerances on the separation distances are difficult to achieve with conventional zero-gap contact lithography. There are two main reasons why contact lithography rarely meets the criteria for near-field lithography. Firstly, the extent of intimate contact required for near-field exposure is in the order of tens of nanometres and the rigid mask plates commonly used in contact lithography can not provide this over large areas due to wedge errors between the mask and substrate. Secondly, resists of up to 1.5 μm thickness are used in contact lithography and exposing the depth of the resist requires the use of the far-field.

The first of these problems was solved with the development of conformable contact lithography. In 1969, a new lithography technique was described by Smith [56], in which mechanical pressure was used to conform a 250-μm thick glass amplitude mask to a resist surface for the fabrication of surface acoustic wave devices. This method achieved modest feature periods of 2.5 μm, but five years later it was followed with 800-nm pitch features using a developed technique that now utilised vacuum pressure to ensure intimate contact [57]. In this paper Smith noted that higher resolution was not sought, and suggested it could be obtained through different resist schemes and

exposure parameters. The resolution of intimate contact lithography was improved further in 1981, when a conformable mask using embedded metal in an epoxy resin produced 100-nm features [58].

Twenty five years after Smith's original work a team at the University of Canterbury in New Zealand developed a near-field lithography technique using the intimate contact principle and named it Evanescent Near-Field Optical Lithography (ENFOL) [59]. The ENFOL process is not limited by diffraction because it does not use propagating fields that undergo diffraction for exposure. Instead, it couples energy from the evanescent near-field; a field without resolution limits, but one that is difficult to image. ENFOL used the flexible masks of conformable contact lithography, combining them with resist schemes that captured only the near-field of a lithography mask. The technique used 2-μm thick silicon-nitride membranes and 356–436-nm wavelengths to achieve 70-nm lines on a 140-nm period [15, 60]. Figure 2.8 shows a schematic for the ENFOL technique.

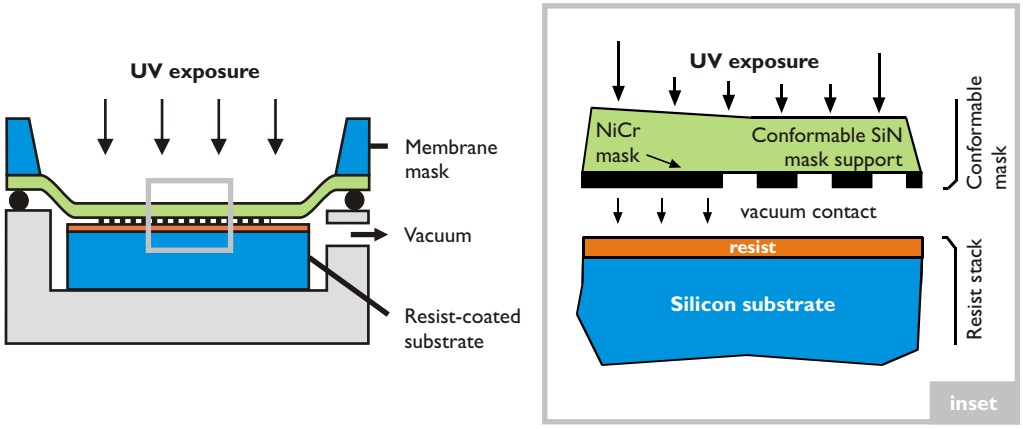

Fig. 2.8: Experimental setup for evanescent near-field optical lithography (ENFOL). Intimate contact lithography is enforced by using a conformable membrane mask and a vacuum.

Very thin resist layers, in the order of 50 nm, are used to capture the near-field intensity profile, and trilayer resist systems can be used to increase aspect ratio before pattern transfer [16, 61, 62]. It was also shown that standing waves and near-field resonances caused inconsistent results across varying grating pitch widths, which were utilised in novel techniques [63]. Near-field work was also attempted by Goodberlet *et al.* in 2002 [17], and previously by Schmid *et al.* [64, 65] with Light Coupling Masks (LCM). In Goodberlet *et al.*'s work, which achieved the best resolution of its time, sub-50nm ($\lambda/4$) lines, holes, and posts were patterned. The mask material was thin, flexible quartz; a change that reduces conformability but increases the robustness of the process, as the previous SiN masks were prone to breakages [16]. A problem for conformable contact masks can be distortion effects due to mask bending. It was shown by Ref. [66] that this can be reduced to less than 60 nm deviation on average across

a 15 mm exposure field. However, this level of deviation affects alignment of multiple layers when overlaying features of the same size.

Recently, there has been an amount of industry interest in ENFOL. Both Fuji Photo Film Co Ltd. [67] and Canon Inc. [4] have produced 30-nm features using a SiN masks. Out of the work at Canon, a research grade near-field automated stepper tool is under development, making near-field lithography a plausible reality for industry [68]. At the University of Canterbury dense 100-nm pitch gratings have be patterned by Matthew Arnold using 240-nm wavelength exposures with a PMMA photoresist. Both of these ENFOL results are sub-diffraction-limited and by using better quality resists (PMMA and in Canon's case chemically amplified high-resolution i-line resist) performance has been increased. Images of these two recent achievements are shown in Fig. 2.9.

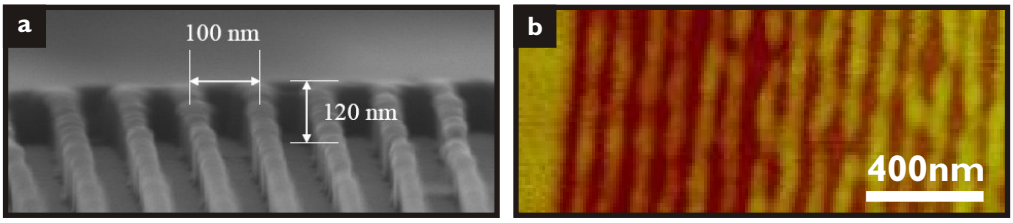

Fig. 2.9: Recent performance of ENFOL systems: (a) is an SEM scan of a resist with 30-nm features at a 100-nm period patterned in resist using 365-nm light by Canon Ltd. [4], and (b) is an AFM scan of 50-nm features on a 100-nm period exposed using 240-nm light produced at Canterbury University by Matthew Arnold.

The perfomance of ENFOL-type systems has overcome the limits of conventional lithography through the utilisation of the near-field generated from a photomask. However, the intimate contact required again raises the issue of contamination. A new technique that projects or enhances the near-field could provide an opportunity for better exposure. Enter the 'perfect lens' ...

2.5 FROM NEGATIVE REFRACTION TO THE PERFECT LENS

Negatively refracting material research is a new field that has developed hastily in recent times, but the idea of negative refraction has been around for nearly 40 years[2]. The concept was first explored by Victor Veselago[3] of the Lebedev Physics Institute in Moscow [21][4]. He investigated the electromagnetic laws that would prevail in a

[2] An excellent review article on the matter is found in Ref. [20]. A brief, independently compiled history is given here.

[3] Other authors have also been attributed with discussion of the negative phase velocity effect before Veselago [69–72].

[4] Note that the orginal version was published in Russian in 1967, not in 1964, as it is erroneously stated in the English translation.

substance that had simultaneously negative permittivity (ϵ) and permeability (μ). In this document this material will be called a Veselago Material (VM)[5].

Veselago began his argument by stating that Maxwell's equations described the relations of electromagnetic waves in any material. This led him to deduce that a VM formed a left-handed triplet (or a left-handed system) with the **E**, **H**, and **k** vectors. Figure 2.10 shows the difference between left-handed and right-handed systems, where the **E** and **H** vectors are the strength and direction of the electric and magnetic field respectively, and the **k** vector is the resulting phase propagation direction of the electromagnetic wave.

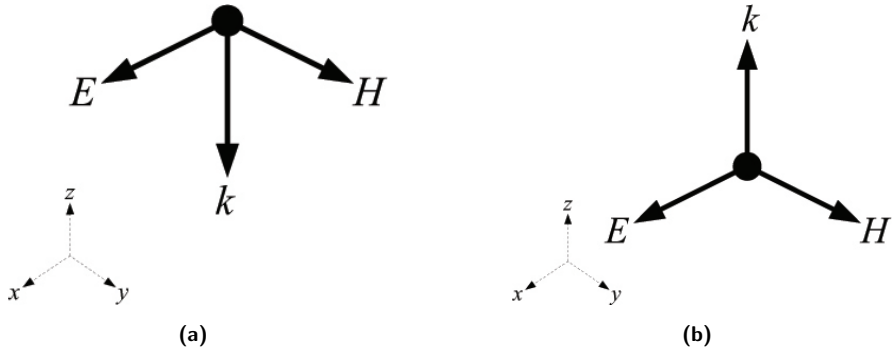

Fig. 2.10: The differences between the direction of wave propagation in (a) a left-handed and (b) a right-handed system.

Veselago discovered a number of other interesting properties that resulted from the left-handed system. He showed that wave propagation and energy flow are in opposite directions, that the Doppler effect is reversed, and that a flat slab could focus a two-dimensional image[6]. Figure 2.11(a) shows the ray diagram for a VM slab focusing a 2D image. The ratio of the source-slab:slab thickness:slab-image distances are set by the source-slab and slab thickness measurements. The standard 1:2:1 ratio will be called the Veselago ratio. With the theoretical physics predicted, the search for VMs could begin. But there was one immediate problem with this: no naturally occurring VMs exist. A fact that lead to Veselago's paper being all but forgotten.

This changed in 2000, when John Pendry of the Imperial College in London mathematically demonstrated that a slab of VM not only focuses propagating waves but also turns the evanescent decay of the near-field to exponential amplification [18]. In other words, the slab causes complete phase reversal allowing reconstruction of every spatial frequency component emitted from the source, at the image plane. Imaging with the help of the near-field could now be possible for an electromagnetic lensing system, re-

[5]A Veselago Material is also referred to in the literature as: a negative refractive index material (NRIM), a double negative material (DNM), a negative phase material (NPM), a backward traveling wave (BTW) material, and a Left-handed Material (LHM).

[6]If the sources are transparent, or allow superposition, the lens is effectively a three-dimensional lens [73].

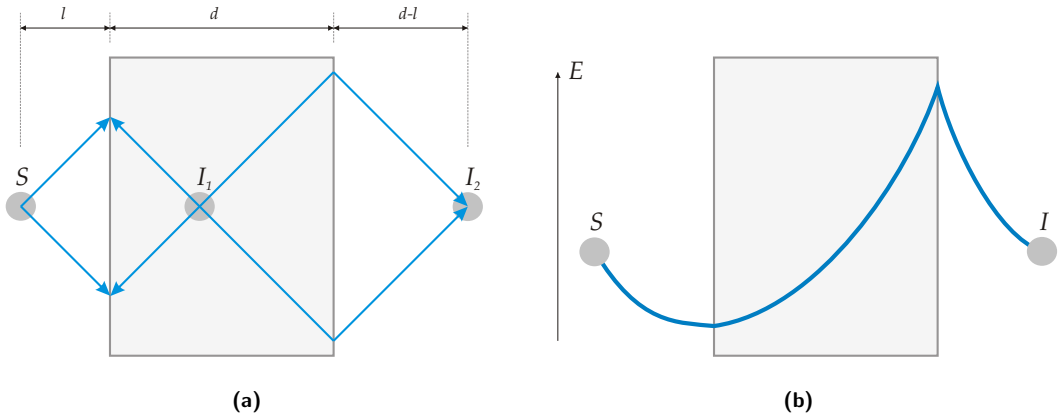

Fig. 2.11: Propagation through a VM: (a) The ray-diagram for propagating electromagnetic wavesfronts through a VM slab of thickness d. S is the source and I is the resulting image. Note that the direction given by the arrowheads is the direction of phase propagation. (b) The proposed amplification of evanescent waves in a VM, or perfect lens.

moving the age-old limitations of diffraction. In the case of no material losses a perfect image could be reconstructed — Pendry dubbed this slab a 'perfect lens'. Furthermore, Pendry suggested that a silver slab exposed with Transverse Magnetic (TM) polarisation under UV light could act as a near-field perfect lens, or a superlens. This gave solid direction for a surface-plasmon-mediated, sub-100nm, super-resolution imaging system. Pendry dubbed the superlens as the 'poor-mans perfect lens'.

Figure 2.11(b) shows the nature of evanescent waves in a perfect lens, where exponential decay becomes amplification. What this meant to electromagnetic and optical engineers alike was a potential reprieve from the sub-wavelength 'dead end'. But was Pendry's result too good to be true?

Pendry had been driven to investigate the physics of a VM after recent developments (which he had inspired) had shown that a negatively refracting material was realisable, if only for a narrow bandwidth [6, 74] (an overview is presented in Section 2.6.1). Pendry's paper had added some much needed impetus to the search for VMs, but progress from this point onwards would prove challenging. Pendry's general case was for a medium where μ and ϵ are exactly equal to -1, and specifically for a steady state environment. The effect of material losses was not studied in detail. Pendry stated that the concept was far from being a closed book, and he couldn't have been more correct. An intense debate broke out over whether a VM was a realisable material.

Initially, comments on Pendry's mathematical calculations claimed there were errors in causality assumptions, that the proposed system would suffer problems with diffraction losses, and even questioned whether a negative index material was a mathematical possibility [75, 76]. Pendry replied to these queries with vigor [77, 78], and concluded that their claims either did not apply to his summation or were wrong. How-

ever, Pendry did state that the perfect lens effect would only occur at one frequency for any real material, because of the necessity for strong dispersion with frequency. This has implications when trying to image a real source, for it will always radiate a bandwidth of frequencies. He also confessed to not being able to answer questions posed by Williams [76] relating to the diffraction losses in a sub-wavelength imaging system. To Pendry's credit, Williams did not fully grasp the negative refraction concept and seemed to be concerning himself with positive refraction phenomena.

The first group to query the physics of a VM, was Valanju *et al.* from the University of Texas in Austin. They claimed that *"causality and finite signal speed always prevent negative wave signal (not phase) refraction"* [79]. The group believed they were proving that the group velocity of a wave packet is always positively refracted, and that only the phase velocity undergoes negative refraction. Pendry *et al.* [80] demonstrated that this claim was based on an incorrect definition of group velocity. Valanju *et al.* had used a dual-frequency wave packet and failed to test a generalised wave packet, for which their arguments fail. In light of Pendry *et al.*'s comments, Valanju *et al.* replied with more theory to back-up their claim [81], and stated that Pendry *et al.* had inadvertently disproved their own case. Valanju *et al.* still believed that negative refraction violated casuality. A new approach was needed, and it came from Foteinopoulou *et al.* [82]. This group performed detailed numerical simulations to study the electromagnetic wave interactions at a freespace-VM interface. The study demonstrated that causality was not violated and negative refraction was physically plausible. The group concluded that an electromagnetic *"... wave is trapped temporarily at the interface, reorganizes, and, after a long time, the wave front moves eventually in the negative direction"*. Similar simulations were also performed by Kolinko *et al.* [83], and their results demonstrated that negative refraction was passive and physically possible. Kolinko *et al.* also simulated superlensing, with a VM slab, which was able to resolve sources that were $\lambda/20$ apart. Although Valanju *et al.*'s argument was now thought to be resolved, the 'for' and 'against' sides of the perfect lens argument were beginning to form. The perfect lens concept was facing typical scientific teething problems, and, as with convincing people that the earth is round, the struggle continued for a number of years.

In 2002, a series of cynical articles, using the titles *'Left-handed materials do not make perfect lens'* [84] and *'Is there an experimental verification of negative refraction yet?'* [85], cast more doubt on the perfect lens concept. Garcia *et al.* attempted to show that the introduction of losses into Pendry's details of his original perfect lens paper destroyed any perfect lensing action [84] (specifically, evanescent field amplification). This paper was the most convincing yet, but its main points were drowned in complicated arguments. Garcia *et al.*'s second paper attacked the first experimental work done to observe negative refraction [85]. This preliminary experimental work, performed by Shelby *et al.*, attempted to show that Snell's Law[7] was consistent in a

[7]Snell's law states that at an interface between two media (a and b), the angle from the normal

material with negative index [7]. Other groups again stepped in to support the negative refraction cause. In April 2003, a paper retaliating against Garcia *et al.*'s claims, provided proof of VM's obeying Snell's Law, *"refuting alternatives posed in the criticisms"* [86]. Further theoretical work was then performed by Felbacq *et al.*, showing that the *"negative refraction effect can be deduced directly from Maxwell Equations, without references to causality or losses"* [87]. This proof avoided Garcia *et al.*'s arguments against negative refraction in its derivation. Recently Pendry commented [88] on Ref. [84], but was immediately countered by a reply from Garcia *et al.* [89]. The issue remains unresolved.

Through claim and counter claim, much effort has been spent on ironing out the theory of perfect lensing and negative refraction. In the most recent opposition of Shelby *et al.*'s experimental proof [7], after comment [90] on Ref. [91], Pokrovsky and Efros wrote *"We have no reason to criticise the results of these experiments."* [92]. Through 2003 the number of papers to emerge supporting Pendry's sentiments increased dramatically and at the time Pendry was quoted as saying *"It is time to move on and start making use of these amazing new materials"*. Pendry's concept of a perfect lens may have been a unobtainable goal, due to real world effects, and Pendry himself agrees that *"absorption does eventually kick in to limit the energy and resolution of a left-handed slab"* [5], but everyone agreed that the developed interest would undoubtedly lead to materials that would strive for similar function and useful application.

2.6 PERFECT LENS EXPERIMENTATION

Controversy on the perfect lens theory created much interest and set the scene for the ensuing experimental achievements. After much negativity, in 2003, progress aligned in a positive direction for negative index material research. The following few sections give an overview of the current state of the experimental evidence for negative refraction and the perfect lens.

2.6.1 The Microwave Range

Although optics has been the driving force behind this thesis so far, the utility of perfect lensing to other electromagnetic frequency applications is equally promising. In fact, much of the early experimental evidence for negative index materials and negative refraction was carried out at microwave frequencies.

The first experimental evidence of a negative indexed material came from the University of California at San Diego (UCSD), and demonstrated the property at frequencies around five gigahertz. This work, by Smith *et al.*, demonstrated the transmission

for a wave at entry (θ_{inc}) and exit (θ_{trans}) are governed by the equation $n_a sin(\theta_{inc}) = n_b sin(\theta_{trans})$, where n_a and n_a are the refractive indices of the two media.

properties of a metamaterial created with arrays of resonating structures [6]. What Smith *et al.* did was construct a structure which combined previously investigated negative ϵ and negative μ materials.

It had long been known that metals produce a negative permittivity at a certain range of frequencies [11]. The phenomenon is produced by inducing resonant vibrations in the metal's conduction electrons, with the resonant frequency ranges (which are defined by the metal's structure) usually being optical. These oscillations are called plasmonic. In 1996, Pendry *et al.* showed that the frequency at which the resonance occurs could be shifted [93]. Thin metallic wire arrays can be embedded in a dielectric at different grid spacings to give resonant structures that would produce negative ϵ values at certain frequencies. A picture of an example wire grid structure is shown in Figure 2.12(a). Pendry *et al.* [74] also designed a structure that would produce a negative μ, which is shown in Figure 2.12(b). These structures, called split-ring

(a) (b)

Fig. 2.12: Structures for producing negative ϵ and μ. (a) A thin wire three-dimensional grid structure capable of producing negative ϵ, and (b) A split-ring resonator structure capable of producing negative μ.

resonators (SRR), managed to produce an effective negative magnetic permeability without the help of magnetic materials. Armed with these two structures, Smith *et al.* engineered a structure capable of producing a negative index material. Figure 2.13(a) shows an example of the material. The SRR and the vertical metal rods can easily be seen.

Smith's experiment was based on the relationship between the transparency of the material and its refractive index [6]. The refractive index, n, of a material, relates to the permittivity and permeability by the equation

$$n = \sqrt{\epsilon\mu}. \tag{2.12}$$

When the refractive index of a material is dominated by its complex component, the material will absorb and/or strongly reflect. If n is real then the material will tend to be transparent. By using a metal rod grid, Smith *et al.* were able to create a negative permittivity material across the microwave frequencies. This arrangement had a negative ϵ and positive μ, thus producing a complex refractive index and an

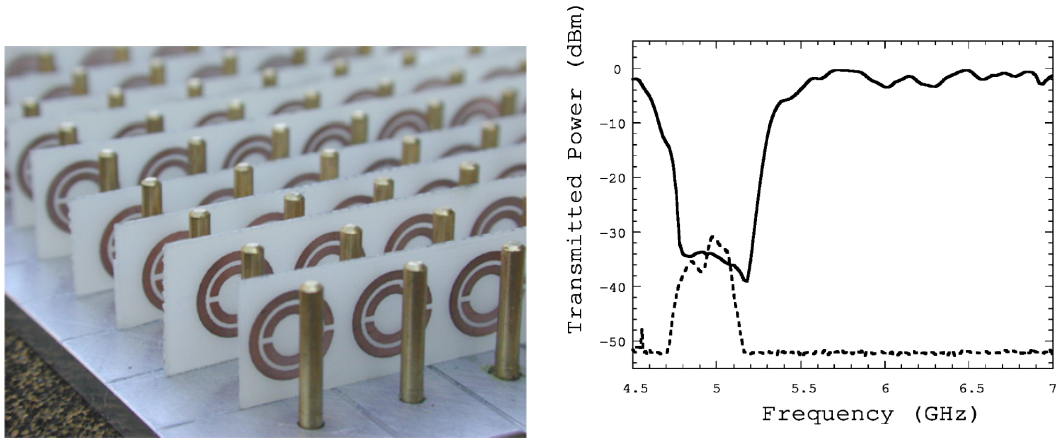

(a) (b)

Fig. 2.13: The first negative index material: (a) a picture of a structured array of metal rods and split-ring resonators capable of producing simultaneously negative ϵ and μ in two dimensions [5]. (b) Results from Smith *et al.*'s transmission experiments. The upper curve (solid line) is that of the SRR array. By adding wires uniformly between split rings, a passband occurs where μ and ϵ are both negative (dashed curve). The transmitted power of the wires alone is coincident with that of the instrumental noise floor (-52 dB) [6].

absorbing material. The group then produced a SRR grid that was able to provide a negative μ, for a bandwidth of 500MHz, in the microwave range. This structure was transparent except for the frequencies at which its permeability turned negative. When these two structures were combined (see Figure 2.13(a)), the predicted result was a bandwidth-limited negative refractive index material. Figure 2.13(b) shows the experimental results from transmission experiments. The solid line dips to show where the SRR structure becomes absorbing (i.e. has a negative μ and a complex n). When the SRR and metal bar structures are combined, the dashed line of Figure 2.13(b) shows where the structure becomes transparent. This is believed to occur because of simultaneously negative μ and ϵ, and therefore, by equation Equ. 2.12, a real refractive index.

What Smith *et al.* had effectively created was a one-dimensional VM. This restricted the group to testing only transmission characteristics. Their next step was obvious; extend the structure into two-dimensions. This time the group was led by Shelby [7]. They constructed a two-dimensional negative-index structure and set out to prove that Snell's law held for negative index materials. Figure 2.14(a) shows the material used. In this figure, the square SRR and the vertical metal rods are apparent.

The group then exposed a wedge made from the structure at frequencies where it was expected to have a negative index, and detected at which angles the radiation was emitted. They performed the experiment for positive and negative structures. The results are presented in Figure 2.14(b), and show that the microwaves were refracted

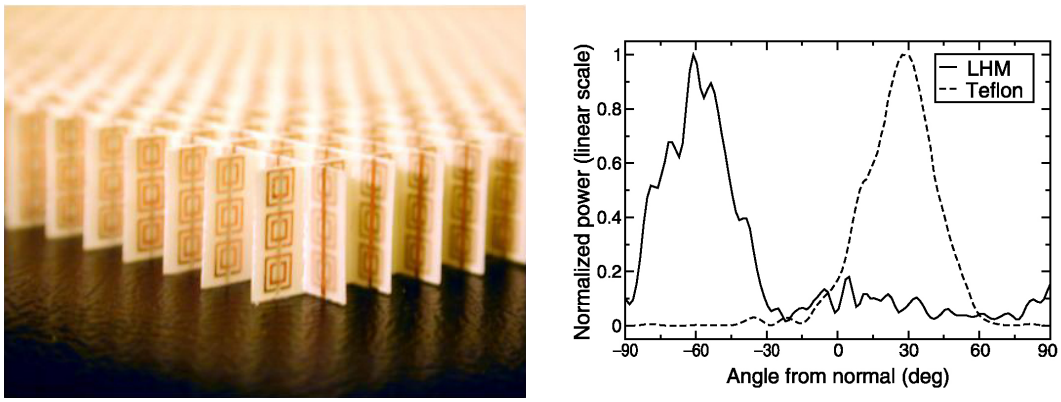

Fig. 2.14: The first negatively refracting material: (a) a picture of a structured array of metal rods and split-ring resonators capable of producing simultaneously negative ϵ and μ in two dimensions [7]. (b) Transmitted power at 10.5 GHz as a function of refraction angle for both a Teflon sample (dashed curve) and a left-handed material (LHM), or VM, sample (solid curve). The two curves were normalized such that the magnitude of both peaks is unity. For the Teflon sample, the refracted power peak was measured to be 27°, corresponding to a positive index of refraction of 1.4 ± 0.1. For the LHM sample, the peak was at 261°, from which we deduce the index of refraction to be -2.7 ± 0.1 [7].

negatively for the left-handed material (LHM) or VM, and positively refracted for teflon, which has a positive refractive index at the frequency used.

Both of these experiments came under criticism [85, 92] (as mentioned in Section 2.5), but other groups have since demonstrated negative refraction at microwave frequencies [82, 86, 94–96]. Experimental proof has even extended into the acoustic-wave [97] and water-wave realms [98].

By early 2004, the fabrication of microwave range negative index materials had progressed far enough to provide proof of both slab lensing and the ultimate goal of sub-diffraction-limited, or near-perfect imaging. A group from Moscow produced a tightly engineered slab $\lambda/20$ thick, which operated at 1.664GHz ($\lambda = 0.180m$) [8]. Figure 2.15 shows a 3D plot of the field intensities across the source, slab, and sub-diffraction-limited image. A resolution of about $\lambda/10$ was achieved at a $\lambda/5$ spacing. However, the sub-diffraction limited lensing is still limited to the near-field, where many believe it will remain [99].

With this experimental evidence the perfect lens took a large leap forward in the microwave regime. And more papers continually report similar effects for a range of configurations [100].

2.6.2 Transmission Line Analogy

The studies in the microwave region have also moved away from electromagnetic waves to look at the electric current analogy. In December 2002, a group from the University of Toronto examined the link between inductor-capacitor (L-C) distributed networks and

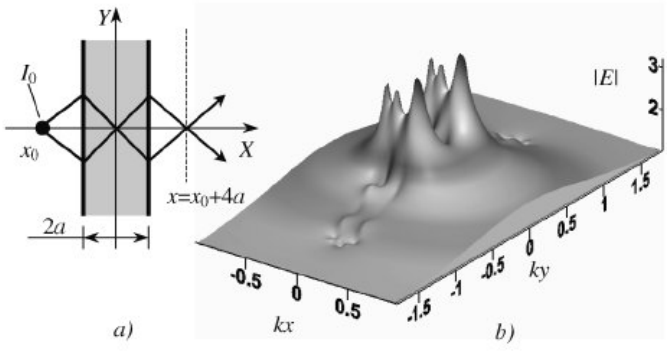

Fig. 2.15: (a) Geometry of the problem on excitation of an infinite VM slab and (b) field intensity of two sources located in the vicinity of a thin finite-width slab. The image internal to the slab and on the far side can clearly be seen. [8]

homogenous dielectrics. The group showed that if the L-C configuration is interchanged in a typical electrical analogy for a positive permittivity and permeability transmission-line (TL), sign inversion is achieved for the permittivity and permeability [101]. They then went on to show that a two-dimensional structure of this modified TL could be used to focus and negatively refract electrical signals. The results were also verified by Iyer *et al.* [9]. An example of a 2D TL media is given in Figure 2.16. These

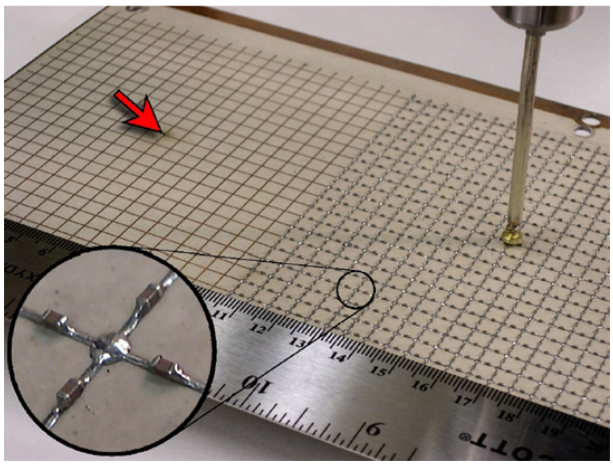

Fig. 2.16: Experimental prototype of electrical analogy VM. The positive refractive index region measures 2121 cells (105mm105mm) (left in image), and the adjacent negative refractive index (NRI) region measures 2140 cells (105mm200mm) (right in image). The inset magnifies a single NRI unit cell, consisting of a microstrip grid loaded with surface-mounted capacitors and an inductor embedded into the substrate at the central node. The near-field detecting probe is also depicted, and the arrow indicates the location of the vertical excitation probe. This image was sourced from Ref. [9].

experimenters did have difficulties trying to achieve the exact values for capacitance and inductance required to generate a refractive index of exactly -1. Instead they often produced values around -2. This meant the focal plane was blurred in the normal

direction. Nonetheless, the experimental evidence showed that a periodic structure of passive elements could provide negative refraction.

2.7 NEGATIVE REFRACTION IN THE OPTICAL REGIME

The path to negative index materials has been more difficult for the optical range. Fabrication and measurement of metamaterials at micron wavelengths and below becomes exceedingly difficult. The next two sections overview experimental attempts in the optical regime.

2.7.1 Photonic Crystals

Advances in material fabrication have allowed engineers to consider the production of nano-structured materials. One type of nano-material is called a photonic crystal [102]. Photonic crystal research is currently prolific. The goal is to try and control the propagation of light in much the same way electrons are controlled in electronic circuits. In electronic circuits, metal wires guide the electrons and transistors act as switches to control their flow. It would be a huge achievement if light could be controlled in the same manner. Photonic crystals rely on a repeated structure, which allows only certain electromagnetic oscillations to occur. These oscillation modes create energy bandgaps[8] in the crystal, and cause light to be permitted only in certain directions. Examples of how photonic crystals could be engineered as wave guides (to direct flow) and to provide semiconducting attributes (to control flow) have been proposed . It has also been shown that by shrinking the resonant structure concepts presented the microwave Section 2.6.1 to the magnitude of light's wavelengths, negatively refracting crystals can be created [103,104]. Other work has looked at how photonic crystal of negatively indexed material will affect light's propagation [105]. Sub-wavelength imaging though photonic crystals has been investigated providing nano-scale structures that could be constructed into metamaterial slabs that can focus optical wavelengths [106, 107]. Photonic crystals have also been design to give sub-wavelength imaging without the need for a negative index of refraction [108].

Creating VM's from photonic crystals would open up a world of opportunities in optical applications. Unfortunately, a lot of work is required in this area to fabricate structures that are well-formed enough to give the desired performance. Work has also been done on the effect of disorder on the properties of fabricated structures [109].

[8] Forbiden energy levels in a crystal. In semiconducting materials it is the separation between the valence and conduction bands.

2.7.2 Into the Visible

Due to fabrication constraints, producing tunable resonant electric and magnetic structures at optical wavelengths has proved difficult. Three groups have managed to form resonant elements by creating gold nano-particle structures in geometries that produce electric and magnetic resonances [10, 110, 111]. Figure 2.17 shows the nano-fabricated structure produced by the authors of Ref. [10].

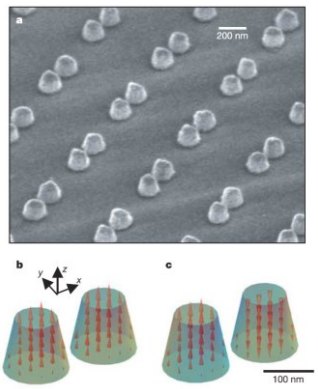

Fig. 2.17: Nanofabricated medium with magnetic response at optical frequencies. (a) Scanning electron micrograph (viewed at an angle) of an array of Au nanopillars. (b) and (c) are numerical simulations of the distribution of electric currents (arrows) inside a pair of such pillars for the symmetric and antisymmetric resonant z-modes, respectively. The non-cylindrical shape of pillars is important to provide an efficient coupling to incident light, and was intentionally introduced in the design through a choice of microfabrication procedures [10].

Both works were restricted to transmission parameters, as only a simple one-layer medium could be created. This places an element of doubt on the legitimacy of the claims as one layer, which is $\lambda/2$ in size, is probably not viewed by an impinging wave as homogeneous. The next goal in this area is to produce multi-layered structures and enable sub-diffraction-limited imaging.

2.8 THE SILVER SUPERLENS

In the original perfect lens paper [18], Pendry provided an analysis on a practical implementation of the idea known as superlensing. The common case of superlensing occurs when a material has no magnetic response and a negative real ϵ with low loss. In this instance, superlensing will occur for the TM-polarised waves. Pendry suggested using a thin slab of silver as it naturally has a negative ϵ at UV wavelengths and additionally has relatively low loss compared with other metals, allowing imaging of the P-polarised light components parallel to the lens to occur. Because of losses the effect is limited to the near-field.

Silver's aesthetic appeal can be attributed to its dispersive nature at optical frequencies. This dispersion is caused by light interacting with charged particles of the silver's surface, generating what is know as a Surface Plasmon (SP) [112]. Silver has a resonant SP frequency in the UV range, causing it to strongly absorb and reflect certain wavelengths of light [11], giving it its characteristic color. Figure 2.18 shows the dispersion curve of silver's permittivity though UV frequencies. Silver achieves its SP resonance at a real relative permittivity of -1 at $\lambda = 338nm$ (with a loss term $\epsilon'' = 0.4$), and occurs when the SP oscilation is 90° out of phase with the electric field. Thus, the negative value of permittivity and hence the potential focusing of the near-field through a thin layer of silver is mediated by strong SP oscillations [113].

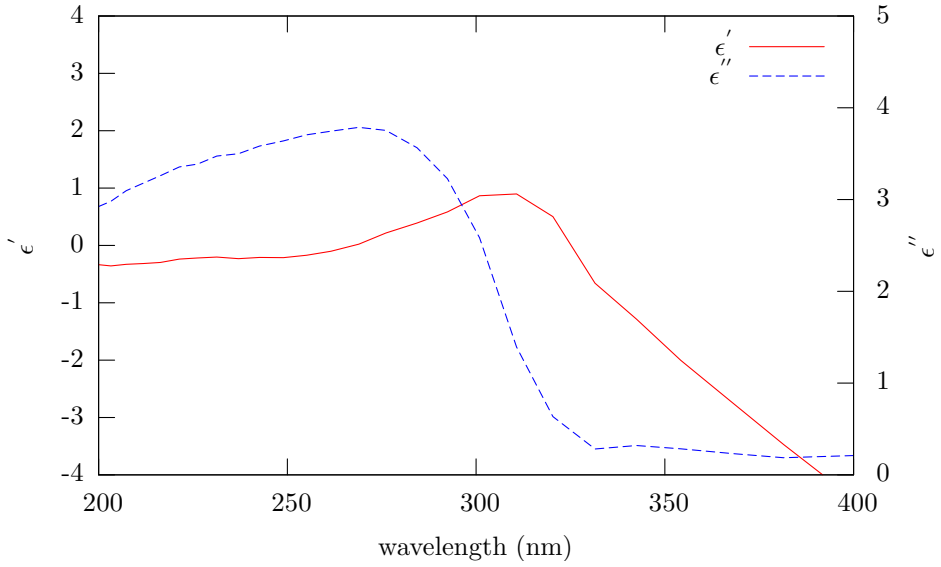

Fig. 2.18: A graph of silver's real and imaginary permittivity values in the UV light range [11].

SPs and their application have gained a lot of interest in recent years after their extraordinary influence on sub-wavelength optics was highlighted [114]. Investigation into their use as optical components has yielded waveguides [115–121], mirrors [122, 123], and interferometers [123,124], as well as possible applications in sensing [125–129] and plasmonic devices [116,124,128,130–132]. SPs have also been employed to enhance far-field [133] and near-field mircoscopy [134–136].

The generation of a SPs relies on the coupling between an electric field and longitudinal charge density oscillations at the interface between a metal and a dielectric. The spatial frequency, given as $k_x = 2\pi/\lambda_x$, is used to describe the oscillation and is given by [112] as

$$k_x(\omega) = \frac{\omega}{c}\sqrt{\frac{\epsilon_m(\omega)\epsilon_d(\omega)}{\epsilon_m(\omega) + \epsilon_d(\omega)}} \tag{2.13}$$

where ω is the angular temporal frequency of the plasmon oscillation, c is speed of light in a vacuum, and ϵ_d and ϵ_m are the real permittivity values for the dielectric and

metal, respectively. Figure 2.19 shows the relationship between temporal and spatial frequencies[9]. The light-line depicts the linear relationship between the two frequencies in a vacuum ($\omega = \epsilon_d c k_x$), and for low k_x (large λ) the silver's dispersion tracks this line. When ω gets close to the SP resonance for the silver-vacuum interface, the relation curves off asymptotically towards high k_x values. At these frequencies the SP spatial period becomes very small, the cause of much excitement among researchers.

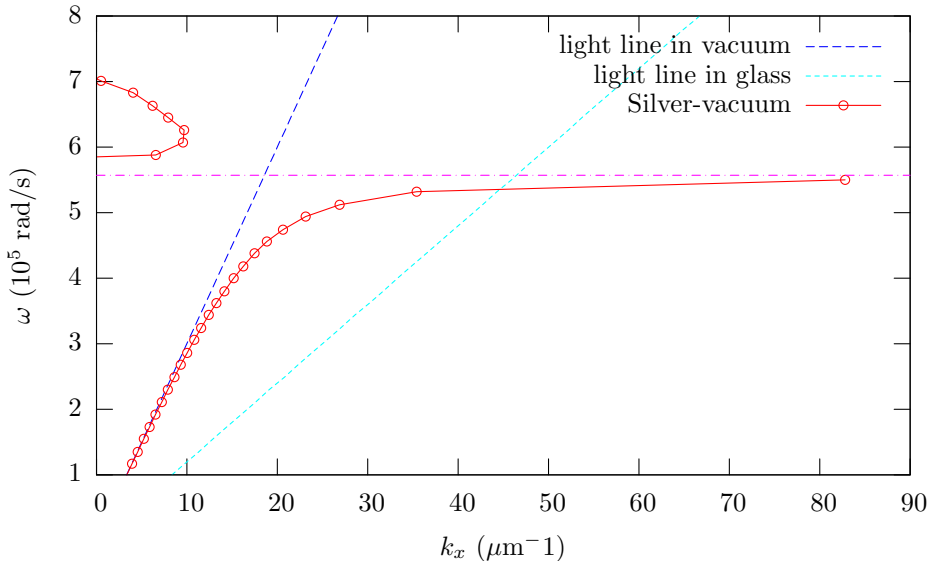

Fig. 2.19: The dispersion of wavenumber versus temporal angular frequency for light in vacuum, in glass, and on a silver-vacuum planar interface.

Energy will only couple into the SP if phase matching occurs (a k_x match), thus energy will not naturally couple from vacuum to a SP. Coupling into SPs can be achieved through a glass-silver-vacuum sandwich, by illuminating from the glass side though a thin layer of silver, giving a k_x match on the vacuum side set by the intersection of the glass light line in Fig. 2.19 (a similar technique was first proposed in Ref. [137]). Roughness has also been shown to be a method to couple into SP modes [138, 139].

A SP polariton, or wave, will travel across the surface at a group velocity given by

$$v_g = \frac{\partial \omega}{\partial k_x}. \tag{2.14}$$

As the stimulated SP gets close to resonance the group velocity tends to zero causing what is called a localised surface plasmon [113]. Away from resonance a travelling wave is generated, the source of interest for SP waveguides [116, 118–120]. It is the nature of the localised plasmon that allows us to give a simplified description of the silver superlens.

For a silver layer at a distance from a light source, the near-field first couples

[9]The dispersion curve above the resonant frequency and inside the light cone does not represent a surface-plasmon, but instead a transparent dielectric.

energy from the source to the top surface of the silver. This requires matching of k_x, which is provided by SP oscillations on the metallic mask. For superlensing, the source radiation is near resonance, producing a localised SP that remains stationary and builds in intensity through sustained excitation. The SP mode then couples through the silver [140, 141]. The efficiency of the coupling is proportional to the exponential of the thickness, thus thicker lenses will fail to produce the superlensing effect. For the thinner lenses, the coupled SP on the second surface is again localised and builds in intensity, producing a near-field on the bottom surface that can be imaged in a resist some distance below. The geometry and dielectric property of the silver allows for amplification of the near-field [139, 142], giving rise to higher contrast fields than one would expect at the source. However, since this amplification is SP mediated the intensity profile of the electric field differs to that of a perfect lens. Figure 2.20 shows the difference between amplification inside a perfect lens and a superlens [22,143]. This profile is similar to profiles through SP waveguides [115]. Another paper has attempted to maximise the amplification through the silver, obtaining the highest transmission at a thickness of 50-nm for $\lambda = 514$nm [142].

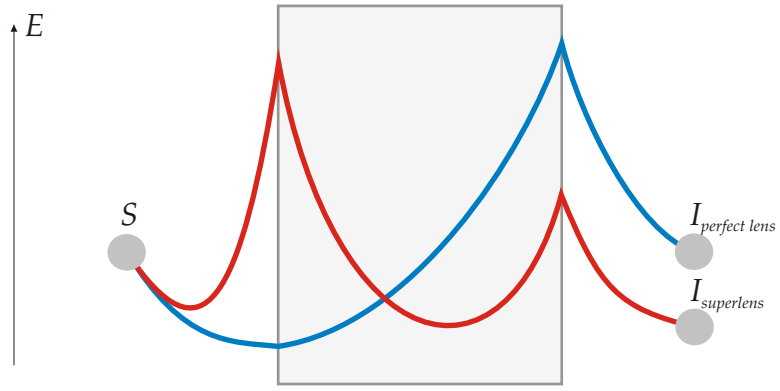

Fig. 2.20: Amplification of evanescent waves in a perfect lens compared with a superlens. The superlens case is mediated by surface waves.

SPs have also been employed via other methods to achieve sub-diffraction-limited imaging [144, 145]. Investigation of the superlens effect at infrared frequencies has seen implementations based on photonic crystals [106, 107, 146, 147] and SiC [148] also produce sub-diffraction-limited imaging.

It is the principle of the superlens technique, in combination with near-field lithography that forms the main focus of this thesis. In the next section, the technique developed by the author that extends the performance of ENFOL by utilising SPs is introduced.

2.9 PLANAR LENSING LITHOGRAPHY

By combining proven near-field lithography techniques with the novel concept of the silver superlens a new technique was been developed, named Planar Lensing Lithography (PLL). Preliminary simulation work showed that a slab of silver could be placed in the near-field region of a lithography mask and project sub-diffraction-limited images into a resist below [22]. The challenge that lay ahead and in turn the focus of this thesis was to gain sub-diffraction-limited imaging and prove Pendry's superlensing idea in a lithography environment.

To begin with, the ENFOL process developed at the University of Canterbury [15, 16] was redesigned to be based on a more robust glass-coverslip membrane mask, along the same lines as Goodberlet *et al.* [149]. Figure 2.21 shows the new setup applied to near-field intimate contact lithography.

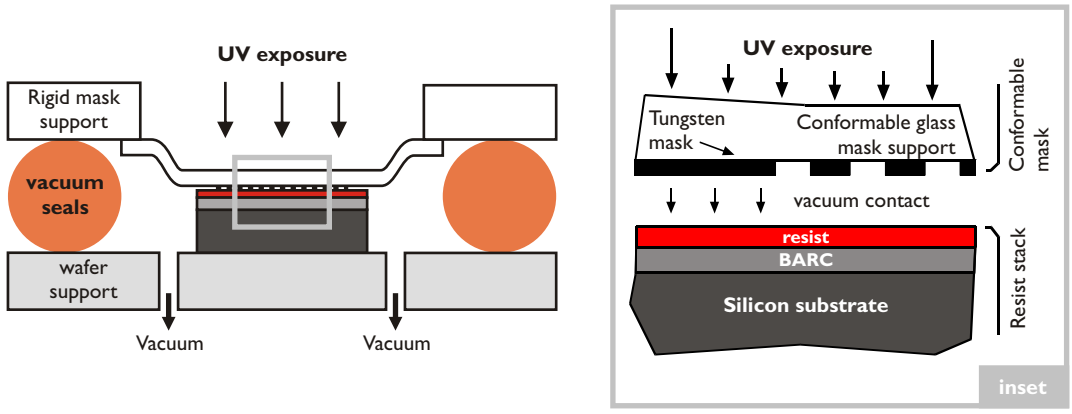

Fig. 2.21: A schematic of the experimental setup for conformable mask evanescent near-field optical lithography.

The modified setup for PLL is given in Fig. 2.22. A silver layer and two spacer layers are introduced, with the spacer layers enforcing controllable separation between mask and lens, and lens and resist. The apparatus, experimental setup, and fabrication are covered in Chapters 4 through 5.

The first work published on imaging through a silver layer showed that a 120-nm thick lens could image sub-micron features [23]. However, just as the perfect lens concept had it critics, so too did PLL. A comment was produced on our work [150], and the fair criticisms were accepted, but other claims were strongly rebutted [151].

The process was developed further to produce sub-wavelength features through a 85-nm thick layer of silver [152, 153], before conclusive proof of sub-diffraction-limited imaging was achieved with a 50-nm thick layer [24], confirming Pendry's controversial theory. Subsequently, improvements to our process have been made by using narrow-band exposures [154], eliminating exposure due to off resonance wavelengths. Previ-

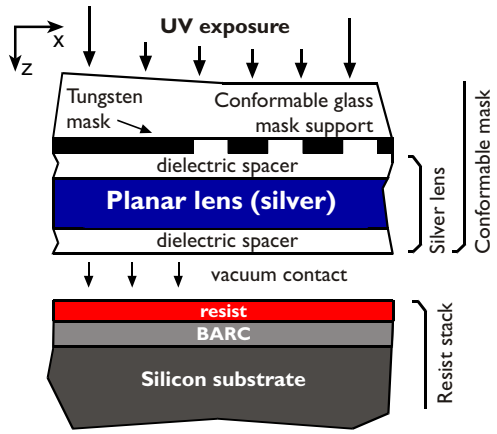

Fig. 2.22: A schematic of the experimental setup for planar lens lithography.

ously, the silver had been relied on to filter unwanted wavelengths [23]. Super-resolution (120-nm pitch feature imaging) was obtained independently by another group at the same time [31]. The two experimental demonstrations are similar in many respects, with both using imaging into a photoresist layer. The distinct difference is that our technique [24] is compatible with subsequent pattern transfer, whereas the method of Fang *et al.* [31] is not, so it cannot be used as a lithographic process. Since then work by the Berkeley group has been improved to obtain a 100-nm pitch feature [143].

Due to the interest around the subject, experimental evidence of superlensing led to publicity on the original 120-nm imaging lens [155] and the attainment of super-resolution [27–30]. Additionally, a time-line on negative refraction was published in the 'New Scientist' journal placing our work and Fang *et al.*'s work as the latest installment in its history. A reproduction of this time-line is shown in Fig. 2.23.

A range of other plasmonic lithography work has emerged in recent years, attempting to utilise a metal's ability to support high spatial wavelengths [156–162]. These techniques have managed to achieve resolutions below 100-nm pitch. For example, in Lou *et al.*'s work, using a 436-nm light source, 50-nm features were patterned on a 100-nm period using interference between SPs generated by 60-nm wide, 300-nm pitch features in a silver mask [156]. However, many of these techniques do not allow accurate control of the patterned produced due to reliance on SP wave-interference patterns or nano-particle manipulation.

Work has also been done to show that a multiple-layered lens could have performance advantages over a single-layered lens [26], increasing tolerance and reducing resolution limits. Recently, this has been experimentally tested by the author [25]. A schematic for double-layer PLL is shown in Fig. 2.24

Fig. 2.23: Reprint of negative refraction time-line published in New Scientist journal on the 4th of June, 2005 – "*Illusions of a starry, starry night*". The time-line includes the work produced here at the University of Canterbury and is highlighted by the grey box.

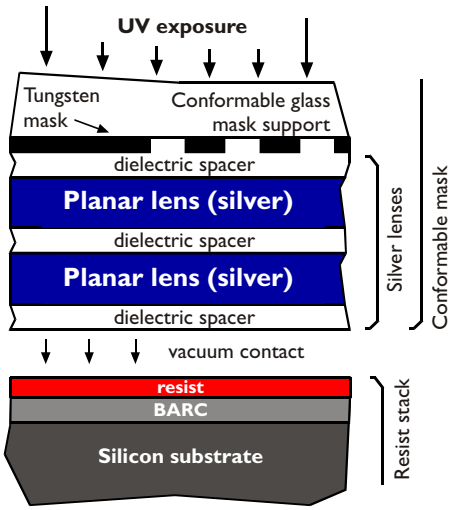

Fig. 2.24: A schematic of the experimental setup for double-layer multiple planar lens lithography.

2.10 ANALYTICAL AND SIMULATION STUDIES

It is a strength in the development of any technology to have the ability to predict performance. With this in mind, a range of methods for simulating PLL's abilities were investigated. There are a number of techniques available for the modelling of electromagnetic waves. These range from full-wave simulations to transmission-line analogies. All techniques have strengths and weaknesses, as all simulations make basic assumptions to create a working model. The following sections give a brief summary of available techniques.

2.10.1 Analytical Techniques

There have been a number of investigations into both perfect lenses and superlenses using analytical techniques [18,163,164]. The general concept is to calculate the transmission of individual wave-vectors through a lensing slab. In Smith *et al.*'s investigation on the limitations of sub-diffraction-limited imaging with a VM slab [164], it was concluded that it was possible but only over a *"restrictive range of parameters"*. They indicated that adhering to the restrictions was demanding, though possible with today's technology. Superconducting and active materials were suggested as structures for loss minimisation. Smith also devised a theoretical limit based on the losses present in the slab for a Transverse Electric (TE) polarised wave:

$$\frac{\lambda}{\lambda_{min}} = -\frac{1}{2\pi} ln \left| \frac{\partial \mu}{2} \right| \frac{\lambda}{d} \tag{2.15}$$

where λ_{min} is the minimum spatial period present, $\partial\mu$ is the deviation from -1 of the permeability, and d is the thickness of the slab. The calculation for a silver superlens requires a TM polarisation formalisation (substitute ϵ for μ), and gives the expected limit for a 50-nm PLL lens of 226 nm (A limit that has been overcome).

The superlens was modelled in more detail by Fang *et al.* [163], who testing a superlens's ability to resolve two point-sources at sub-wavelength spacings. A minimal resolution of $\lambda/6$ was obtained with a 36-nm thick silver film with 364-nm wavelength light. Another paper demonstrated that the superlens effect is fundamentally a near-field effect [99].

For the purpose of exploring PLL, analytical solutions are limited because they do not take into account the interaction effect with the near-field mask. The next few sections cover three methods for full-vector numerical simulation that have been used in VM and superlens research. These are the multi-multipole, the finite element, and the finite-difference time-domain methods.

2.10.2 Multiple Multipole Method

In a Multiple Multi-pole (MMP) [165] simulation areas are divided into domains, where material parameters can be set as constants. Around the edges of these domains boundaries are created which are set with conditions that relate to the nature of the boundary, for example periodic or metal boundaries. A number of basis expansions, which are solutions to Maxwell's equations, are then used to describe the fields in the domain that are bound by the conditions set on the boundaries.

MMP was the first method used to explore the nature of the PLL setup [22]. in which Blaikie *et al.* demonstrated that PLL could achieve a resolution of below $\lambda/4$. The method had previously been used to demonstrate that ENFOL could acheive $\lambda/20$ resolution [16, 166, 167].

2.10.3 Finite Element Method

The Finite Element Method (FEM) is a now commonly used numerical method that was originally devised for structural modelling. It is based on an integral method that breaks a simulation domain up into individual elements and attempts to minimise the energy in the system. By using integration functions that solve Maxwell's equations, electromagnetic propagation can also be modelled. A 2D analysis of the first experimental evidence of negative refraction [6] was perform using the FEM [83], as well as a study of the silver superlens [168]. This paper investigated multiple layer superlenses, but not in a near-field lithography environment.

2.10.4 Finite-Difference Time-Domain Method

The bulk of numerical simulation work on VMs has been performed with Finite-Difference Time-Domain (FDTD). Historically, this is the result of disputes about the reality of negative refraction that cited violations of casuality [84], and the ability of the FDTD method to facilitate temporal investigations of VMs and superlens made it an excellent tool.

The first FDTD simulation of VMs was produced by Ziolkowski *et al.* who analysed the temporal performance of the system and the effect of loss [169]. He concluded that *"the Pendry perfect lens effect is not realisable with any realistic metamaterial"*. The basic result, which is the conclusion of many simulation papers, was that losses limit resolution for a VM slab lens. Other researches have investigated similar effects [82, 170–173], as well as disorder in realistic metamaterial slabs [109]. The FDTD method has also been used to study surface plasmons in 3D for the application of nanometer focusing of light by heterowaveguides [121].

Due to the strength of support for FDTD in the literature, the method was chosen to explore the performance of PLL. The next chapter details the formulation of the FDTD algorithm, the development of software to perform the simulations, and simulation validation. Detailed results of PLL analysis for both the FDTD and a developed analytical model is provided in chapter 8.

Chapter 3

SIMULATION TECHNIQUES

"You can predict exactly what a machine will do if you have sufficient knowledge of it."

- Barry Long

Accurate and concise experimental work is always aided by theory and simulation. Simulation can provide a good grounding for the prediction of results and help guide decisions on experimental setup and evaluation. However, decisions based on simulations are only as good as the simulation technique used. This means that the careful design of simulation tools and an understanding of their limitations are essential requirements.

An overview of a selection of available simulation tools was given in Section 2.10. It was found that FDTD was a commonly used tool among VM researchers [9, 82, 101, 169–171]. For this reason and because of FDTD's ability to produce temporal data important to the dynamic superlens experiment, the PLL setup was thoroughly investigated with FDTD. Validation was also performed against simulations using a FEM and exact solutions for particular geometries. The following sections detail the background of FDTD and how the simulation environment was setup to study PLL. The FDTD formulation is provided for 1D and was extended to two- and three-dimensional simulations. The 2D simulation was used extensively but the 3D was not due to a lack of computational power which was needed for accurate simulation.

3.1 FINITE-DIFFERENCE TIME-DOMAIN METHOD

FDTD was first proposed by Yee [174]. Yee noticed that a first order approximation of Maxwell's Equations could be made to allow discretisation in space and time. Maxwell's

equations are given as

$$\nabla \times \mathbf{E} = \mathbf{K} - \mu_r \mu_0 \frac{\partial \mathbf{H}}{\partial t}, \tag{3.1a}$$

$$\nabla \times \mathbf{H} = \mathbf{J} + \epsilon_r \epsilon_0 \frac{\partial \mathbf{E}}{\partial t}, \tag{3.1b}$$

$$\nabla \cdot \mathbf{E} = \sigma, \tag{3.1c}$$

$$\nabla \cdot \mathbf{H} = 0, \tag{3.1d}$$

where $\mathbf{E}$ and $\mathbf{H}$ are the electric and magnetic fields, respectively, and $\mathbf{J}$ and $\mathbf{K}$[1] are the electric and magnetic polarisation currents, respectively. Yee took Equ's 3.1a and 3.1b and constructed linear approximations for the space and time derivatives over discrete steps. Here we will see how this is done for a plane wave travelling in the z-direction, with magnetic and electric components in the y- and x-directions, respectively. This is called the one-dimensional problem. By extending the formulation presented here, both 2D and 3D FDTD code was developed. For this case we will assume an isotropic medium with no charge (i.e. no polarisation currents). In this situation, Equ's 3.1a and 3.1b are written as

$$\frac{\partial E_x}{\partial z} = -\mu_r \mu_0 \frac{\partial H_y}{\partial t}, \tag{3.2a}$$

$$\frac{\partial H_y}{\partial z} = \epsilon_r \epsilon_0 \frac{\partial E_x}{\partial t}. \tag{3.2b}$$

The equations are now discretised, with a spatial step of Δz and a time step of Δt. Yee then constructed a sampling grid for E_x and H_y, which were offset by half a sampling step in space and time[2]. Figure 3.1 shows the spatial and time dimensions mapped onto a two-dimensional grid. For this example, H_y lies on the half steps of the space and time grids.

If we discretise Equ. 3.2a around the point $(x, y, z = k + \frac{1}{2}, t = n)$, the derivatives are replaced with the following discrete versions:

$$\frac{\partial E_x}{\partial z} \rightarrow \frac{E_x|^n_{i,j,k+1} - E_x|^n_{i,j,k}}{\Delta z}, \tag{3.3}$$

and

$$\frac{\partial H_y}{\partial t} \rightarrow \frac{H_y\big|^{n+\frac{1}{2}}_{i,j,k+\frac{1}{2}} - H_y\big|^{n-\frac{1}{2}}_{i,j,k+\frac{1}{2}}}{\Delta t}. \tag{3.4}$$

Repeating this for equation Equ. 3.2b around the point $(x, y, z = k, t = n - \frac{1}{2})$, we

[1] The magnetic polarisation current is added for symmetry.

[2] The notation used here is as follows: the sample given as $E_x|^t_{x,y,z}$ corresponds to the E_x field value at the point (x, y, z) in space, at a time step t. For this example the references to points in the x and y plane are arbitrary.

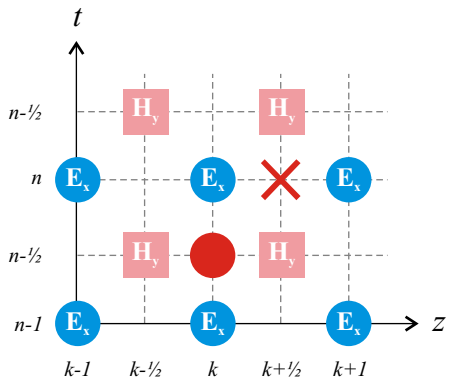

Fig. 3.1: Two-dimensional map of the space and time dimensions of the plane wave example. E_x and H_y are offset by half a step size in space and time. The dark cross is the point at which equation Equ. 3.2a is discretised, and the dark circle is for equation Equ. 3.2b.

arrive at the two equations

$$\frac{E_x|^n_{i,j,k+1} - E_x|^n_{i,j,k}}{\Delta z} = -\mu_r\mu_0 \frac{H_y|^{n+\frac{1}{2}}_{i,j,k+\frac{1}{2}} - H_y|^{n-\frac{1}{2}}_{i,j,k+\frac{1}{2}}}{\Delta t}, \tag{3.5a}$$

$$\frac{H_y|^{n+\frac{1}{2}}_{i,j,k+\frac{1}{2}} - H_y|^{n+\frac{1}{2}}_{i,j,k-\frac{1}{2}}}{\Delta z} = \epsilon_r\epsilon_0 \frac{E_x|^n_{i,j,k} - E_x|^{n-1}_{i,j,k}}{\Delta t}. \tag{3.5b}$$

These equations can now be solved for the only unknowns, namely $H_y|^{n+\frac{1}{2}}_{i,j,k+\frac{1}{2}}$ and $E_x|^n_{i,j,k}$. This sets up what is called a time-step leap-frog simulation. One equation solves for E_x using H_y[3] and the other for H_y using E_x. The final Yee FDTD algorithms equations are

$$E_x|^n_{i,j,k} = E_x|^{n-1}_{i,j,k} + \frac{1}{\epsilon_r\epsilon_0}\frac{\Delta t}{\Delta z}(H_y|^{n+\frac{1}{2}}_{i,j,k+\frac{1}{2}} - H_y|^{n+\frac{1}{2}}_{i,j,k-\frac{1}{2}}), \tag{3.6a}$$

$$H_y|^{n+\frac{1}{2}}_{i,j,k+\frac{1}{2}} = H_y|^{n-\frac{1}{2}}_{i,j,k+\frac{1}{2}} - \frac{1}{\mu_r\mu_0}\frac{\Delta t}{\Delta z}(E_x|^n_{i,j,k+1} - E_x|^n_{i,j,k}). \tag{3.6b}$$

With these equations the time evolution of an electromagnetic field can be simulated, as long as the initial state of the system is known. By assigning different values of ϵ_r and μ_r[4] at different points on the grid, different media can be simulated. This is the focus of the next section where we attempt to find a way to simulate a highly dispersive material, like a perfect lens.

[3] Past values of E_x are also used.

[4] This effectively translates to a scalar grid of ϵ and μ, i.e. $\epsilon|_{x,y,z}$.

3.1.1 Dispersive Media

The FDTD simulation, as Yee described it, did not come with the capability of simulating dispersive media. This is understandable considering the equations it was based on did not allow for dispersion. Thus the simulation equations require re-deriving for the dispersive case. It is noted in Ref. [169] that *"... there is no possibility of inserting a constant negative permittivity or permeability into a leapfrog staggered grid FDTD simulator and having it run stably"*. This is because of the implied material properties at frequencies of zero and infinity.

A material is made dispersive as a result of polarisation currents, which appear in Equ's 3.1a and 3.1b. The polarisation currents are linked to their respective field through a term called susceptibility. The relations between susceptibility and field are given in Ref. [175] as

$$\mathbf{J} = \epsilon_0 \chi_e \frac{\partial \mathbf{E}}{\partial t}, \tag{3.7a}$$

$$\mathbf{K} = \mu_0 \chi_m \frac{\partial \mathbf{H}}{\partial t}, \tag{3.7b}$$

where χ_e and χ_m are the electric and magnetic susceptibilities, respectively. To provide the dispersive properties present in known negative index materials, a Lorentz model is used for the susceptibility. A one-zero Lorentz model for susceptibility is given in Ref. [176] as

$$\chi = \frac{\omega_0^2[\chi_\alpha - i(\frac{\omega}{\omega_0})\chi_\beta]}{\omega_0^2 - \omega^2 - i\Gamma\omega}. \tag{3.8}$$

where ω_0 is the resonant frequency, ω is the frequency in radians per second, and χ_α, χ_β, and Γ are variables related to the material. This was generalised, to allow more flexibility and simpler programming, to give

$$\chi = \frac{i\omega\gamma_e + \delta_e}{\omega^2 a_e + i\omega b_e + c_e} \tag{3.9}$$

for the electric susceptibility where, for the Lorentz model, $\gamma_e = -\frac{1}{\omega_0}$, $\delta_e = \omega_0^2$, $a_e = -1$, $b_e = -\Gamma$, $c_e = \omega_0^2$. By substituting equation Equ. 3.9 into Equ. 3.7a and doing the inverse Fourier transform we get

$$-a_e \frac{\partial^2 \mathbf{J}}{\partial^2 t} + b_e \frac{\partial \mathbf{J}}{\partial t} + c_e \mathbf{J} = \gamma_e \epsilon_0 \frac{\partial^2 \mathbf{E}}{\partial^2 t} + \delta_e \epsilon_0 \frac{\partial \mathbf{E}}{\partial t}. \tag{3.10}$$

The same is done for the magnetic case. These equations are then taken through the same steps as above (section 3.1) to discretise them onto the FDTD grid. In this case there is a second derivative present, so new substitutions are required and are

performed around a different node. For the electric field these are

$$\frac{\partial \mathbf{E}}{\partial t} = \frac{\mathbf{E}|^{n+1} - \mathbf{E}|^{n-1}}{2\Delta t}, \tag{3.11a}$$

$$\frac{\partial^2 \mathbf{E}}{\partial^2 t} = \frac{\mathbf{E}|^{n+1} - 2\mathbf{E}|^{n} + \mathbf{E}|^{n-1}}{(\Delta t)^2}. \tag{3.11b}$$

Note these equations do not depend on space and are structured around the node $(x, y, z, t = n)$. By substituting the respective variations of Equ's 3.11a and 3.11b into Equ. 3.10, and solving for $\mathbf{J}|_{i,j,k}^{n+1}$, we arrive at an equation for the electrical polarisation current

$$\begin{aligned} \mathbf{J}|_{i,j,k}^{n+1} = {} & c_{JE_1}\mathbf{E}|_{i,j,k}^{n+1} + c_{JE_2}\mathbf{E}|_{i,j,k}^{n} + c_{JE_3}\mathbf{E}|_{i,j,k}^{n-1} \\ & + c_{JJ_2}\mathbf{J}|_{i,j,k}^{n} + c_{JJ_3}\mathbf{J}|_{i,j,k}^{n-1}, \end{aligned} \tag{3.12}$$

where the coefficients are given in appendix A. Here a causality problem is met; equation Equ. 3.12 requires $\mathbf{E}|_{i,j,k}^{n+1}$ and the equation for $\mathbf{E}|_{i,j,k}^{n+1}$ (derived from Equ. 3.1b) requires $\mathbf{J}|_{i,j,k}^{n+1}$. To solve this, Equ. 3.12 is substituted into the electric equation, which is then computed before Equ. 3.12. The resulting equations are given in appendix A, and, through the control of their coefficients, they provide flexible dispersive material modelling.

3.1.2 Absorbing Boundary Condition

Any simulation technique must be able to provide natural conditions at its boundaries. This can often be provided through wrap-around conditions, where the fields from one plane are copied to the opposite side, or an Absorbing Boundary Condition (ABC), where a layer attempts to absorb any incoming wave without reflection[5]. Figure 3.2 shows the ABC typical scenario, in which a wave impinging on a planar interface at any angle is completely absorbed without reflection.

An ABC allows 'open' regions, or unbounded simulations. For years the FDTD algorithm was without an effective ABC, then in 1996, J.P. Berenger introduced an ABC, which is now called a Perfectly Matched Layer (PML) [177]. He showed that by producing a field-splitting formulation of Maxwell's equations, where fields are split into orthogonal components, an effective absorbing layer could be created. This was a huge development for the practicality of FDTD simulations, and is now the most common termination condition for FDTD simulations. The one problem with the PML is that is creates an unnatural layer, which is governed by different equations from the rest of the simulation. This leads to programming and computational problems. For these reasons a new type of ABC was investigated.

[5] An FDTD simulation cannot simply be unterminated, for this actually leads to an implied perfect conductor termination, and gives total reflection.

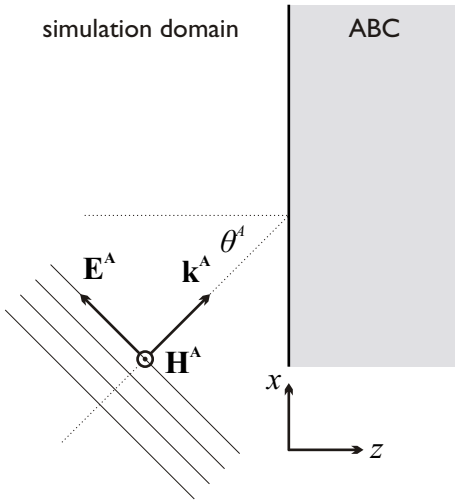

Fig. 3.2: Configuration for a TM-polarised plane wave impinging on an absorbing boundary.

In 1994, Chew *et al.* [178] produced a derivation of an anisotropic perfectly-matched lossy medium. They showed that only the transverse components of a planar medium's properties affect reflections. This left the normal component of the anisotropic medium's properties to be lossy without disturbing transmission. This idea lends itself perfectly to an ABC. A year later, Sacks *et al.* [179] investigated the idea's performance as an ABC. And then in 1997, Ziolkowski [180] showed how an ABC of this type could be designed. Ziolkowski used a Lorentz model (Equ. 3.8 with $\chi_\beta = 0$) to implement the ABC. He showed that this implementation was limited by its absorbing bandwidth, but two papers which followed broadened the performance of the ABC [176], [181]. In Ref. [176], the new ABC was compared to the PML, and was found to perform as well as the PML for specific frequencies. Here the concept of an anisotropic material is explained and the details for its use as an absorber given.

To create an anisotropic medium we must have a construct which can handle different permittivity and permeability along the three axes. To allow this, a diagonal matrix (tensor) is created, where the diagonal terms relate to the x,y, and z values of the material's properties, like so

$$\boldsymbol{\epsilon}_r = \begin{bmatrix} \epsilon_x & & \\ & \epsilon_y & \\ & & \epsilon_z \end{bmatrix} \quad \text{and} \quad \boldsymbol{\mu}_r = \begin{bmatrix} \mu_x & & \\ & \mu_y & \\ & & \mu_z \end{bmatrix}. \tag{3.13}$$

If a ABC is now required in the x-y plane, the requirements for the anisotropic medium

are given from Ref. [178] as

$$\epsilon_x = \mu_y = \frac{1}{\epsilon_z}, \tag{3.14a}$$

$$\mu_x = \epsilon_y = \frac{1}{\mu_z}, \tag{3.14b}$$

$$\mu_x = \epsilon_x. \tag{3.14c}$$

If it is a free-space boundary, the ABC condition is provided as long as these conditions are held. Thus we can make ϵ_x and μ_x lossy (complex) to provide the absorbing condition.

The Lorentz model gives us tools to provide the inverse parameters. Using Equ. 3.9 and

$$\boldsymbol{\epsilon}_r = 1 + \boldsymbol{\chi}, \tag{3.15}$$

we attempt to find the parameters that will be entered into the model to achieve the inverse parameters required by Equ's 3.14a and 3.14b. For Equ. 3.14a we have

$$\epsilon_x = 1 + \chi_x = \frac{1}{\epsilon_z} = \frac{1}{1 + \chi_z}, \tag{3.16}$$

therefore

$$\chi_z = \frac{-\chi_x}{1 + \chi_x}. \tag{3.17}$$

Finally, if we substitute equation Equ. 3.9 for χ_x we have

$$\chi_z = \frac{-i\omega\gamma_x - \delta_x}{\omega^2 a_x + i\omega(\gamma_x + b_x) + (\delta_x + c_x)}, \tag{3.18}$$

and by assuming χ_x takes on the same form as Equ. 3.9, we have the following parameter settings for an ABC

$$\begin{aligned} \gamma_z &= -\gamma_x, \\ \delta_z &= -\delta_x, \\ a_z &= a_x, \\ b_z &= \gamma_x + b_x, \\ c_z &= \delta_x + c_x. \end{aligned} \tag{3.19}$$

The one-zero model (Equ. 3.8) is preferred over an all-pole model, so a broader absorbtion bandwidth could be achieved [176].

Unfortunately, the Lorentz ABC derived here could not perform well over a wide enough bandwidth, thus another ABC option was sought. This meant that a PML had to be implemented and was derived from the field splitting technique presented in

Ref. [182]. As the technique that was implemented from source of Ref. [182] the details are not present here, but for completeness they are reproduced in Appendix B.

3.2 PLANE-WAVE SOURCE

A simple source can be implemented in an FDTD simulation by setting grid points in the simulation to the required value. However, this creates what is called a 'hard' source that reflects any impinging radiation causing standing waves between the source and reflective objects in the simulation. The source required for a lithography simulation must replicate the radiation produced by a lamp in a lithography system. This is covered by the following criteria:

1. The source must behave as if it was a great distance away, i.e. no standing waves should exist between the source and any element in the simulation.

2. The spectrum of the source must be similar to that of a lithography lamp spectrum.

These two criteria are addressed in the next two sections.

3.2.1 A Transparent Source

A transparent source in a simulation provides a propagating source field travelling at a direction away from the source interface, while allowing scattered waves to pass though the interface unimpeded in the opposite direction.

A total-field/scattered-field (TF/SF) technique is a common solution to this problem [182]. In this technique the linearity property of Maxwell's equations is exploited, by decomposing the total electric and magnetic fields into scattered and incident fields like so,

$$\mathbf{E}_{total} = \mathbf{E}_{inc} + \mathbf{E}_{scat} \tag{3.20a}$$

$$\mathbf{H}_{total} = \mathbf{H}_{inc} + \mathbf{H}_{scat} \tag{3.20b}$$

With these equations in mind two regions are created; a total-field region for the simulation, and a scattered field region to allow unimpeded flow of the scattered waves. The key to this technique is to carefully manage the interface between these two regions. This is most easily analysed in the one-dimensional case. The layout for the single space dimension was given in Fig. 3.1.

In this formulation

$$H_{y,total}\big|_{k+\frac{1}{2}}^{n+\frac{1}{2}} = H_{y,total}\big|_{k+\frac{1}{2}}^{n-\frac{1}{2}} + \frac{\Delta t}{\mu \Delta z}\left(E_{x,total}\big|_{k+1}^{n} - E_{x,total}\big|_{k}^{n}\right), \tag{3.21}$$

and using Equ. 3.20a we can substitute for $E_{y,total}|_i^n$ giving us the result

$$H_{y,total}|_{k+\frac{1}{2}}^{n+\frac{1}{2}} = H_{y,total}|_{k+\frac{1}{2}}^{n+\frac{1}{2}} + \frac{\Delta t}{\mu \Delta z} \cdot \left(E_{x,total}|_{k+1}^{n} - E_{x,scat}|_{k}^{n}\right) - \frac{\Delta t}{\mu \Delta x} \cdot E_{x,inc}|_{k}^{n} \quad (3.22)$$

This is repeated for the electric field to provide an FDTD algorithm formulation for a transparent source at $z = k$. $E_{x,inc}$ and $H_{y,inc}$ determine the nature of the incident wave. For example, $H_{y,inc}$ can be set as a sine wave leaving $E_{x,inc}$ to be determined by Equ. 3.6a. To stop the scattered field from returning through the transparent source a PML is placed at $z = 0$ to absorb the scattered waves.

3.2.2 Broadband Source

In was important to achieve a simulation that would emulate a broadband lithographic exposure with a Mercury lamp. It would be incorrect to simply super-impose all wavelengths together in a source for one simulation, for this would imply coherence between the wavelengths. Instead, a number of simulations where run at the key wavelengths present in the Mercury lamp spectrum and the resulting averaged fields from each simulation added together with an appropriate weighting as set by the Mercury lamp intensities. The spectrum for the Mercury lamp used in lithographic exposures is shown in Fig. 3.3.

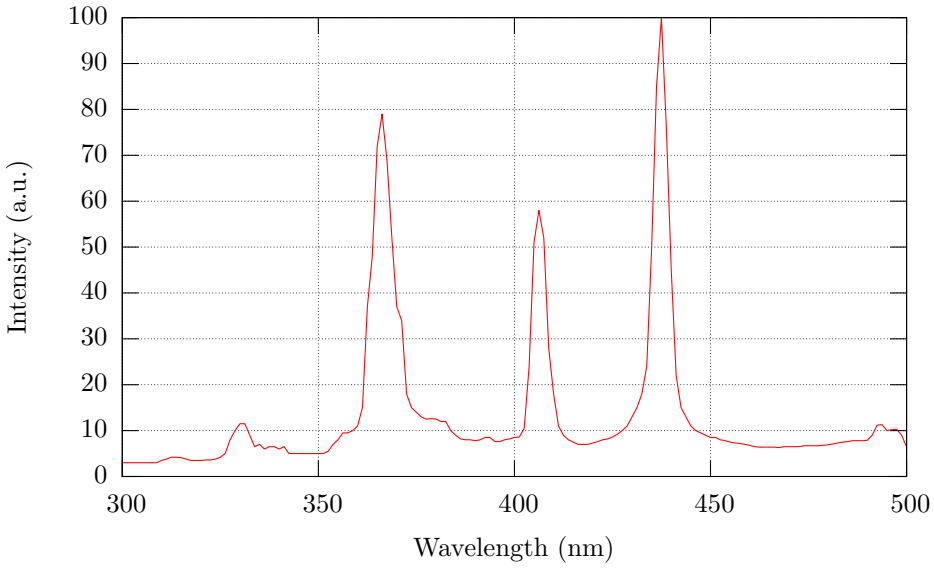

Fig. 3.3: Spectrum of UV400 Mercury Lamp used for PLL lithographic exposures [12].

The selected wavelengths and their weightings are given in Table 3.1. Additionally, the background noise from the lamp is around 6-7%. Wavelengths above 436 nm were not taken into account due to selectivity by the photoresist, and the 312 nm wavelength was included because of silver's transparency at that wavelength [11].

Table 3.1: Relative intensities of wavelength peaks in the UV400 Mercury Lamp spectrum.

Wavelength (nm)	312	337	365	405	436
Intensity	0.04	0.12	0.79	0.58	1

When adding up the final field intensities, a resampling was often required as the spatial sampling of the simulations was related to the source wavelength. Since simulations were often symmetric this allowed relatively clean resampling, and the effects on the results were generally not noticeable. Resampling would always be a interpolation process so no information would be lost.

3.3 FDTD DIFFICULTIES

The FDTD method has a number of 'pit falls' that were important to understand during code development so that the irregularities in the simulation could be classified as fundamental or code error. Issues pertaining to the stability of the simulation commonly arose during code development. The main stability concerns related to, the time-to-space sampling ratio, spatial over-sampling, irregular grids, and high-frequency components in sources.

One of the most important parameters of an FDTD simulation is the sampling ratio between space and time. The stability issues relating to this are covered extensively in Chapter 4 of Ref. [182]. The problem relates to how fast numerical errors can propagate across the grid. For a 1D case

$$\Delta x = c\Delta t \tag{3.23}$$

where c is the speed of light, and Δx and Δt are the spatial and temporal sampling steps, respectively. For this 1D case there is no error in the sampling because the wave moves at exactly the speed of light. If we move to a 2D grid, we encounter the problem of varying wave speeds for varying directions through the grid. To minimise this effect the grid is over-sampled[6] and the space-time sampling ratio is modified. For 2D simulations a ratio of $\Delta x = 2c\Delta t$ produced stable results with less than 0.1% error. Other FDTD simulation work on VMs have also used $\Delta x = 2c\Delta t$ [121, 171], as well as $\Delta x = \frac{\sqrt{2}}{0.95}c\Delta t$ [169].

It was discovered that the resonant nature of a FDTD Lorentz model (necessary for perfect and superlens simulation, see Section 3.1.1) required a considerable amount of over-sampling to stabilise the boundaries between it and a surrounding dielectric [169]. Commonly, over-sampling on the order of 100-150 times is used in FDTD simulations [82,169,173], and in this work 150 samples-per-wavelength (SPW) was used as standard.

[6]Over-sampling is when a number of discrete sampling points (greater than 2) are taking for each wavelength in the simulation.

It was found that 20 SPW was about the point at which a boundary would become unstable, and 40 SPW was considered safe. As a result of the over-sampling, simulation length and size grows considerably. It is thus generally a trade off with accuracy and time-of-simulation when choosing the spatial sampling.

Although the Yee grid was used in the beginning and by the end, there were a couple of other grid types investigated. The other main grid layout investigated was the square grid. When compared to the diamond grid (Yee) the square grid simply has all electric and magnetic fields lined up in rows and columns, and thus to create the fields in the required places to perform the leap frog, employs an averaging step first. This averaging step returns the fields to their diamond grid locations. The square grid was investigated to find out if both electric and magnetic field could be co-located on grid points, to overcome the roughness and asymmetry caused by the staggered diamond grid [172]. Unfortunately, the square grid was unstable for Lorentz materials.

The final instability issue related to the profile of the sources. It was found that starting a source with a step function would introduce large-amplitude high-frequency spatial components, which due to insufficient over-sampling resulted in instabilities at Lorentz medium boundaries. To overcome this, ramped sources were used that slowly increased the sources amplitude over a number of periods, limiting high frequency components [169, 173].

A study into the limitations of simulating VMs with FDTD is provided in Ref. [183]. In Chen *et al.*'s work, it was found that *"because of the frequency dispersive nature of the medium and the time discretization, an inherent mismatch ... exists between the slab and its surrounding medium."*. This mismatch limits the resolution for a lossless VM material.

3.4 MATERIAL DESIGN

Once the FDTD code had been finalised there was a need to calculated parameters for the Drude and Lorentz models so that the different materials could be developed. For simple dielectrics (SiO_2, Photoresist) and metals (W, Cr) it was straightforward to find values for ϵ' and ϵ'' from experimental tables [184]. However, for silver a lot of care was taken to arrive at parameters which would accurately describe the metal's performance at different frequencies.

3.4.1 Describing Silver

Because FDTD is a time-dependent discretised numerical simulation there will always be a bandwidth of frequencies present, even if you desire just one. For this reason is was important to match the model to silver's characteristics at, as well as around, the frequency or frequencies of interest.

Data on the refractive index and losses of a thin film of silver can be found in Ref. [11], where silver's reaction to ultra-violet (UV) through infra-red light is recorded. An attempt to match this data with a Drude model is sufficient for the paper to discuss the nature of silver compared to other noble metals, but is not accurate enough to describe the metal of the bandwidth proposed.

An iterative multi-dimensional method was employed to find a Lorentz or Drude model which could be as close as possible to silver over the bandwidth of the experimental UV lamp. This proved too difficult, and the model would often be out by over 50% at particular wavelengths of interest. This was yet another reason for using narrowband simulations for performance analysis.

To find silver's parameters for single-frequency simulations, the closest possible match was made, over a bandwidth of 60-70nm, to the parameters provided by Ref. [11]. The parameter model allowed 6 degrees of freedom for controlling the silver, and at each iteration a quality parameter was investigated, which is related to how well the model fits at the wavelengths of interest. Six wavelengths would be used to calculate this quality parameter, which was basically an Least-Mean-Square (LMS) error. The program would also use a weighting at each wavelength that described its importance, and the program therefore trys 'harder' to fit the higher weighted wavelengths. This method provided sufficient matching of both the real and imaginary components of silver, and the resultant Lorentz model parameters are shown in Table 3.2. A visualisation of the table's parameters is provided in Fig. 3.4

Table 3.2: Calculated silver parameters for the Lorentz model of the electric permittivity.

Wavelength (nm)	ϵ_r	γ_e	δ_e	a_e	b_e	c_e
312	6.41	-2.23×10^{20}	-6.83×10^{36}	3.18×10^{4}	-1.72×10^{17}	-2.20×10^{3}
337	8.66	-8.95×10^{14}	-1.67×10^{32}	5.57×10^{-1}	9.07×10^{9}	-4.54×10^{-2}
365	7.05	-7.06×10^{13}	-1.53×10^{31}	5.96×10^{-2}	8.44×10^{8}	-4.75×10^{-2}
405	3.71	5.55×10^{11}	-1.37×10^{31}	7.63×10^{-2}	-9.45×10^{12}	2.65×10^{-2}
436	5.18	-1.30×10^{14}	-2.18×10^{32}	1.02×10^{0}	-7.73×10^{13}	-7.97×10^{-3}

3.5 TWO DIMENSIONAL SIMULATION

The most regularly run simulation was for the 2D grating exposure. The diffraction limit is well know for a two dimensional grating and thus a 2D infinite grating is the perfect candidate for exploring a system's ability to break that limit.

Figure 3.5 shows the simulation layouts used for both ENFOL (Fig. 3.5(a)) and PLL (Fig. 3.5(b)). The two-period domain was chosen so that asymmetric effects could be monitored. Asymmetry is unfortunately fundamental to the FDTD Yee-grid because

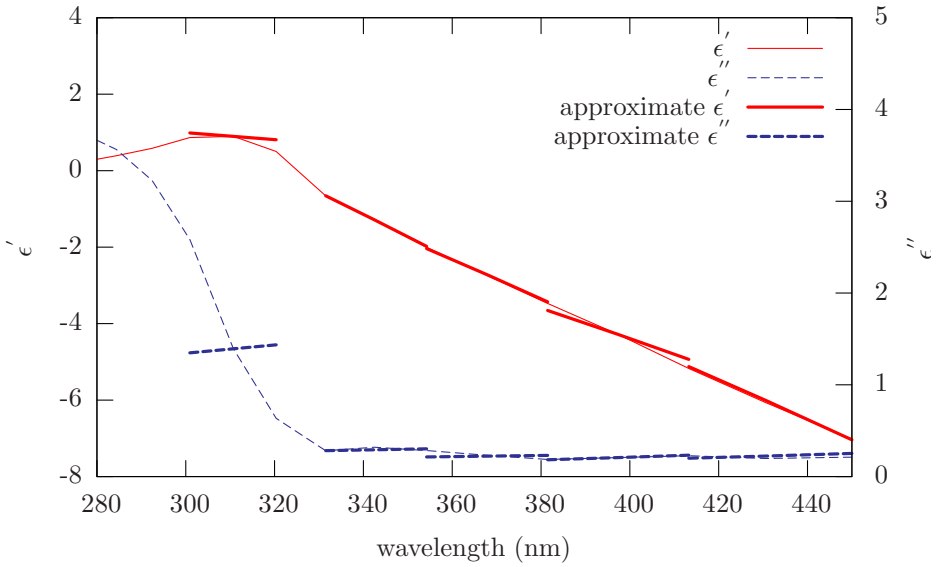

Fig. 3.4: The parameters in Table 3.2 are used to evaluate the lorentz model around the wavelength of interest and plotted against silver's permittivity.

an element that is made up from standard cells with have a magnetic node on its right boundary and and electric node on the left [172].

3.5.1 Simulation Visualisation

An important part of creating a working simulation tool is to provide useful means for result visualisation. The mechanism of photoresist exposure requires photons to break or make bonds, and this is a discrete process. An FDTD simulation models light as electromagnetic waves, so a link must be made between the continuous wave model and the discrete mechanism to give guidance as to what information should be extracted from the simulations. The gathered data needs to show where the photoresist has been exposed.

The approach used was to take the electric field and average its intensity over a number of wavelengths. Unfortunately, this is not a strength of the FDTD method as it is a time-domain method and normally focuses on transient responses. Therefore, careful investigation was required to give an accurate representation of the steady-state solution. What follows are the results used to determine how long the simulation should be run before the average was taken, and for how long the average should be taken.

3.5.2 Steady State Convergence

Once the simulation is run for long enough it can be said that transients have died down and a steady state solution has prevailed. To determine when this has occurred, certain data points in the simulation are monitored and when they appear to reach

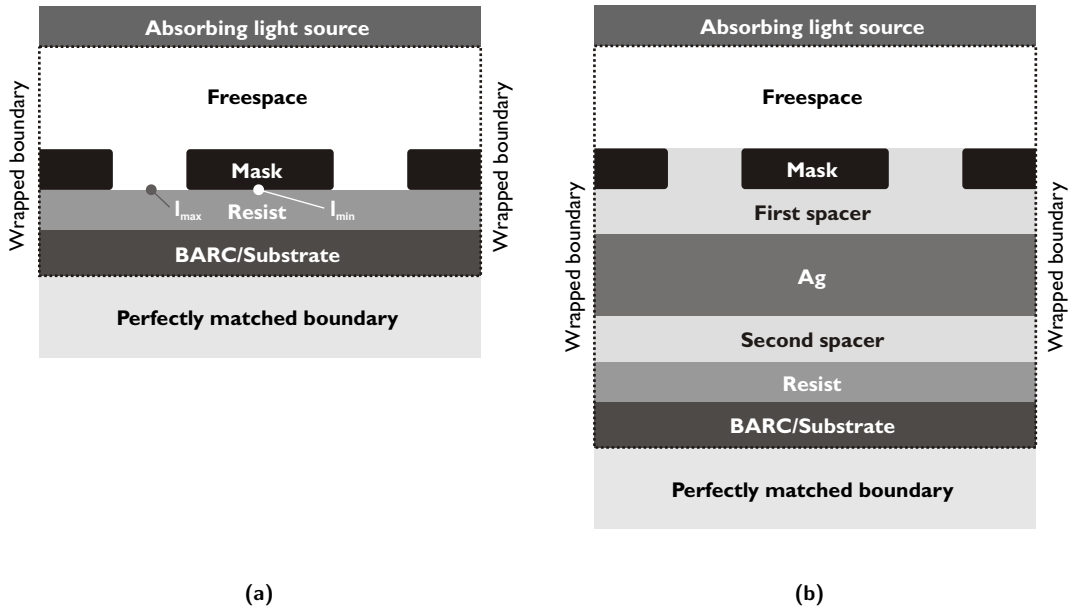

Fig. 3.5: Schematics of the simulation layouts for (a) ENFOL and (b) PLL, showing wrapping boundary conditions left-to-right, an absorbing light source at the top, a PML at the bottom, and internal materials including, mask, spacer and silver layers, photoresist, and substrate.

an acceptable level of convergence the simulation is said to be in steady-state. Before simulations are run a transient wait time and averaging time are determined.

Figure 3.6 shows the time-evolution of the electric field intensity under the aperture and below the mask's shadow, or I_{max} and I_{min} in Fig. 3.5(a), respectively, for three simulations (system parameters are given in figure caption). All simulations use a source ramp time of two periods, and the plot is taken from a moving-average with the same averaging length as the temporal wavelength. Taking the moving-average in this way removes the intra-cycle oscillations, which reduce the clarity of the plots without adding information. Note the differences in simulation length.

The first (Fig. 3.6(a)) is for a proximity exposure for a 90-nm period mask. The plot shows that once the simulation has been running for 10 periods a steady-state has been reached with little to no contrast in the image. As there are no resonant elements in the simulation we should expect it to reach steady state quickly. Thus for proximity exposures averaging can safely begin after 20 wavelengths and averaging can occur over a few wavelengths.

The second plot (Fig. 3.6(b)) is for the perfect lens ($\epsilon = \mu = -1$). Being a highly-resonant structure with no loss, this simulation struggles to find a steady state. This tendency for the simulation to oscillate makes the difficult to find a numerical solution for the loss-less perfect lens experiment. However, this case is somewhat academic as a loss-less lens could never be manufactured.

Figure 3.6(c) is for the Pendry silver-lens set-up, with a 40-nm thick silver lens

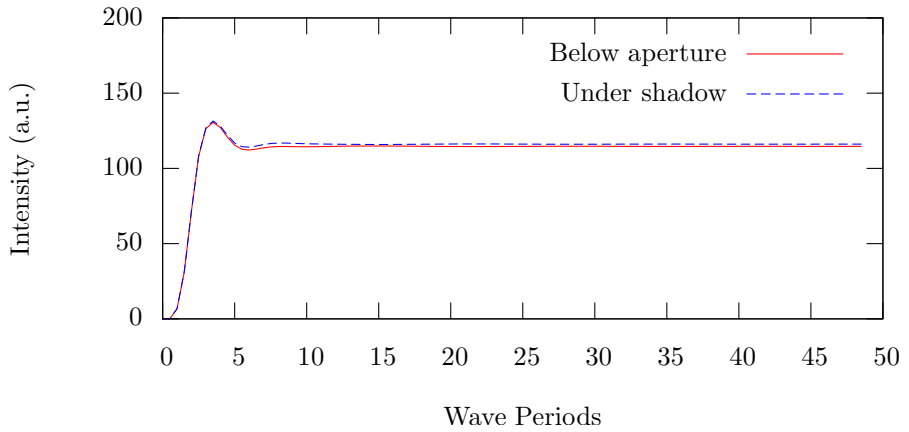

Fig. 3.6: The time evolution of simulated intensities under the aperture and below the shadow of a 90-nm period mask for (a) a proximity exposure, (b) a perfect lens using a 20|40|20 - Air|P.L.|Air stack, and (c) a Pendry superlens stack (20|40|20 - Air|Ag|Air). All simulations use a 365-nm wavelength.

sandwiched between two 20-nm spacers and an exposing wavelength of 365 nm. Because the silver has loss associated with its refractive index the fields more readily converge to a steady-state than the perfect lens case, but this takes a number more wavelengths than the proximity case to occur. Based on a range of examples it was determined that 50 was an sufficient number periods to reach a steady-state, and averaging over more than 10 periods was favoured.

In the end, to speed up proximity simulations and to ensure the convergence of some PLL simulations, a dynamic simulation length was coded. This meant that simulations that converged to an acceptable level before the end of the total simulation length would end early. The criteria for convergence relied on the normalised range ($\frac{max-min}{max+min}$) of the moving average meeting an certain level for a set number of periods. The rule was if there was less than 0.05% range in the moving average for 10 periods then the averaging, over 10 periods, could begin. The total length of a simulation was set at 200 periods; some would end after 30 periods, some after 80, and occasionally the criteria would not be met and the simulation would run for the full 200 periods. When results were compiled the simulations that ran for the full time were investigated to ensure that the had reached a steady state. All simulations converged to an acceptable level ($< 0.2\%$ range in moving average over last 10 wave periods).

3.6 VALIDATION

To validate the results produced by the designed simulation tool two comparisons were made; one with a commercial finite element package called 'FEMLAB' [185], and another through an analytical comparison with field solutions for perfect-conduction gratings using modal expansion [186, 187].

3.6.1 Finite Element Validation

The first validation was carried out on the developed FDTD Matlab code and a finite element package known as 'FEMLAB'. The simulation domain was a 2D 650-nm square cell that wraps left-to-right, has an absorbing boundary at the bottom, a transparent plane-wave source at the top, and a 50-nm diameter infinite cylinder in the centre with the material properties of tungsten ($\epsilon_r = 4 + 16i$). A schematic of the layout is presented in Fig. 3.7(a). This setup was chosen to ensure that the absorbing properties of the top and bottom PMLs and the source were sufficient.

The first major difference between the two simulations was the time required to run. Both the finite element and modal expansion method are steady state results, and because of this will always be faster than an FDTD simulation due to its temporal nature. In performing these simulations there is a lot of information about the transient response of the system that is discarded as it is not important for averaged intensity.

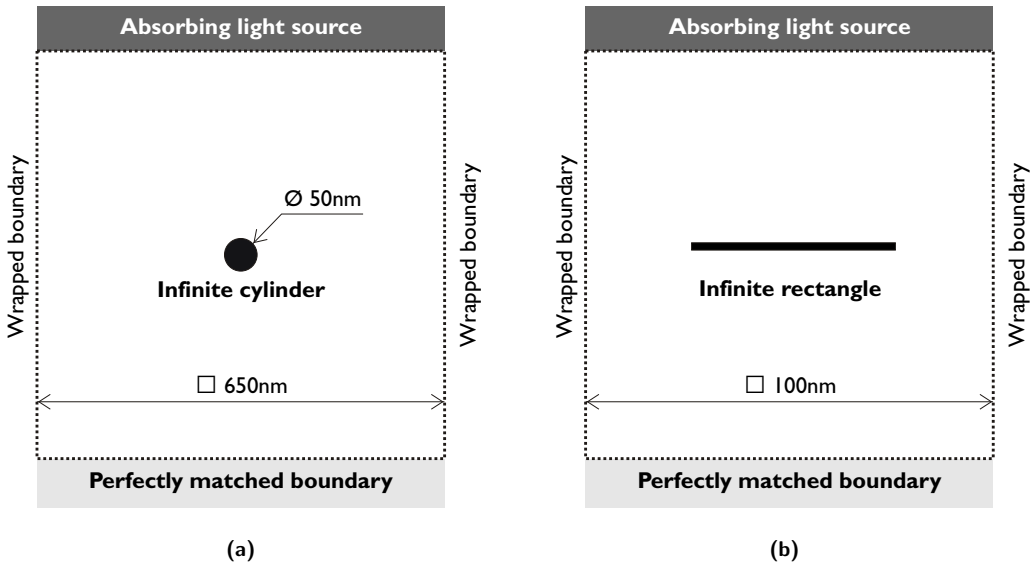

Fig. 3.7: Schematic layout for validation for (a) FEMLAB and (b) a modal expansion technique versus FDTD.

Figure 3.8 presents the results for FDTD and FEMLAB simulations. The similarities in the images can be used to demonstrate two important design features of the FDTD simulation. Elements to note are: the lack of standing waves between the top and bottom - demonstrating the matched boundaries, the expected cylinder dipole, and the standing wave between the source and the cylinder that is not resonant with the top boundary, but instead at infinity (i.e. a transparent source). The absolute values of the fields are comparable, but do not match exactly. Figure 3.9 shows line traces as per the dashed lines in Figures 3.8(a) and (b). The intensities are out by a factor of around 1.3, and the FDTD trace shows more 'wash out' with lower peaks and higher troughs. Differences in the simulated values at small distances from the cylinder are more pronounced due to differing sampling methods.

3.6.2 Analytical Validation

An analytical solution was derived from modal expansion theory [186,187] to model the transmission of a grating in free space. This was a good validation test for the FDTD code to show that it could produce the correct field for a sub-diffraction-limited mask. The setup uses a 100-nm square domain as shown in Fig. 3.7(b), with the source now impinging on a thin perfect-conductor grating, rather than a cylinder.

Figure 3.10 shows the 2D result of the two simulations. Once again the simulations are well matched, with the only slight difference being the intensity values. These differences are most noticeable around the grating. Figure 3.11 shows line traces through the 2D plots at locations indicated by the dashed lines in Fig. 3.10. A slight variation in intensity can be seen.

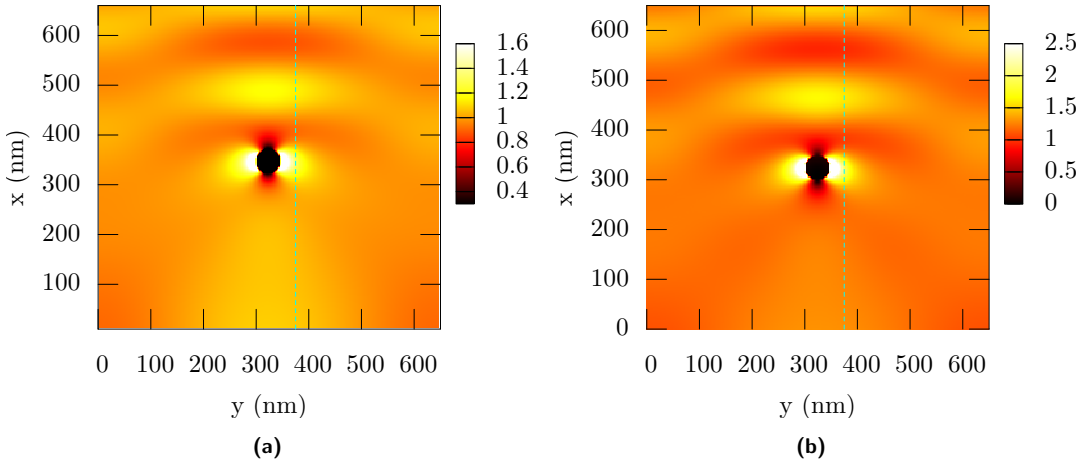

Fig. 3.8: Comparison of (a) FDTD code and (b) commercial FEMLAB software for the simulation domain as shown in Fig. 3.7(a).

The FDTD code shows good agreement with two forms of steady-state electromagnetic field profile generation. The major note to come out of validation tests was the need for the FDTD simulations to reach an acceptable level of convergence before averaging could begin (as has been previously discussed).

3.7 POLARISATION EFFECTS

Performance of the system under both TM (magnetic field normal to the 2D simulation plane) and TE (electric field normal to the 2D simulation plane) polarisation needed to be investigated because the exposing radiation used for the experimental work was not polarised. However, FDTD simulation results in this work have been carried out only using TM polarisation. This is for two main reasons. First, in recent work studying near-field exposure through a metallic grating it was shown that in the sub-wavelength regime the TE polarisation penetrates 2D gratings at a reduced amplitude to the TM polarisation [16, 167]. This is due to the polarising nature of an infinite 2D grating [188, 189]. Secondly, analytical studies of the transmission of polarised light through a silver layer demonstrated that TE transmission is significantly less than TM [31]. The high transmission of TM through a silver layer as a result of coupling between surface plasmons generated by the oscillation of an electric field normal to the surface. In the TE case, the electric field is never normal to the surface and thus never excites the surface plasmon. Instead the magnetic field is normal to the surface, but fails to excite any magnetic response as silver has none.

To investigate the differences between TM and TE polarisation a sample of simulations have been performed with the commercial finite-element simulation software FEMLAB. The full 2D simulation cross-sections for each polarisation and the total fields are presented in Appendix C. Simulations were performed at both polarisations

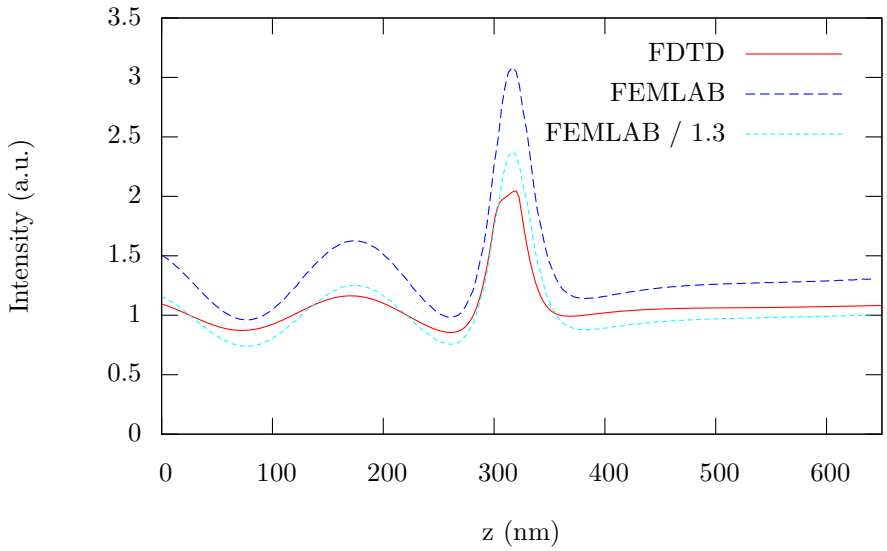

Fig. 3.9: Traces through 2D FDTD and FEMLAB validation simulations as marked by the dashed lines shown in Figures 3.8(a) and (b).

for 40-nm thick tungsten gratings suspended in free-space at 5-μm, 1-μm, and 170-nm periods, with additional simulations performed at 1-μm and 170-nm periods with a 40-nm thick silver layer suspended 20-nm below the mask.

Figure 3.12 shows traces for the TM and TE electric intensities and their average for a 5-μm period grating in free space. This is a typical result for gratings with half-periods greater than the wavelength of exposing light. The differences between TM and TE are limited to the magnitude of the intensity fluctuations across the aperture, and the TM simulation is a reasonable approximation for the intensity profile of the total field.

Figure 3.13 is for a 1-μm period simulation and introduces a comparison between an ENFOL and a PLL simulation. In this regime, where the wavelength of exposure is on the same order as the half-period of the grating, differences become apparent between the TM and TE polarisations. For the case without silver (Fig. 3.13(a)) the TM polarisation is being affected by diffracted light and contrast has been lost. The difference between the TM polarisation and the total field is most prominent at the centre of the aperture and the corners of the mask.

Figure 3.14 shows the same comparison for a sub-diffraction-limited period of 170 nm. When no silver is present (Fig 3.14(a)) the TM polarisation gives good contrast, while the TE polarisation gives a weakened and inverted intensity profile. The averaged total field has a reduced contrast to the TM, but is still dominated by the TM's profile. Figure 3.14(b) shows that the effect of the TE polarisation is almost completely removed by including a layer of silver. The reduced transmission of the TE fields through sub-diffraction-limit period gratings and the large reduction of TE's

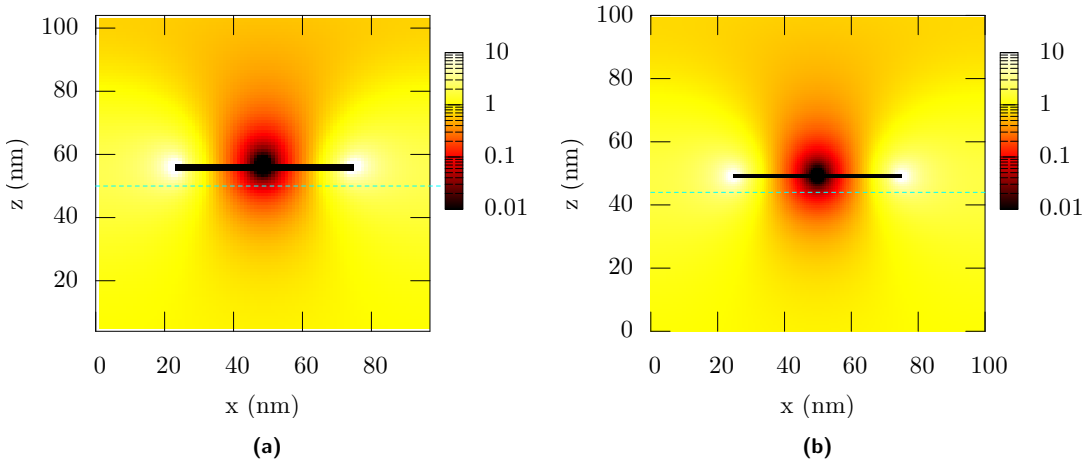

Fig. 3.10: Comparison of (a) FDTD code and (b) analytical modal expansion simulation.

transmission through the silver [31] demonstrates that the TM polarisation dominates exposure and is thus an acceptable indication of the performance of the system for sub-diffraction-limit grating periods.

The intensity below the tungsten mask for the TE polarisation, which produces an image inversion, reduces contrast in the total feild. The effect of various metals has previous been investigated (Ref. [16] page 123) and showed similar effects. It was also shown that chromium did not invert the image, which is due to chromium being a metalic absorber at these wavelengths while tungsten in a dielectric absorber. This suggests that tungsten would limit resolution in an unpolarised near-field system, and that chromium would be a better choice for a metallic mask. However, tungsten was used in this work due to the ability to dry etch it with available gases.

Simulations performed in the future sections where the mask half-period is on the order of the exposing light's wavelength will only give a valid representation for a TM polarised exposing light. In these cases, however, the TE polarisation tends to provide better contrast in the final image and thus the TM simulations will provide a worst case estimate of contrast. The complexity of the TM and TE fields at periods where the wavelength is on the order of the grating period has been previously analysed in detail (Ref. [16] page 133).

3.8 PERFORMANCE ANALYSIS

Quantitative methods were required to analyse the simulation results, to allow trends to be investigated and commented on. To arrive at a method for analysing the results we must be able to characterise what is a 'good' result.

Essentially, all that we require from a simulation is a line trace though the resist. This gives us our exposure profile, which allows us to determine the expected developed

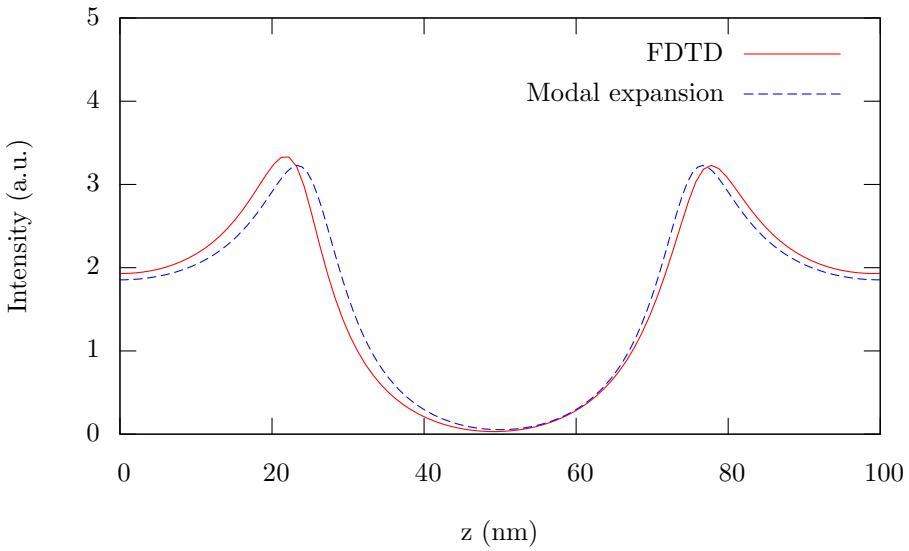

Fig. 3.11: Traces through 2D FDTD and modal expansion validation simulations as marked by the dashed lines shown in Figures 3.10(a) and (b).

profile of the resist, and hence the ability of the process to transfer a pattern. The ideal exposure profile would be a sharp step-like function. Post development, this would leave a perfectly transferred pattern in the resist with vertical side walls and is considered a 'good' result. Due to diffraction, refraction, reflection, and an imperfect mask, a smoother function is produced by the simulations and is indeed what we would expect in real life. Figure 3.15 shows the difference between a typical two-period grating exposure, an inverted exposure, and the ideal case. We will use this case to arrive at a range of quantitative values that can characterise the ability of a certain result to provide pattern transfer. The next few sections describe these quantitative measures of quality.

3.8.1 Contrast

The first and most common method to rate a exposure profile is contrast, or a Modulation Transfer Function (MTF) [190]. Contrast is simply a normalised ratio between a light and dark intensity, which value varies between 0 and 1. If high, it indicates that an exposure is providing good pattern transfer and allows for process variation and, if low, signals a degrading process window and a reduced quality to the pattern transfer process. Contrast can be found in two simple ways.

The first is to take the minimum and maximum intensities in a line trace and normalise their difference like so:

$$C = \frac{(I_{max} - I_{min})}{(I_{max} + I_{min})}, \tag{3.24}$$

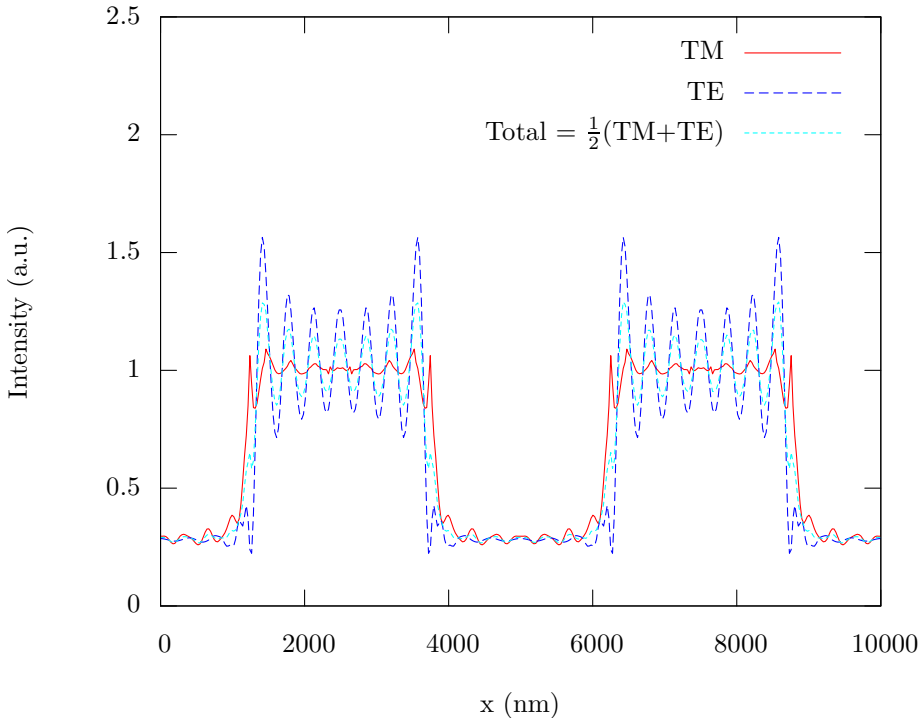

Fig. 3.12: Traces through 2D FEMLAB simulations for a 5-μm period, 50% duty-cycle grating for TM (long-dash), TE (solid-line), and their average (short-dash). The traces are taken 20 nm below the mask.

where where I_{max} is the maximum intensity value in the trace and I_{min} is the minimum intensity. This is considered acceptable if if the maximum and minimum intensities reside where they are expected, beneath an aperture and under the shadow of the mask, respectively. In the near-field regime, due to resonances caused by certain periods of mask gratings, the minimum and maximum intensities are often not in the desired places. For example, if the simulation produced an inverted pattern transfer the measure would give a high contrast value, but this is misleading because the transferred pattern is the opposite of what is required.

To overcome this the contrast is consistently taken from the correct location. Thus the equation becomes

$$C = \frac{(I_{apt} - I_{shw})}{(I_{apt} + I_{shw})}, \tag{3.25}$$

where I_{apt} is the intensity from beneath the aperture and I_{shw} is under the shadow of the mask. This method leads to reduced contrast if a sideways shift has occurred in the trace.

With reference to Fig. 3.15 the two equations give a contrast value of 1 for the trace of the ideal case. For the actual case (closer to reality) a value of 0.8 is found from both equations, which would be an excellent and realistic exposure profile through a resist. For the inverted case, Equ. 3.24 gives the same contrast value that it found for the non-inverted trace. The inverted pattern is obviously not as desirable, thus Equ. 3.25

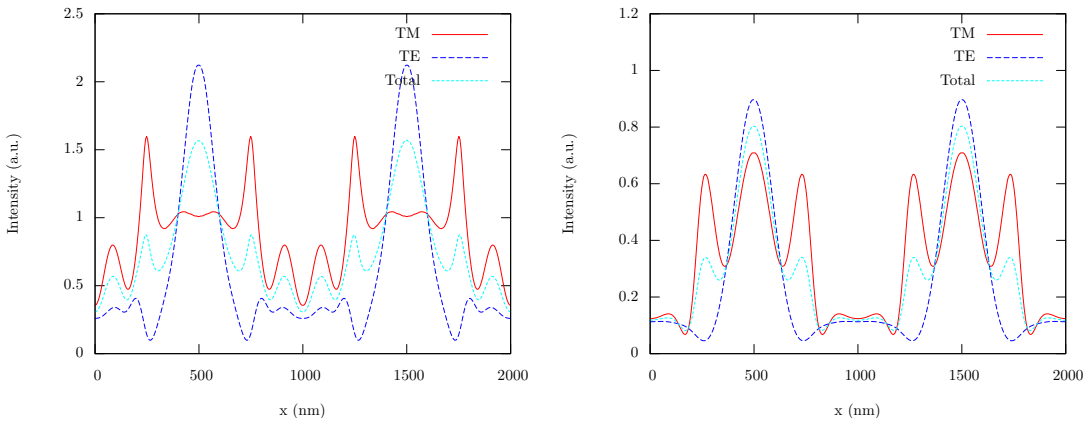

Fig. 3.13: Traces through 2D FEMLAB simulations for a 1-μm period, 50% duty-cycle grating, with (b) and without (a) a 40-nm thick silver layer 20nm below the mask, for TM (long-dash), TE (solid-line), and their average (short-dash). The traces are taken (a) 20 nm below the mask and (b) 20 nm below the silver.

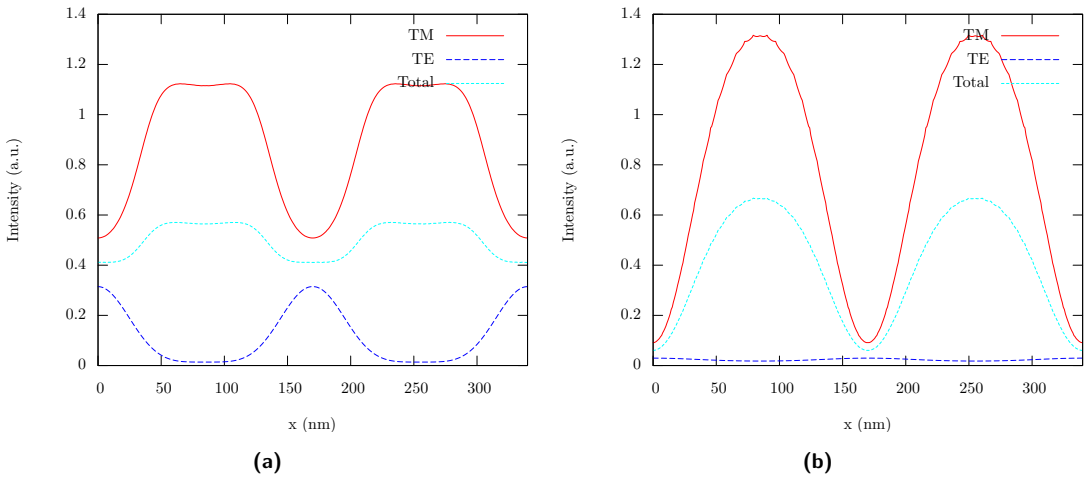

Fig. 3.14: Traces through 2D FEMLAB simulations for a 170-nm period, 50% duty-cycle grating, with (b) and without (a) a 40-nm thick silver layer 20nm below the mask, for TM (long-dash), TE (solid-line), and their average (short-dash). The traces are taken (a) 20 nm below the mask and (b) 20 nm below the silver.

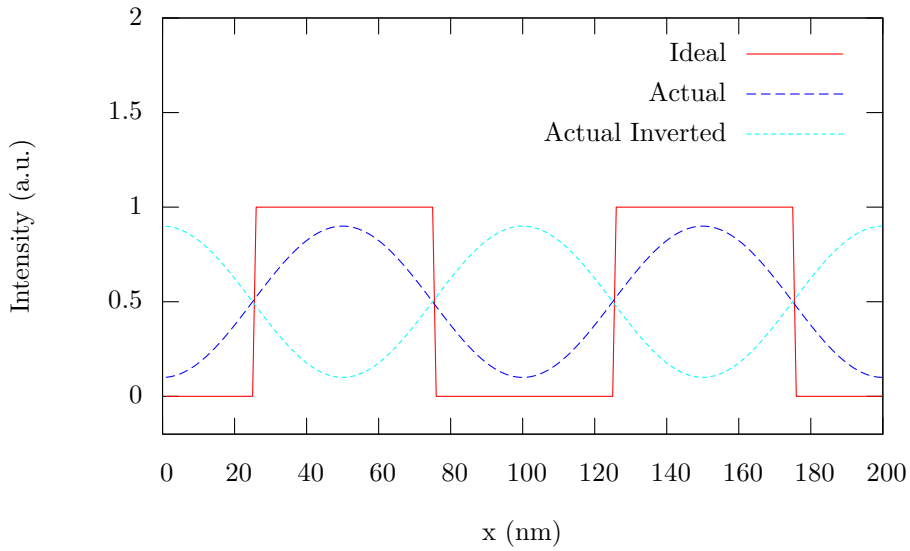

Fig. 3.15: An example comparison of ideal versus actual electric-field intensity traces through resist for an exposure.

becomes very useful at picking up inversions. The contrast value for the inverted image using Equ. 3.25 would be -0.8. However, it is still important to use Equ. 3.24 as mini troughs and peaks that occur under the aperture or in the shadow, respectively, can lead to a quality assessment that is unfair.

By observing the contrast variation as a distance from the source, the ability of the system to produce an image at a depth from the mask can be evaluated. This concept will be termed pattern visibility, and was employed in a superlensing simulation paper to gave important insights into the lensing ability of silver [22].

3.8.2 Least-Mean-Square Image Comparison

A secondary measure of performance was investigated to add to the information obtained by the contrast measurement. The contrast gives an indication on how simple it would be to transfer the image into a photoresist, but it doesn't tell you much about the quality of that image. An overall image quality was taken by providing a measure of the 'closeness' of the simulation's exposure profile to a reference profile, which is what would be expected in a near-field eposure. To achieve this a LMS method was used to calculate the normalised sum of the distance between the two cases. To make an appropriate comparison the compared traces are normalised to one before the LMS value is calculated. If I^{ref} is a 1D vector of a reference trace and I^{sim} is a 1D vector of the simulated trace then

$$FOM = \frac{1}{n}\sqrt{\sum_{y=1}^{n}\left|\frac{I^{ref}(y)}{max\left(I^{ref}(y)\right)} - \frac{I^{sim}(y)}{max\left(I^{sim}(y)\right)}\right|^2} \tag{3.26}$$

is a figure-of-merit (FOM) based on the LMS value, where n is the number of samples of the line trace (taken over two periods). The reference intensity profile was chosen to be a raised-cosine curve (with $\alpha = 0.5$ [191]), the final version of which is shown in Fig. 3.16.

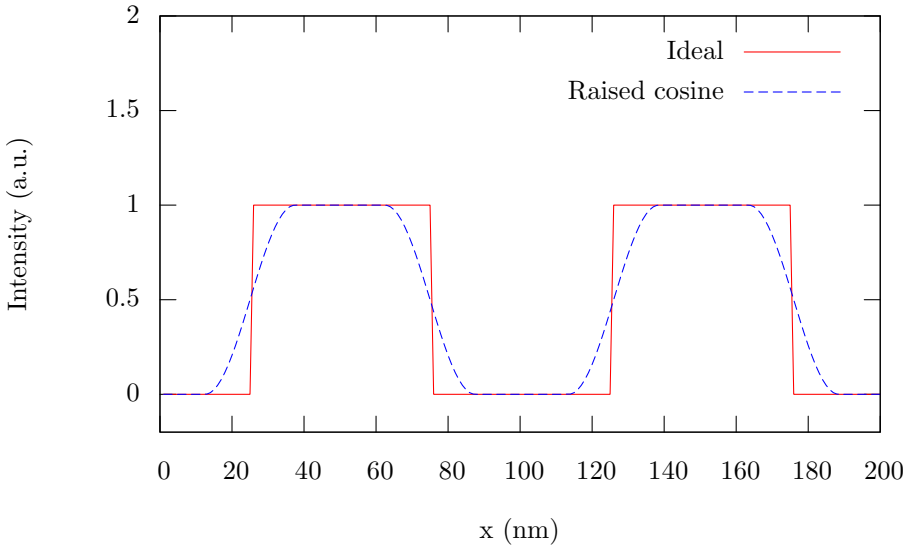

Fig. 3.16: A raised-cosine shaped trace used for LMS image comparison. An ideal step function is provided for comparison.

The LMS comparison picked up a number of useful factors. If the value of the FOM, is around 0.1 or less this denotes an excellent image, while FOMs around 0.7 indicate image reversal. The real use of the FOM is its ability to pick out a period halving or quartering effect, which will give an FOM of around 0.3-0.5. Resonances that cause a change in the period of the image are often not picked up by the contrast calculation. Figure 3.17 gives a graphical representation of the bands associated with the FOM

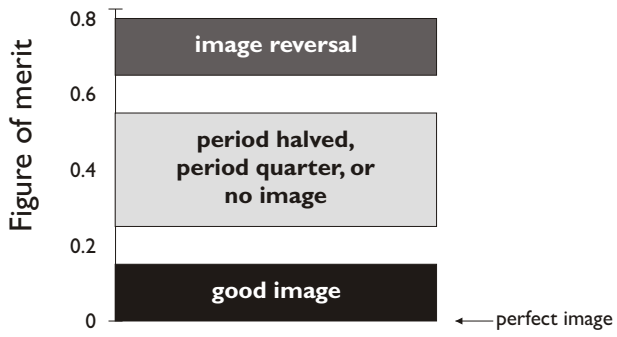

Fig. 3.17: The image quality associated with different bands of the Figure of merit. Any thing above a merit value of 0.2 is considered a poor image.

3.9 EXAMPLE: IMAGE EVOLUTION

To demonstrate the FDTD tool's ability to simulate a superlens an investigation was carried out to study the image evolution in a near-field lithography environment. It is important to investigate the ability of the near-field superlens to form an image. Understanding the image formation process can give us insight into ways to optimise geometry when designing the lenses' imaging stack.

Image formation through perfect and superlens has been studied by numerous groups for both analytical models [18, 163, 164, 192] and full vector simulations [22, 83, 169]. Here, a comparison of image formation between a proximity and a superlens system is presented.

The conditions for this investigation are selected to be of interest to the PLL work and to correspond with the specifications of the superlens example in Pendry's paper [18]. For the superlens simulation a 40-nm thick silver layer surrounded in a dielectric is positioned 20 nm below a 40-nm thick tungsten layer set up as a periodic shadow mask. A wavelength of 365nm is used, which corresponds to the i-line used in lithographic exposures and is close to matching the real part of silver's permittivity to that of the surrounding dielectric, so that reflections are minimised. At this wavelength, tungsten acts more like a high-refractive-index dielectric than a metal, therefore, its use as the absorber limits the performance of both PLL and the proximity simulations, thus the results are not optimal for either system. However, this does provide a valid comparison of the lithographic process developed in this thesis (reasons for using tungsten are given in section 5.1). The proximity simulation has the same set up with the exception of the silver. Here the performance at a sub-diffraction-limited period of 140 nm is investigated.

Figure 3.18 shows a 2D cross-section of a TM-polarised FDTD simulation for the proximity case. A large amount of energy is transferred, as indicated by the intensity below the mask, which is expected [114]. The contrast present at the bottom of the mask provides us with the option of doing an intimate-contact exposure (a.k.a. ENFOL).

The contrast in the near-field is further examined in Fig. 3.19, where line traces through the simulation are taken at 10 nm intervals. Here, the need for intimate contact with the mask for exposure is apparent as the contrast fades to zero very quickly, being virtually gone at 20nm below the mask.

The 2D superlens simulation cross-section is shown in Fig. 3.20. The effect of the silver is dramatic. The simulation has modelled the surface plasmons generated on the silver as it is exposed near resonance, coupling from the near-field of the mask, storing the energy on the surfaces of the silver, and increasing the contrast below the silver.

The apparent increase in contrast in Fig. 3.20 can clearly be seen in Fig. 3.21.

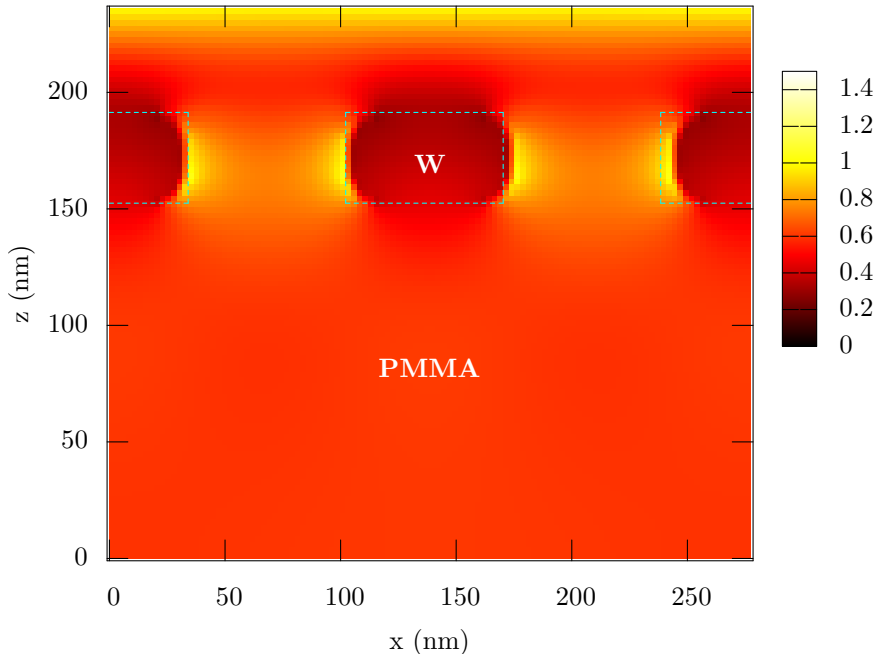

Fig. 3.18: A 2-D FDTD simulation for TM polarisation of a 140-nm period grating suspended in a dielectric.

Again traces have been plotted as a function of distance from the bottom of the mask. The silver is positioned between $z = 20$ and $z = 60$ nm and the expected image plane is at $z = 80$ nm. Not only has the silver produced an image of the mask at the $z = 80$ nm plane, but it has also provided a depth to the image which lasts from the bottom of the mask to around $z = 110$ nm giving a 30 nm deep image, which has better quality than the proximity or ENFOL case.

In summary, the tools for simulating the PLL system have been developed and validated. The next section introduces the experimental side of the thesis and investigates the tools required to create an experimental platform testing the superlens concept in a lithography environment.

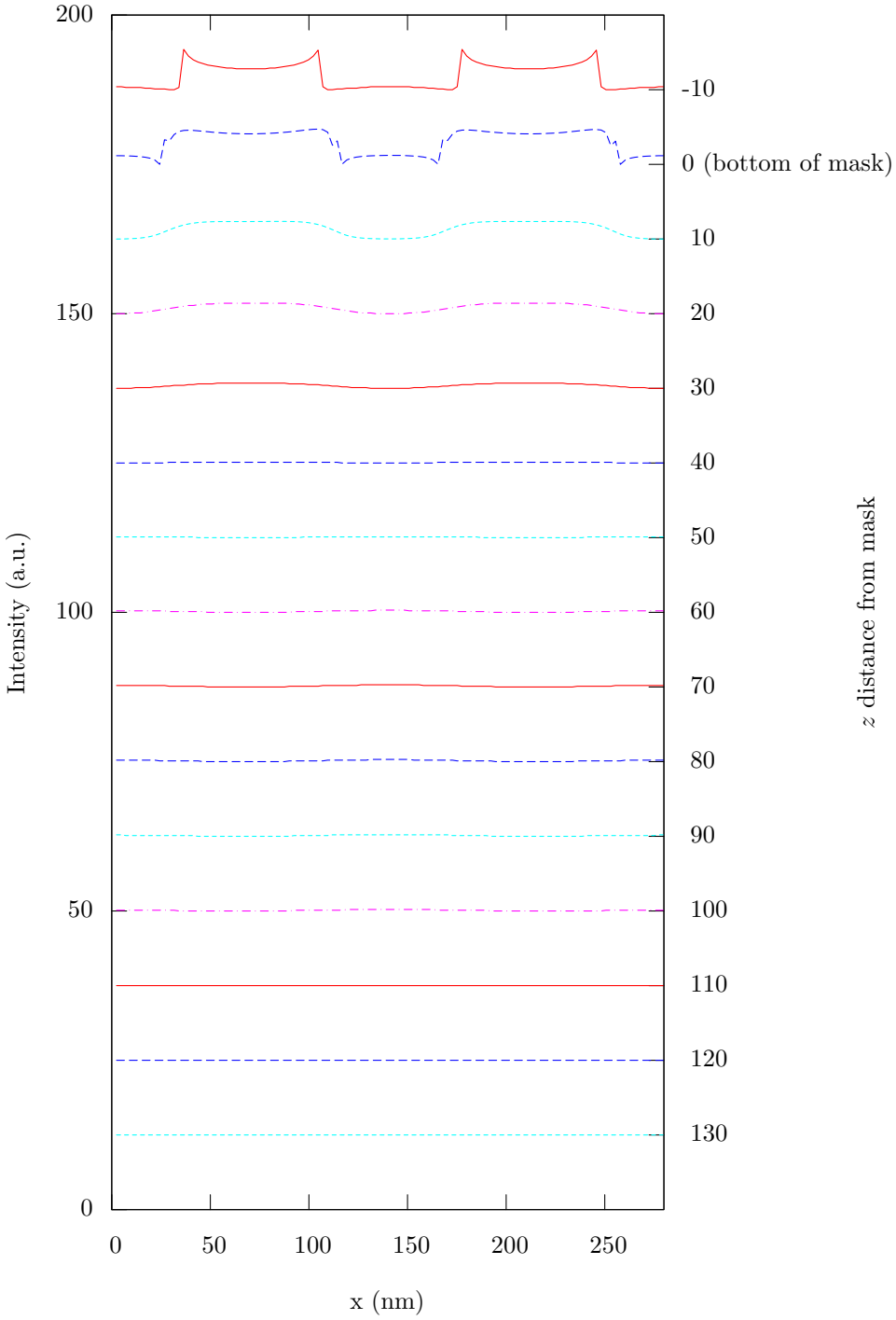

Fig. 3.19: A range of traces through the 2D simulation of the 140-nm period grating suspended in a dielectric. Traces are for different distances from the bottom of the mask (intensity traces have been offset from one another for clarity).

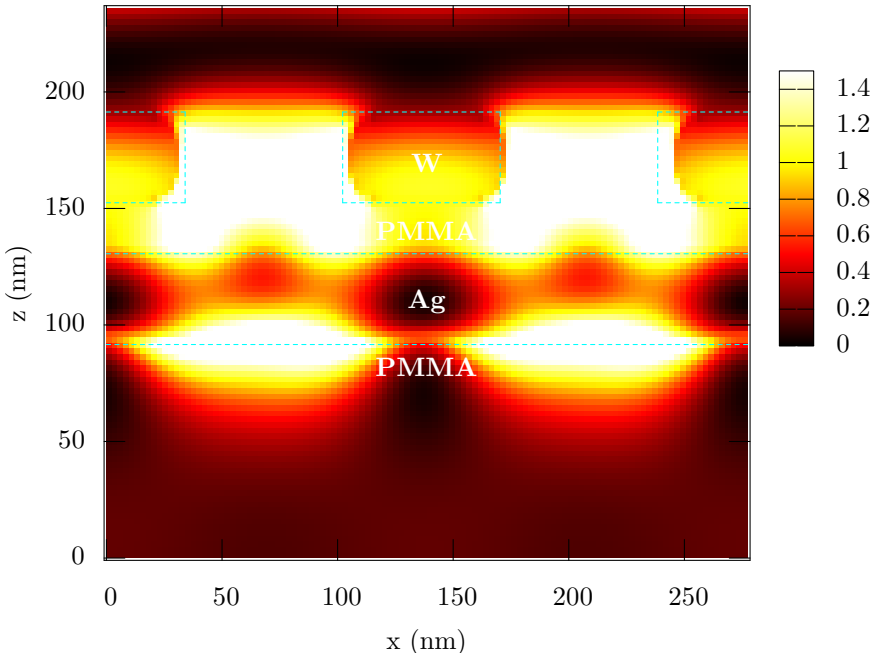

Fig. 3.20: A 2D FDTD simulation for TM polarisation of a 40-nm thick silver superlens below a 140-nm period grating. The silver is sandwiched between to PMMA spacers.

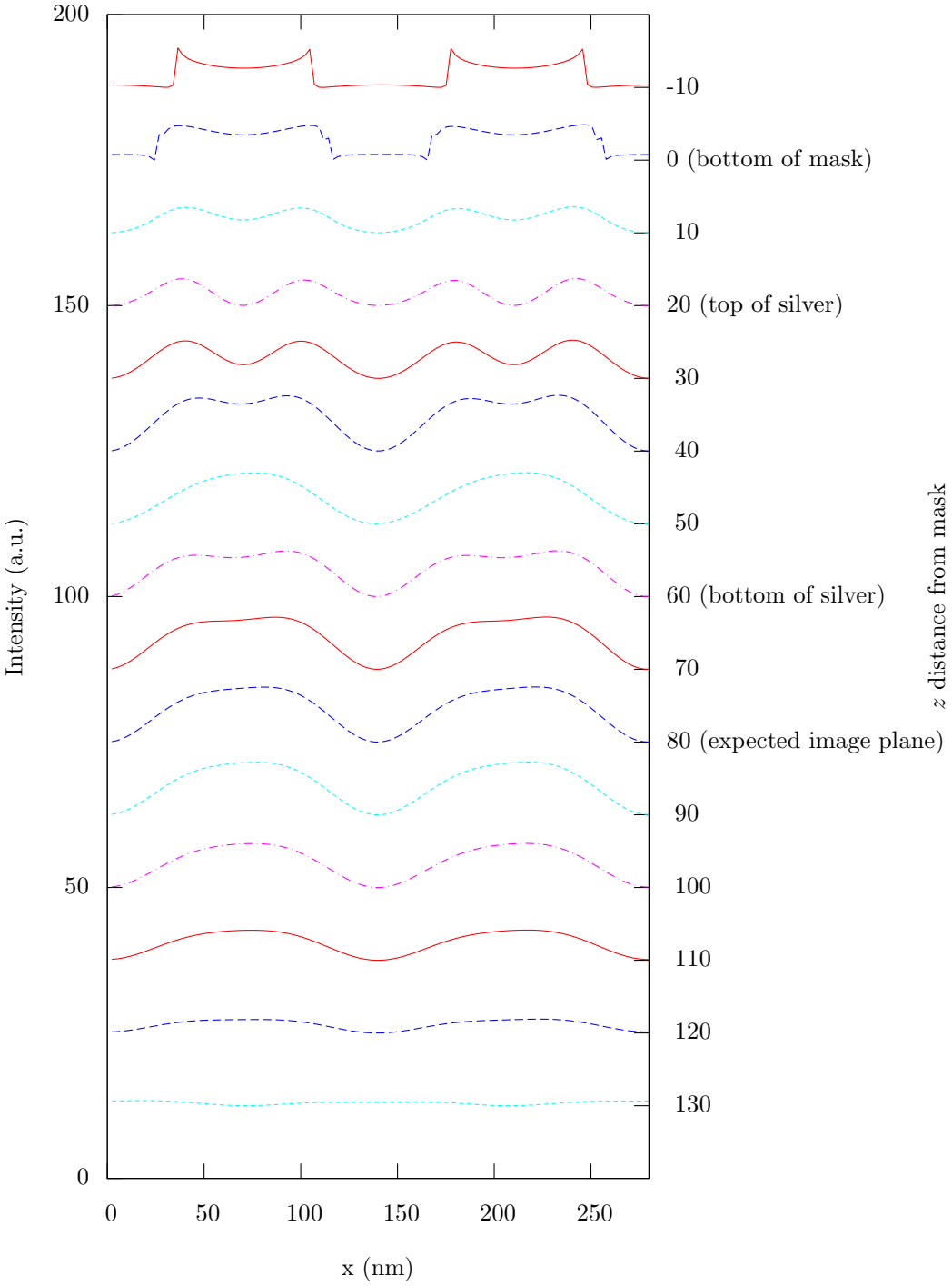

Fig. 3.21: A range of traces through the 2D simulation of the 40-nm thick silver lens. Traces are for different distances from the bottom of the mask (intensity traces have been offset from one another for clarity).

Chapter 4

EXPERIMENTAL TECHNIQUES

"Man is a tool-using animal"

- *Thomas Carlyle*

To perform the required experimental work needed to test PLL, a range of experimental techniques and apparatus were required. This chapter covers these techniques and any specific details regarding the processing of masks or obtaining experimental results.

4.1 APPARATUS

The processes which were developed to produce the experimental results required expert knowledge of a number of apparatus. The following sections detail a number of standard semiconductor and photolithography tools that were used.

4.1.1 Electron Beam Lithography

For near-field mask development a process was required to produce features with dimensions below the diffraction limit to test the resolution of PLL. Electron Beam Lithography (EBL) provided this by allowing sub-100nm features to be patterned into a polymer mask. The mask-less nature of the EBL also accommodated the production of arbitrary patterns, giving a great flexibility to the mask making process.

A newly-installed Raith 150 system provided a fully integrated high-resolution large-area pattern generation system by combining a LEO 1500 series Scanning Electrical Microscope (SEM) with addition hardware, software, and a laser-interferometer-controlled stage. The system was largely automatic, simplifying load and unload procedures as well as system setup. A schematic of the Raith 150 system is given in Fig. 4.1(a) and a picture is shown in Fig. 4.1(b).

In EBL, a controlled beam of electrons exposes patterns into a electron-sensitive resist. Obtaining a stable focused beam is achieved through a number of elements. The first is the electron source. In EBL systems electrons are produced by either field

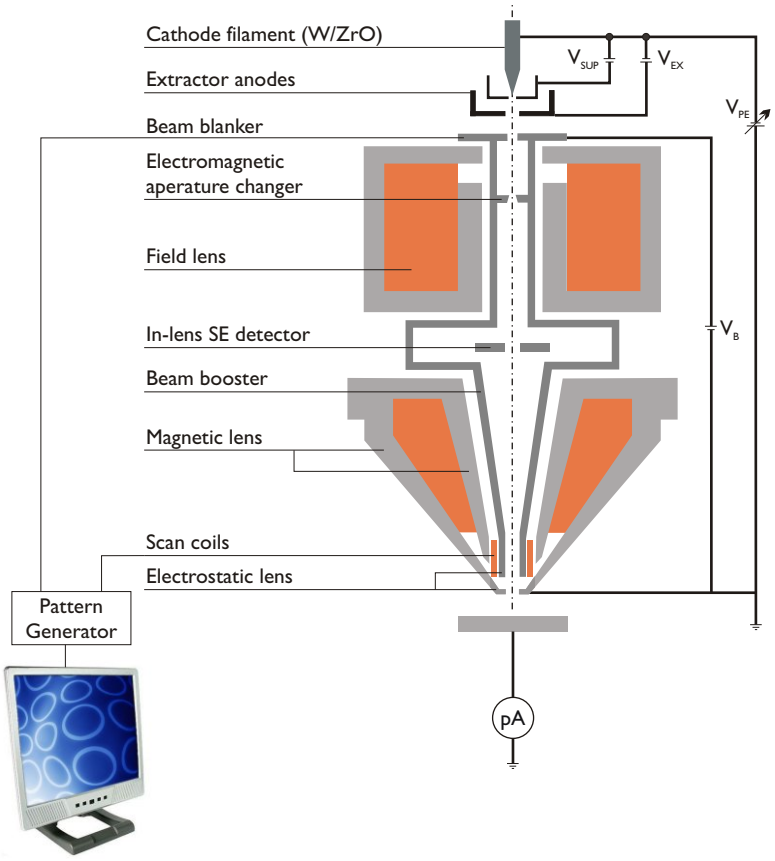

(a)

(b)

Fig. 4.1: Electron Beam Lithography System: (a) a schematic diagram of the system and (b) a picture of the Raith 150 electron beam lithography tool with main housing (left) and computer control (right).

emission, where the electrons are extracted from a sharp electrode by an accelerating voltage, or thermal emission, where electrons are thermally ejected from a heated metal element. In the case of the Raith 150, the column uses a sophisticated combination of both thermal and field emission to attain both high beam current and low beam spread.

Once an electron flow has been created, it must be formed into a narrow beam. This is done by a series of lenses and apertures, which guide the beam down the column. The lenses are provided by magnetic coils which must be adjusted regularly to maintain acceptable stigmation and focus. Scanning coils at the base of the column deflect the beam to facilitate vector scanning of patterns during lithography exposure. To produce arbitrary patterns a high-speed beam blanker is added to the LEO column, to allow 'pattern islands' to be created. The high-data rates required by the scanning coils during operation necessitate additional pattern generation hardware.

The entire system is in a high vacuum to increase the mean-free-path of the electrons to that the can travel unabated to the sample. A particular advancement to note with the LEO SEM column is the in-lens Secondary Electron (SE) detector. Scattered electrons that have enough energy to return back up the column are focused and captured by this detector allowing normal incidence imaging of the sample.

The most common electron-sensitive resist used in EBL is PMMA. PMMA is spun on to the layer requiring patterning using various schemes to thicknesses of about 100-200 nm. Once exposed with the EBL, the exposed PMMA is removed with a developer. An aqueous solution of methyl isobutyl ketone (MIBK) in isopropyl alcohol (IPA) is often used and should be used at a consistent temperature as the development process has thermal dependence. The remaining PMMA then acts as a mask for the layer underneath, and various techniques of pattern transfer are implemented.

The performance of a Raith 150 system was recently investigated with a number of PMMA schemes used to benchmark the processes [193]. The system's resolution, stability, intra-field distortion, overlay and stitching performance were tested. The most important factors for this work was the resolution and intra-field distortion performance, where the Raith was easily able to outperform requirements for the testing of ENFOL and PLL by producing sub-20nm features with pattern-placement accuracy below 20nm (mean plus one standard deviation). This demonstration of performance points to the limits of the system, however much optimisation is required to achieve such numbers and values twice these amounts were typical for Canterbury's system.

Long writes were often performed as it was important to cover large areas of the mask with patterns to increase the probability of obtaining good contact during optical exposures. These long exposures, of up to 18 hours, meant that beam drift was a issue, and would sometimes result in the degradation of high-resolution features patterned near the end of the exposure.

The EBL system also doubles as an SEM and can be a powerful tool for metrology. However, the SEM mode could often not pick up the shallow features in the resist produced by the near-field exposures, and charging on the glass coverslips also limited investigation of the tungsten mask features using this tool.

4.1.2 Reactive Ion Etching

The Reactive Ion Etch (RIE) is a common dry-etching procedure that has the advantages of fewer waste products and a more anisotropic profile than wet-etches. The RIE process was an important development for the near-field mask fabrication as previous lift-off procedures were not favoured due to the probability of 'tags' being introduced causing unwanted spacers between mask and substrate (Ref. [16] page 58). This technique was also used to control the height of planarisation layers. A picture of the Oxford Instruments Plasmalab RIE is shown in Fig. 4.2(a)

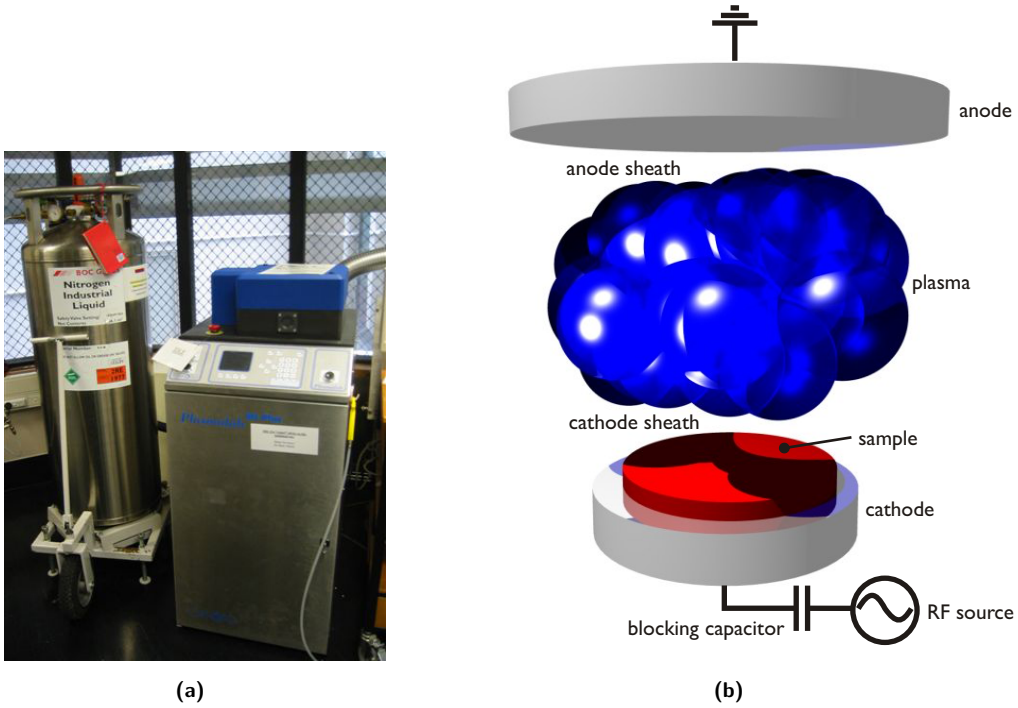

Fig. 4.2: Reactive Ion Etcher: (a) A picture of the Oxford Instruments Reactive Ion Etcher with liquid nitrogen cooling system, and (b) a schematic diagram of the system.

An RIE process is controlled through a number of parameters including pressure, temperature, plasma power and frequency, and etchant chemistry. Figure 4.2(b) presents the components in a typical RIE system. The RIE uses an Radio-Frequency (RF) source to create a plasma, where electrons have been ejected from the present atoms and molecules. The plasma is a mix of reactive and neutral species. The reactive species are a mix of ionised atoms and electrons, which either become etchants

or recombine, a process that can be visualised through photon emission. Due to their higher mobility, the lighter electrons tend to recombine at the walls of the chamber. This results in a more positive charge on the plasma and areas of lower charge density near the walls, which are known as sheath regions. The lower densities allow ions to be accelerated across these regions to impinge on the substrate. The acceleration is performed by a bias voltage, which is set up when an equilibrium of positive and negative charge is met on the cathode. Since the charge flow on the cathode is initially dominated by electrons the equilibrium is found with a negative bias on the cathode and the cathode's bias voltage is stablises at a greater magnitude than the anode due to the cathode's smaller size. The bias influences the bombardment velocity and hence the anisotropy and speed of the etch.

Once the plasma and the bias voltage is set the etching is performed through three mechanisms: sputtering, chemical gasification, and energetic ion-enhanced chemistry. Sputtering is simply an ion bombardment process and hence has low selectively about the material it etches. To facilitate vertical etching a long mean free path is required to allow normal incidence on the substrate surface. The long mean free path is provided by the low charge density sheath region.

In contrast to sputtering, chemical gasification is a chemical etching process and thus provides excellent selectivity between a substrate and masking material. Plasma gases are chosen wisely to obtain beneficial surface chemistry to allow ions to react with the substrate and increase etching speed. This process tends to be isotropic.

To increase the anisotropy of the etch, sputtering and chemical gasification work together to produce energetic ion-enhanced chemistry. Here, the activation energy for the chemical gasification is provided through ion bombardment, which results in faster etches. Finally, ion-enhanced chemistry also allows passivation of vertical walls on the substrate. This protects the sidewalls, inhibiting sideways etching and allowing for a more anisotropic etch.

4.1.3 Direct Current (DC) and Radio Frequency (RF) Magnetron Sputtering

Sputtering was a frequently used technique for precision metal and dielectric layer deposition. The University of Canterbury's Edwards Auto-500 magnetron system was designed to provide two sputtering functions, Direct-Current (DC) sputtering and RF sputtering. A picture of the sputter tool is shown in Fig. 4.3(a).

In a sputtering process a vacuum is first created to remove impurities from the chamber where the components of the system are located. Figure 4.3(b) shows the main components of a magnetron sputterer. The components include the target, the plasma, biasing electronics, magnetic confinement hardware, and the sample. Once the vacuum is created, gases (e.g. Argon) are released into the chamber and energised

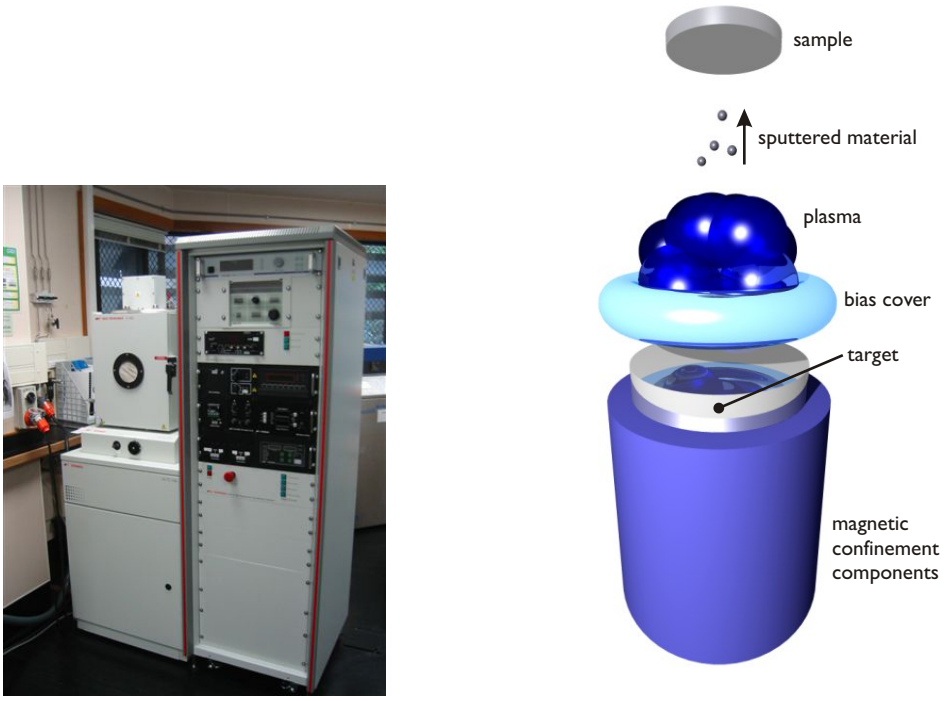

Fig. 4.3: Magnetron Sputtering: (a) An Edwards Magnetron Sputter with chamber (left upper), pump housing (left lower), and system control tower (right), and (b) a schematic diagram of system's internal components.

to create a plasma, which is confined above the target with a magnetic field. At this stage the DC and RF sputtering processes differ in the manner in which a potential is applied to the target. In the case where the target is a dielectric or semiconductor RF sputtering is used because the use of DC produces charge on the weak-conducting target which in turn causes heating. This heating can lead to the destruction of the target through cracking due to thermal expansion effects. The potential difference between the plasma and target causes ion bombardment of target resulting in sputtering of the target atoms. The sputtered atoms, which are sufficiently energised, travel through the chamber and deposit on the sample. The power in the RF or DC source is the main control parameter of the apparatus and influences the rate and quality of the deposition.

4.1.4 Electron Beam Evaporation

The Edwards sputtering system also housed an Electron-beam Evaporation (EBE) unit, and this was investigated as a means to deposit materials. A diagramatic representation on an EBE is shown in Fig. 4.4. In an EBE, a beam of electrons is emitted from a filament (usually tungsten) which is then bent and focused onto a charge of material

located in a crucible. The beam is scanned across the charge to create a molten section, producing energetic atoms that are deposited onto the sample.

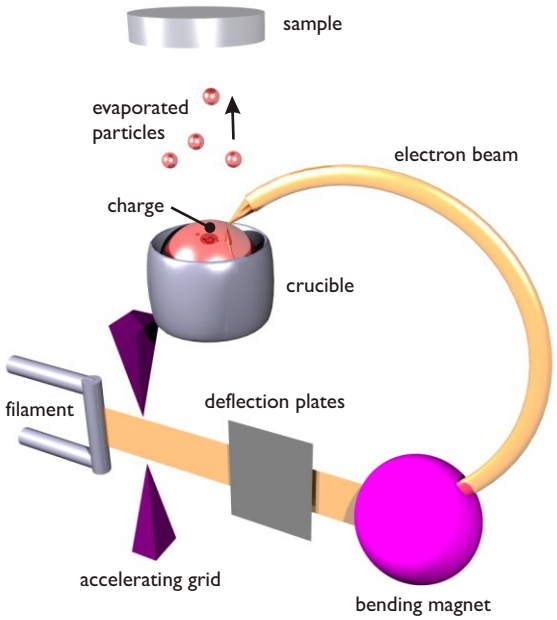

Fig. 4.4: Electron beam evaporation: a schematic setup of the apparatus internals.

For controlling the depostion in an EBE parameters include beam current, extraction voltage, scan rate, and scan area. It is very common to ramp the beam current carefully as heating areas of the charge too quickly can result in fractures and micro-explosions that emit unwanted clumps tens of microns in diameter.

EBEs are considered useful because of their wide range of available materials they can deposit, however the materials that were of most interest to this thesis, namely silver and silicon dioxide, were difficult to deposit effectively because silver is a relatively soft metal and would thus deposit too quickly resulting in rough surfaces, and silicon dioxide was too thermally insulating to evaporate consistently.

4.1.5 Thermal Evaporator

The thermal evaporator was an essential apparatus used for silver and SiO_2 deposition. It proved to be the most reliable and effective tool for smooth deposition of the additional layers in the PLL stacks. Its reliability steams from the simple nature of the machine.

Figure 4.5(a) shows a schematic of the internals of an Balzers 510-A evaporator system, which is pictured in Fig. 4.5(b). A vacuum is created in a inside the chamber where a crucible holds the charge, or material to be evaporated, while the sample is

attached to a location in the chamber such that material is deposited at a desired angle. The sample will generally be located normal to the material flux.

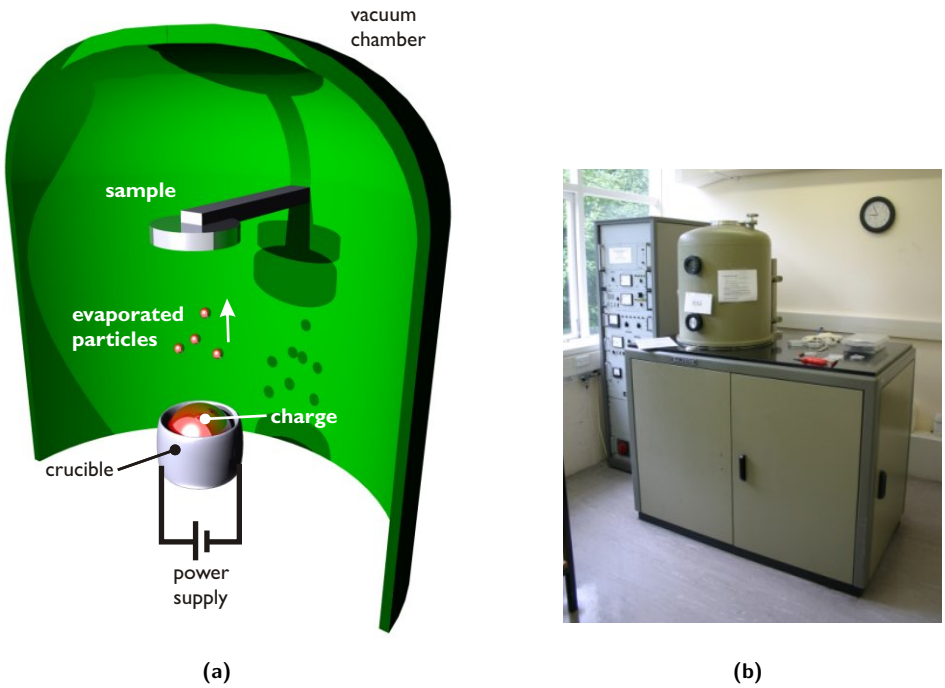

Fig. 4.5: Thermal evaporator: (a) a schematic of the thermal evaporator's internals and (b) the a Balzers 510-A thermal evaporator with chamber (right, upper), pump housing (right, lower), and system control tower (left).

Two materials were able to be loaded in the chamber simultaneously, allowing evaporation of silver and SiO_2 without breaking the vacuum. This was beneficial for the quality of the silver layer as exposing it to air caused oxidation.

4.1.6 Mask Aligner

A S*ü*ss MA6 mask-aligner was used for optical lithography exposures. It houses a UV light source, optical systems for light collimation, a mask support, and a substrate stage. There are many different setup conditions, including: vacuum settings, mask substrate gap, exposure times, light wavelength, mask-substrate alignment, and others. A picture of the mask-aligner is shown in Figure 4.6(a).

In previous work, silicon-nitride membranes were used as the comformable supports [15], but these masks were brittle a broke regularly. A similar problem encounted with the glass membranes was overcome by using the soft-vacuum-contact mode of the mask aligner, which provided a controllable vacuum pressure, allowing the force on the thin conformable masks to be monitored. The mask aligner process used is briefly discussed here.

(a)

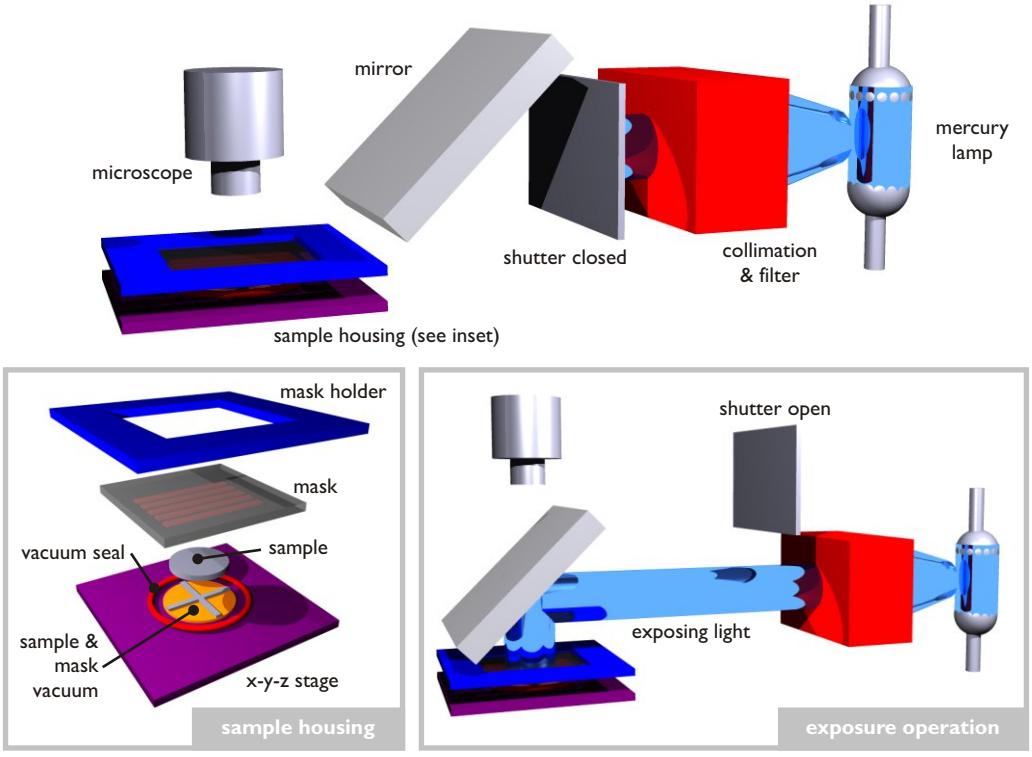

(b)

Fig. 4.6: Mask aligner: (a) A Süss MA6 mask aligner, and (b) a schematic of the mask aligner's operation showing elements during alignment and exposure, as well as the detail of the sample and mask housing.

Figure 4.7(b) details the basic elements of the mask aligner, as well as its simple operation. The mask and sample are inserted their respective holders and are secured by vacuum. The stage supporting the sample is then brought into contact with the mask while the pitch and roll of the stage are adjusted to provide parallel positioning of the mask and sample (wedge-error-correction (WEC)). The stage then moves down a set value in the z-direction to allow alignment between the mask and sample to take place with the use of the microscope. In soft-vacuum-contact mode, the length of exposure and vacuum parameters are set before a seal is inflated to provide a vacuum-tight chamber that is subsequently evacuated. The microscope is then displaced by optics that, once the shutter is opened, guides the exposing light through the mask and onto the sample. After the exposure the vacuum and seal process is reversed and the sample lower and removed.

4.1.7 Atomic Force Microscope

Although some assessment of patterned features can be done with an optical microscope, it cannot resolve features that are below the wavelength of light. It was crucial to the PLL technique's development that sub-wavelength features be evaluated in a consistent and effective manner. To perform this essential task an Atomic Force Microscope (AFM) was used. Hours of work were performed on the department's Digital Instruments' Dimension 3100 (DI 3100), shown in Fig 4.7(a), which provided the measurement technique for nearly all experimental work performed.

The AFM is essentially a mechanical device which achieves nanometre-scale resolution by measuring force interactions between a material's surface and an ultra-sharp probe tip. Figure 4.7(b) shows a schematic representation of the elements in the AFM system. The system images by moving a sharp tip over a sample, while the tip is at a very small distance or in contact with the material, and measuring the forces applied to the tip. The tip is attached to a cantilever, allowing the forces applied to the tip to be obtained through cantilever deflection measurements. The back-side of the cantilever is made reflective so that a laser-diode beam reflected off the cantilever can be captured by a photodiode detector and deflection measured by path difference.

In-plane sample positioning and tip height location is coarsely controlled by stepper motors attach to the stage and piezo-column, respectively. An optical camera is used to locate the desired position to scan. After the tip has been lowered to an appropriate separation distance by the z-stepper motor, fine-tuning and oscillation is performed by a piezoelectric scanner. To arrive at similar nano-scale resolution in the in-plane (x,y) direction, scanning of the tip is controlled by precision piezos on the column that holds the cantilever. Unfortunately, this limits the size of the image to the maximum achievable swing of the in-plane piezos, which is usually around 100 μm. The surface can now be be scanned in range of ways, giving x, y, and z topology information.

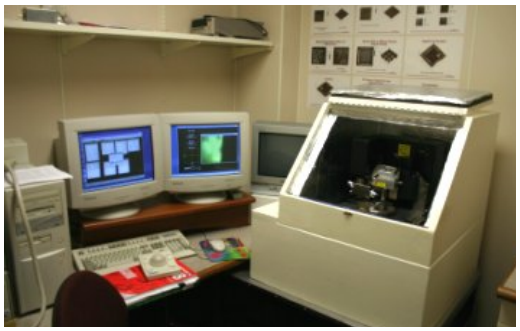

(a)

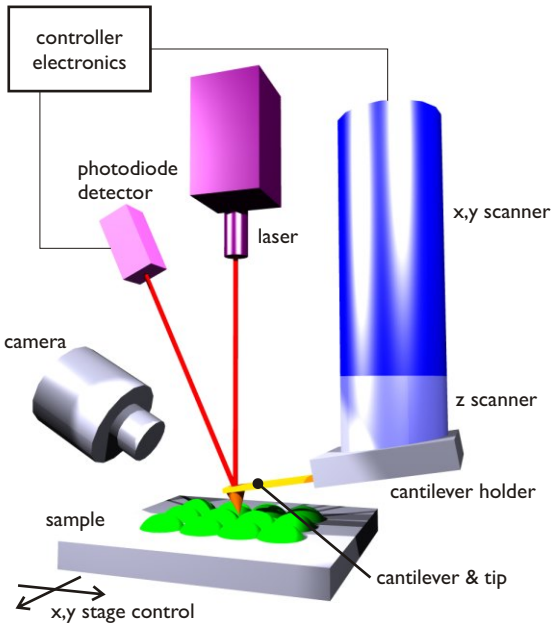

(b)

Fig. 4.7: Atomic force microscope: (a) A Digital Instruments' Dimension 3100 with AFM head-unit (right) and computer control (left), and (b) a schematic of the AFMs main components.

The AFM has three main modes of operation, contact, non-contact, and tapping. The type of sample being examined determines the required mode. In contact mode, the tip is simply dragged across the surface. This mode introduces large forces between surface and tip, thus small variations can be measured. These large forces can also cause modification of the surface by the tip if the sample is soft relative to the force applied. Non-contact mode oscillates the cantilever in the z-direction near its mechanical resonance and measures the dampening of those oscillations as the tip experiences attractive forces from sample at small separation distances. The dampening of the oscillations are then interpreted to get sample height or material information. Feedback is used to maintain a force between the surface and tip to ensure no contact. Non-contact mode relies on smaller forces and is thus not as accurate as contact mode, however, the advantage of no contact means soft materials can be imaged. Tapping mode is similar to non-contact but with the allowance of brief contact with the surface. This increases the accuracy of the height measurements from non-contact mode without introducing the damage caused by constant contact.

4.1.7.1 AFM Imaging Artifacts

Imaging artifacts during AFM scans are a direct result of the mechanical nature of the system. Most artifacts which occur as a results of setup parameters and be minimised by reducing the speed of the tip (to stop tip 'launching' off edges) and modifying feedback loop parameters (to fix overshoot and unwanted oscillations). One physical limit that is difficult to overcome is the problem of tip convolution. Figure 4.8(a) shows a typical end-on view of an AFM probe, which has a cone like shape with an edge slope from 13 to 20°. The height of such a probe is usually on the order of 15 to 20 μm with an tip radius of 10 nm. The cone shape immediately causes a limit to the tip's ability penetration into deep sub-100nm lines and pits. The scan produced by such a tip will end up being a convolution of the surface of the sample an the tip, as depicted in Fig. 4.8(b). A de-convolution can be applied to reverse the effects, but in this case assumptions must be made about the tip's profile. Image fidelity can also be seriously reduced by tip degradation and contamination.

An SEM of a typical AFM probe is shown in Fig. 4.8(c), and due to the effects mentioned above this tip did not perform well imaging gratings with periods less than 250 nm. This was obviously an issue for this work as it was essential for smaller periods to be imaged. To improve performance, an new type of tip, called a STING, was used [194]. An SEM of the end of the STING tip is shown in Fig. 4.8(d), where the key advantage of the tip can be seen. A micron-long dendrite made from built up carbon deposits is grown in the end of the tip. The radius of the dendrite is typically 50-80nm across the structure with a sub-10nm tip, allowing the probe to fit into sub-100nm crevices. The dentrite is also angled at 10° to match the angle that the probe

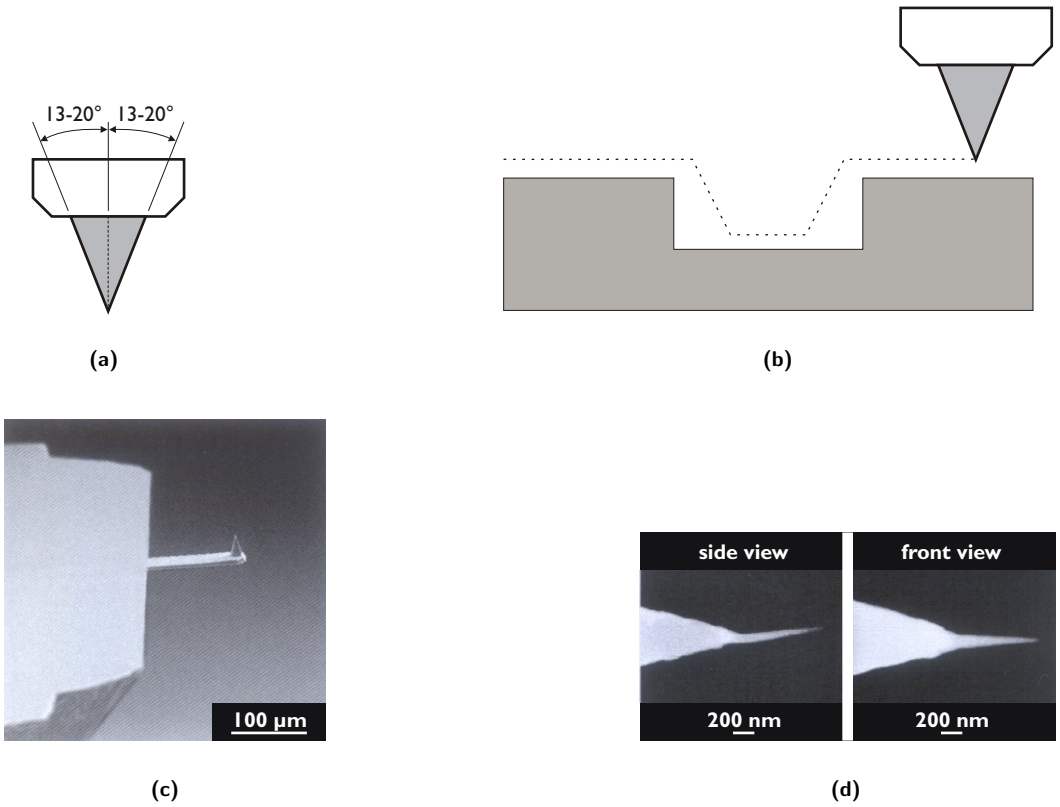

Fig. 4.8: AFM tips: (a) schematic of AFM tip profile, (b) schematic representation of the introduction of tip convolution artifacts, (c) SEM image of typical AFM cantilever structure, (d) SEM image of an AFM STING tip with ultra-sharp tip.

makes with the surface so that the dendrite stands normal to the surface. STING tips were used extensively.

4.2 MATERIAL PROPERTIES

The characteristics of the deposited layers, namely surface roughness and layer thickness, were extremely important to the success of the process. The tool at the centre of layer investigation was the AFM, which offered accurate nano-scale roughness and height measurements, and the AFMsoftware proved by Digital Instruments (Nanoscope III 5.12r3) proved to be very effective at extracting accurate data in a timely manner.

4.2.1 Classifying Surface Roughness

Classifying surface roughness was a major part of the experimental optimisation process. Smooth surfaces were essential for delivering high-fidelity planar lens imaging. The AFM was used to obtain surface roughness values for all deposited layers. AFM scans would be obtained of a surface on such a scale so that the major roughness influences were spatially over-sampled. Statistics are then performed on the image

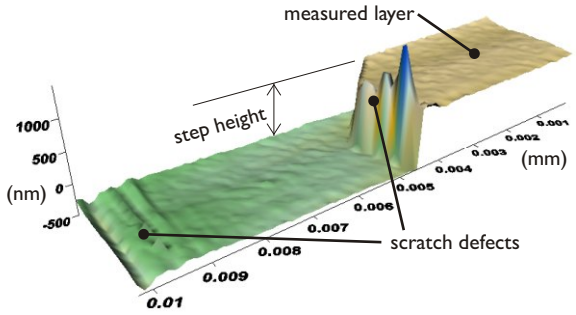

Fig. 4.9: AFM scan of a scratch used to determine the height of a layer.

through the AFM application, providing the classification through two values – root-mean-square (rms) and peak-to-peak. The later is simply the maximum range of the heights present in the image, while the former is a measure of the height distribution and is the square-root of the average of the squares of all height values in the image relative to the mean height. The rms value tells you about the distribution of the entire image, while the peak-to-peak is the worst case height fluctuation.

Typically, a smooth layer of PMMA resist will have roughness of around 0.5 nm rms with a peak-to-peak of around 4 nm across a 1 μm scan. The goal of layer deposition was to achieve around 1 nm rms and less than 10 nm peak-to-peak for Ag and SiO_2 depostion.

4.2.2 Calculating Layer Thicknesses

Having precise thickness information about deposited layers was essential. Thickness measurements standardised the process and allowed comparisons to be made. A step height was the common method used for thickness measurement, and was found to be very reliable. Ellipsometry was also experimented with and backed up step-height measurements.

4.2.2.1 Step-Height Measurements

Using either the AFM or the Surface Profilometer (Detak) a step-height between to layers could be measured. The AFM was used extensively, but this often required a scratch through a layer to provide the step. This scratching process was somewhat unreliable as it required the top layer to be completely removed and the bottom layer to remain unscathed. Figure 4.9 shows an example of scratch scanned by the AFM. The figure shows some of the drawbacks of this technique. Scratches can be seen on the lower level, which are caused by the scratching tool. These areas must be avoided when scratch measurements are taken. The AFM sofware tool allows step heights to

be calculated by averaging the height over two selected areas and then finding the difference of those two averages. Using this technique the scratches are avoided. If there is not a material under the layer in question that can withstand the force of the scratch the technique was unusable and other methods need to be employed.

To avoid the question of whether the material underneath the layer is able to remain unscathed during scratching, reference samples of silicon were used. To overcome the scratch problem altogether, a reference sample and lift-off process was used where the sample was patterned with resist before layer deposition. After deposition, acetone was used to lift-off the resist leaving an AFM scanable step. This was a common technique for sputtering or evaporation thickness measurements and proved to be an excellent way to determine deposition thickness as it was non-destructive process.

The AFM's ability to reliably measure height was questionable. The performance of the AFM's height calibration was tested by using samples of a known height [195]. Figure 4.10(a) shows AFM measured values against the actual values of the calibration samples. The correlation is clearly evident with a average scaling factor (calibration ratio) of 1.13. It was important that the calibration was regularly checked to ensure consistency. Figure 4.10(b) shows the temporal effect on the AFM's calibration. An as yet unsolved glitch appeared at the 22-month point which resulted in a modified ratio. The linearity across a variety of step heights was remained consistent.

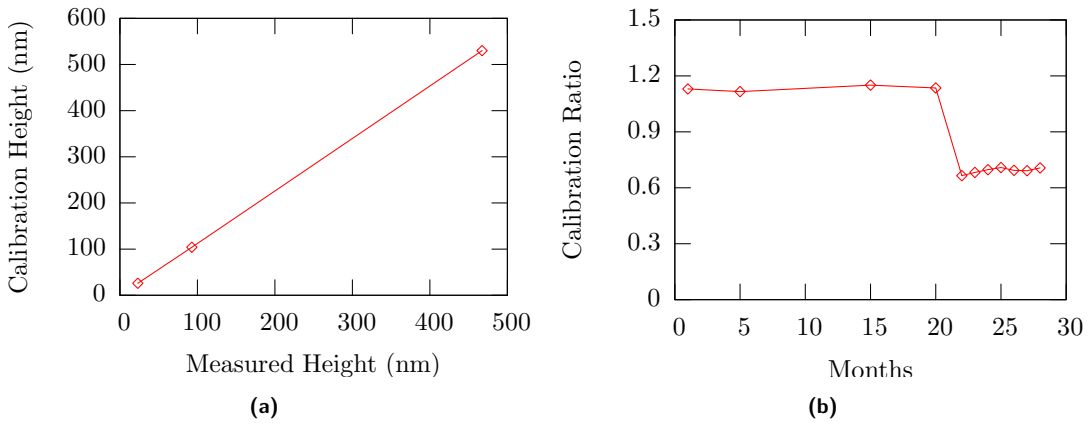

Fig. 4.10: AFM calibration: (a) height calibration for a range of calibration samples, and (b) movement of calibration ratio over time.

4.2.2.2 Ellipsometry

A more involved technique used for layer thickness measurements was ellipsometry. Ellipsometry functions by reflection a beam of polarised light off a sample at a known angle and measuring polarisation change after reflection. Ellipsometry was mainly used to confirm the AFM measurement technique. With the help of ellipsometry analysis software to determine the thickness of layers, a range silver and $Si0_2$ layers were mea-

sured with both techniques with differences of no more than a 4%. The ellipsometry measurement process was easier if a reference sample was used, as multiple layer stacks decreased the precision of the technique due to the complex multi-dimensional space that is created to gain a solution. Because of the AFM's availability and its ability to measure quickly, ellipsometry was rarely used.

Chapter 5

MASK FABRICATION

"Don't lower your mask until you have another mask prepared"

- *Katherine Mansfield*

At the centre of the experimental work is the mask fabrication process. The goal was to fabricate a photomask that can be used in a setup which enables repeatable pattern transfer of the optical near-field. This process required extensive development to achieve high quality sub-100nm mask features and exact control over layer deposition.

Three types of masks have been created; ENFOL masks, proximity lithography masks, and PLL masks. The work here is based on previous work by Alkaisi *et al.* [15] and Goodberlet *et al.* [17], where conformable masks were placed under vacuum pressure to insure intimate contact between the mask and substrate. This method was used to overcome the relatively low probability of gaining intimate contact across large areas when using rigid mask plates. Intimate contact provides the opportunity for the near-field intensity distribution produced by the optical mask to be transferred into a photoresist, allowing it to be studied. Recently, an industry-based development system has achieved impressive sub-100nm results using this technique [4]. The experimental setup for ENFOL was shown previously in Fig. 2.21 and the modified PLL setup, which included the extra lensing stack, was shown in Fig 2.22.

To summarise the mask fabrication process, tungsten features are first patterned on conformable glass substrates for both ENFOL and PLL, before the PLL mask is deposited with additional stack layers. The finished masks are attached to a rigid support and brought into vacuum contact with a resist stack for lithographic exposures. The details of these processes follow. Figure 5.1 shows the mask making steps performed in the process.

5.1 PATTERNED METALISED MASK

For both the ENFOL and PLL work a metalised mask was required. Tungsten was chosen as the metal absorber for the mask because of its ability to be dry etched using

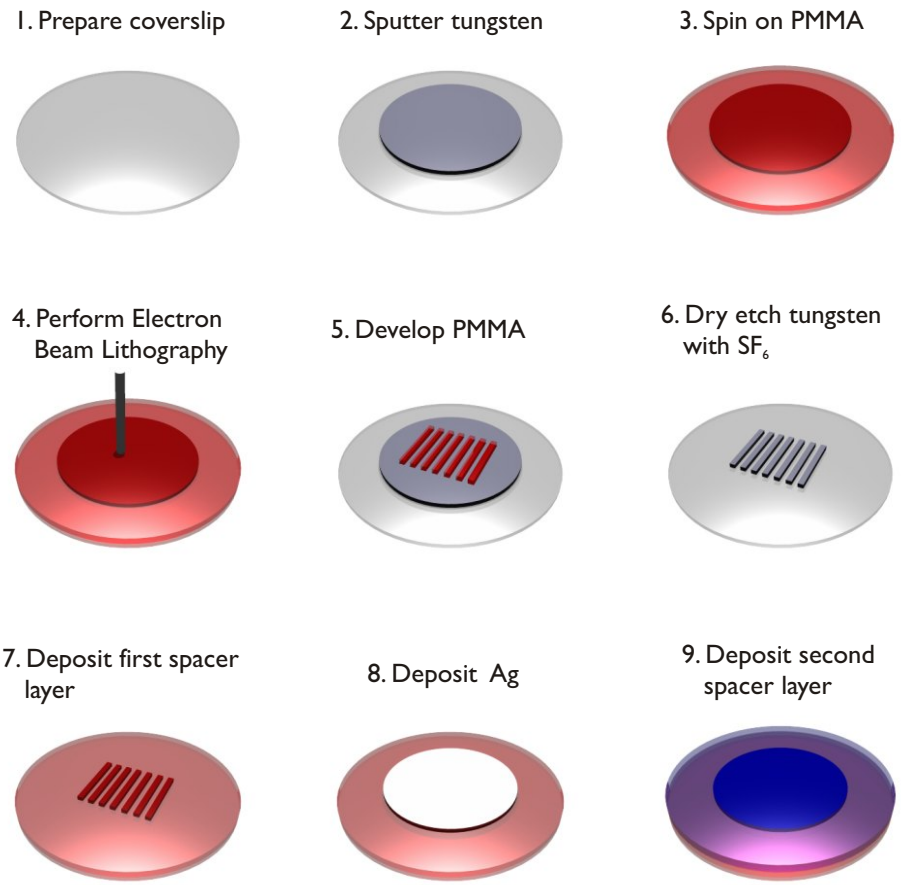

Fig. 5.1: Mask fabrication process: a schematic representation of the steps required to produce a mask.

available gases (SF_6). This avoided the difficulties of associated with the alternative lift-off process. Previous work demonstrated that 'tags' produced by lift-off processes introduce unwanted spacers between the mask and substrate when trying to perform intimate contact lithography [16].

These conformable contact masks have been built on both 100-μm and 200-μm thick coverslips, ranging in size from 25 mm to 75 mm in diameter. The range in coverslip thickness and size was used to investigate the ability of a mask to conform over an uneven surface. In general, the thinner and larger the mask, the better the conformability, which in turn makes the mask more fragile. The transmission properties for the 200-μm thick glass slips is given in Fig. 5.2, measured with a Carey spectrometer. The cross-hairs in Fig. 5.2 give the lower 3dB bandwidth for transmission at a 316-nm wavelength. Transmission at the required i-line wavelength of 365nm is good (>80%).

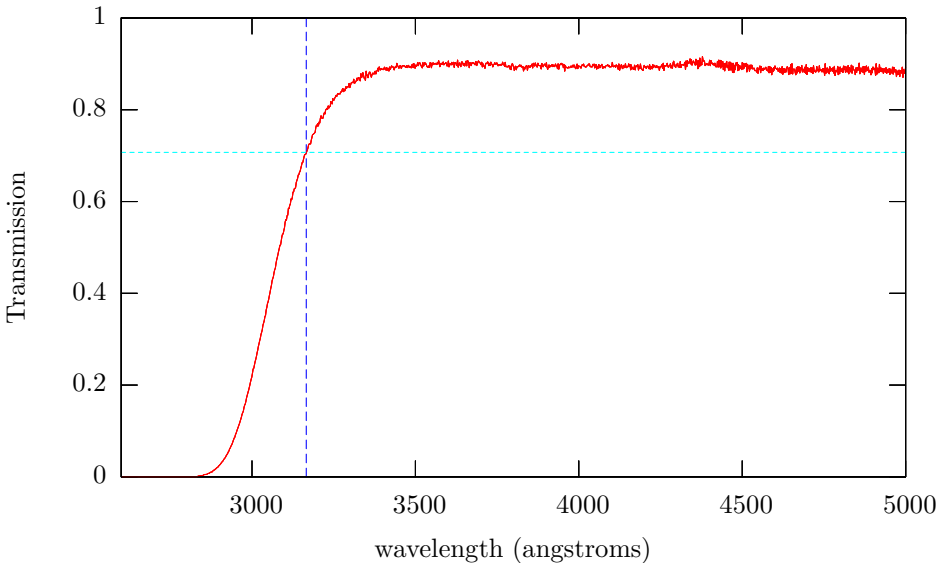

Fig. 5.2: The transmission properties of a 200μm thick glass coverslip.

5.1.1 Tungsten Sputter

The coverslips are first metalised with a tungsten film to a thicknesses of 30 or 40 nm. This was performed in the Edward AUTO 500 DC magnetron sputterer described in Section 4.1.3 with the process parameters given in Table 5.1. Through AFM analysis typical surface roughness parameters were measured as 0.4 nm rms and 4 nm peak-to-peak. This is sufficiently smooth for producing features down to 50 nm from subsequent ENFOL masks.

Table 5.1: Sputterer process parameters for tungsten.

Target	Power	Rate	Temp.	Process Pressure
W (99.99%)	300W DC	0.24 nm/s	25°C < T < 40°C	8.5e-3 mBar

5.1.2 Coverslip Spin-on Procedure

Working with thin coverslips introduced major difficulties when trying to spin on the PMMA electron sensitive resist. The wafer spinner uses a vacuum to hold the material to the chuck. It is the application of this vacuum which causes defects in the layer spun onto the coverslip when it conforms to the underlying vacuum channels, which introduces a distorted height profile of the resist. In order to overcome the need for the vacuum an adhesion material (Blu-tak^{TM}) was introduced between the chuck and the coverslip. The coverslip is then placed on top of the smoothed out Blu-tak and light air-pressure applied from above to achieve even adhesion across the area of the coverslip. Once the layer has been spun on the coverslip is carefully removed and any

unwanted material that was transferred to the coverslip from the Blu-tak is gently cleaned with a cotton swab.

This process is by no means perfect because it introduces unwanted contamination and inconsistencies during attachment. In the future it would be beneficial to create a chuck that could hold the coverslip during spinning without distorting it.

5.1.3 PMMA Scheme

A range of PMMA schemes were attempted with the requirements of high resolution (50-nm features) and enough height to provide the masking requirements for the tungsten etch. The final scheme was a single layer of high-molecular-weight (HMW) PMMA spun onto the coverslip at 4000 rpm for 60 seconds with an acceleration of 2000 rpm/s. The mask is then placed in an oven at 185°C for 30 minutes. The final PMMA thickness was measured to be 120nm ± 5nm.

5.1.4 Electron Beam Lithography Pattern Design

Before performing the EBL work the pattern to be written must be designed. Pattern design was initially performed on the Raith EBL system (see Section 4.1.1), which uses the GDSII[1] format for storing graphical data and provides a simple editor. The main focus of all the experimental work was to investigate the resolution of the process, therefore, patterns with gratings at a range of pitches and duty cycles were designed. The Raith EBL software became sluggish and unstable once design work started to produce large files. To limit the reliance on this system, a text-based software engine was designed, which utilised hierarchical methods for object control. The code for the pattern generation was written in php, which is s hypertext preprocessor engine for generating dynamic internet pages. By using php the pattern generation program could be internet-based allowing easy access. The full script of the code is provided in Appendix D. This software exported files that could be imported[2] into the Raith software at the time of patterning, thus removing the dependence on the Raith software.

An evolving series of masks were created which were patterned with a range of features including: gratings with pitches from 100 nm to 5 μm with variable duty cycles, isolated line pairs with separations from 50 nm to 500 nm, isolated text features, and isolated corner features. The features used provided an effective way to analysis the resolution limits of the system.

[1] GDSII, or Geometric Data Stream II, is a generic 2D graphical data format commonly used to describe mask patterns for lithography processes.

[2] Files where imported into the Raith EBL software in an ASCII format.

5.1.5 Electron Beam Lithography

Once the lithography pattern had been designed the EBL work could begin. The process required optimisation to gain the correct clearing doses for line and box features. Typical dose parameters are given in Table 5.2 that were used with a beam voltage of 10kV. The exposed PMMA was developed at a temperature of 23°C for 25-30s in a solution of methyl isobutyl ketone (MIBK) diluted 1:3 with IPA.

Table 5.2: Electron beam lithography dose parameters for a beam voltage of 10kV.

Draw type	Dose
Area	150 μC/cm^2
Line	600 pC/cm
Dot	300 fC/dot

5.1.6 Tungsten Etch

RIE was used to transfer the PMMA etch mask into the tungsten film. An Oxford Instrument's Plasmalab 80 Plus etcher was used with the etch parameters found in Ref. [196], which are shown in Table 5.3. With this process a 10 s etch was used to ensure complete etching of 30-nm thick tungsten. Longer etches were used for the 40-nm thick tungsten masks.

Table 5.3: Process parameters for reactive ion etching of tungsten and PMMA.

Material	Etch Mask	Etch Rate	Gases	Flow Rate	RF Power	Temp.	Process Pressure
W	PMMA	3.8 nm/s	SF_6	80 sccm	200W	313°K	150 mTorr

At this point an ENFOL mask has been completed. Figure 5.3 and Fig. 5.4 show images of a range of mask features for SEM and AFM scans, respectively. The SEM scans show features etched in 40-nm thick tungsten including a 25% duty-cycle 1-μm pitch grating, and three gratings at 170 nm, 145 nm, and 100 nm with approximately 50-nm line widths. SEM cross-sections are not presented as it was extremely difficult to capture an image due to charging effects of the glass substrate and the thickness of the tungsten.

In Fig. 5.4(a), an AFM scan of 1-μm pitch features with text is shown and is an example of a good quality etch into a 40-nm thick tungsten layer. Figure 5.4(b) shows a poor quality etch that was performed using the exactly same conditions as the etch used to produce Fig. 5.4(a). Figure 5.4(c) shows a trace taken through the dashed line in Fig 5.4(b). The variability in the results of the etch were initially common, but through standardising all factors of the etch the process become reliably repeatable. The major

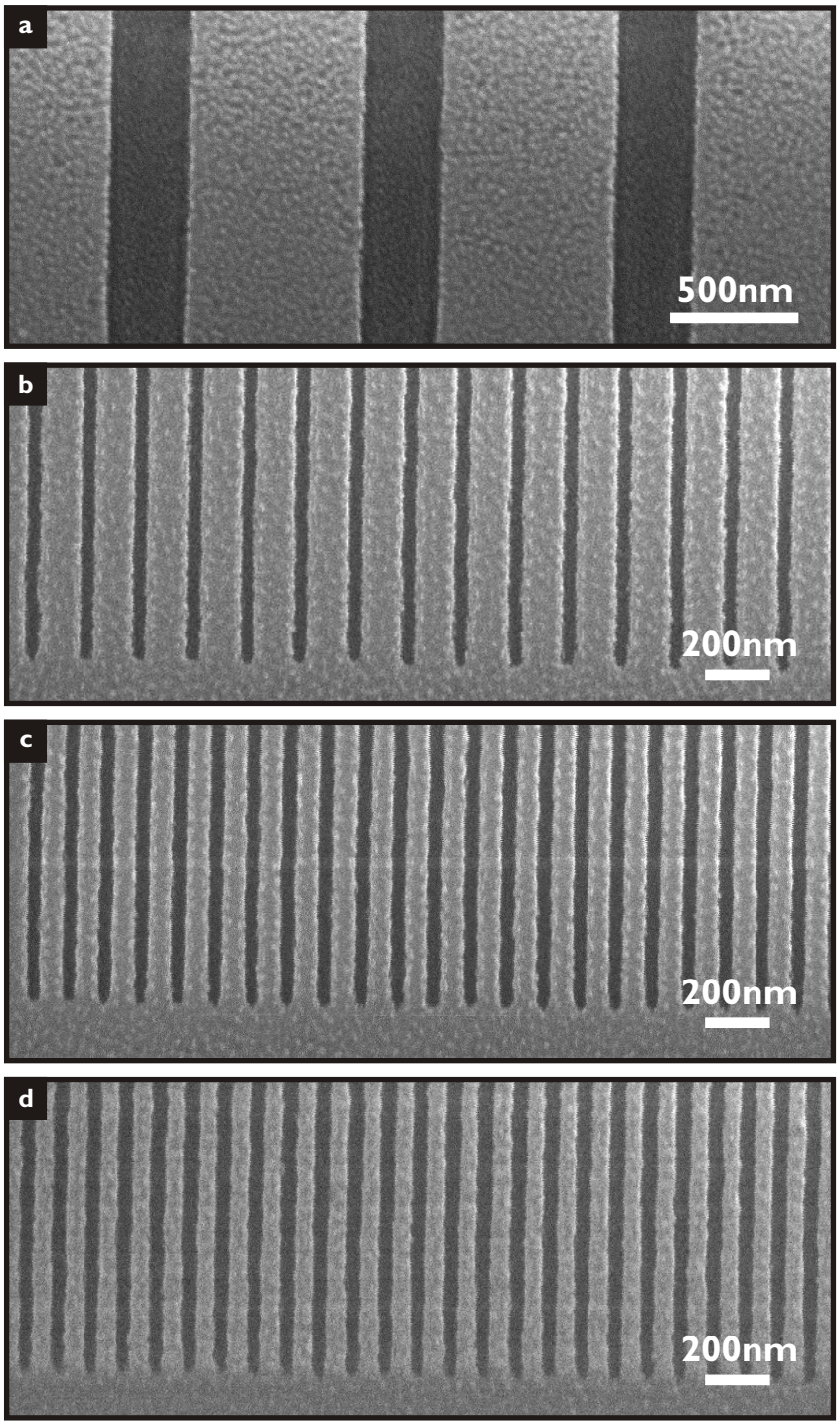

Fig. 5.3: Scanning electron micrographs of the final etched tungsten mask, including (a) a 25% duty-cycle 1-μm pitch grating, and three 1.0 dose line gratings at (b) 170 nm, (c) 145 nm, and (d) 100 nm.

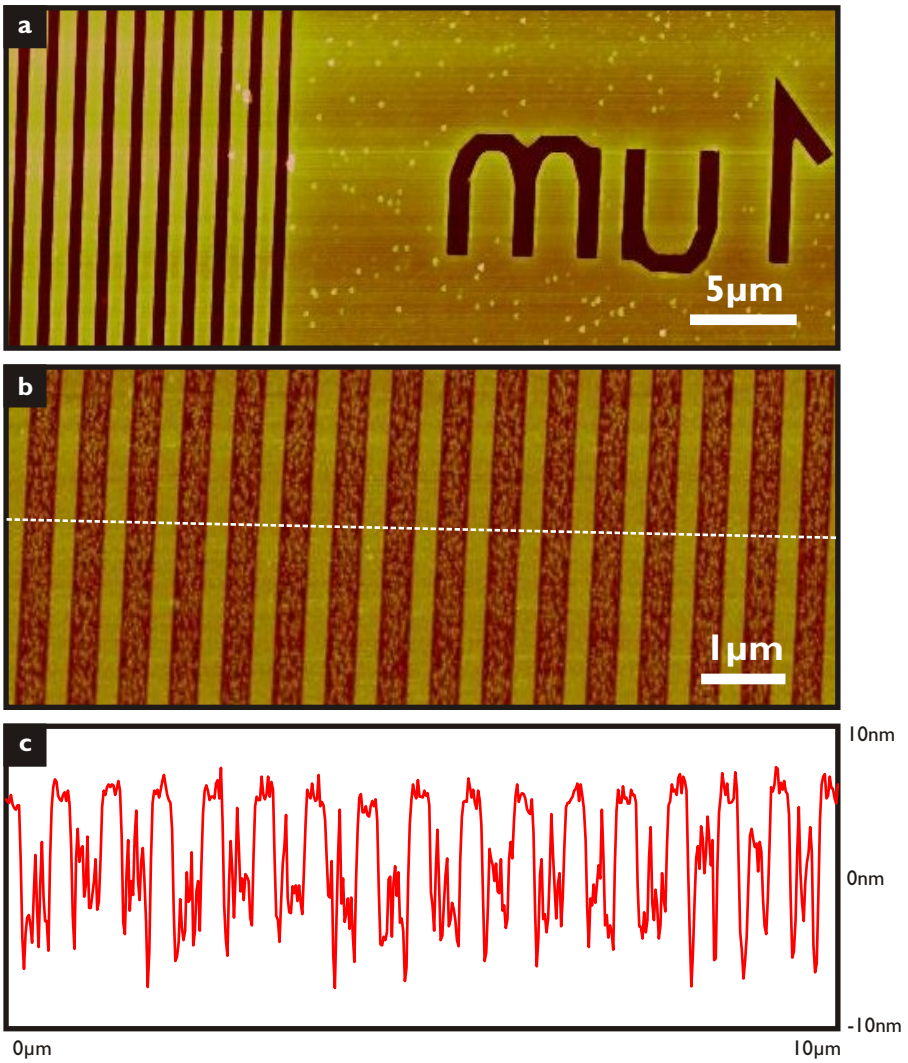

Fig. 5.4: Atomic force micrographs of the final etched tungsten mask, including (a) a 1-μm pitch features with text, (b) an under etched 500-nm pitch features, and (c) a trace through (b) as indicated by the dashed line.

factors affecting the etch quality outside of the parameters given in Table 5.3 were the age and type of the electrode used, and contamination caused by unwanted gases present in the chamber. New NiCr electrodes caused variability because of an increase in sputtering from the electrode. This is what has caused the quality reduction between the metal features shown in Fig 5.4(b). The trace (Fig 5.4(c)) shows how the etch has failed to get through the 40 nm of tungsten. Hence, new electrodes were processed in an hour long oxygen clean before being used. Often when new electrodes were used this "residue" would remain in the spaces, however, it would appear transparent. It was not clear whether the AFM was providing a valid representation of the profile, or if the material was causing non-linearities in the measurement of the height. The residue issue was avoided rather than understood. To combat inconsistencies in the

gases present in the system, prior to an etch all lines were pumped clean and 20 minute oxygen and 5 minute SF_6 cleans were completed.

The final step for an ENFOL mask was to attach it to a rigid glass plate to make it compatible with the available optical lithography system. For the PLL mask additional layers are required first; the construction of these layers is explained in detail in the next few sections.

5.2 FIRST SPACER LAYER

The process of applying the first spacer layer is extremely important to produce good PLL results. The first layer has two functions: providing a means of spacing the silver from the mask, and planarising the tungsten mask to smooth out the uneven topology to allow the necessary planar silver layer to be subsequently deposited. The effectiveness of the spacer layer was characterised in two ways: through the ratio of grating depression heights before and after planarisation at a certain pitch, and surface roughness.

In earlier experiments, when thicker spacer and silver layers were used, the first spacer layer was simply constructed by spinning it on to the required thickness. However, this limited the experimentation to spacer layers thicker than 60 nm and thus, to achieve Pendry's ratio (1:2:1), silver layers thicker than 120 nm. The reason for this was that a 60 nm spacer layer would reduce the 40-nm thick tungsten mask modulation to around 15 nm peak-to-peak, which is of the order of the silver layer peak-to-peak roughness and thus can be considered small enough to not affect the results. Figure 5.5 shows the planarisation above a 1-μm grating (Fig. 5.5(a)) for a spun on layer of PMMA that has been measured to have a height of 61 nm. This layer was 2.5% HMW PMMA spun on at 5000 rpm with 4000 rpm/s acceleration, and the planarisation is about 15 nm peak-to-peak. Figure 5.5(c) gives an the step height measurement for the same layer. After leveling, the average of the height in the 'y' box is taken and subtracted from the average height in the 'x' box to give a step-height of 61 nm.

If the PMMA was spun on thinner, the topology of the tungsten mask was transferred though the stack at an unacceptable level. An advanced technique for planarisation was developed with the goal of a final modulation below 10-nm peak-to-peak. This technique is explained below.

5.2.1 Advanced PMMA Planarisation

To achieve better planarisation a layer of PMMA is spun on to about 3-5 times the thickness required, before being re-flowed to increase planarisation and then dry-etched back to give the necessary thickness. A solution of 4% HMW PMMA is spun on (4000 rpm speed and 2000 rpm/s acceleration) to the mask to provide an initial spacer

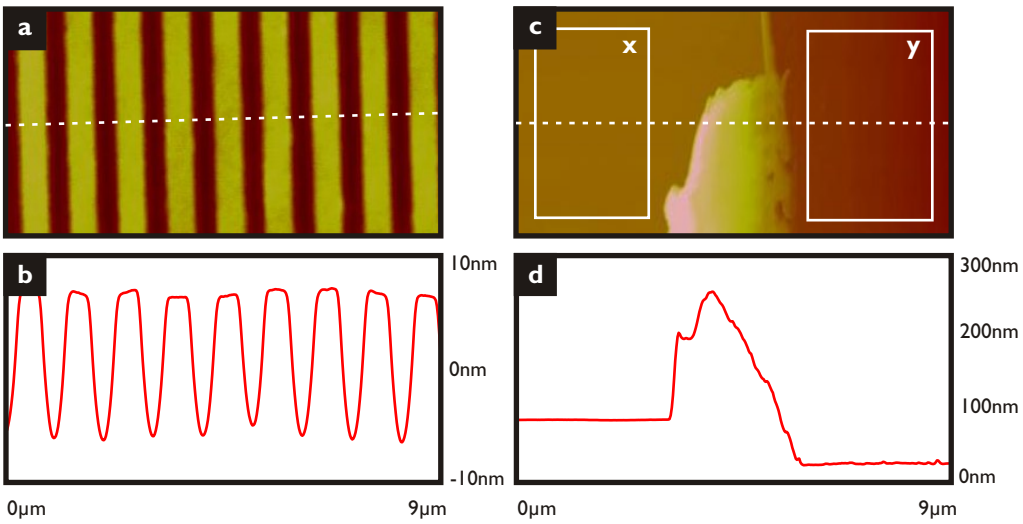

Fig. 5.5: AFM scans of PMMA for a 61-nm thick first spacer layer spun onto a 40-nm thick tungsten mask for (a) the surface above a 1-μm pitch grating and (c) the scratch made to test the layer's height. (b) and (d) are averaged line scans taken through (a) and (c), respectively. The averages are taken over 480 line scans.

of about 150-nm thickness. The mask is then placed in a 185°C oven overnight to allow the polymer to re-flow and smooth over the tungsten mask patterns; example AFM scans of the resultant surfaces are shown in Fig 5.6. Typical peak-to-peak modulation above 1-μm 50% duty-cycle pitch features was 8-nm peak-to-peak, and improves to 2-nm peak-to-peak above 250-nm pitch features. The roughness of the re-flowed surface was on the order of 0.5-nm rms, which is similar to the underlying tungsten surface.

The next step is to etch back the PMMA to an exactly determined height. A PMMA RIE recipe was developed to perform this action, with the goal of the etch being to maintain a smooth surface while controlling the etch depth. The final etch recipe is given in Table 5.4. It was determined that a lower power and high gas flow rate etch produced the smoothest surface, with typical values for the roughness of the final PMMA surface being less than 0.8 nm rms. Figure 5.7 shows an AFM scan and trace of a typical PMMA surface after the planarisation etch. This surface is for a 35-nm thick first spacer layer, and has a roughness of 0.4 rms with a peak-to-peak of 5 nm.

Table 5.4: Process parameter table for reactive ion etching of PMMA spacer layer.

Material	Etch Mask	Etch Rate	Gases	Flow Rate	RF Power	Temp.	Process Pressure
PMMA	-	3 nm/s	O_2	40 sccm	100W	295°K	100 mTorr

Once the PMMA etch was optimised, experimental tests on its ability to control the height and to planarise were performed. During height-control tests it was found

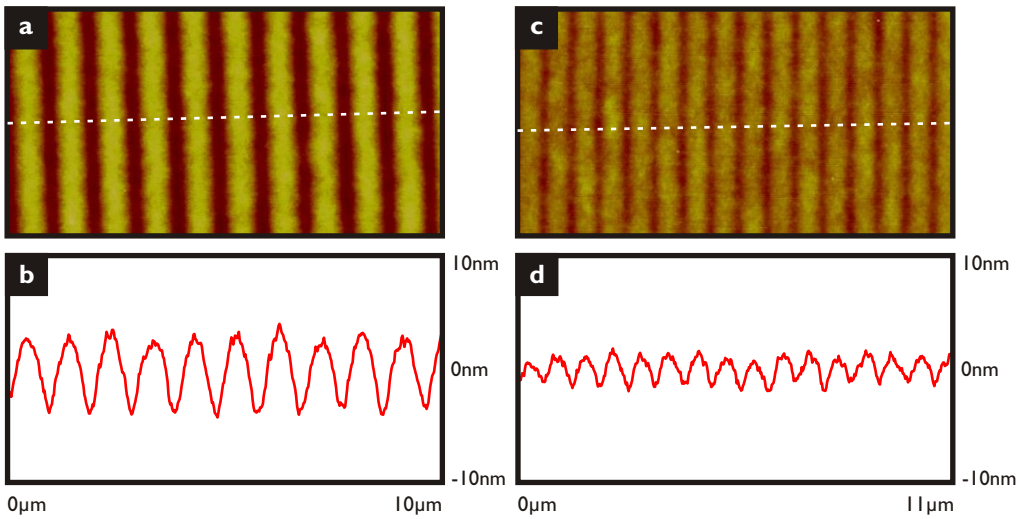

Fig. 5.6: AFM scans of a PMMA surface for a 154-nm thick first spacer layer after 8 hours of reflow bake at 185°C above (a) 1-μm and (c) 700-nm pitch gratings etched into a 30-nm tungsten film. (b) and (d) are line traces through (a) and (c), respectively (as marked by the dotted line).

that the O_2 etch was non-linear with respect to time. This resulted in etches performed for twice the time resulting in up to 8-times the height change. Figure 5.8 gives the experimental data for the etch rates of the PMMA for a range of etch times. The variability in etch times was attributed to heating of the insulating glass coverslip. Temperature-controlled etching could not overcome this issue, so etches were performed in small bursts to minimise heating. The key of Fig. 5.8 indicates where data was gathered from multiple etches of a certain length (i.e. if a marker for three etches lies at 15 s it means that three 15-s etches were run with the corresponding average etch rate). Shorter etches produced fairly consistent results and also provided smoother etched surfaces.

Figure 5.9 gives the experimental data for the planarisation of the PMMA at different stages of etch-back. Excellent planarisation is achieved across all pitches after re-flow and before the etch, when the PMMA is around 150nm thick. Major effects in planarisation values are seen for the larger pitch features as the thickness of the PMMA is reduced. Here, the substrate heating effects that caused the variable etch rates are also causing a certain amount of re-flow, and surface tension is causing the PMMA to re-conform to the underlying tungsten features.

The graph shown in Fig. 5.9 demonstrates some poor planarisation, especially for for the 1-μm pitch features, which show minimal planarisation when the layer thickness goes below 100 nm. However, this graph's purpose is to demonstrate the effect of reflow during etching and hence, earlier results that suffered from this effect have been plotted. The graph does not feature optimised results that were produced by pulsing the etch and achieved less than 10-nm planarisation for all features.

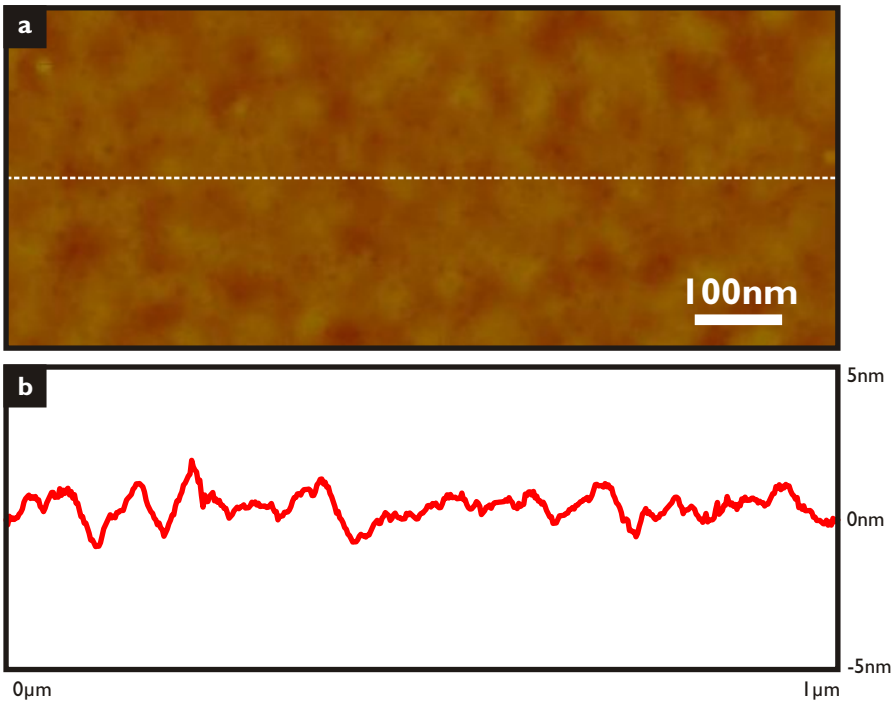

Fig. 5.7: An AFM scan of a PMMA surface for a 35-nm thick first spacer layer: (a) presents an image of the scan, while (b) shows a trace taken as marked by the dotted line.

Figure 5.10 shows an optimised result for the planarisation of 500-nm pitch features by a first spacer layer that has been spun onto a 30-nm thick tungsten mask and subsequently etched back to a height of 25 nm. Here, the planarisation has performed well with around 6-nm peak-to-peak fluctuations, which is similar to the planarisation when the PMMA was 150-nm thick.

5.2.2 Other Planarisation Issues

It was found that PMMA would perform better as a planariser if it was spun onto PMMA, thus spinning on a thin layer before a thicker one would result in better planarisation. This was due to surface wetting phenomena.

A few different types of electrodes were used during the PMMA etch. All were Si substrates that were either bare, or had NiCr or Cr coating. It was found that with the NiCr and Cr electrodes that were first used extra roughness would be seen after the etch. This relates to the issues experienced during tungsten etching (see section 5.1.6). For the PMMA etch, bare silicon, and specifically roughly etched, or 'black' silicon, was found to give the most consistent results.

Additional layers deposited onto the stack further planarise the features to the extent that the planarisation is better than the roughness of the layers. Deposition of the additional layers are described below.

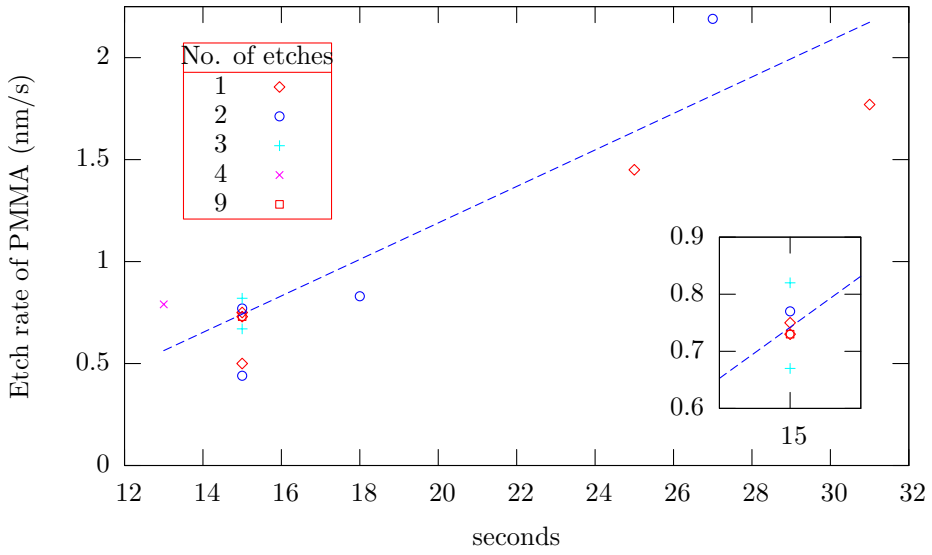

Fig. 5.8: Experimental data for etch rates of the oxygen PMMA RIE process. Data points are given for different numbers of consecutive etches of a certain length. For example, a '+' point at 15 s indicates three consecutive etches of 15 s each, which corresponds to a 0.65 etch rate per second for the total time of 45 s.

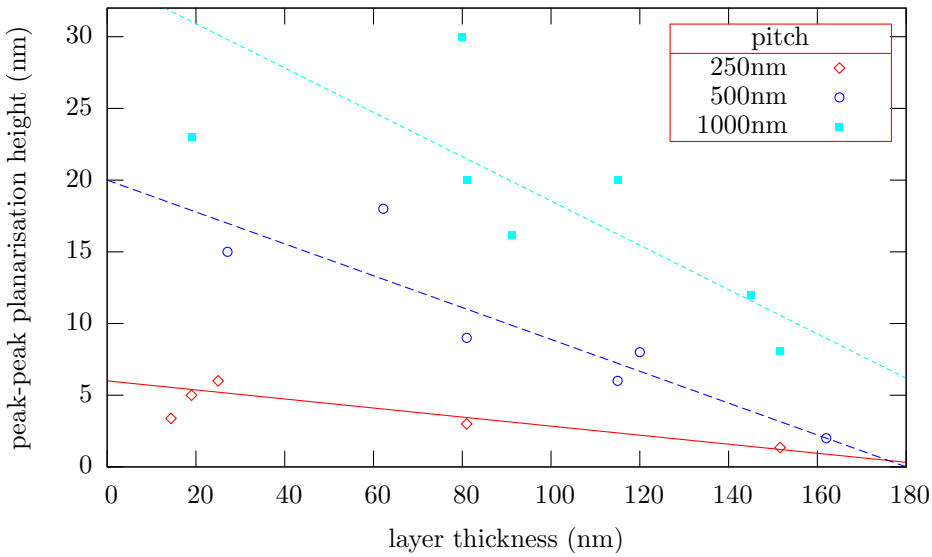

Fig. 5.9: Experimental AFM measurements of planarisation for different thicknesses of PMMA. Values around 150 nm are for unetched PMMA.

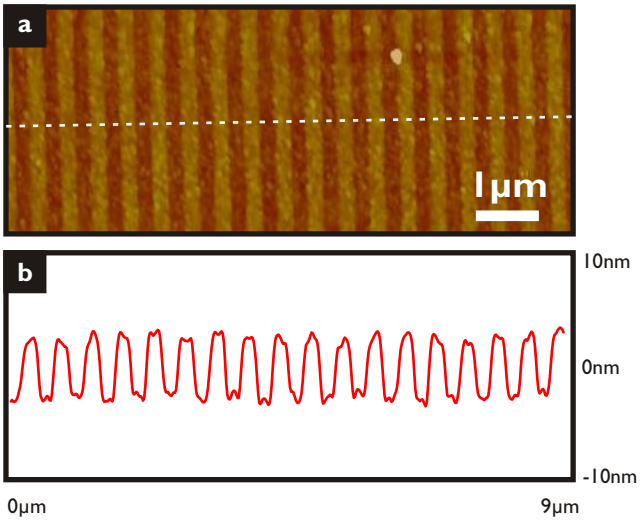

Fig. 5.10: An AFM scan of a PMMA surface for a 25-nm thick first spacer layer above a 500-nm pitch grating: (a) presents an image of the scan, while (b) shows an averaged trace as marked by the dotted line. The average is taken over 120 line scans.

5.3 THE SILVER LAYER

Deposition of the silver was achieved in a variety of ways, including DC magnetron sputtering, electron beam evaporation, and thermal evaporation. The quality of the silver layers deposited was of the utmost importance, as porous or uneven films would result in inconsistent PLL results.

5.3.1 Silver Direct Current Sputtering

The details for how DC sputtering is performed are set out in section 4.1.3. The process parameters for the optimised sputter are given in Table 5.5. This deposition delivered an average roughness of 1.3-nm rms. It was found that as power was increased above 200W the roughness of the silver also increased. The rms roughness achieved at 200W was considered acceptable. Any reduction in the power simply resulted in slower deposition rates.

Table 5.5: Process parameters for deposition of Ag by direct current magnetron sputtering.

Target	Power	Rate	Temperature	Process Pressure
Ag (99.9%)	200W DC	0.5 nm/s	$25°C < T < 40°C$	8.5×10^{-3} mBar

The plasma generated during the DC sputter resulted in a major issue when depositing the silver onto the first spacer layer. The problem was due to the slowness of the silver deposition and the proximity of the mask to the plasma. At the beginning of the sputter, when there is little or no silver on the mask, the mask spends time close

to the plasma. This results in partial, and in some cases complete removal of the first PMMA spacer layer. When this became a limiting problem, DC sputtering was no longer used.

5.3.2 Silver Electron Beam Evaporation

An attempt to deposit the silver layer with electron beam evaporation was made but with little success. Due to silver's low melting point it was difficult to control the rate and consistency of the silver evaporation. This resulted in large surface roughness values on the order of 10-nm rms. The size of the ejected silver clusters is too large for the thin layers trying to be deposited. The location of the electron beam evaporation source in relation to the target also meant that highly directional films were unavoidable.

5.3.3 Silver Thermal Evaporation

Thermal evaporation become the most commonly used means of silver deposition. This was the result of two factors: its ability to produce the smoothest films and most consistent films, and the advantages of simple combination with a silicon dioxide evaporation for the final spacer layer. One notable problem when dealing with silver is its tendency for sulphidisation. If silver was left uncovered for a number of days, areas of the silver layer would become tarnished. It was found the best way to deal with this was to put a layer of SiO_2 onto the silver immediately after the silver was deposited. The process parameters for thermal evaporation of silver are shown in Table 5.6.

Table 5.6: Process parameter table for thermal evaporation of silver.

Target	Power	Rate	Process Pressure
Ag (Ag pelets)	4 (on-dial)	2 nm/s	4e-6 Bar

The roughness of the silver film was dependent on the speed of the deposition, and in general faster rates gave smoother films. AFM measurements of the surface rms roughness were used to measure a processes ability to produce a smooth surface, with the selected conditions giving surface roughness values of less than 1.2 nm rms (approx 8 nm peak-peak). Figure 5.11 shows an AFM scan of a typical silver layer with roughness of 0.9-nm rms.

5.4 SECOND SPACER LAYER

The final spacer layer for the PLL mask was initially PMMA [23], but deposition of SiO_2 was found to give more consistent and robust results. A reason to not use PMMA was its tendency to disolve in solvents. It was suspected that PMMA was disolving

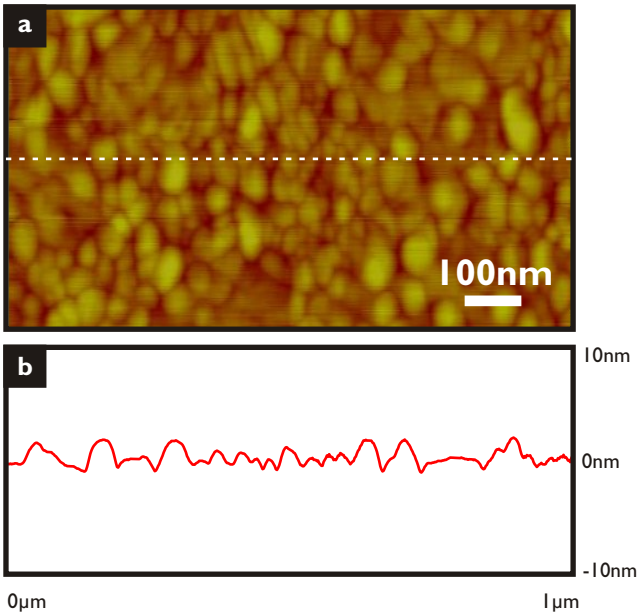

Fig. 5.11: An AFM scan of the surface of a 50-nm thick silver layer: (a) presents an image of the scan, while (b) shows a the trace taken though the image as marked by the dotted line.

after coming in contact with the resist. When PMMA was used it was spun on to the coverslip in the same manner as the first spacer layer. To produce thinner layers the acceleration and speed of the resist-spinner would be increased.

Three types of SiO_2 deposition were investigated: RF magnetron sputtering, thermal evaporation, and electron beam evaporation. The parameters used for each method are given in Table 5.7. Both RF sputtering and thermal evaporation were used in mask fabrication as surface roughness could be kept below 1 nm rms. Results from electron beam evaporation were again inconsistent, with the thermal and electric insulation properties of the $Si0_2$ limiting attempts to produce smooth melting of the charge.

Table 5.7: Process parameters for deposition of SiO_2 by radio frequency magnetron sputtering, thermal evaporation, and electron beam evaporation.

Deposition type	Target	Power	Rate	Temperature	Process Pressure
RF sputter	SiO_2 (99.995%)	150W RF	0.008 nm/s	$25°C < T < 40°C$	8.5×10^{-3} mBar
Thermal Evaporation	SiO powder	3.5(on dial)	0.5 nm/s	N.A.	4×10^{-3} mBar
EB Evaporation	SiO_2 (99.995%)	0.15mA	0.04 nm/s	$25°C < T < 40°C$	8.5×10^{-3} mBar

The final process used only thermal evaporation for the dielectric spacer layers as it consistently provided fast deposition of 10-nm thick layers with roughness of less than 0.5-nm rms. The SiO_2 is deposited without breaking vacuum after the silver evaporation to limit the contamination of the silver film through sulphidisation and particulate accumulation. Although the stoichiometry of the thermally evaporated

SiO_2 could not be relied upon (the source is SiO powder), the layers were investigated to insure optical transparency and low roughness.

Figure 5.12(a) shows an AFM surface scan of a 22-nm thick SiO_2 thermally evaporated onto PMMA. The line scan (Fig. 5.12(b)) gives the surface roughness of 0.5-nm rms, which is below the 1-nm rms target for this work.

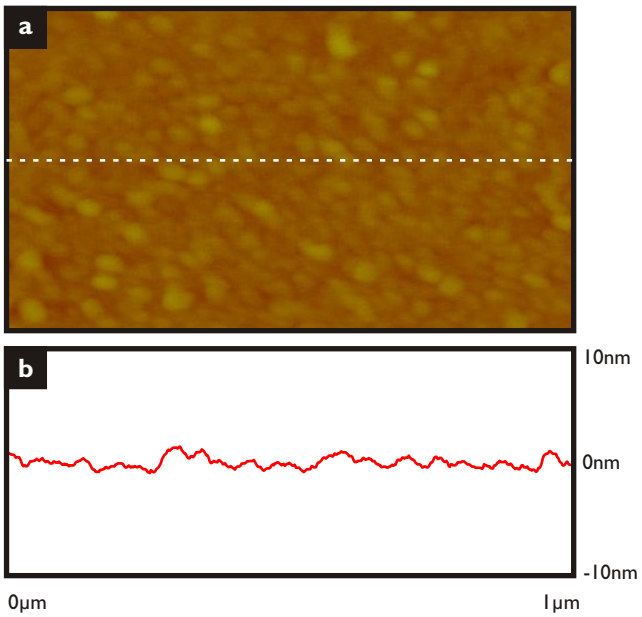

Fig. 5.12: An AFM scan of the surface of a 22-nm thick SiO_2 layer: (a) presents an image of the scan, while (b) shows a the trace taken though the image as marked by the dotted line.

5.5 THE FINAL MASK

An AFM image of the surface of this final spacer layer is shown in Fig. 5.13 for a mask with a 25-nm thick PMMA spacer, a 50-nm thick thermally evaporated silver lens and a 10-nm thick thermally evaporated SiO_2 spacer. The notation used in this thesis describes such a stack as a 25|50|10 - PMMA|Ag|SiO_2 stack. The image is taken on top of a region with a 350-nm period grating in the 30-nm thick tungsten layer, and none of this topography has been transferred through the subsequent layers. The surface roughness of this final mask is approximately 1.2-nm rms, which is similar to that of the roughest layer – the silver layer. This is common for a mask produced by the optimised mask fabrication process.

5.6 MULTIPLE AG AND SIO_2 LAYERS

An extension to the work was to investigate multiple silver-layer lensing stacks. For this a repeating deposition of silver and SiO_2 was required. This was simple to achieve

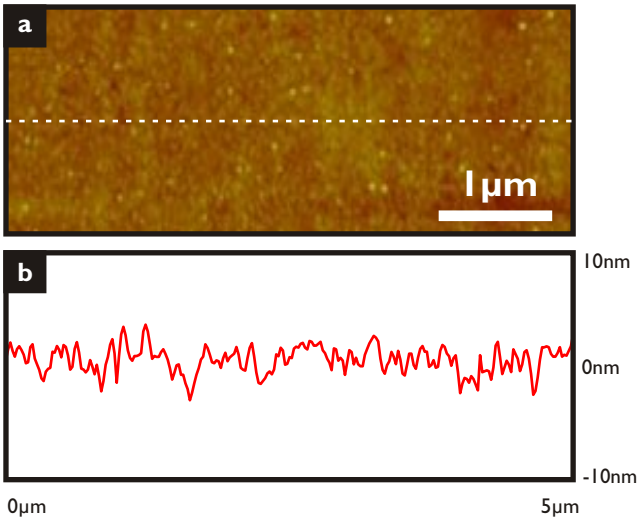

Fig. 5.13: (a) An AFM image and (b) a line trace taken on the surface of the SiO_2 layer of a 25|50|10 - PMMA|Ag|SiO_2 lens stack, directly above a 350-nm period grating in the underlying tungsten.

once thermal evaporation was established as the best deposition technique for both materials. Multiple evaporations would be performed under the a continuous vacuum to insure silver quality. Due to the increase in the number of interfaces greater surface roughness was found for multiple-layer masks. Final roughness measurements of the double-layered masks were around 2 nm rms, almost twice the roughness of previous masks. Figure 5.14 presents a scan of the multi-layered mask's surface above 350-nm period features. The trace provided in Fig. 5.14(b) shows that no 350-nm period features have been transferred through the deposited layers, but the surface has greater roughness when compared to previous single-lens masks. A comparison scan over 350-nm pitch features for a single-layer 25|50|10 - PMMA|Ag|SiO_2 mask stack is provided in Fig. 5.14(c) (a re-trace of Fig. 5.13(b)). The increase in surface roughness can be clearly seen.

5.7 MASK ADAPTION FOR OPTICAL LITHOGRAPHY SYSTEM

After the processing the mask is mounted onto a rigid glass plate to allow integration with the available Karl S*ü*ss MA6 optical lithography system. A 19-mm circular hole is drilled into the centre of the glass plate and the conformable mask is centred and glued over the hole so that the mask features have the correct orientation for exposure. A Dymax 621 UV-curing adhesive was used, which cures after five minutes under a small UV lamp. Figure 5.15 shows a finished mask that has been attached to a rigid mask plate.

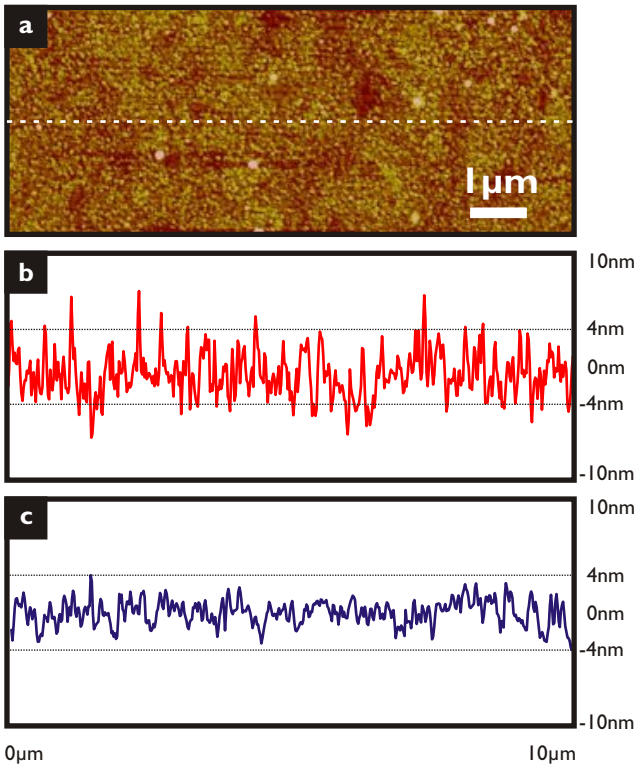

Fig. 5.14: AFM scan of 25|50|50|50|10 - PMMA|Ag|SiO_2|Ag|SiO_2 mask surface below 350-nm pitch mask features is shown in (a). A trace through the scan is given in (b). (c) shows a comparable trace below a single-layer 25|50|10 - PMMA|Ag|SiO_2 lensing stack.

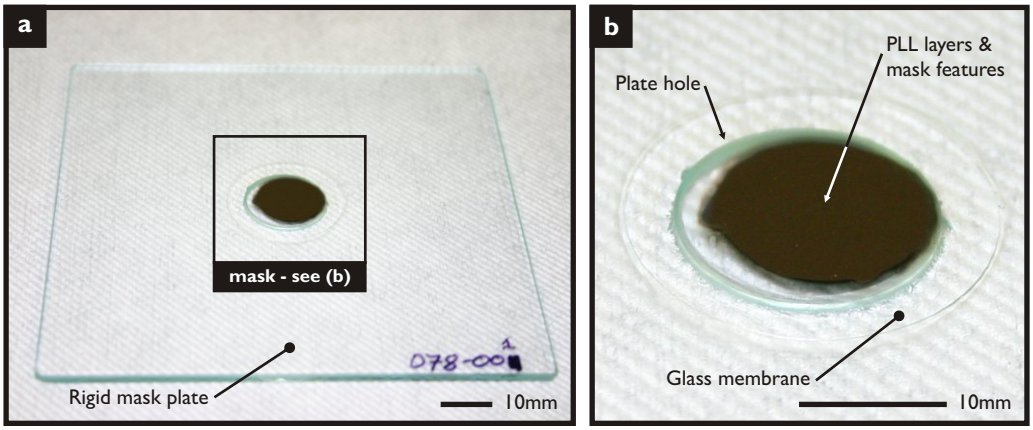

Fig. 5.15: A picture of a final mask that has been attached to a rigid mask plate. (a) shows the entire mask, while (b) is a zoomed image of the conformable mask membrane and plate hole.

5.8 MASK FABRICATION ISSUES

A total of 86 masks were EBL patterned on coverslips, with 25 getting past the first planarisation stage and a total of 18 were attached to a rigid mask plate and tested. There were a number of fabrication issues that caused this relatively modest rate of success.

Some of the limiting factors that result from the process steps covered above are: resolution restrictions for gratings using the EBL and RIE patterning process; sufficient planarisation of the first spacer layer; exact control of the first spacer layer's thickness; and roughness of the silver. These four limitations have restricted or limited experimental testing.

The tungsten mask patterning process has a resolution limit of between 100 and 120 nm for the pitch of periodic gratings. This means that resolution limits of the near-field lithography processes may not have been reached due to insufficient contrast from the mask. The mask limit is mainly due to proximity effects during the EBL patterning of the PMMA, and we are currently investigating ways to overcome this. Irregularities in the performance of the tungsten etch (as discussed in Section 5.1.6) also limited resolution.

When the first spacer layer is planarised, control over the final thickness is difficult. The oxygen RIE process used to etch back the PMMA layer is controllable to $\pm$ 3nm, which then puts limits on the stack's following layers, as the ratio of spacer to silver lens is predetermined [21]. This has meant that performing comparisons between single- and double-layered masks with exactly the same total thickness of silver has been difficult.

The silver evaporation process has been tuned to produce the smoothest layers possible, which is achieved through increased deposition rate. This works for film thicknesses greater than 35nm with great success, but below this the roughness of the silver increases. This roughness increase can be attributed to a lack of surface 'wetting', which results in beading due to surface tension. These effects are overcome for thicknesses above 35nm. Thinner layers of the SiO_2 spacer also suffer from pin-holes, which can cause shorts between conducting layers. This has limited us to the study of single- and double-layer lenses, whereas improved performance for larger numbers of layers has been proposed [26]. To allow faster deposition of silver to minimise these problems, a more robust planarisation layer may be required.

Once masks were fabricated and classified the experimental pattern transfer process could begin. At the start of the next chapter the experimental procedures for near-field lithography are summarised before the remainder of the chapter details the experimental results for ENFOL and single layer PLL.

Chapter 6

EXPERIMENTAL RESULTS

"The proof of the pudding is in the eating"

- Miguel de Cervantes, Don Quixote (1967)

Only through experiments can we verify our theoretical predictions and simulation conclusions. For any lithography process, this is the step that will give the true indication of its future potential. This chapter outlines the experimental efforts that have proved the ability of PLL to produce sub-diffraction limited results and confirm Pendry's superlensing theory for silver films [18].

A range of masks were created, including ENFOL masks, proximity masks, and PLL masks with silver lenses from 40 to 240 nm thick. Masks were constructed using the techniques presented in the previous Chapter. After mask fabrication it was important to characterise the lithographic parameters to arrive at protocols for the exposures. The following section presents these protocols and the key experimental results are presented thereafter.

6.1 LITHOGRAPHY PROTOCOLS

Lithography protocols were required for effective and systematic reproduction of the optical pattern transfer step. This involves protocols for substrate preparation, photoresist scheme implementation, and exposure procedures.

6.1.1 Substrates

Substrate preparation for near-field exposures required a number of distinct differences from standard lithography procedures. One of the main differences is the thickness of resist required on the substrate. In near-field exposures thin resists are used for a number of reasons. Firstly, the near-field components are only available in a useable sense for less than a wavelength, compared to a propagating system where penetration is over a distance of many wavelengths. Secondly, by having a thin photoresist layer

the opportunity for the light to diffract is limited. Finally, excessive reflections from the substrate are reduced.

Selecting a substrate type for the process was not particularly important as no pattern transfer step was attempted. Initially, *n*-type prime-grade 4-inch wafers were diced into approximately 25-mm squares. The 25-mm size simply needed to be larger than the 19-mm hole cut through the mounting glass. Much of the early work was performed with these square substrates. However, it was found that these substrates caused two issues which hindered the performance of the process: they lead to a configuration of the mask-aligner that had insufficient vacuum to pull the substrate and mask together, and that the dicing of the silicon created to a larger amount of silicon dust that limited contact. To overcome these issues round 25-mm diameter silicon wafers were used. These wafers allowed the favourable configuration in the mask-aligner and didn't require resizing, limiting dust creation.

6.1.2 Cleaning Protocols

Through all processing steps great care is taken to ensure the cleanliness of surfaces, as the largest problem faced by an intimate contact lithography is dirt and dust that introduces unwanted micron scale spacers, which is enough to yield a failed exposure. The biggest cause of dirt and dust was substrate preparation. Common procedures for cleaning silicon wafers include an RCA clean, H_2O_2-NH_4OH-H_2O for removing organic residue, and solvent cleaning with acetone, methanol, and IPA to remove remaining contaminates. RCA was rarely used as wafers had no detectable organic material coating. Initially, solvent cleaning was used in conjunction with an ultra-sonic bath to provide the basis for cleaning. This was found to not completely clean all spots of contamination from the substrates, thus cotton swabs were used to remove the final elements of unwanted dirt.

After an amount frustration it become clear that the ultra-sonic cleaning procedure was introducing as many contaminants as it was removing; it was causing the silicon substrates to vibrate against the glass beakers that house them resulting in a large amount of silicon dust to be generated. For this reason, a new protocol was implemented which limited the need for ultra-sonic cleaning. The final procedure ran as follows: first, the sample was ultra-sonically cleaned in acetone; next, the sample was sprayed with the three solvents in turn (acetone, methanol, IPA) and after each was rubbed with a cotton swab to remove any contaminants; then finally, the sample was closely observed and the swabbing process repeated if any contamination remained. This procedure tended to produce better results in a more timely manner.

6.1.3 Resist Schemes

A range of resist schemes were used to produce the near-field exposures. In previous near-field work [15, 16] resist stacks were used to allow the shallow near-field to be captured in thin resist while having subsequent layers to allow transfer of the shallow resist patterns into lower layers used for lift-off or etch transfer. However, for this thesis the aim was to look into the absolute limits of the resist pattern transfer step, thus there was no need for full-transfer stacks. However, there was still a need for resist schemes that limited reflections, as standing waves between the mask and substrate tend to cause a blurring of feature edges limiting resolution.

The first exposures employed a simple thin-resist layer approach. A Shipley S1805 resist solution was diluted 1:4 with propylene glycol monomethyl ether acetate (PGMEA) solvent and spun onto a silicon substrate to a thickness of 50 nm (spin-speed 4000 rpm, acceleration 2000 rpm/s). There was an issue with substrate attachment for such a thin layer, so a silicon substrate primer was used, namely hexamethyl-disilazane (HMDS). The primer promoted adhesion by providing a mono-layer of compounds with one end adhering to the silicon surface and the other to the organic resist compound.

To further reduce substrate reflections the standard industry approach of apply a Bottom Anti-Reflection Coating (BARC) was investigated. The BARC has a number of tasks: first, it must match the refractive index of the resist on top to limit reflections at that interface; next, it has to be extremely lossy to the exposing wavelengths so that the light is absorbed and limited amounts are reflected back from the substrate; and thirdly, it needs to have a characterised etch process so that it can be etched through for pattern transfer. For this process a Clariant BARLi-II-200 BARC was spun on to 200-nm thick (spin-speed 2000 rpm, acceleration 2000 rpm/s).

The performance of the lithography process was also hindered by the function of the Shipley resist. The resist was originally designed for g-line wavelength exposures, so high-resolution using i-line exposure was always going to be difficult. Aging processes also introduced congealed polymer, and hence an increased line edge roughness.

A high-resolution i-line resist was investigated to improve the performance of the system. Clariant HiR1075 resist was used for its claimed performance down to 100-nm features. The resist spun-on to around 200 nm, which was too thick for the near-field exposures, so it was diluted by a ratio of 1:4 with methyl amyl ketone. The diluted resist was spun-on at 4000 rpm (and an acceleration of 2000 rpm/s) to give a thickness of 100 nm.

6.1.4 Exposure Conditions

For exposures the S*ü*ss MA6 mask aligner was used. The 350W Mercury lamp's light was employed with and without a range of interference filters. The unfiltered intensity

of the lamp held at around 6.5 mW/cm^2 at the sample plane through the work and the spectrum of a typical MA6's lamp is shown in Fig. 6.1 [12]. The intensity of the exposing radiation and bandwidth parameters for the different interference filters used for narrowband exposures are given in Table 6.1.

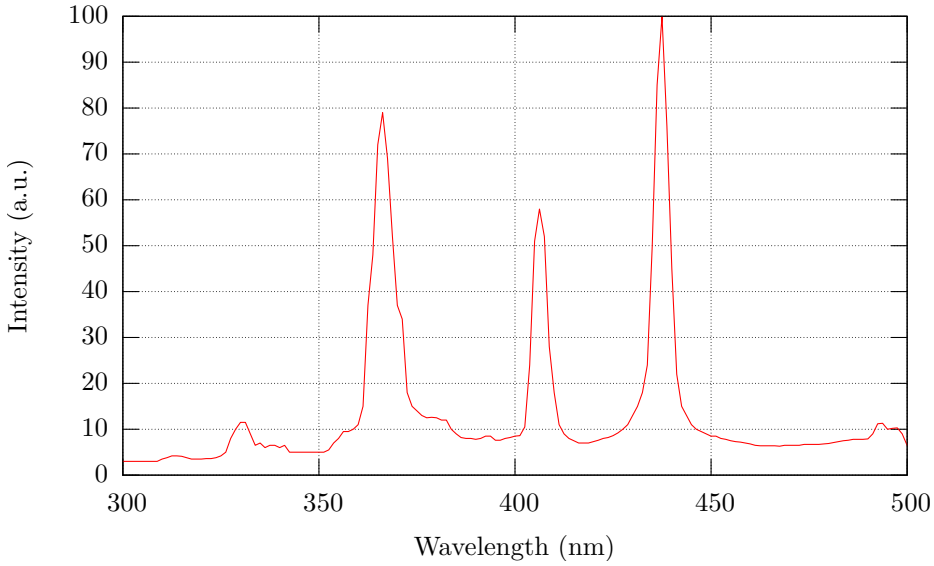

Fig. 6.1: Typical Süss MA6 mask aligner UV400 lamp spectrum [12].

Table 6.1: Optical interference filter parameters.

filter center wavelength	Center frequency attenuation	bandwidth	Relative lamp intensity	Measured lamp intensity without filter	Resulting intensity
365nm	5dB	9nm	78	6.5mW/cm^2	2mW/cm^2
341nm	4dB	7nm	6.5	-	0.22mW/cm^2

Generally, exposure times were calibrated by running a series of exposures and finding clearing doses for the features that were desired. Exposure times varied considerably as the silver layers were mismatched and lossy, reducing the transmitted intensity by over 80%. Times ranged from 4 s for ENFOL experiments, to 3 hrs for thick silver lenses with filtered lamp exposures.

The mask aligner is used in soft vacuum contact mode when the mask and substrate are brought into contact with each other. Intimate contact was the main goal and it was troublesome to achieve. Initially, to find out whether there had been good contact, a first effort would be to check exposed and developed resist patterns under a microscope, and if features could be seen down to sub-1-μm pitch then the sample would be checked by the AFM. This process proved to be slow and didn't provide fast enough feedback on whether there was contamination on the mask, which was hindering contact. A new technique was employed to speed up this process. It simply involved over-exposing the

sample to produce 'Newton's rings'[1], which demonstrated the contact performance of the exposure immediately after development. The features that remained in the centre ring had the best contact and were investigated first. This resulted in longer exposure times, but this was favourable as near-field exposures were often required higher dose.

6.1.5 Development

Development was performed with AZ300-MIF developer (2.18% tetra-methyl ammonium hydroxide (TMAH)). The developer was used at either full strength concentration, or diluted 2:1 with de-ionised water. Development times were often short, ranging from 3 s to 10 s. Samples would be rinsed thoroughly in deionised water.

6.2 PERFORMANCE CRITERIA

Before determining the resolution limit of the system a 'goal post' had to be set to provide clarity on the limit set by diffraction. There are a number of ways to measure the resolution limit of an optical system, a few of which were presented in section 2.2.

Here, the technique for determining the resolution limit was with the use of a semi-infinite grating. There are two main reasons for this: firstly, the diffraction limit for an optical system is well defined for an infinite grating; and secondly, simulating an infinite grating was simple, making comparison between simulation and experimental results straight forward.

For the PLL cases presented here the diffraction limit can be given by Equ. 2.9 as 243 nm. This is calculated with the immersion nature of the system taken into account. As ENFOL is not an optical system as such, but rather a capturing of the exact source profile at the source, a diffraction limit is not defined. ENFOL's resolution is technically unlimited, and only restricted by the lithography process.

The following sections detail the experimental results achieved with ENFOL and PLL. All details about the mask making for these sections can be found in Chapter 5.

6.3 EVANESCENT NEAR-FIELD OPTICAL LITHOGRAPHY

In order to understand the resolution limits of our setup and to optimise exposure conditions ENFOL experiments were carried out. It was important to show that the newly-developed near-field lithography process could achieve sub-diffraction-limited imaging. Limitations to achieving this included, mask fabrication, resist resolution, and imaging restrictions.

[1] Newton's rings apear when interference of coherent incident and reflected waves produces high and low field intensities that vary based on the travelling distance of the reflected wave.

Figure 6.2 shows a range of larger features patterned with ENFOL. Periods down to the diffraction limit were straight forward to image, and produced good height contrast in the resist.

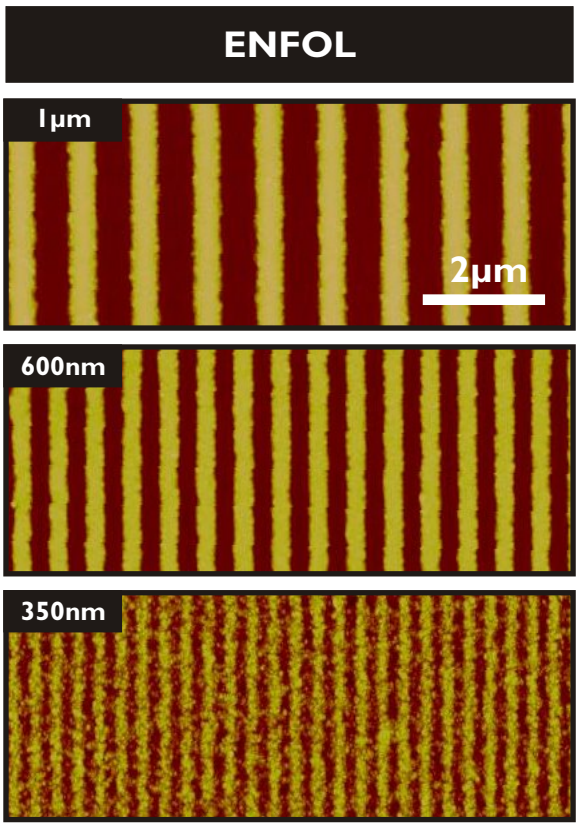

Fig. 6.2: AFM scans of gratings after exposure and development for ENFOL, under grating periods of 1 μm, 600 nm, and 350 nm. The 1 μm features have a height scale of 100 nm, while the remain two use a 50 nm height scale.

Figure 6.3 shows sub-wavelength features, including features which would be considered sub-diffraction-limited in a lensing system. The features are distinguishable, however, the image fidelity has been reduced. In the early stages of this work, the simple presence of features was significant. It was important to sense sub-diffraction-limited resolution so that the process could be optimised, even if the contrast in the resist was so low that no subsequent pattern transfer step could plausibly be completed. To sense the presence of features through surface roughness, background exposure, and resist granularity, the 2D discrete-Fourier-transform (DFT) was used to find periodic spatial structure captured in the resist. The 170-nm pitch features in Fig. 6.3 are somewhat difficult to visualise but, with the help of the DFT shown in Fig. 6.4, the peak at the wavenumber 5.88 μm^{-1} indicates the presence of a 170-nm period structure. At this point it could be concluded that the system had the ability to pattern sub-diffraction-limited images.

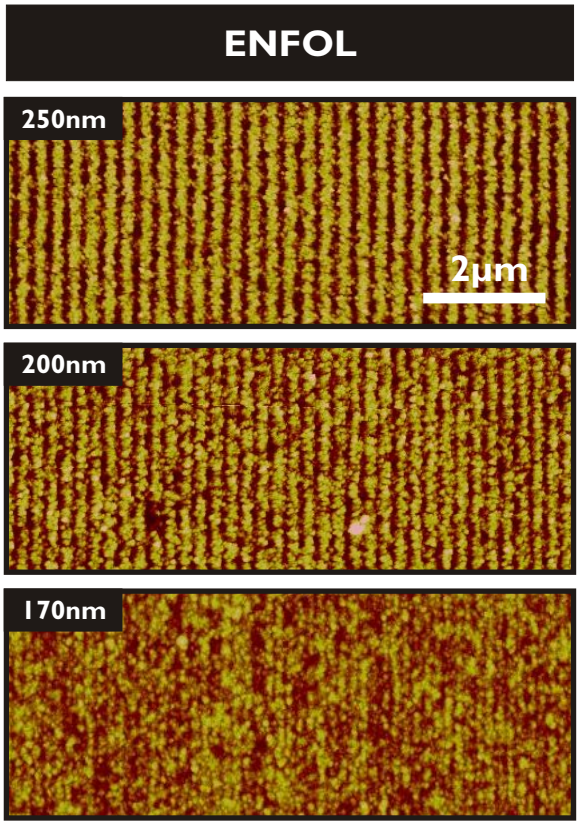

Fig. 6.3: AFM scans of gratings after exposure and development for ENFOL, under grating periods of 250 nm, 200 nm, and 170 nm. The 200-nm and 170-nm pitch features are considered sub-diffraction-limited. All scans use a height scale of 50 nm.

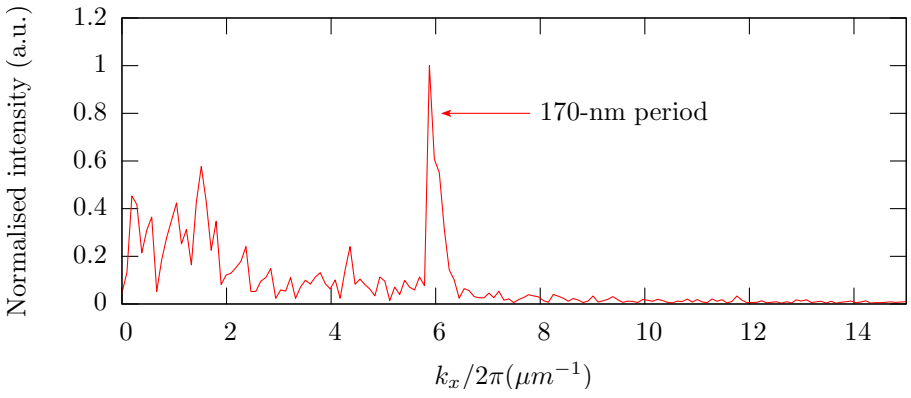

Fig. 6.4: Normalised DFT calculated from an AFM scan of an ENFOL exposure below a 170-nm pitch grating.

The focus of work now turned to PLL experiments. The following sections detail the performance of the newly developed planar lensing lithography process.

6.4 SINGLE-LAYER PLANAR LENSING LITHOGRAPHY

The thesis of this work is that a planar slab of silver can act as a near-field lens and provide lithographic exposures with resolution beyond current lithography systems. In this section, experimental results confirming this thesis are presented. The experimental setup for single-layer PLL was presented in Fig. 2.22.

The first PLL experimental work was with a 120-nm thick silver lens [23]. To build up the lensing stack profile of 60|120|60 - PMMA|Ag|PMMA, 60 nm of PMMA was first spun onto the metalised mask, before Ag thermal deposition, and subsequent spinning on of the final 60-nm thick PMMA layer. A planarisation of 15 nm peak-to-peak was achieved for the first spacer layer. The spinning on of the first spacer layer required that the layer be a thickness of 60nm or more to achieve an acceptable planarisation .

A range of exposures were performed to characterize the silver layer's ability to image the mask. Experiments compared the performance of a 60|120|60 - PMMA|Ag|PMMA stack with a 120-nm proximity stack. Both experiments were performed on the same mask, where the proximity mask was produced by shielding a section of features from the Ag deposition. This meant that the 120-nm proximity gap was enforced with two 60 nm spun-on PMMA layers. Exposures were performed with a broadband Mercury lamp light source into a 50-nm thick layer of Shipley S1805 resist, dilluted 1:4 with PGMEA, spun onto a diced 25-mm square silicon substrate. The conditions for the experiments are presented in Table 6.2.

Table 6.2: Conditions for 120nm Ag lens and 120nm proximity experiments. (DC = Duty Cycle)

Figure	Stack	Feature	Source	Exposure Time	Developer	Develop Time
6.5(a)	$\frac{60\|60}{PMMA\|PMMA}$	1μm 50% DC Boxes	Broadband	120s	AZ300	8s
6.5(b)	$\frac{60\|120\|60}{PMMA\|Ag\|PMMA}$	1μm 50% DC Boxes	Broadband	120s	AZ300	8s
6.5(c)	$\frac{60\|120\|60}{PMMA\|Ag\|PMMA}$	700nm 50% DC Boxes	Broadband	120s	AZ300	8s
6.6	$\frac{60\|60}{PMMA\|PMMA}$	1μm 50% DC Boxes	Broadband	4s	AZ300	3s

Figure 6.5 shows comparative results for exposures with and without the silver lensing layer. All images are AFM scans from a single sample that was exposed under broadband illumination for 120 s and developed for 8 s, with the exposure time being determined as the clearing dose for larger ($\geq$2 μm) features under the silver. Figure 6.5(a) shows an AFM scan of a 1 μm period grating pattern exposed through a 120-nm thick PMMA spacer (i.e. no silver lens). A combination of diffraction around the mask and over-exposure has caused features that are on the order of a wavelength in size to be washed out at a depth that is well within a wavelength.

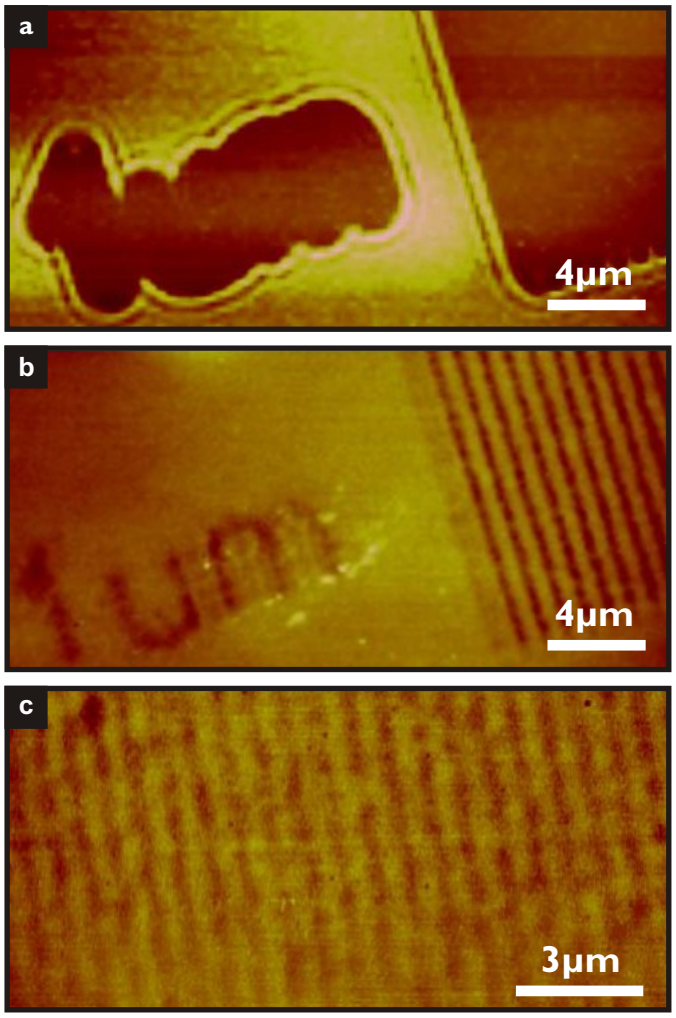

Fig. 6.5: AFM scans of gratings after exposure and development: (a) A proximity exposure of a 1 μm grating and; (b) a silver lens exposure of a 1 μm grating; (c) the smallest features resolved during the 60|120|60 - PMMA|Ag|PMMA silver lens exposures, a 700 nm period grating with 350 nm lines and spaces. (a) has a height scale of 30 nm, while (b) and (c) use a 20 nm height scale.

Figure 6.5(b) presents the comparative exposure through the 120 nm-thick silver layer (sandwiched between its PMMA spacers). Here the diffraction around the mask has been compensated for by the imaging properties of the silver and the 1-μm period grating is now resolved. This was the first experimental demonstration of optical imaging through a planar silver lensing layer [23].

The image of Fig. 6.5(a) was previously used as a control, however, it has been noted that the resist is over-exposed or over-developed [150] rendering the exposure an invalid control. The parameter space was search to find a better performing proximity result with exposure times down to 4 s used with a range of development times and at no point were clear features found under the 1-μm pitch mask features. Figure 6.6 shows a result of a 4 s exposure, developed for 3 s, which produced a very shallow resist profile of 500-nm pitch features. This is a period halving effect, which is a result of standing

waves being created by diffraction that has produced unwanted images in the resist. This exposure removes the confounding factors of over-exposure and over-development, and demonstrates that diffraction is limiting performance of the proximity exposure. The claims in Ref. [150] were rebutted in Ref. [151].

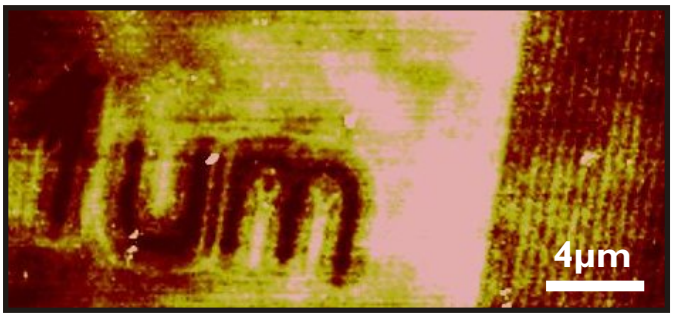

Fig. 6.6: An AFM scan of a 1 μm grating exposed below a 120-nm thick PMMA proximity stack after exposure and development. Scan has a 10 nm height scale.

Imaging was observed on gratings down to a pitch of 700 nm (350 nm lines and spaces), which is on the order of the exposure wavelength (as shown in Fig. 6.5(c)). This was the imaging limit of the 60|120|60 - PMMA|Ag|PMMA mask. Although sub-micron imaging was demonstrated, no sub-wavelength imaging was evidenced due to the thickness chosen for the lens and spacer layers.

These initial results demonstrated two interesting features of the process. First that gratings can be imaged to the order of the wavelength, and secondly that isolated features can be imaged (as indicated by the text features).

FDTD simulations were performed to investigate the performance of these two systems. Figure 6.7 shows a comparison of 2D simulations between the 60|120|60 - PMMA|Ag|PMMA stack and 120-nm proximity exposure. The 2D data plotted is only for the 365-nm wavelength exposure. An immediate difference between the two images is apparent as the intensity of the electric field in the resist for the PLL exposure is more than two orders of magnitude higher that the proximity simulation. This confirms that using the same exposure times for the PLL and proximity masks will result in an over-exposure for the proximity case, especially when the exposure time is designed to provide a clearing dose for the PLL mask.

These two images do not facilitate a clear visual comparison thus line traces through 2D simulations are provided. These simulations also perform averaging across a number of wavelengths to give an impression of a broadband exposure. Figure 6.8(a) shows line traces along the x-direction from 1 μm period grating simulations at a depth of 30 nm into the 50-nm thick resist. This time appropriately weighted traces are taken from a number of simulations run at the required wavelengths (see Section 3.2.2) to produce a broadband simulation replicating an unfiltered Mercury lamp. The PLL simulation for

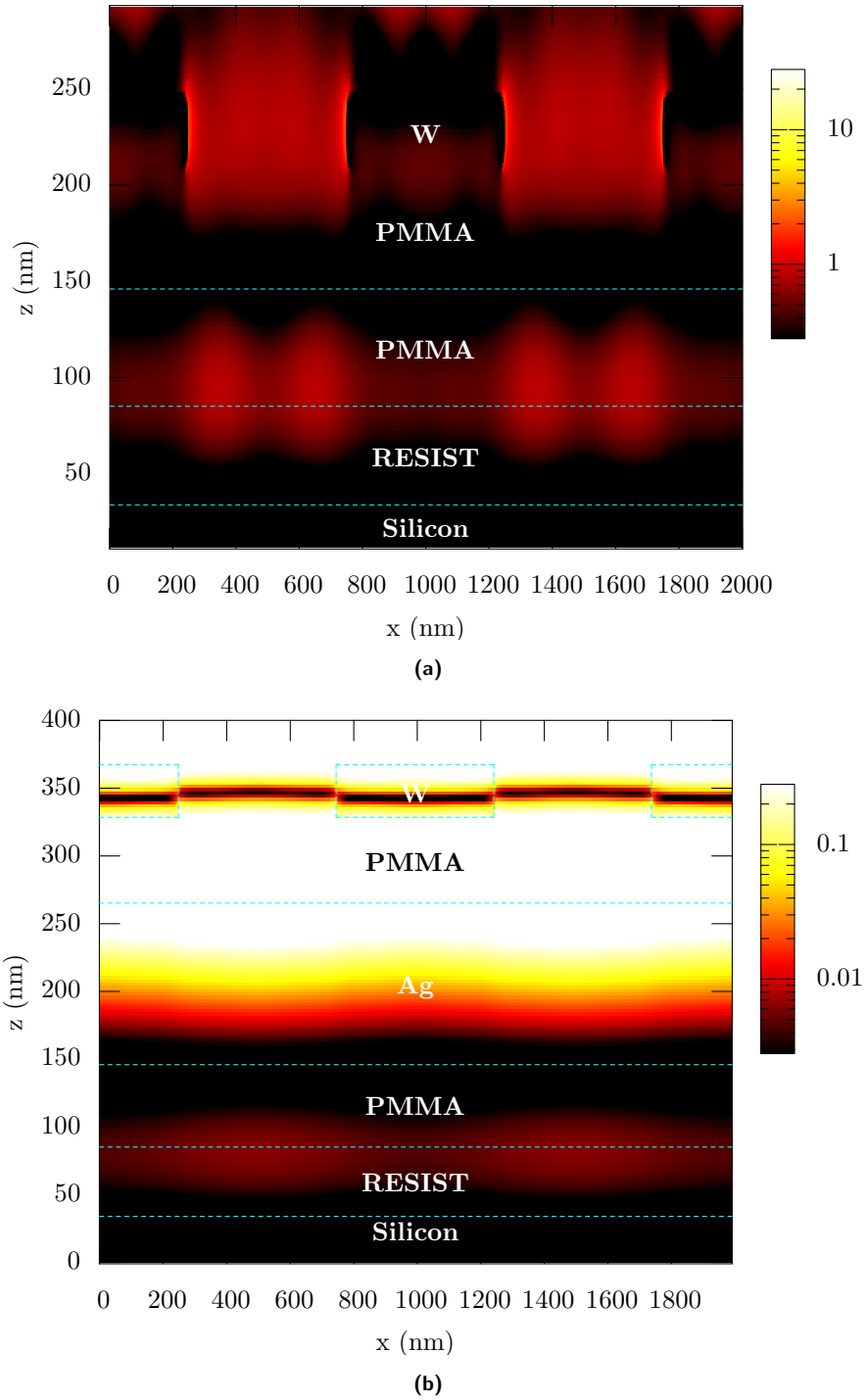

Fig. 6.7: Simulated cross-sections of the electric field intensities for (a) a proximity exposure and (b) a silver lens exposure. Below the tungsten, the proximity exposure has a 120 nm spacer, and the silver lens exposure has two 60 nm spacers and a 120 nm silver layer. A 50 nm resist and substrate are placed below the bottom spacers. The intensity is normalized to the incident intensity and the grating is at a 1 μm period with a 50% duty-cycle. Both simulations were run for an illumination wavelength of 365 nm and transverse magnetic (TM) polarisation. Please note the two-orders of magnitude difference in the intensities of the two graphs.

a 60|120|60 - PMMA|Ag|PMMA stack (dashed line) demonstrates the ability of the silver layer to transfer the mask detail into a high-contrast image in the resist. However, the proximity exposure (solid line) with a 60|60 - PMMA|PMMA|stack has poor image fidelity and contrast, which correlates well with experimental observation. Figure 6.8(b) shows the line traces at the spacer/resist interface. The proximity exposure trace (solid line) is an indication of the exposure conditions during the short exposure/develop times used to produce the result in Fig. 6.6. The presence of features at fractions of the desired pitch is consistent with experimental data.

The diffraction limit for this PLL system is given by Equ. 2.9 as 243 nm, being the minimum period resolvable by a projection lithographic system. The 700 nm minimum period size recorded by the first experiments showed that work needed to be done to improve the resolution of the process. The losses in the silver, which result in longer exposure times, needed to be reduced to increase the transmittance of the higher wavenumbers through the system, and hence increasing the resolution. The only means by which to do this was to reduce the thickness of the silver. The following two sections detail masks with silver thicknesses of 85 and 60 nm.

6.4.1 85nm Single-layered Lens

By employing the advanced PMMA etch-back planarisation process (see Section 5.2.1) to create the first spacer layer, the tungsten mask feature modulation was able to be reduced to less than 5 nm peak-to-peak and the spacer height made controllable. This allowed thinner spacer layers to be fabricated and, driven by the Veselago ratio, thinner planar silver layers were required thus reducing losses.

An 85nm silver layer was RF sputtered onto a 40nm PMMA spacer layer, before the final SiO_2 layer was RF sputtered to create a 40|85|26 - PMMA|Ag|SiO_2 mask stack. The resist stack was modified from previous experiments by the introduction of a BARC and a new high-resolution i-line photoresist. The BARC (Clariant BARLi-II-200) was spun on to a thickness of approximately 200 nm, and the photoresist (Clariant HiR1075 diluted 1:4 with methyl amyl ketone) was spun on at 4000 rpm for 60 s, giving a thickness of 120 nm.

Figure 6.9 shows that grating periods under the 40|85|26 - PMMA|Ag|SiO_2 stack have been resolved down to a 350 nm pitch. The sample presented here was exposed under broadband illumination for 110 s and developed in AZ300MIF developer for 3 s. Unfortunately, the expected large drop in exposure time was not observed because of the new resist stack. The improvement from the previous 120 nm silver lens is clear and through this mask sub-wavelength features have been imaged.

The results from this mask illustrate an issue that regularly appeared during exposures for certain masks - the issue of ‘hot spots‘. Hot spots can be seen through all the images presented in Fig. 6.9 as round, dark areas that break up the grating images

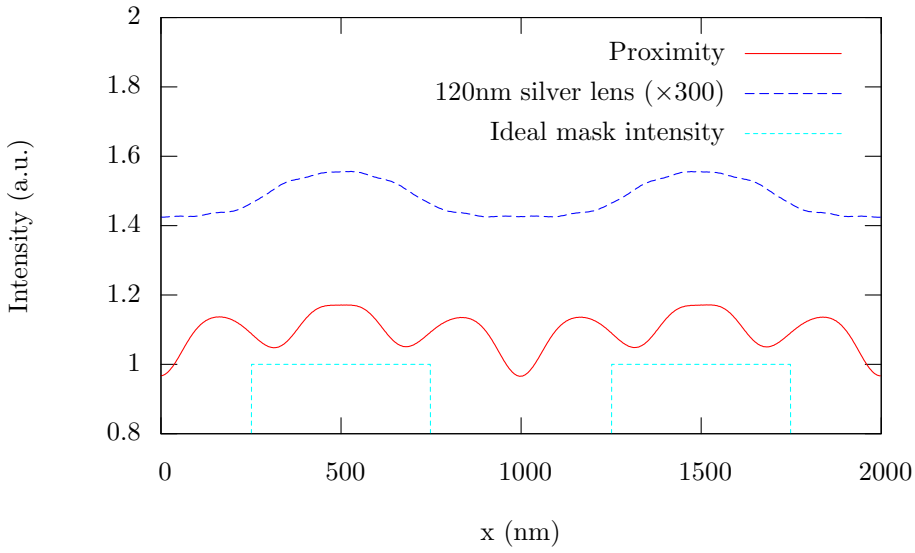

(a)

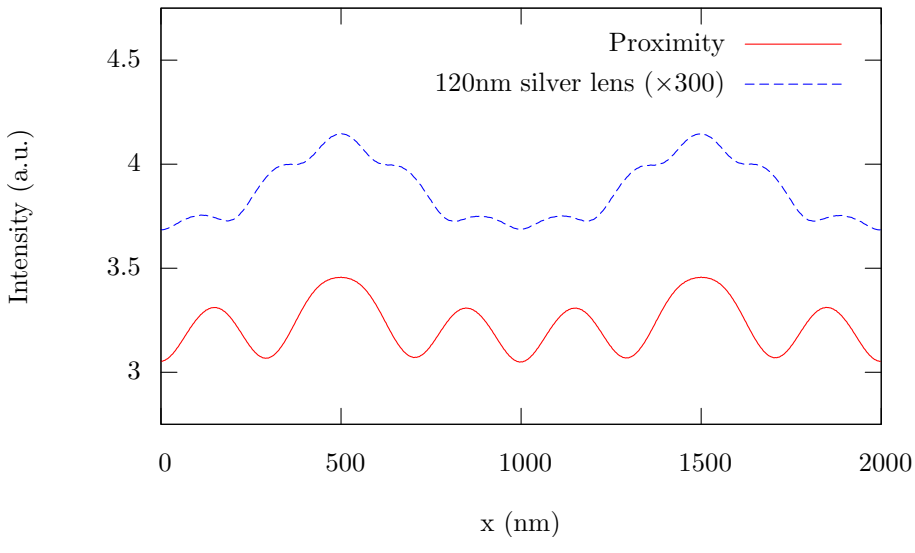

(b)

Fig. 6.8: Simulated broadband intensity line traces for (a) a depth of 30 nm into the 50 nm thick resist and (b) at the spacer/resist interface for a 1 μm period grating. The PLL simulation (long-dashed line) uses a 60|120|60 - PMMA|Ag|PMMA mask stack and has had its intensity increased by 150 times in (a) and 150 times in (b) compared to the proximity simulation (solid line), which uses a 60|60 - PMMA|PMMA mask stack, to enhance the visual comparison. In (a) an ideal mask intensity is provided (short-dashed line) to denote where the areas of high and low intensity should be located.

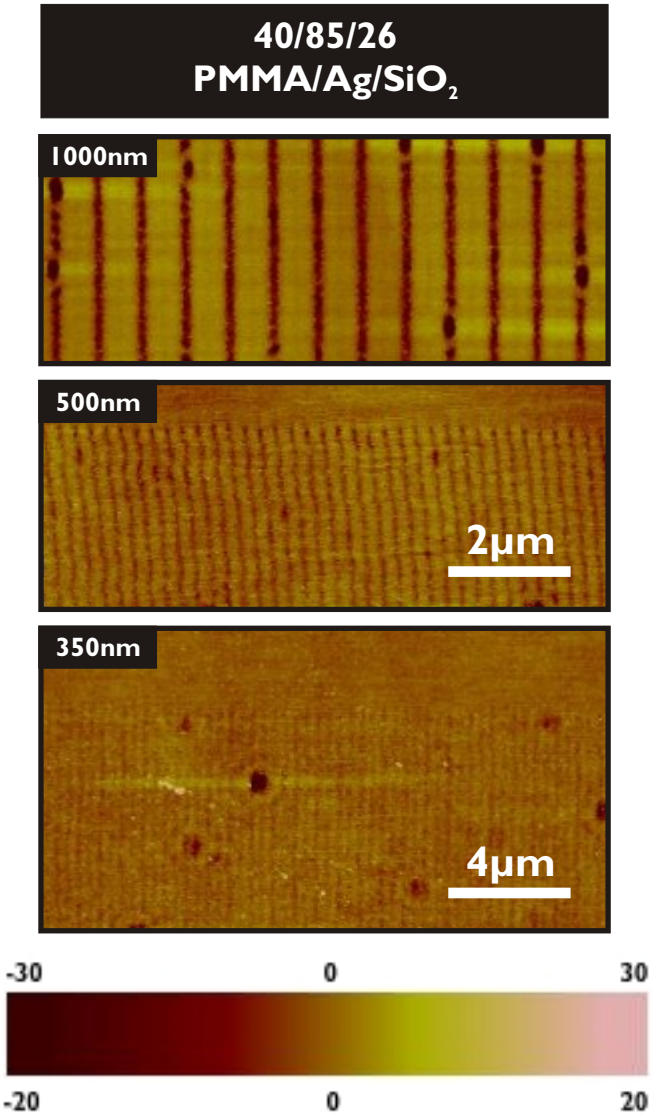

Fig. 6.9: AFM scans of gratings below 40|85|26 - PMMA|Ag|SiO_2 stack after exposure and development for (a) a 1 μm, (b) a 500 nm, and (c) a 350nm grating pitch. (a) has a 30 nm height scale, while (b) and (c) use a 20 nm height scale.

(for example, the dark spot in the center of the 350-nm image). It is believed that defects have been transferred from the mask or first spacer layer into the silver leading to peaks on the surface of the silver. These peaks disrupt the surface plasmons on the silver and then provide a localised enhancement of the field. This field enhancement then causes local over-exposure. Ringing can be seen around the hot spot exposures which suggests the defects have become a point source for surface plasmons.

An interesting observation made during exposures was the appearance of fringing effects around exposed grating patterns. Figure 6.10 presents an example of the fringing effects for a 500 nm pitch grating exposure through a 40|85|26 - PMMA|Ag|SiO_2 mask stack. On the left side of the dashed line in Fig. 6.10 the exposed features lie beneath the mask's features, but to the right of the dashed line extra features have been exposed that do not lie underneath a mask feature. These fringe features are exposed from standing plasmonic waves on the surface of the silver, which are driven by the exposure through the grating. These effects were seen at a range of pitches and for each instance the spatial periods of the standing waves is dependent on the pitch of the gratings and not the exposing wavelength. Although these fringing effects were not common, they do occur at certain pitches for broadband exposures. These fringing effects could be a result of off-resonant frequencies generating travelling surface waves that propagate at different spatial periods and then result in standing waves due to the inteference between the differently moded surface plasmons on the top and bottom of the silver. This interference phenomina has been reported previously [141], and elsewhere gratings have been used to couple into travelling SP waves [197].

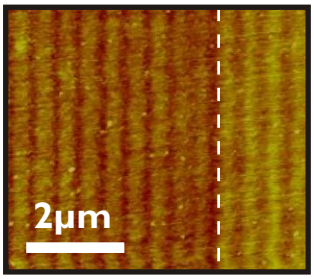

Fig. 6.10: AFM scan of developed resist patterns of 500 nm pitch gratings exposed beneath a 40|85|26 - PMMA|Ag|SiO_2 PLL stack. The features to the left of the dashed line are beneath mask features, but the features to the right of the dashed line are not and are being exposed by fringing effects. Height scale is 10 nm.

6.4.1.1 Simulations: Comparisions of 85-nm and 120-nm Thick Lenses

Simulations were run to investigate the performance improvement between the 120 nm and 85 nm lenses. Here, broadband simulations for 350 nm, 500 nm, and 1000 nm period grating are compared. Figure 6.11 shows results for the three different periods

at a depth of 30 nm into the resist. The results show that we should expect two changes in performance. The first being the improved resolution limit, as the simulations show features can be imaged down to at least 350 nm for the 85-nm lens case in contrast to the 120 nm case where the image is very weak and has become inverted. The second is the increase is intensity by an order of magnitude, which would indicate a reduction in required exposure time for the 85-nm thick lens. Unfortunately, this former point could not be experimentally seen as the substrate stack was modified between the two experiments

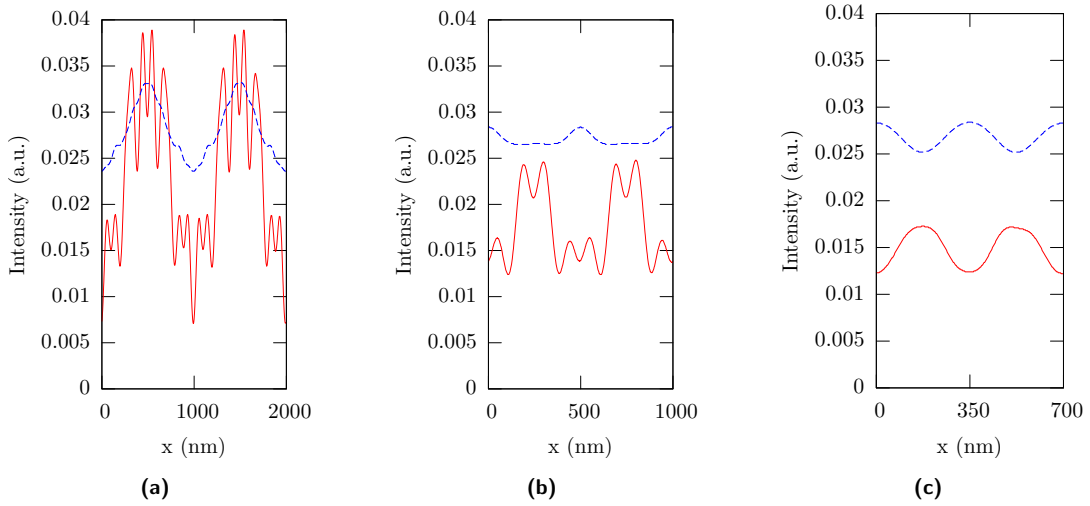

Fig. 6.11: Simulated intensity line traces comparing 120-nm (dashed lines) and 85-nm (solid lines) thick lenses for grating periods of (a) 1000nm, (b) 500nm, and (c) 350nm. The 120-nm traces have had their intensity increased by 10 times to enhance the visual comparison.

6.4.1.2 Reducing Final Spacer Layer

For the 40|85|26 - PMMA|Ag|SiO_2 stack the final spacer thickness was reduced from the standard Veselago ratio of 1:2:1. This reduction was motivated by simulation results that showed the best contrast was located nearer the lens for the superlens case. In Ref. [22] results from full-vector simulation of a PLL environment demonstrated that better resolution was achieved as the imaging layer is moved closer to the bottom of the superlens. More recently, a paper investigated the optimisation of the location of the imaging layer to gain best resolution [198], and concluded that it should be placed directly after the superlens. However, this experimental set up is not beneficial to PLL because the silver layer requires the protection provided by the final spacer layer, which stops sulphidisation and oxidation. Better resolution has been achieved through a silver layer by placing the imaging layer on the silver [31], but this process is not lithographic. Additional to the resolution enhancement, reduction of the final spacer layer also provides deeper penetration of the image into the resist.

6.4.2 60nm Single-layered Lens

The next mask tested was constructed with a 30|60|30 - PMMA|Ag|SiO_2 stack. Again the Ag and SiO_2 were RF sputtered and in this case the Veselago ratio is maintained. Figure 6.12 shows features imaged with the mask using broadband illumination, and an above diffraction-limit minimum feature size was again the best achieved. However, the features are a definite improvement of the 85-nm thick lens results presented in Fig. 6.9. The 'hot spots' found in the previous images have also been removed by improving the process control of the first spacer and the silver layers.

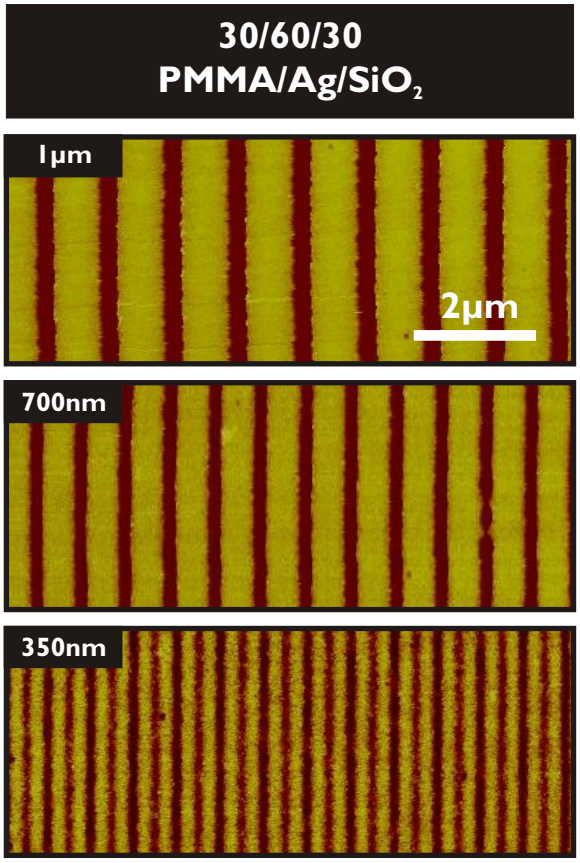

Fig. 6.12: AFM scans of features imaged through a 30|60|30 - PMMA|Ag|SiO_2 stack. Periods from 1μm to 350nm are shown. No dense grating features with periods below 350nm were found. All height scales are 50nm.

These results are another example of sub-wavelength imaging and together with the previous results this shows that imaging through PLL masks occurs for a range of silver thicknesses, with a resolution dependent on the silver thickness. The results cannot therefore be attributed to the well-known Talbot effect [199], which only predicts self-replication (imaging) of periodic structures at a single object-image separation - the so-called Talbot distance.

6.4.3 Thicker Lenses

Silver layers up to 240nm thick were investigated using PLL. For the thicker lenses transmission and resolution became very poor, with exposure times in the order of hours and all imaging being diffraction-limited.

6.5 BEYOND THE DIFFRACTION-LIMIT

The diffraction-limit for the PLL experiments using the i-line was set at 243nm (as calculated by Equ. 2.9), and resolving features at a period less than this was the goal. Super-resolution imaging was achieved by a 50-nm thick silver layer under broadband illumination. The lens was part of a 25|50|10 - PMMA|Ag|SiO_2 mask stack.

An example imaging result is shown in Fig. 6.13, for a 1-μm period grating exposed for 120 s through the 25|50|10 - PMMA|Ag|SiO_2 mask and developed for 3 s. The image fidelity is much improved over earlier results, and the line scan shows that the image is fully developed into the 120-nm thick resist. Imaging of sub-micron features has therefore been greatly improved by using thinner silver and spacer layers, and by reducing the surface roughness of the lens stack.

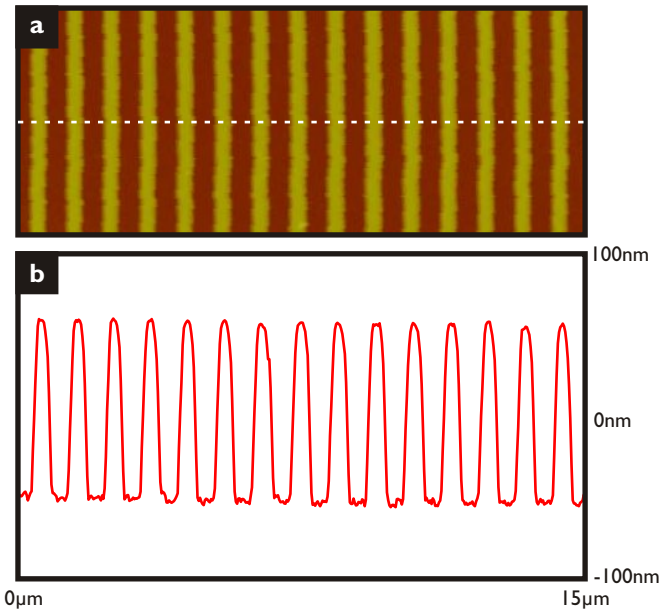

Fig. 6.13: AFM image and line scan of a 1-μm period grating exposed through the 25|50|10 - PMMA|Ag|SiO_2 lens stack. The height scale on the AFM image is 130 nm.

Figure 6.14 shows a series of grating images, exposed through the 25|50|10 - PMMA|Ag|SiO_2 lens stack under the same conditions as for the 1-μm period grating shown in Fig. 6.13. Gratings with periods from 500 nm down to 170 nm are resolved, with the depth of the modulation in the resist reducing as the grating period reduces. All of the gratings with periods above the diffraction limit (243 nm) are well resolved.

Even though this resolution is not sub-diffraction-limited, the silver lens is still having a beneficial effect in reconstructing the image, as such high resolution is not expected in proximity exposures through dielectric spacers of the same thickness as this lens stack [153]. Key results of this thesis are the 200 nm and 170 nm scans shown in Fig. 6.14 – images of sub-diffraction- limited pitch gratings. The contrast has degraded in these images compared to the gratings with periods greater than 250 nm, but the fact that they were present at all gives experimental confirmation of Pendry's controversial superlensing proposal [18].

Gratings with periods down to 145 nm have also been resolved in this exposure, as shown in Fig. 6.15. In this case the grating is weaker than the background roughness of the developed photoresist, so a DFT calculated on an averaged line scan of the image is required to confirm that the grating has been resolved; this is shown in Fig. 6.15(b) for the direction parallel to the grating vector k_x. Similar analyses of the images of 120-nm period gratings do not reveal any features in the spatial Fourier transform at 120-nm period, so the resolution of this lens for the exposure and development conditions used lies between 120- and 145-nm period.

6.5.1 Narrowband Exposures

The presence of a large amount of background exposing wavelengths is apparent in the spectrum of a broadband exposure presented Fig. 6.15(b). It was concluded that off-resonance wavelengths in the Mercury lamp spectrum (e.g. 405 nm and 436 nm) were causing unconfined surface plasmons to propagate and wash out the desired features. To overcome this problem an optical filter was used to select the desired 365 nm exposing wavelength. This step led to higher quality images. A disproportional increase in exposure times, when compared with the centre frequency attenuation of the filter, demonstrated that unwanted wavelengths were having a significant effect on exposures.

Figure 6.16 shows the same features presented in Fig 6.14 exposed with the same mask except this time a 365 nm filter was used to produce a narrowband exposure. The sample was exposed for 720 s and developed for 3 s in full strength AZ300-MIF. Similar quality imaging is produced for gratings with pitches above the diffraction-limit (500 nm through 290 mn). The important features to note here is the increased image fidelity for the 200 nm and 170 nm periods, both of which are sub-diffraction-limited.

An interesting factor to note is the reduced contrast in the 200 nm image when compared with the 170 nm image. Figure 6.17 presents traces of AFM images that have been averaged over 10 μm. It is apparrent that the contrast in the 170-nm trace (dashed line) is of a higher contrast to the 200-nm trace. This is evidence of effects that are commonly seen in near-field work, where non-linearities in contrast are present due to resonances and standing waves. These resonances can be attributed to the mask-stack heights, resist stack heights, grating periods, and wavelengths of light present. These

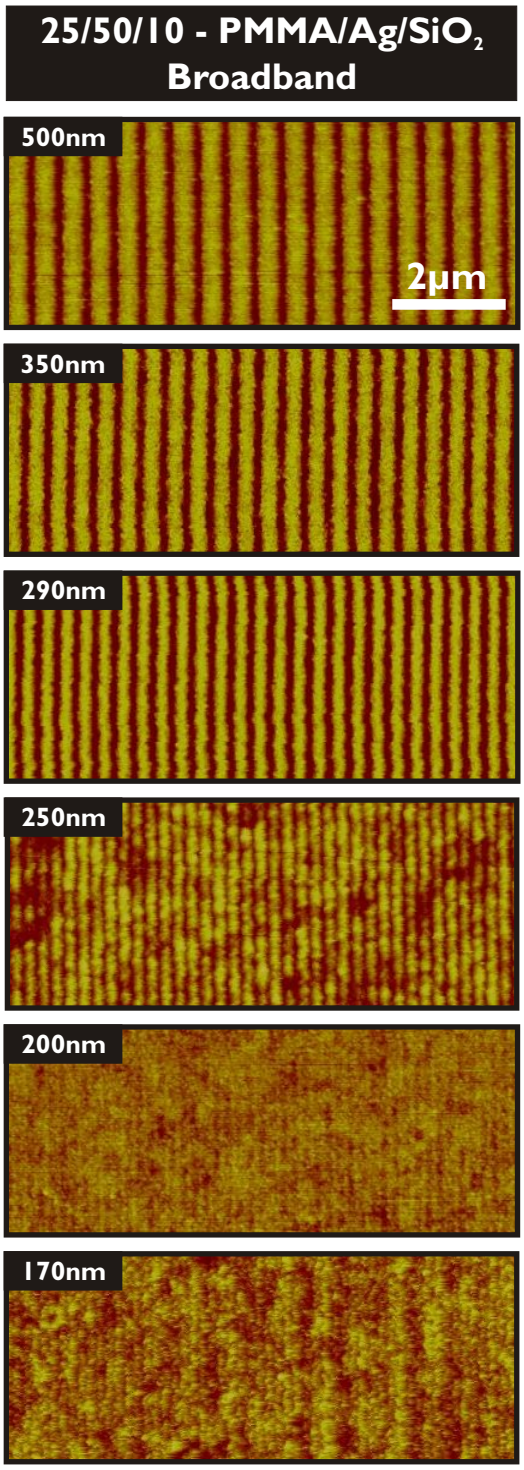

Fig. 6.14: AFM images of gratings imaged through the 25|50|10 - PMMA|Ag|SiO_2 lens stack, with periods of 500 nm down to 170 nm.

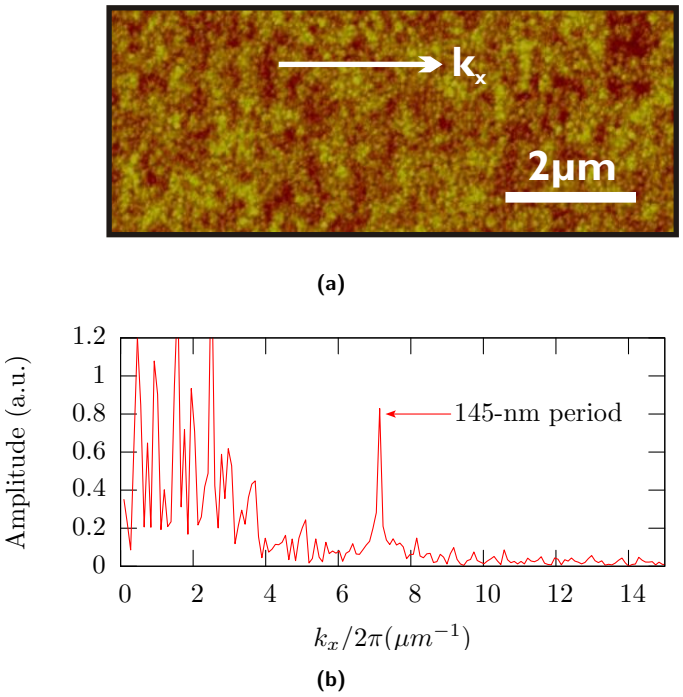

Fig. 6.15: Results for a 145-nm period grating exposed through the 25|50|10 - PMMA|Ag|SiO_2 lens stack: (a) AFM image and (b) Fourier transform in the direction of the grating vector k_x.

inconsistances in intensity effect the performance and practicality of an ENFOL or PLL system. The effects would have to be compensated for through Optical Proximity Correction (OPC) in the design of the mask. This adds complications to the mask design process, but is very common in today's semi-conductor processes.

The best resolution achieved by the narrowband exposures was again 145-nm pitch. Figure 6.18 presents an AFM scan and a DFT (spectral information) of the 145-nm grating resolved during a narrowband exposure, which is compared with the DFT of the 145-nm period grating formed by broadband exposure.

The maximum resolution of the current system is approximately 145 nm for both broad and narrowband exposures. The broadband exposure spatial spectrum was required to show that the 145-nm pitch gratings had been transferred into the resist (Fig. 6.15). It also demonstrated the reason for the loss in image fidelity. The low-spatial-frequency energy, which has been caused by background exposure due to off-plasmon-resonance wavelengths, has higher intensity than the 145 nm peak, and thus causes enough distortion in the patterns to hide the 145-nm pitch features. In the narrowband case, the 145 nm peak in the spatial spectrum is more intense than any low frequency noise allowing the 145-nm pitch features to be visible in the image. This is a graphic representation of how the narrowband exposure has increased image fidelity through the removal of unwanted wavelengths to limit background exposure. No grating features were imaged below the 145 nm node, but the ultimate resolution may

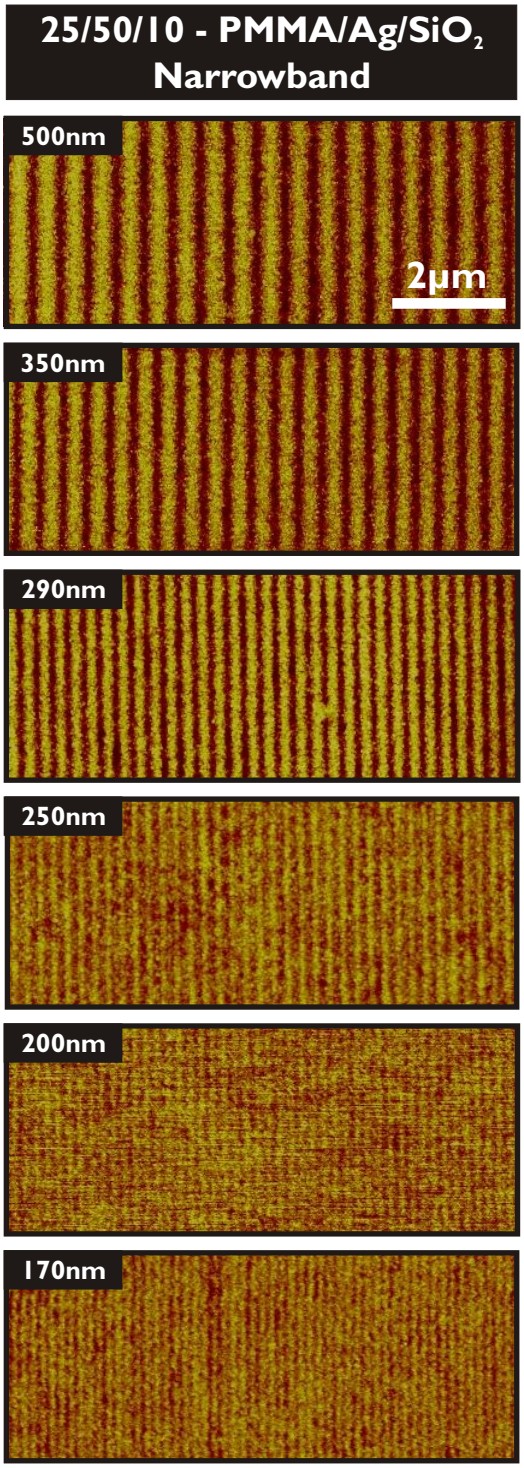

Fig. 6.16: AFM images of gratings imaged with an 365-nm wavelength exposure through the 25|50|10 - PMMA|Ag|SiO_2 lens stack, with periods of 500 nm down to 170 nm.

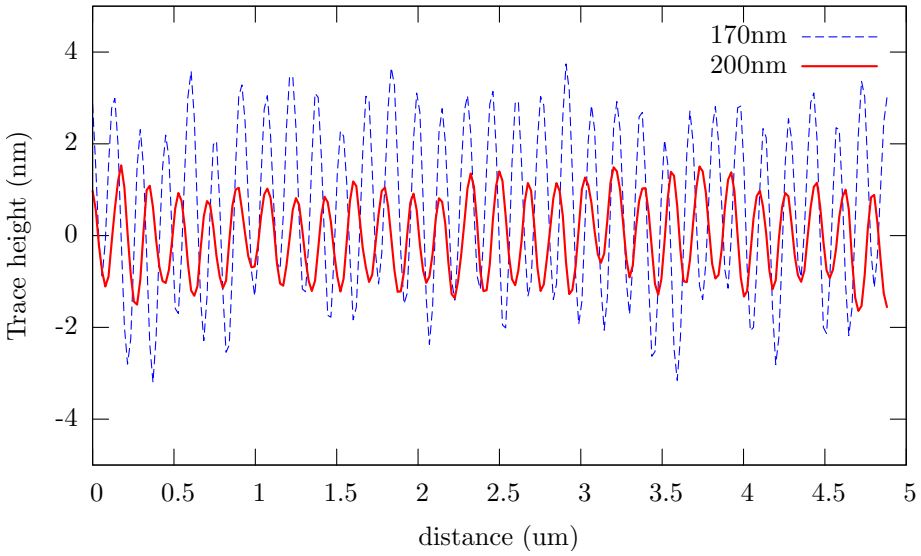

Fig. 6.17: Traces from AFM images of gratings imaged with an 365-nm wavelength exposure through the 25|50|10 - PMMA|Ag|SiO_2 lens stack. Traces presented are for 200 nm (solid line) and 170 nm (dashed line) features.

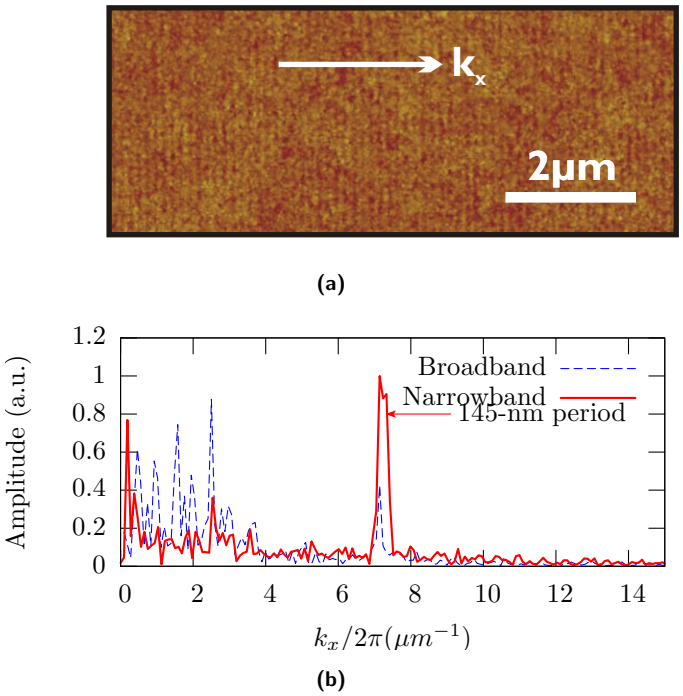

Fig. 6.18: Results for a 145-nm period grating exposed with a narrowband source through the 25|50|10 - PMMA|Ag|SiO_2 lens stack: (a) AFM image and (b) Fourier transform in the direction of the grating vector k_s. The AFM scale is 10 nm. The broadband spectrum is also added, which is normalised to have an equal amount of spectrum energy.

not have been achieved at this point as the mask-making process has a dense grating limitation at around the 100-120 nm pitch level (a summary of fabrication issues was given in Section 5.8).

6.5.2 Isolated Features

Isolated features and line pairs have also been imaged through the 50-nm thick silver superlens. The results for the better-performing narrowband exposures have been analysed. The sample used has an exposure time of 720s. Figure 6.19(a) shows line pairs separated by around 500nm imaged into resist and Figure 6.19(b) shows an averaged line scan.

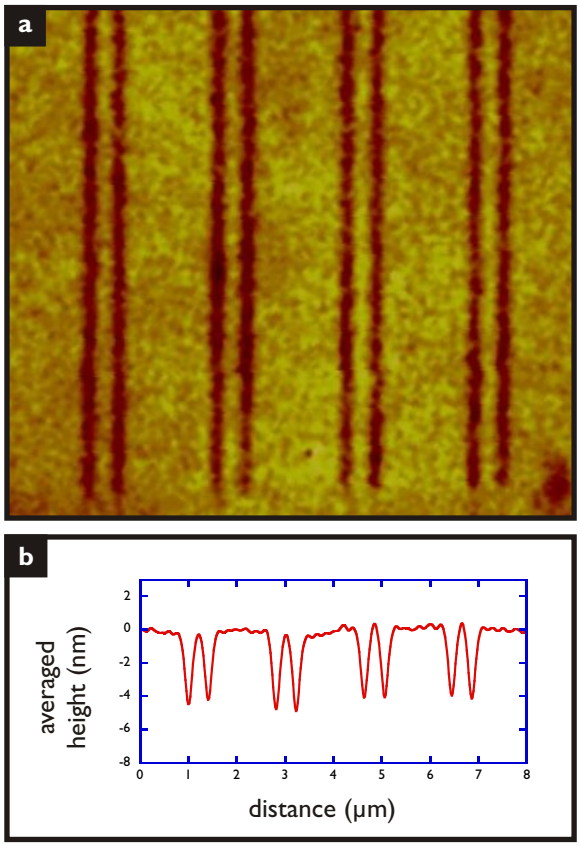

Fig. 6.19: AFM scans for line-pair features imaged below a 25/50/10 - PMMA/Ag/SiO_2 stack. line-pair separations are approximately 500nm. Height scale is 50nm.

The lines have a width of approximately 150 nm and are clearly resolved. Interestingly, there is very little ringing around the edges of the lines. This small amount of ringing indicates that the surface plasmon generated on the silver are localised, which is what we would expect for near-resonance illumination.

The tightest criterion for resolving focused line pairs in the far-field has been de-

vised by Sparrow [34], and has been summarised in Section 2.2. The calculation for this technique, using Equ. 2.7, results in a diffraction-limited minimum resolvable line-pair separation of 101 nm for a refractive index of n=1.5 (The numerical aperture is set to be limited to n). The less stringent Rayleigh criterion (Equ. 2.6) produces a 121 nm separation limit.

Figure 6.20 shows the ability of the system to image line pairs of varying separation. Averaged line scans show line-pair separation from 315 nm down to 95 nm demonstrating a classic deterioration in line-pair resolvability due to proximity effects. At a line separation of 315 nm the lines are still clearly resolvable, however, the centre peak has started to drop as the spatial intensity profiles begin to overlap. Once the spacing has been reduced to 117 nm the centre peak has almost been completely lost due to proximity effects from the two sources. At 95-nm separation the central peak has been almost completely gone, with only a hint remaining. Since the traces are averaged over 2.5 μm it is believed that this saddle on the 95-nm separated features indicates the slight separation of two intensity peaks and is not caused by random resist roughness or AFM distortion, however, this result is far from conclusive. If this is the result of a image separation, the extremely tight Sparrow criterion limit, of 101 nm for this experimental setup, has been slightly out performed. The more commonly used Rayleigh criterion has however been beaten, by both the 117 nm and 95 nm separated line pairs. It must be noted that even though the diffraction-limits have been approached and beaten in some cases, only poor images have been exposed in the resist, which would be insufficient for a lithographic transfer into a layer beneath. It does, however, demonstrate the presence of an electric field profile with spacial information beyond the detraction limit. Therefore through improving the performance of the exposing and development of the resist the transfer of this information is possible.

PLL's ability to image isolated text features has also been tested. The sample used here had an exposure time of 360s. Figure 6.21(a) shows a '50nm' text feature that has been fully developed into the 100nm resist. A line scan of the text is given in Fig. 6.21(b) and shows the good aspect ratio that has been achieved by the method. The line widths for these clearly defined features is around 250nm and again there is no sign of ringing around the edges of the features. This shows that this technique has the ability to image small and large scale features simultaneously.

In conclusion, PLL has been experimentally tested, bringing about proof of Pendry's orignal superlens theory [18] by producing sub-diffraction-limited results at UV frequencies through planar silver lenses. Imaging has been improved with the use of narrowband exposures. In the next chapter, this work has been extended to achieve super-resolution through multiple silver layers.

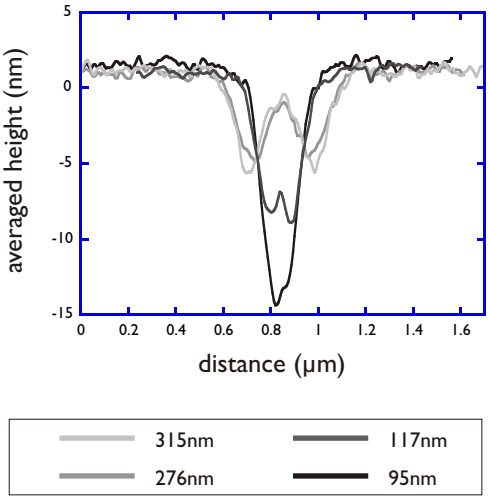

Fig. 6.20: Averaged line scans of AFM images of line-pairs for a range of separations imaged below a 25/50/10 - PMMA/Ag/SiO_2 stack. Lines have been averaged over at least 2.5 μm or 250 traces.

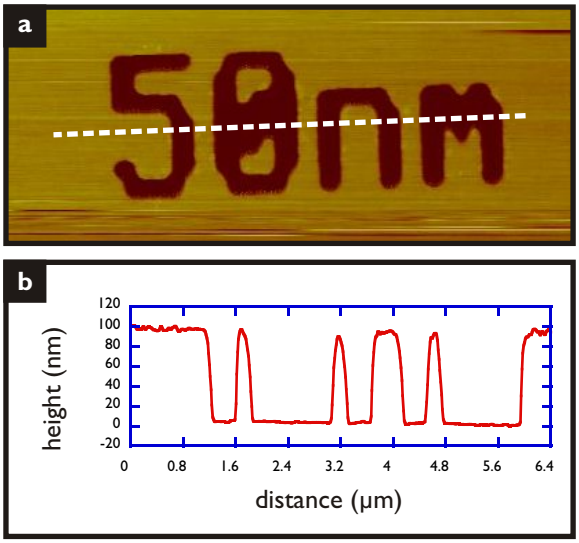

Fig. 6.21: (a) An AFM scan of an isolated '50nm' text feature imaged below a 25/50/10 - PMMA/Ag/SiO_2 stack. (b) is a line scan of the resist profile indicated by the dashed line in (a). Height scale is 150nm.

Chapter 7

MULTIPLE-LAYER PLANAR LENSING LITHOGRAPHY

"The more the merrier"

- Italian Proverb

The performance of PLL using multiple silver layers has also been experimentally investigated. A double-layer mask was constructed to test the hypothesis that a multi-layered stack would improve the resolution and overcome limitations due to imperfections in the stack's layers [26]. Simulations had also been performed to demonstrate that the performance of a multi-layer stack would be an improvement on a single layer for the same overall thickness of silver. The following sections detail the results from two multiple layer lenses that were fabricated.

7.1 2 × 50NM DOUBLE-LAYERED LENS

The first multi-layered mask fabricated incorporated an 25|50|50|50|10 - PMMA|Ag|SiO_2|Ag|SiO_2 stack. The Ag and SiO_2 layers were thermally evaporated one after the other without breaking the vacuum. The final surface roughness of the mask was around 2 nm rms, or almost twice the roughness of previous single-layer masks. Figure 5.14 of Section 5.6 demonstrated the presence of increased surface roughness.

Figure 7.1 shows a number of features imaged during a 900-s narrowband exposure below a 25|50|50|50|10 - PMMA|Ag|SiO_2|Ag|SiO_2 double layer stack. Features have been imaged down to a minimum pitch of 350 nm, however, image fidelity is not high.

The total silver thickness of this mask is 100 nm which places it in between the 85- and 120-nm thick single layer lenses. Table 7.1 summarises the performance of each of these masks (the 60-nm thick silver PLL mask is also added for comparison). Unfortunately, a clear comparison is difficult to make between these masks. It can be said that both the 50-nm double-layer and 85-nm single-layer masks have better resolution and better image quality than the 120-nm single-layer mask. The improvement in image quality can clearly be seen by investigating the 1-μm patterns. It is hard to separate

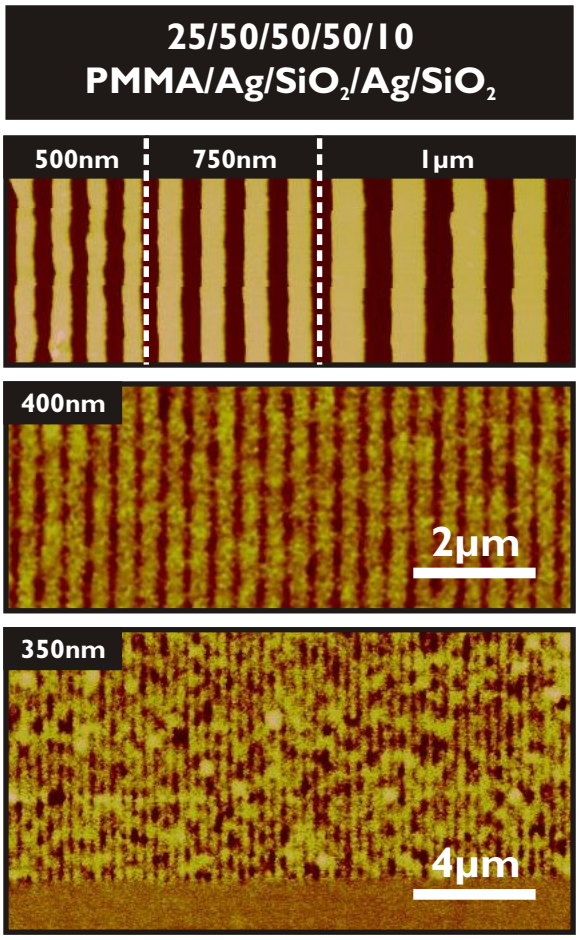

Fig. 7.1: AFM scans for features imaged below a double-layer 25|50|50|50|10 - PMMA|Ag|SiO_2|Ag|SiO_2 stack. All height scales are 50nm.

the 50-nm double-layer and 85-nm single-layer masks in terms of image quality. The 50-nm double-layer exposures do possess higher contrast, but this could simply be a function of exposure dose.

7.2 2 × 30NM DOUBLE-LAYERED LENS

The second double layered mask constructed used a 15|30|30|30|10 - PMMA|Ag|SiO_2|Ag|SiO_2 stack. Through this lens super-resolution was achieved and the theory of multi-layered silver lenses by Ramakrishna *et al.* [26] largely confirmed. The performance of the mask for features above the diffraction-limit is presented in figure 7.2. Here, the process has clearly imaged features down to 350 nm in pitch. The exposure time for the double-layer sample is 420s, which is almost half the length of time required for the exposures through the single 50 nm silver layer (720 s). This indicates an increase in transmission through the double layer stack despite the increase in total silver thickness. The fidelity

Table 7.1: Specification and performance of PLL masks that were unable to achieve sub-diffraction-limited imaging.

Mask	Total silver (nm)	Total spacer (nm)	Final spacer (nm)	Exposure	Minimum period (nm)
120-nm single	120	120	60	Broadband	700
85-nm single	85	66	26	Broadband	350
60-nm single	60	60	30	Broadband	350
2 × 50nm double	100	85	10	Narrowband	350

of the 1 μm period grating is similar to that produced by the single-layer 25|50|10 - PMMA|Ag|SiO_2 stack (see Fig. 6.13).

The performance of this mask in the sub-wavelength and sub-diffraction limited regime is compared to a 25|50|10 stack in Fig. 7.3. Again, the features above the diffraction-limit are imaged with good clarity, as seen by the 290nm grating period image in Fig. 7.3. Sub-diffraction-limited resolution is also achieved by the double-layer lens, however image fidelity is reduced considerably. This is clearly depicted by the increased granularity in the 200nm and 170nm grating period images compared with their counterparts imaged through the 25|50|10 stack.

Figure 7.4 shows the DFT for both the 170-nm images from Fig. 7.3, and presents normalised spatial spectrum of the scans. The peaks located at the wavenumber 5.9 μm^{-1} represent the presence of the 170-nm pitch in both images, thus it can be stated that both exposures have imaged features below the on-axis diffraction limit. What is clear, however, is that the single layer lens has performed better. The 170-nm pitch peak present in Fig. 7.4(a) is an order of magnitude higher than the other features in the spectrum, hence the 170-nm period is clearly seen in the original image. In the case of the double-layered mask (Fig. 7.4(b)), the 170-nm pitch peak has a relatively small energy associated with it when compared with the low frequency components of the spectrum. This in-turn leads to an image that has a much reduced fidelity.

The reduction in fidelity is the result of increased surface roughness for the double layer stack. The increased surface roughness is attributed to three effects: firstly, in the 15|30|30|30|10 stack case roughness is caused by the reduction in the thickness of the silver layers (deposition of silver to a thickness less than 35 nm results in rougher films as the granularity due to surface tension and cluster size has not yet been overcome by heating and bombardment); secondly, the two additional interfaces in the double layered stack tend to amplify any defects in the lower layers, compounding the roughness from layer to layer; finally, for the thinner layers there is a greater the likelihood of pin-hole shorts between conducting layers - these shorts dampen the plasmonic effects that the technique relies on. Nonetheless, these results show that a double-layer stack can achieve similar resolution to a thinner single-layer stack, with higher light transmission.

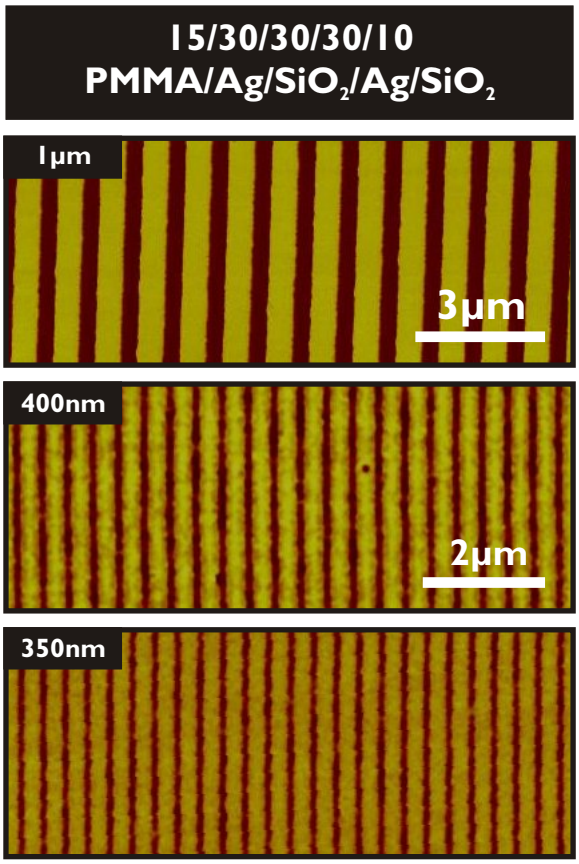

Fig. 7.2: AFM scans of large features patterned with a 15|30|30|30|10 - PMMA|Ag|SiO_2|Ag|SiO_2 PLL masks. Images of 1 μm, 400 nm, and 350 nm are shown. The 1-μm period scan's height scale is 150 nm, while the remain two use 50 nm.

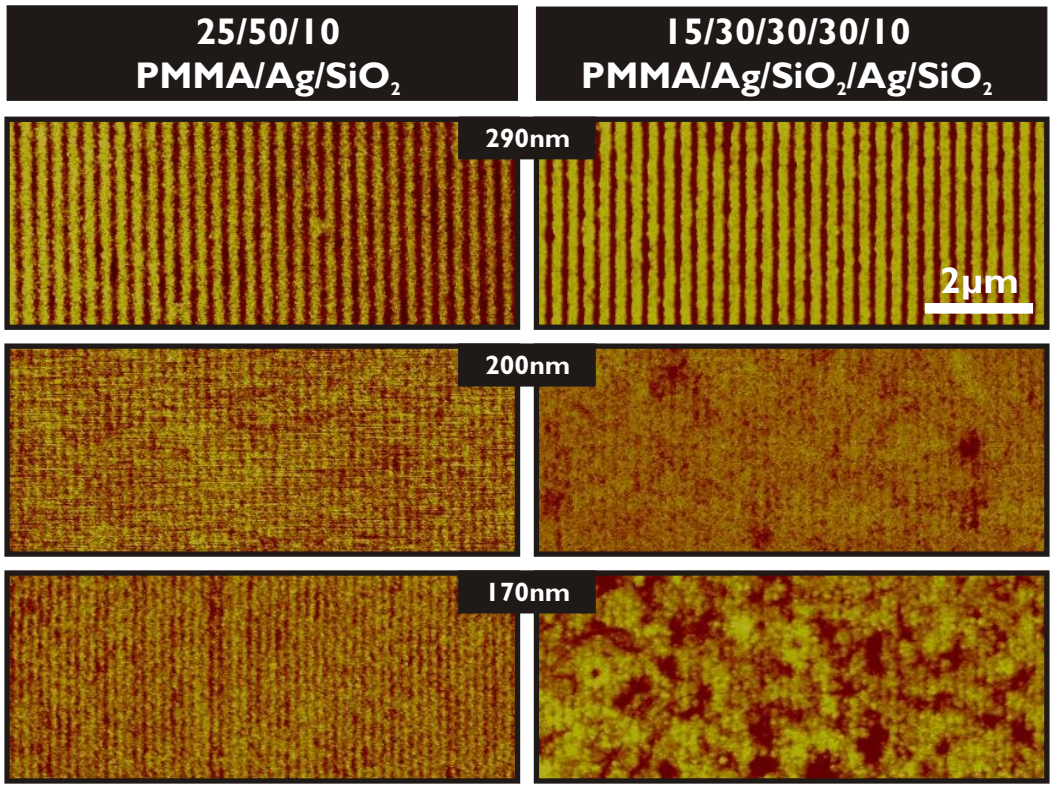

Fig. 7.3: A comparison of AFM scans for features imaged below a single-layer 25|50|10 - PMMA|Ag|SiO_2 stack and a double-layer 15|30|30|30|10 - PMMA|Ag|SiO_2|Ag|SiO_2 stack. All height scales are 50nm.

7.2.1 Simulations

FDTD simulations were compiled for no-lens, single-layer lens, and double-layer lens systems under the 170-nm period grating to investigate the performance numerically. Figure 7.5 shows a 2D cross-section comparison between an 25|50|10 - PMMA|Ag|SiO_2 single-layer lens stack (Fig. 7.5(a)) and a 15|30|30|30|10 - PMMA|Ag|SiO_2|Ag|SiO_2 double-layer lens stack (Fig. 7.5(b)). Here, the ability of the single- and double-layer silver superlenses to project the sub-diffraction-limited source features to an image plane is demonstrated.

Traces through these simulations at a depth of 30 nm into the resist (as indicated by the thick dashed line through the images in Fig. 7.5) are shown in Fig. 7.6 along with a trace from a no-lens 85-nm PMMA proximity spacer simulation. For the no-lens case (solid line) the limitations of proximity exposure for sub-diffraction-limited features is evident in the lack of contrast in the resist, thus, no features would be transferred into the resist. In the case of the superlenses (the two dashed lines), the traces show that there is sufficient contrast to produce clear features in the resist. The traces for the double- and single-layer lens also show that we expect higher transmission (about two-times) for the double-layer lens, which is what is seen experimentally. As was predicted

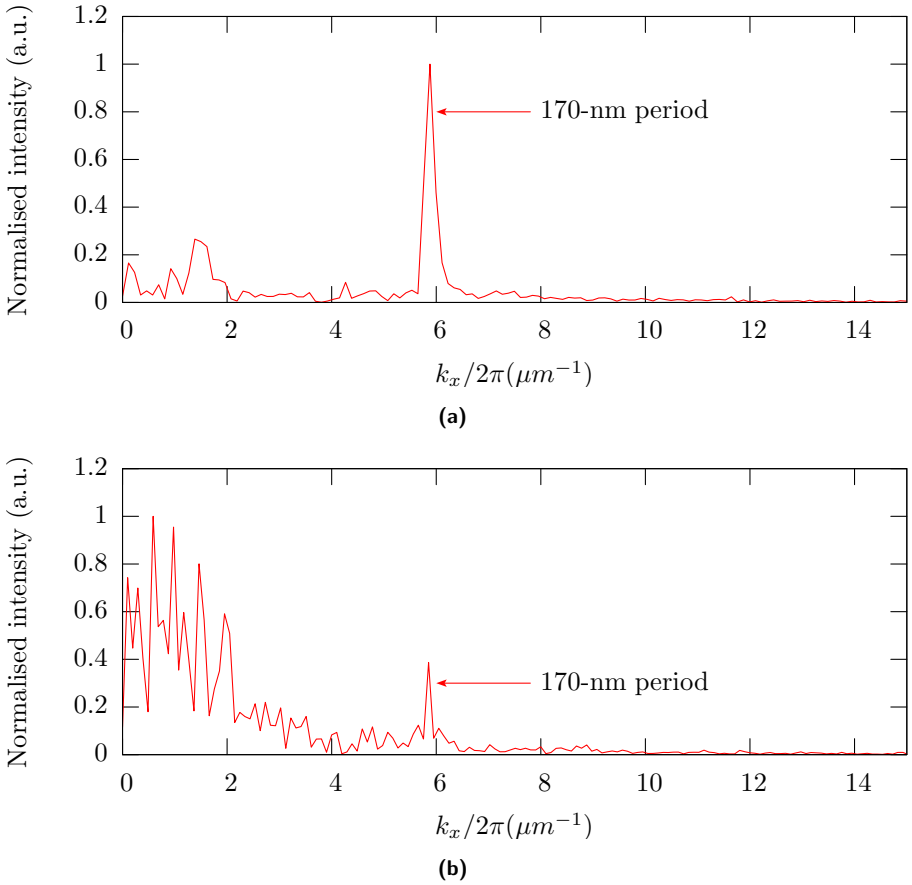

Fig. 7.4: Spatial spectrum of 170-nm features for 15|30|30|30|10 - PMMA|Ag|SiO_2|Ag|SiO_2 double-layer and 25|50|10 - PMMA|Ag|SiO_2 single layer stacks.

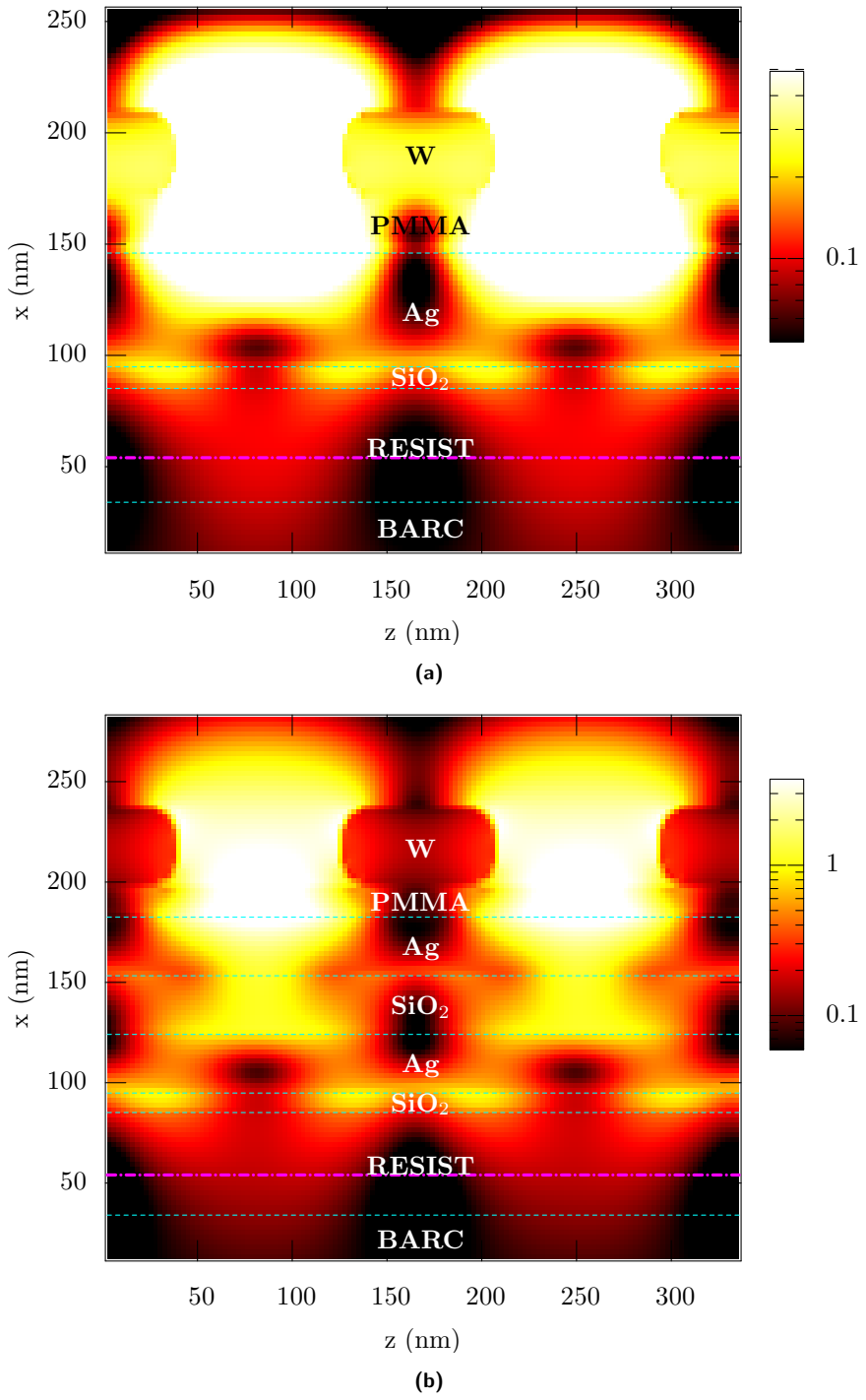

Fig. 7.5: Simulated cross-sections of the electric field intensities under a 170-nm pitch grating for (a) a 25|50|10 - PMMA|Ag|SiO_2 single layer exposure and (b) a 15|30|30|30|10 - PMMA|Ag|SiO_2|Ag|SiO_2 double-layer silver lens exposure. Both simulations were run for an illumination wavelength of 365 nm and transverse magnetic (TM) polarisation.

by Ramakrishna *et al.* [26], higher contrast is also expected for the double-layer lens, however, this information is difficult to gleam from the images produced in non-linear resist.

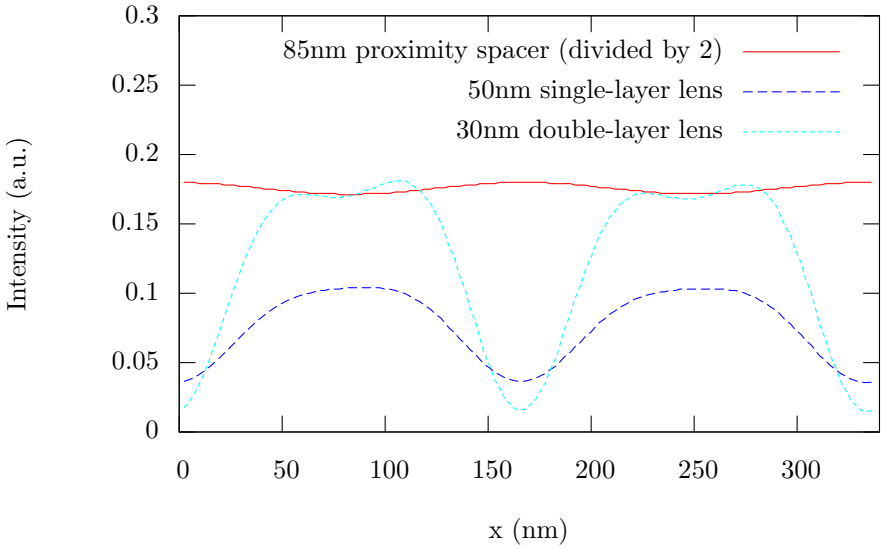

Fig. 7.6: Simulated intensity line traces for a depth of 30 nm into the 50-nm thick resist under a 170-nm period grating for a 25|50|10 - PMMA|Ag|SiO_2 single-layer lens (solid line) and a 15|30|30|30|10 - PMMA|Ag|SiO_2|Ag|SiO_2 double-layer lens (dashed line).

In addition to proving Pendry's single layer superlensing theory in the previous chapter, the work has been extended to achieve super-resolution through multiple silver layers. The performance of the double-layer masks was below that of the single layer performance due to increases in surface roughness.

In the next chapter, the parameter space of PLL is explored by simulations and analytical methods, in order to understand the performance variation for different pitches and an optimise the performance of a multi-layer lens stack.

Chapter 8

ADVANCED SIMULATIONS

"Prediction is very difficult, especially about the future."

- Niels Bohr

To increase the understanding of the performance of ENFOL, proximity lithography, and PLL systems a large number of simulations were performed. This chapter looks at the analysis of those simulations and makes conclusions about performance limitations. Both numerical and analytical techniques have been utilised.

For the numerical FDTD simulations, the setup of the simulation domains and sources are detailed in Section 3.5. To recap, the most common simulation is a 2D, two-period domain with wrapped boundary conditions on the sides, an absorbing source at the top and a PML at the bottom (see Figure 3.5). Sections 8.1 and 8.2 detail the results of the FDTD simulations; Sections 8.3 and 8.4 describe an analytical approach for approximating PLL performance and the results obtained, respectively.

8.1 RESOLUTION PERFORMANCE VERSUS GRATING PERIOD

The most relevant simulation parameters to investigate were contrast[1] and FOM over a range of grating periods for various PLL stacks. TM FDTD simulations were run with 50% duty cycle gratings for periods from 50 nm through to 1000 nm.[2] The effect of duty-cycle has been covered elsewhere [16]. Figure 8.1 shows a comparison for broadband exposure between a 60|120|60 - PMMA|Ag|PMMA and two proximity exposures for 120-nm and 240-nm gaps. Both the contrast (Fig. 8.1(a)) and the FOM (Fig. 8.1(b)) are provided from the simulations which employed substrates with 50 nm of resist on silicon.

[1] Two types of contrast are covered in Section 3.8.1. The contrast used here is the the normalised difference between the intensity under the aperture and the intensity under the shadow (or under the absorber). With this definition the contrast goes negative when there is image inversion.

[2] Higher period simulations were also run, but the details are unimportant to this discusion.

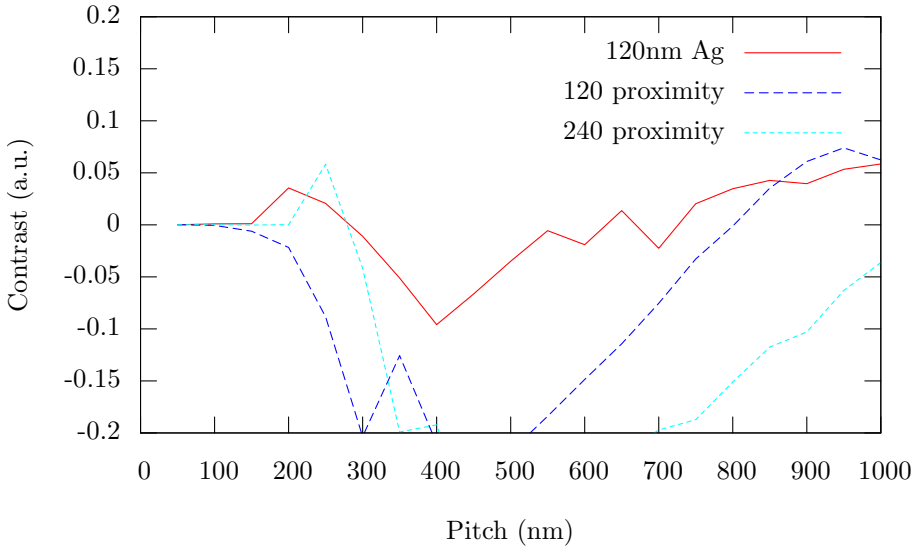

(a)

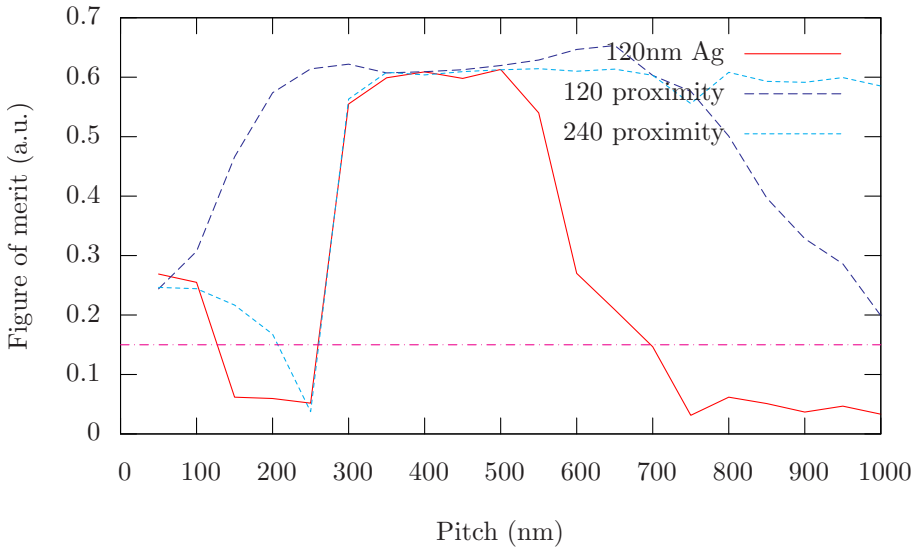

(b)

Fig. 8.1: The (a) contrast and (b) FOM is plotted against grating period for TM simulations of a 60|120|60 - PMMA|Ag|PMMA stack, and two proximity stacks (120nm and 240nm). A FOM below the red dot-dash line in (b) (FOM = 1.5) signals a good image the the resist. All simulations are for a resist thickness of 50 nm and a silicon substrate.

There are a number of points raised by these simulations. Firstly, the results are generally quite poor, with little contrast or quality in the FOM. Secondly, all contrast curves go negative below 700 nm — the effect of diffraction and standing wave — and all contrast curve reduce to about-zero below 200 nm — the diffraction limit. Thirdly, although both the 120-nm silver stack and the 120-nm proximity exposure show similar contrast above 800-nm pitch, it is the 120-nm silver simulation that attains a very respectable FOM of less than 0.1 (almost perfect image), while for the proximity case resides at 0.3-0.5, which is consistent with image spatial frequency doubling. This was seen experimentally [152]. And finally, the 120-nm silver simulation holds a good quality FOM to around 700-nm period – the period acheived in the first experimental results [23].

Figure 8.2 explores two of the changes made to the experimental procedure during the development of the process: the use of a BARC and narrowband rather than broadband exposure. All simulations are for a 60|120|60 - PMMA|Ag|PMMA stack. They show that the reflective nature of the silicon substrate actually helps rather than hinders the imaging process. This is actually expected in many cases and has been investigated previously [200–202]. Further, the important conclusion from this plot is the quality improvement for narrowband exposure. The stack now has higher image fidelity down to 400 nm periods, but note that the contrast is still limited by diffraction.

From this point on all simulations are narrowband to allow the best performance of the system to be investigated. The following section focuses on the sub-diffraction-limited performance of a range of single-layer lenses.

8.2 SUB-DIFFRACTION-LIMITED PERFORMANCE

The sub-diffraction-limited performance of various near-field silver superlens configurations were investigated for 50% duty-cycle objects with periods below 220 nm. For these periods the TM polarisation is dominant due to discrimination by the grating and silver (see Section 3), thus TM-only simulation comparisons are presented. All simulations are for narrowband 365-nm light.

Figure 8.3 shows the contrast and FOM curves for three silver superlenses used to image grating with periods between 50 and 200 nm. The values for the graphs are calculated from traces through the 2D simulations at a depth corresponding to the Veselago ratio (1:2:1), e.g. for the 50-nm thick lens a trace is taken 25 nm below the silver (each lens has its respective Veselago ratio above the lens). Proximity exposures are also provided as a comparison, at 25-nm and 100-nm separation.

All three silver lenses show contrast above 0.2 in the sub-diffraction-limit regime, however, the contrast is variable ranging from barely present at 200 nm to peaks above 0.4 in the 110-130nm range. The 40-nm thick lens gives the broadest contrast range, with a peak contrast of around 1 at 130 nm, but does not out perform the 50-nm thick

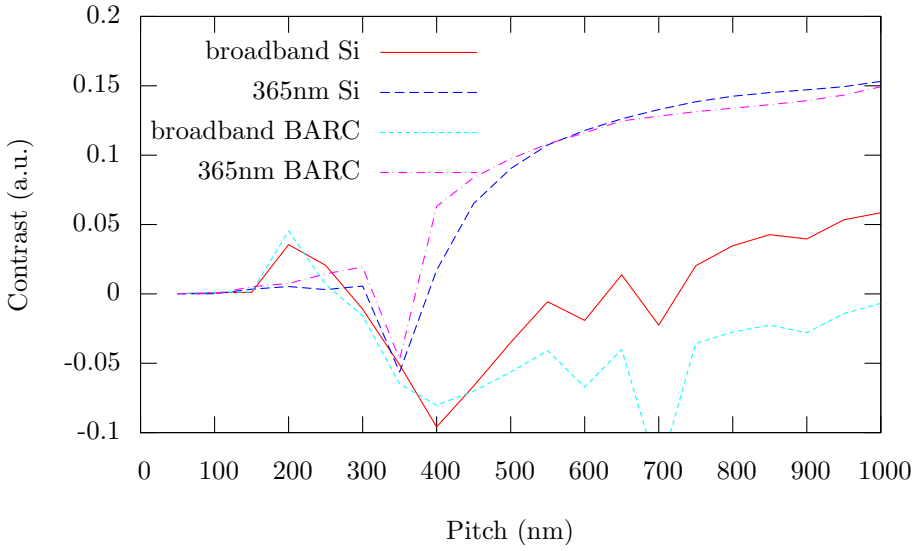

(a)

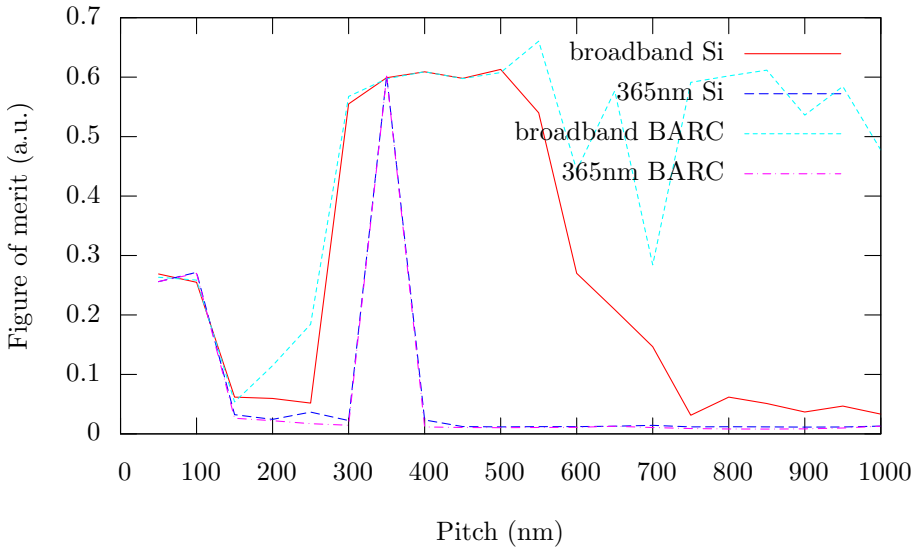

(b)

Fig. 8.2: The (a) contrast and (b) FOM is plotted against grating period for TM simulations of a 60|120|60 - PMMA|Ag|PMMA stack, and two proximity stacks (120nm and 240nm). All simulations are for a resist thickness of 50 nm on either silicon substrate or a bottom anti-reflection coating (BARC) substrate that is perfectly matched.

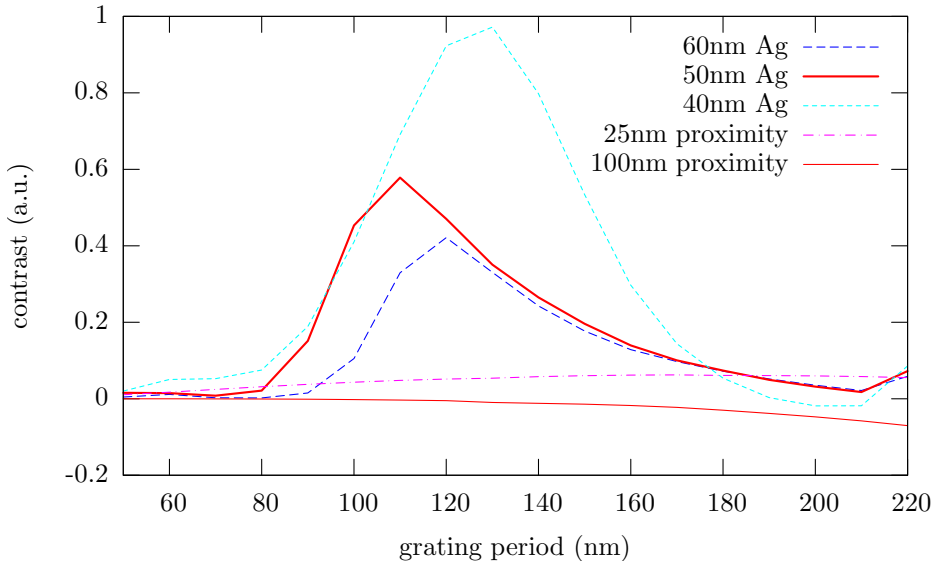

(a)

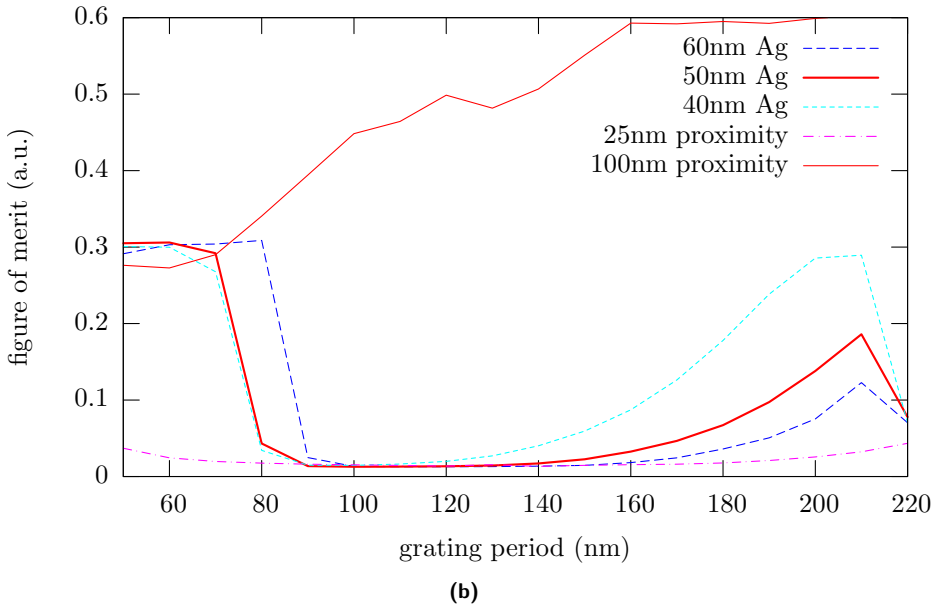

(b)

Fig. 8.3: (a) The contrast of the intensity profiles through 2D TM simulations for a range of grating periods and thicknesses of single-layer silver lenses. The profile is taking at the depth corresponding to the Veselago ratio (1:2:1). The figure-of-merits for the traces are shown in (b).

lens in terms of a resolution limit. Both drop off at slightly below 100-nm pitch. The proximity exposures demonstrate the effect of diffraction, with flat-low contrast below the diffraction limit.

In Figure 8.3(b), the FOM shows that the 50- and 60-nm thick lenses both have good quality images across a 80-200-nm period range, while the 40-nm thick lens tends to produce a period-halved image as the pitch nears 200 nm.

Figure 8.4 shows the contrast at a fixed distance of 10 nm from the silver. The proximity comparison at 10nm from the mask shows a low, but flat level of contrast, which shows reasonably linear increase from the 25-nm proximity trace taken previously. It is this contrast that is utilised in an ENFOL exposure.

For the silver lenses there is a shift to a better resolution limit in imaging closer to the silver layer, with both the 40- and 50-nm thick lenses giving good contrast down to at least a 80-nm pitch. The FOM, shown in Fig. 8.4(b), shows an interesting effect emerging as we move closer to the silver layer. Between the 140- and 220-nm periods the three lenses show period halving, and indicate there is not a clear image at a 10-nm separation from the lens. The fact that the FOM decreases as we move away from the mask towards the Veselago ratio distance, shows that the silver is forming a better image at a separation distance from the lens rather than at the surface.

Although the simulations suggest that the 60-nm thick lens is capable of producing sub-diffraction-limited imaging, nothing was obtained experimentally. Among other issues, this could be due to weak intensity. Figure 8.5 show a comparison of the contrasts for the same silver lens simulations after they have been multiplied by the maximum intensity value in the trace, i.e. the contrast is no longer normalised. We can see that a thinner lens out performs a thicker one. The low intensity of the features through a 60-nm thick lens could be a reason for not obtaining this resolution experimentally (see Section 6.4.2). Unfortunately, no good quality 40-nm thick lenses were constructed to experimentally test the increase in performance expected, however 100-nm pitch features have been acheived with a 35-nm thick silver layer by another group [143]. This result was produced by placing the photoresist layer directly on the silver, i.e. no second spacer, which also provides some validation of the effects shown in Fig. 8.4.

A more detailed exploration of the contrast landscape is shown in Fig. 8.6 where the sub-diffraction-limit contrast is plotted against grating period and distance into resist. Figure 8.6(a) is for a proximity, or ENFOL case, while Fig. 8.6(b) is the result for a 25|50|10 - PMMA|Ag|SiO_2 PLL stack. The bottom of the mask is at 0 nm for ENFOL and the bottom of the silver is at -10 nm for PLL. ENFOL exhibits the expected performance – good, consistent sub-diffraction-limited resolution across all periods, but with limited penetration into the resist (best contrast at the resist/grating interface). The slight inversion of the contrast at larger depths, beginning for the 220nm pitch and then becoming present for smaller pitch features, is the Talbot effect [199].

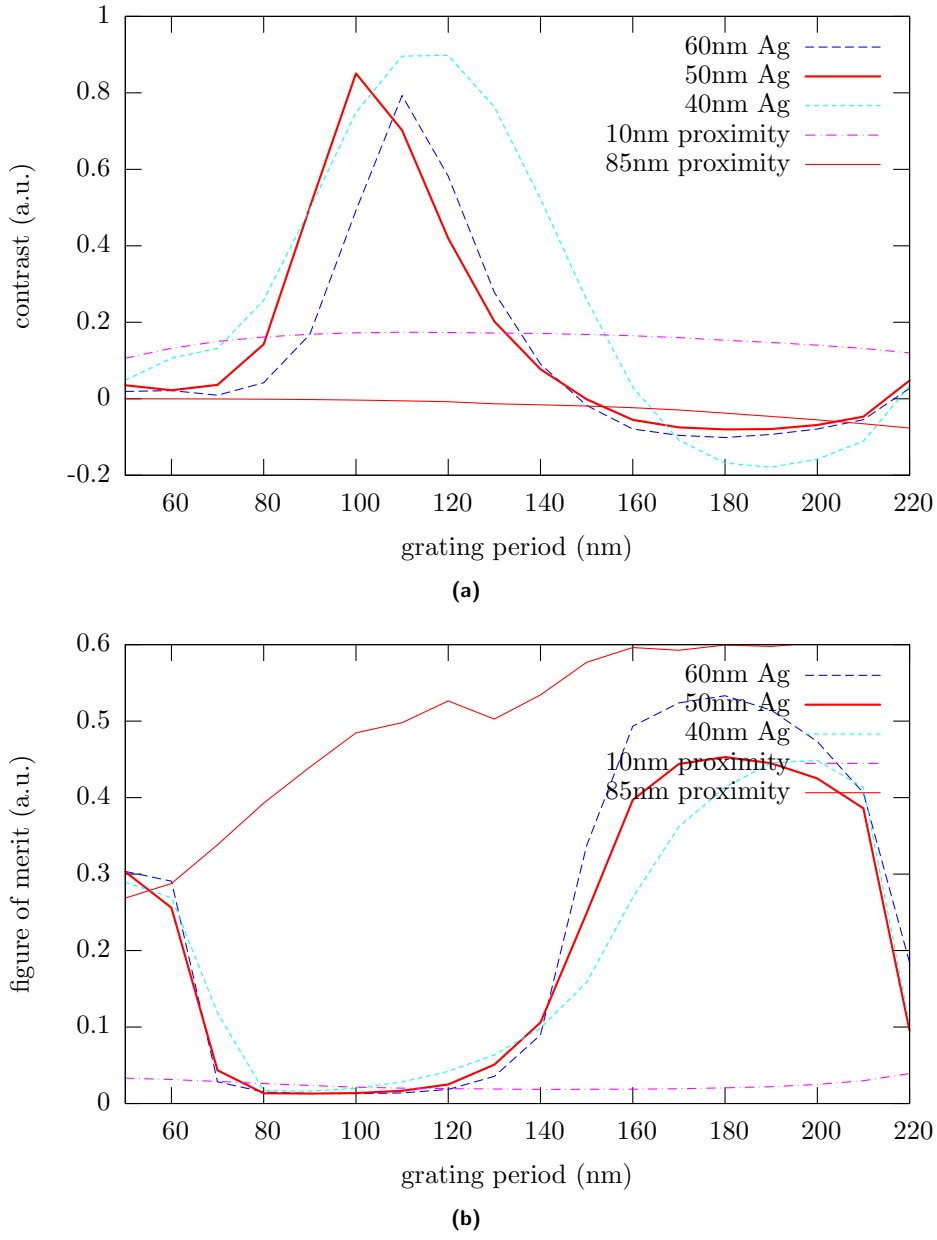

Fig. 8.4: (a) The contrast of the intensity profiles through 2D TM simulations for a range of grating periods and thicknesses of single-layer silver lenses. The profile is taking at a depth of 10nm from the silver layer. The FOM for the traces is shown in (b).

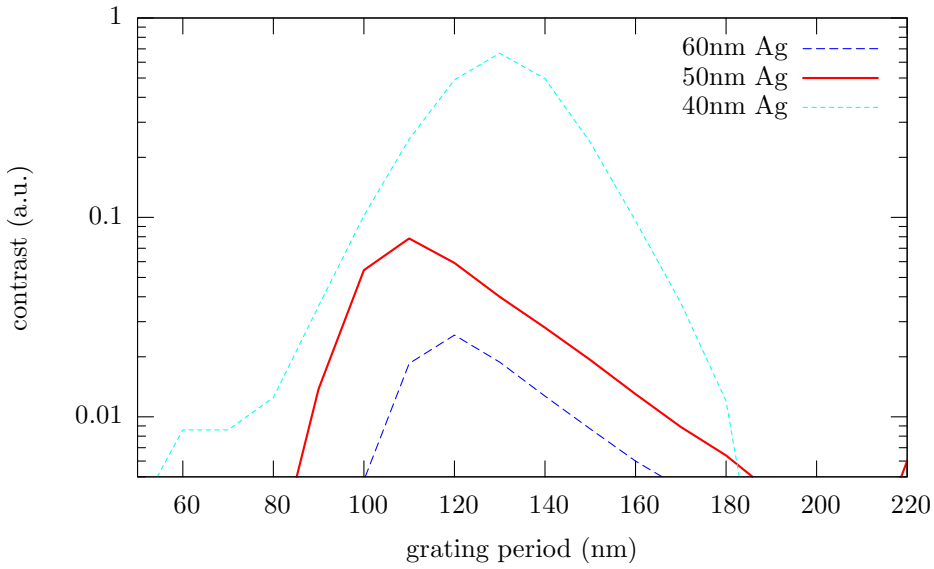

Fig. 8.5: Normalised contrast values that have been multiplied by the maximum intensity in a trace and shown for 40-, 50-, and 60-nm silver stacks.

For PLL, the effect of the 50-nm thick silver is dramatic. Bearing in mind that at 0 nm into the resist the distance from the mask is already 85 nm, there is clearly a projection of the near-field by the superlens as sub-diffraction-limited features appear with good contrast below the silver. However, the performance of the contrast is no longer consistent across all periods. Excellent contrast is present for 100-nm pitch features at the resist interface and, interestingly, for 120-nm periods and above the best image is formed at a separation from the lens. Thus, the plane of highest contrast of the lens is dependent on the period imaged [203]. For 100-nm through 170-nm periods a good quality image is found at a depth into the resist of 30 nm, or at a total working-distance of 40-nm from the silver. It is this working-distance enhancement that could allow a relaxation of the contact requirement for the mask and the resist, as the best contrast is not necessarily at the silver surface.

For a period of 170 nm, PLL has contrast above 0.3 for a depth range of over 30-nm in the resist. This compares with a depth range of about 20 nm for ENFOL, and increases the ability of the near-field lithography technique to expose a resist layer — a major PLL advantage.

8.2.1 The Multi-layer Silver Lens

The expected increase in performance for a multi-layer silver lens has been investigated by running a number of simulations with single- through to quad-layer stacks. Figure 8.7 shows the sub-220 nm performance of two single-, two double-, one triple-, and one quad-layer system. Table 8.1 provides the data for the thicknesses in each stack.

In general, the multi-layer systems do give a performance enhancement, providing

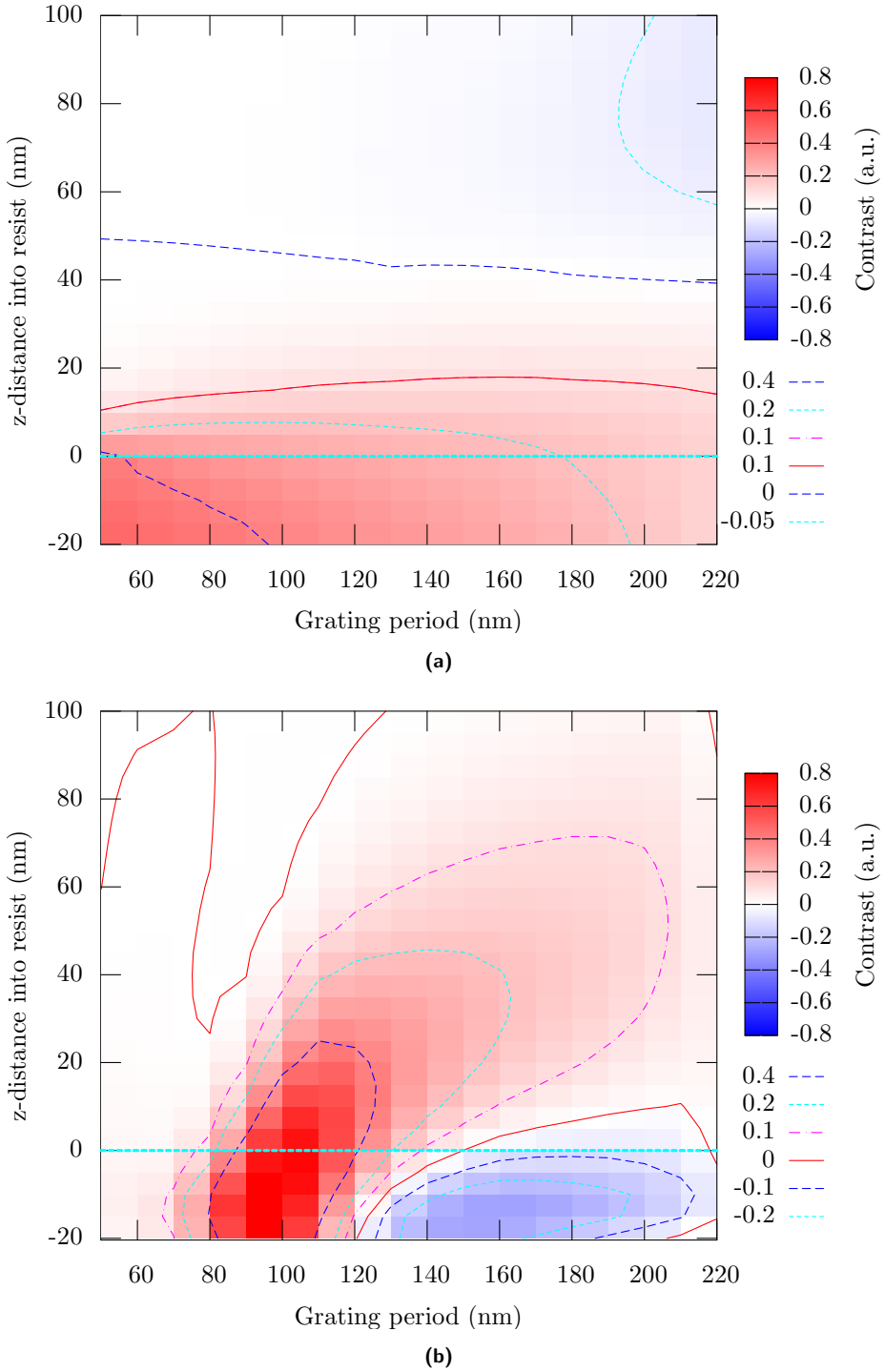

Fig. 8.6: Contrast plotted against grating period and distance into resist for TM simulations of (a) ENFOL and (b) a 25|50|10 - PMMA|Ag|SiO_2 PLL stack. The thick dashed line denotes the resist surface. For ENFOL the mask is at the resist surface, and for the PLL simulation the silver is at -10 nm on the z-axis.

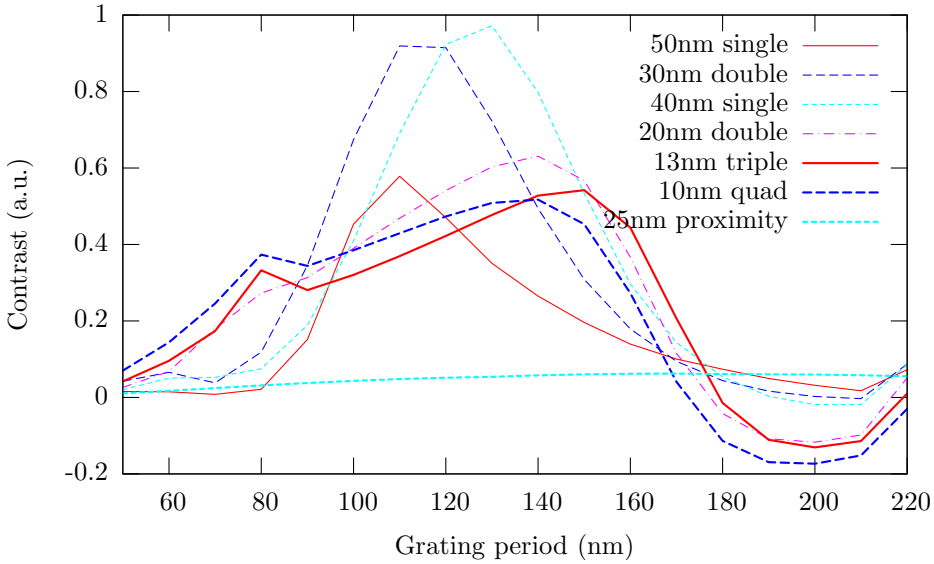

(a)

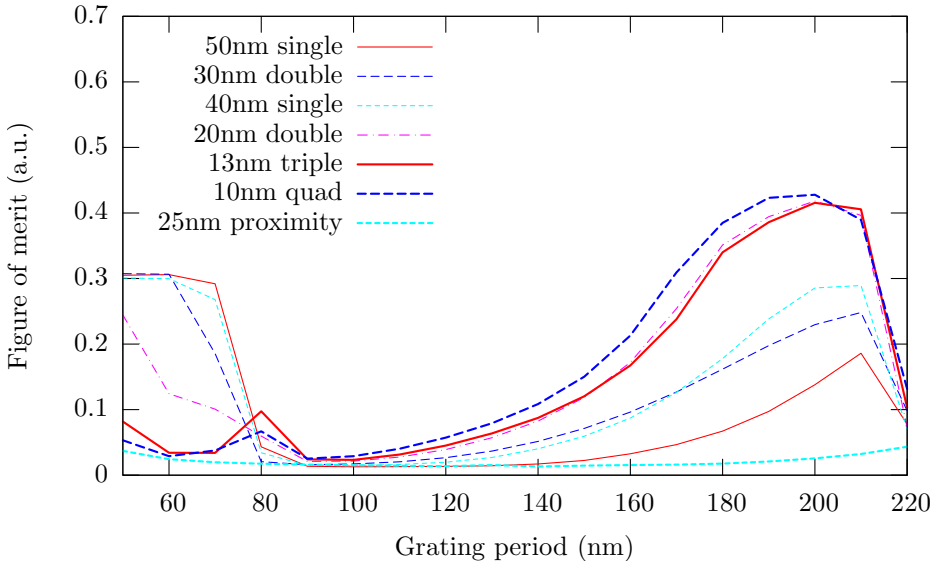

(b)

Fig. 8.7: The (a) contrast and (b) FOM is plotted against grating period for TM simulations of a two of single- (50nm and 40nm) and two double-layer (30nm and 20nm) stacks. A 25-nm proximity exposure is shown for comparision. Traces for calculation of contrast are taken at the Veselago ratio depth.

Table 8.1: Layer thicknesses of the PLL stacks presented in Figure 8.7. The silver layers are in bold text.

Multi-layer stacks	dimensions (nm)
50 nm single	25 | **50** | 25
30 nm double	15 | **30** | 15 | **30** | 15
40 nm single	20 | **40** | 20
20 nm double	10 | **20** | 20 | **20** | 10
13.3 nm triple	6.7 | **13.3** | 6.7 | **13.3** | 6.7 | **13.3** | 6.7
10 nm quad	5 | **10** | 10 | **10** | 10 | **10** | 10 | **10** | 5

better contrast than the single-layer stacks for sub-100-nm features. If we focus on the four stacks that have the same total thickness of 40-nm, we see that there is a trade off between higher contrast for smaller features and peak contrast. This is evidenced by the continually decreasing contrast peak as the total silver thickness is divided up into more layers. For the multi-layer stacks contrast levels hold strong down to below 70-nm pitch features. There is clearly a performance enhancement for sub-diffraction-limited features. Figure 8.8 shows the un-normalised contrast for the stacks with 40-nm total silver thickness. There is clearly a performance increase expected for the multi-layered stacks at sub-100-nm pitch resolution, although this was not able to be verified in our experiments (see section 7.2).

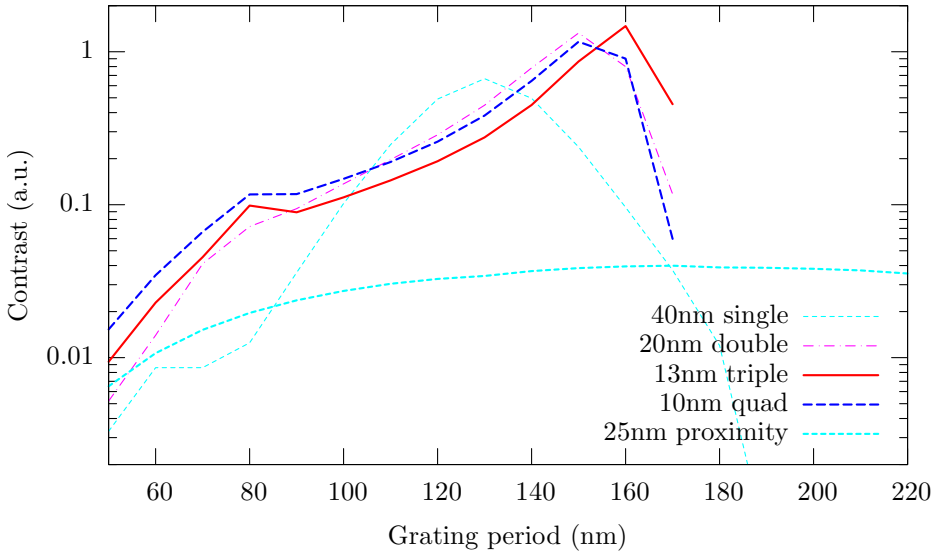

Fig. 8.8: Normalised contrast values that have been multiplied by the maximum intensity in a trace and shown for a range of multi-layer PLL stacks.

Running the FDTD simulations was a time consuming process, with individual points on a contrast graph taking from 20 minutes to 4 hours to calculate. An analytical approach was devised that quickly calculates the transmission properties of a stack, to provide estimates of performance. The main difference to the FDTD simulation is that

this approach does not take into account the interaction with the near-field mask. The technique's derivation is detailed in the next section, which is followed by an in depth look at the optimisation of a multi-layer stack.

8.3 ANALYTICAL TECHNIQUE FORMULATION

There are an number of analytical techniques that have been used to give estimates of silver and negative-index layers' ability to image near-field features [18, 163, 164]. This work has been discussed in Section 2.10.

A simple analytical technique was derived to investigate the performance of silver lenses from the transmission and reflection coefficients of individual wavenumbers, which relate to the silver's ability to image the correspond grating period. The analytical technique was based on a transmission matrix derivation that is commonly used for electron tunnelling [204]. In our case it is photon tunneling that we are most interesting in (also discussed in Ref. [205]). The strength of the T-matrix technique is the simple expansion to multi-layered stacks, the focus of the analytical investigation.

8.3.1 T-matrix Derivation

The T-matrix principle works by defining interface transmission and reflection ratios, defined as a function of wavenumber. This requires a solution to the 1D transmission-reflection problem, which is defined by incoming and outgoing plane waves (or evanescent modes) on both sides of an interface. Once an interface can be described fully anywhere in space, layers of interfaces can be built up though phase-shifting and matching to describe a stacked system. By knowing the coefficients of the two incident waves, we arrive at a fully determined system.

The full T-matrix derivation is provided in Appendix E. Here, the key results are presented. To arrive at a T-matrix to describe an interface with incident plane waves in TM polarisation, a domain is set up as shown in Fig. 8.9.

The electric fields on each side of the interface, which are all of the same temporal frequency, can be described by

$$\mathbf{E}(x,z)|_{z<0} = \mathbf{E}^A e^{i(\mathbf{k}^A.\mathbf{r}-\omega t)} + \mathbf{E}^B e^{i(\mathbf{k}^B.\mathbf{r}-\omega t)} \tag{8.1a}$$

$$\mathbf{E}(x,z)|_{z>0} = \mathbf{E}^C e^{i(\mathbf{k}^C.\mathbf{r}-\omega t)} + \mathbf{E}^D e^{i(\mathbf{k}^D.\mathbf{r}-\omega t)} \tag{8.1b}$$

where $\mathbf{k}^A$ is the wavenumber for the incident plane wave described by $\mathbf{E}^A$ and $\mathbf{H}^A$, and so on for B, C, and D. By assuming phase matching across the interface, taking

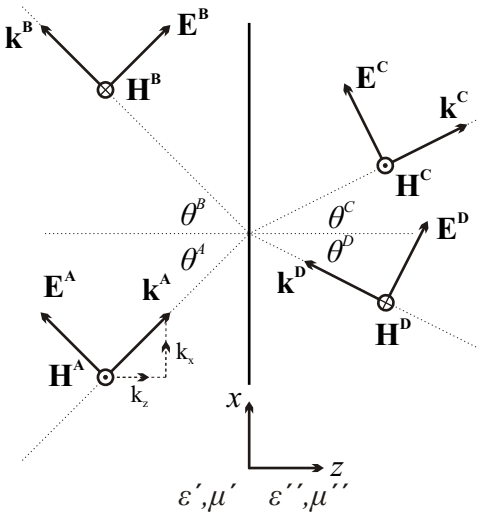

Fig. 8.9: Domain setup for two impinging and two reflecting plane waves from a flat interface.

a steady-state field, and by setting

$$k^A = k^B = k^{'} \tag{8.2a}$$

$$k^C = k^D = k^{''}. \tag{8.2b}$$

we can arrive at a description for the electric and magnetic fields in the x-direction and y-direction, respectively, on both sides of the interface:

$$E_x(x,z)|_{z<0} = |\mathbf{E}^A|\cos(\theta^A)e^{i(k_x^A x + k_z^A z)} + |\mathbf{E}^B|\cos(\theta^B)e^{i(k_x^B x - k_z^B z)} \tag{8.3a}$$

$$E_x(x,z)|_{z>0} = |\mathbf{E}^C|\cos(\theta^C)e^{i(k_x^C x + k_z^C z)} + |\mathbf{E}^D|\cos(\theta^D)e^{i(k_x^D x - k_z^D z)} \tag{8.3b}$$

and

$$H_y(x,z)|_{z<0} = |\mathbf{H}^A|e^{i(k_x^{'} x + k_z^{'} z)} - |\mathbf{H}^B|e^{i(k_x^{'} x - k_z^{'} z)} \tag{8.4a}$$

$$H_y(x,z)|_{z>0} = |\mathbf{H}^C|e^{i(k_x^{''} x + k_z^{''} z)} - |\mathbf{H}^D|e^{i(k_x^{''} x - k_z^{''} z)}. \tag{8.4b}$$

At $z = 0$ the fields must be continuous, and we can arbitrarily take the point $x = 0$ to get

$$E_x^A + E_x^B = E_x^C + E_x^D \tag{8.5}$$

and

$$H_y^A - H_y^B = H_y^C - H_y^D \tag{8.6}$$

which use $E_x^A = |\mathbf{E}^A|\cos(\theta^A)$ and $H_y^A = |\mathbf{H}^A|$ etc. By relating each H_y to its E_x

component through

$$H_y = \frac{E_x \omega \epsilon}{k_z} \tag{8.7}$$

we can solve for E_x^C and E_x^D and place the equations in matrix form to describe the modification of the wave coefficients by through the interface:

$$\begin{bmatrix} E_x^C \\ E_x^D \end{bmatrix} = \frac{1}{2}\frac{k_z''}{\epsilon''} \begin{bmatrix} \frac{\epsilon'}{k_z'} + \frac{\epsilon''}{k_z''} & \frac{\epsilon''}{k_z''} - \frac{\epsilon'}{k_z'} \\ \frac{\epsilon''}{k_z''} - \frac{\epsilon'}{k_z'} & \frac{\epsilon''}{k_z''} + \frac{\epsilon'}{k_z'} \end{bmatrix} \begin{bmatrix} E_x^A \\ E_x^B \end{bmatrix} = T(0) \begin{bmatrix} E_x^A \\ E_x^B \end{bmatrix}. \tag{8.8}$$

The transmission and reflection coefficients of this interface can now be determined.

If we set the incident wave travelling in the positive z-direction to unity and suppose that there is no incident wave on the other side of the interface, i.e. set $E_x^A = 1$ and $E_x^D = 0$, then $E_x^B = r$ and $E_x^C = t$, where r and t are the reflection and transmission coefficients, respectively. By substituing and solving in Equ. 8.8 the reflection and transmission coefficients for an interface at the origin become

$$r = \frac{\epsilon'' k_z' - \epsilon' k_z''}{\epsilon'' k_z' + \epsilon' k_z''} \tag{8.9a}$$

$$t = \frac{2\epsilon' k_z''}{\epsilon'' k_z' + \epsilon' k_z''}. \tag{8.9b}$$

To extend this formulation to describe an interface at an arbitrary position d on the z-axis we apply appropriate phase shifts to give

$$T(d) = \begin{bmatrix} e^{-ik_z'' d} & 0 \\ 0 & e^{ik_z'' d} \end{bmatrix} T^d(0) \begin{bmatrix} e^{ik_z' d} & 0 \\ 0 & e^{-ik_z' d} \end{bmatrix} \tag{8.10}$$

which calculates the coefficients in the $z = 0$ plane. By using appropriate phase shifts we can then determine the fields at any point on the z-axis, but care must be taken to ensure the correct wavenumber is used and that the fields of interest are valid at the point of interest. The solution for a TE polarised wave follows trivially by substituting

$$\frac{k}{\epsilon} = \frac{\mu}{k} \tag{8.11}$$

8.3.2 Slab Example

By referring all T-matrices back to the one co-ordinate system we can combine multiple matrices for different interfaces together to get an overall T-matrix for the system. Figure 8.10 shows the domain setup for a $d'' - d'$ thick slab started at $z = d'$.

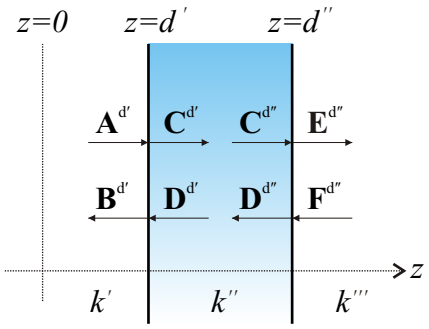

Fig. 8.10: Schematic setup for a material slab positioned between $z = d^{'}$ and $z = d^{''}$.

This setup gives us T-matrics for the two interfaces as

$$T(d^{'}) = \begin{bmatrix} e^{-ik_z^{''}d} & 0 \\ 0 & e^{ik_z^{''}d} \end{bmatrix} \frac{1}{2}\frac{k_z^{''}}{\epsilon^{''}} \begin{bmatrix} \frac{\epsilon^{'}}{k_z^{'}} + \frac{\epsilon^{''}}{k_z^{''}} & \frac{\epsilon^{''}}{k_z^{''}} - \frac{\epsilon^{'}}{k_z^{'}} \\ \frac{\epsilon^{''}}{k_z^{''}} - \frac{\epsilon^{'}}{k_z^{'}} & \frac{\epsilon^{''}}{k_z^{''}} + \frac{\epsilon^{'}}{k_z^{'}} \end{bmatrix} \begin{bmatrix} e^{ik_z^{'}d} & 0 \\ 0 & e^{-ik_z^{'}d} \end{bmatrix} \tag{8.12}$$

and

$$T(d^{''}) = \begin{bmatrix} e^{-ik_z^{'''}d} & 0 \\ 0 & e^{ik_z^{'''}d} \end{bmatrix} \frac{1}{2}\frac{k_z^{'''}}{\epsilon^{'''}} \begin{bmatrix} \frac{\epsilon^{''}}{k_z^{''}} + \frac{\epsilon^{'''}}{k_z^{'''}} & \frac{\epsilon^{'''}}{k_z^{'''}} - \frac{\epsilon^{''}}{k_z^{''}} \\ \frac{\epsilon^{'''}}{k_z^{'''}} - \frac{\epsilon^{''}}{k_z^{''}} & \frac{\epsilon^{'''}}{k_z^{'''}} + \frac{\epsilon^{''}}{k_z^{''}} \end{bmatrix} \begin{bmatrix} e^{ik_z^{''}d} & 0 \\ 0 & e^{-ik_z^{''}d} \end{bmatrix}. \tag{8.13}$$

The amplitudes of the coefficients at the origin are given as

$$\begin{bmatrix} E_x^C \\ E_x^D \end{bmatrix} = T(d^{'}) \begin{bmatrix} E_x^A \\ E_x^B \end{bmatrix}. \tag{8.14}$$

and

$$\begin{bmatrix} E_x^E \\ E_x^F \end{bmatrix} = T(d^{''}) \begin{bmatrix} E_x^C \\ E_x^D \end{bmatrix}. \tag{8.15}$$

These two equations can then be combined to give the overall transmission matrix:

$$\begin{bmatrix} E_x^E \\ E_x^F \end{bmatrix} = T(d^{''})T(d^{'}) \begin{bmatrix} E_x^A \\ E_x^B \end{bmatrix} = \mathbf{T} \begin{bmatrix} E_x^A \\ E_x^B \end{bmatrix}. \tag{8.16}$$

The transmission coefficient is defined as $t = E_x^E$, however, E_x^E is only valid past $z = d^{''}$, thus it is more correct to say

$$t = E_x^E e^{ik_z^{''}z}|_{z>d''} \tag{8.17}$$

noting that E_x^E must be translated using the k'' wavenumber.

8.3.3 Transmission of a Spatial Period

The previous sections have given us the tools to calculate the amplitude and phase change of a plane wave impinging on a system of flat slabs. The interest for this work lies in the calculation of transmission for a certain spatial period or wavenumber generated from a mask grating. Figure 8.11 schematically details the setup required for analytically predicting the performance of a PLL setup.

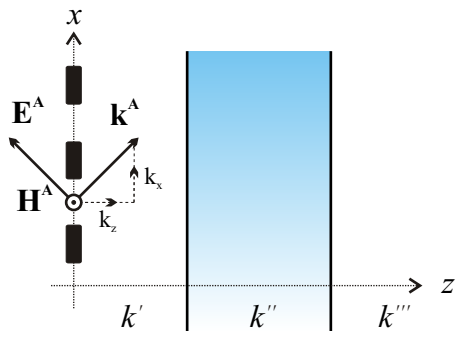

Fig. 8.11: Schematic of the setup for a grating located parallel to a slab. This is similar to the PLL setup.

The total **k** of the wave can be written in terms of it components as

$$\mathbf{k} = \sqrt{k_x^2 + k_y^2 + k_z^2}. \tag{8.18}$$

In this TM case $k_y = 0$, thus given the definition of the wavenumber as

$$\mathbf{k} = \frac{\omega}{\upsilon} \tag{8.19}$$

where

$$\upsilon = \frac{1}{\sqrt{\mu_r \mu_0 \epsilon_r \epsilon_0}} = \frac{c}{\sqrt{\mu_r \epsilon_r}} \tag{8.20}$$

we can substitute Equ. 8.18 into the square of Equ. 8.19 to give

$$k_z = \sqrt{\mu_r \epsilon_r \frac{\omega^2}{c^2} - k_x^2} \tag{8.21}$$

If a certain k_x is produced as a result of scattering from a grating, Equ 8.21 gives the k_z required for the formulation of the corresponding T-matrices for each slab of material that follows.

To reconstruct the electric field we must form the original equation $\mathbf{E}(x, z) =$

$\mathbf{E}e^{i(\mathbf{k}^C.\mathbf{r}-\omega t)}$. To find $|\mathbf{E}|$ we have the equation

$$|\mathbf{E}|^2 = |E_x|^2 + |E_z|^2 \tag{8.22}$$

and from previous trigonometric relationships we have

$$E_z = E_x \frac{\cos^2\theta}{\sin^2\theta} \tag{8.23}$$

and

$$\frac{\cos^2\theta}{\sin^2\theta} = \frac{k_z}{k_x} \tag{8.24}$$

which gives

$$|\mathbf{E}|^2 = |E_x|^2 \left(1 + \frac{k_z^2}{k_x^2}\right). \tag{8.25}$$

If $|\mathbf{E}| = 1$, then

$$E_x = \frac{1}{\sqrt{\left(1 + \frac{k_z^2}{k_x^2}\right)}}. \tag{8.26}$$

After transmission through a stack we multiply by the coefficient to give tE_x as the intensity of the new field. Substituting Equ. 8.26 into Equ. 8.25 gives

$$|\mathbf{E}|^2 = |t|^2. \tag{8.27}$$

Given this result it is sufficient to simply set $E_x = 1$ and take the final result as $\mathbf{E}$. The transmission properties of the phase also follow the same logic.

For transmission of periodic features we can simply take a Fourier decomposition of all the k_x present in a feature trace, which includes the interesting factor of phase in the calculation. Each k_x and complex coefficient can then be transferred through the system and reconstructed with modified amplitude and phase to give the field at some point past the system. It should be noted that negative k_x values must also be incorporated into the calculation for periodic features, as for every k_z there are two valid k_x values that are generated from the square-root. By investigating the amplitude and phase we can investigate a system's ability to reconstruct a grating profile. Producing this reconstruction quickly is useful and allows easy classification of a stacks performance, however, FDTD (or a similar full-vector simulation) is still required for ultimate accuracy as the analytical solution does not account for interaction between the silver layer and the mask.

8.3.4 Validation

There are a number of other formulations present in literature that allow us to validate this derivation. Pendry [18], Smith *et al.* [164], and Fang *et al.* [163] have all produced 1D transmission functions for a slab of thickness d.

Figure 8.12 presents a comparison with two of the models (Pendry's and Smiths) using the parameters presented in Fang's paper [163]. The parameters are for a $\lambda/10$ thick slab, using $\mu = 1$ and $\epsilon = -1.05 + 0.001i$, suspended in vacuum. The source and imaging planes are placed at spacing of $d/2$ on either side of the slab. Note that for Pendry's solution the phase propagation through the vacuum must be added and that Simth's derivation contains an error in the redefining of k_z for phase advancement. All models match perfectly, and do so for any slab.

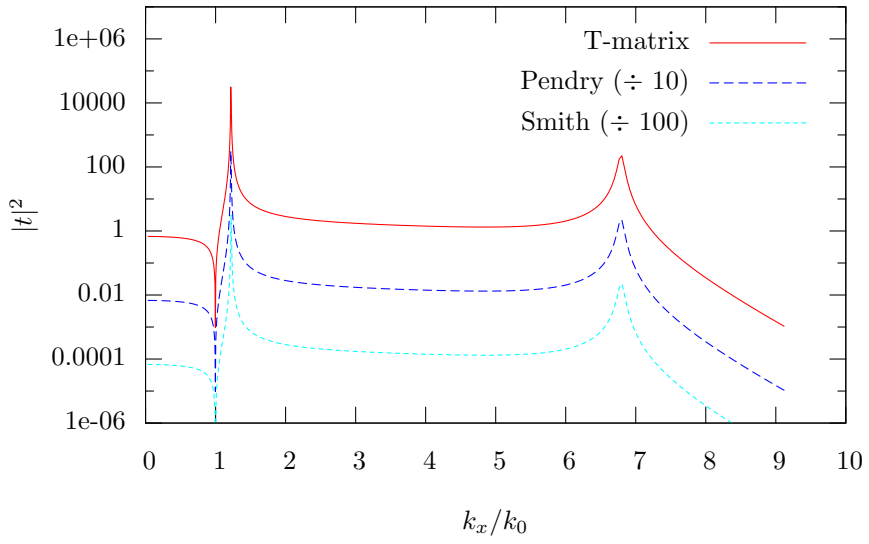

Fig. 8.12: A comparison of transmission coefficients of a $\lambda/10$ thick plasmonic slab ($\mu = 1$ and $\epsilon = -1.05 + 0.001i$) for three models: T-matrix, Pendry's, and Smith's. The values have been scaled to aid the visual comparision.

Although there are a number of implementations of analytical solutions, the T-matrix method derived here is considered more powerful than the aforementioned formulations due to its ability to quickly model arbitrary stack geometries. The following section looks at the transmission properties of various stacks, as well as the ability of these stacks to reform images.

8.4 ANALYTICAL TRANSMISSION INVESTIGATION

Many groups have focused on the ability of a VM or superlens slab to transfer spatial frequencies while the media properties or thicknesses are varied [18, 163, 164, 171, 192]. Others have attempted to optimise the geometry, or location, of the slab [198]. The main focus of this section is to investigate the optimisation of a practical multi-layered

silver superlens stack. Previous work has shown performance increases due to multi-layered configurations [26,168], and by varying the geometry of a these systems, insight into the optimisation of PLL stacks is gained.

8.4.1 Equi-thickness Multi-layer Lenses

Figure 8.13 shows spatial transmission coefficients for stacks with a variable number of layers, for five TM illumination schemes and one TE scheme. All stacks have a total of 40 nm of silver and 40 nm of PMMA, with dielectric constants of $\epsilon_{Ag} = -2.7+0.23i$ and $\epsilon_{PMMA} = -2.3013 + 0.0014i$, respectively[3]. For each stack 40 nm of silver is divided evenly into the number of layers required, for example, in the case of the 10-nm four-layer stack there is a four consecutive 5|10|5 - PMMA|Ag|PMMA stacks. Proximity and TE cases are provided for comparison and show the expected fast drop off for sub-diffraction-limited features, which begin when the k_z turns imaginary in the PMMA.

Figure 8.13(a) shows a marked increase in the transmission of higher order wavenumbers as the number of silver layers increases, the principal conclusion of Ref. [26]. The layer variation causes a shift in the intensity and position of the system's resonant peak. The peak shifts from an intensity of 18.6 at 170-nm pitch for the 40 nm single-layer to 119 at a 180-nm pitch for the 10 nm four-layer lens. The multi-layered lenses also demonstrate a flatter dispersion at higher wavenumbers enabling better reconstruction of arbitrary sub-diffraction-limited features.

In Fig. 8.13(b) the thickness of the final dielectric layer is modified to a fixed value of 10 nm. This approach is employed to 'level the playing field'. In PLL, or for any near-field lithography, it is important to have the best field possible (in terms of contrast and depth of the field) exposing the resist. For a PLL mask a final spacer is required only to protect the silver from oxidation and sulphidation, therefore, maintaining the Veselago ratio is not as important as the quality of the image. Thus, if we state that a final spacer layer needs only be 10-nm thick, then we can ask the question of which system can provide the best image at this location. With this criterion, the thicker silver layers give more amplification over a certain range, but the thinner layers still provide flatter dispersion over a larger bandwidth of wavenumbers.

It is interesting to also compare the coefficients with that of a 10nm proximity exposure, or ENFOL. Here, the amplifying properties of the silver is clear with an order-of-magnitude more intensity for the superlenses at high wavenumbers.

[3]Values are taken for a exposing wavelength of 365 nm [11].

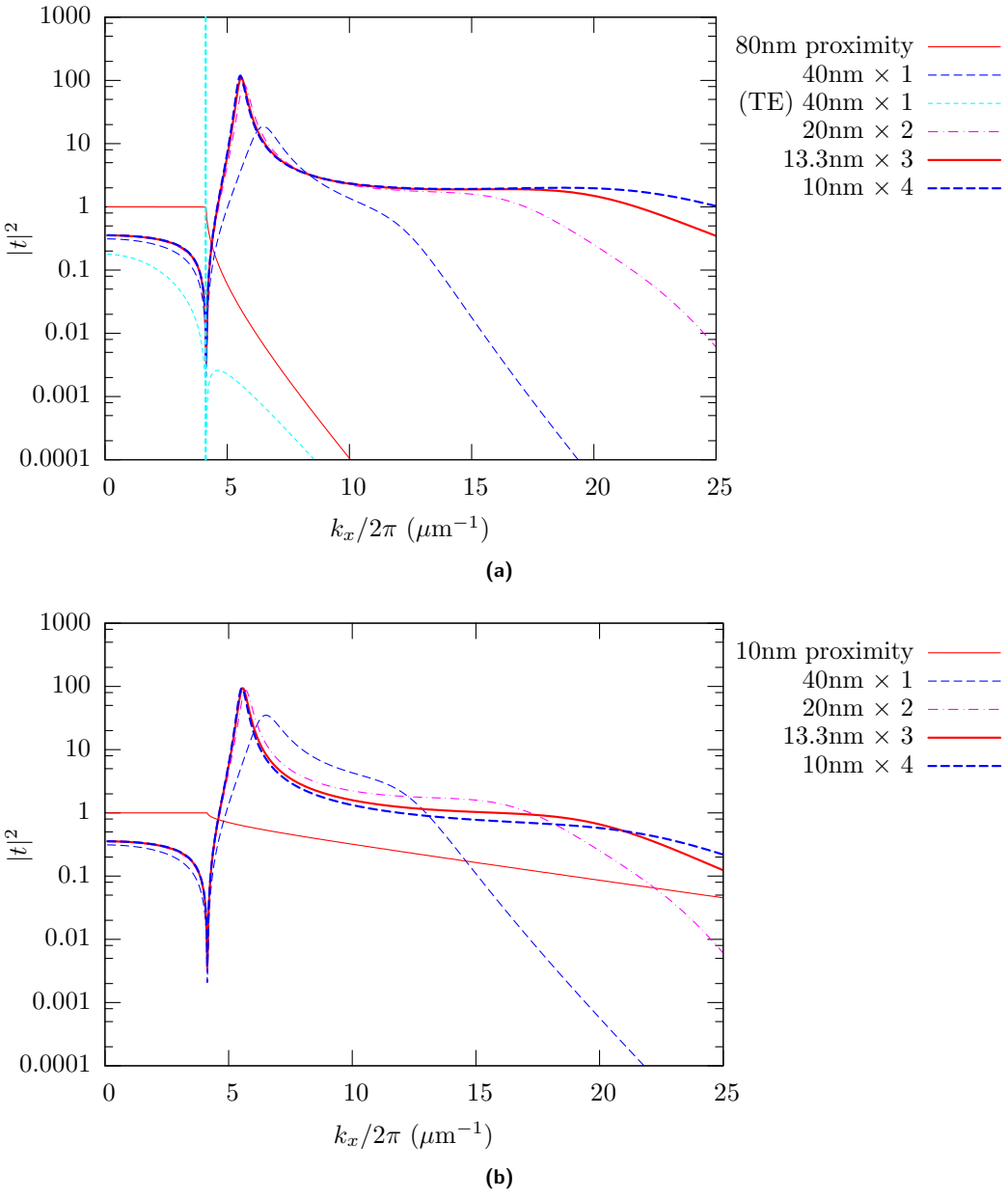

Fig. 8.13: Transmission co-efficients for lensing systems with 1, 2, 3, and 4 layers of silver. For each stack 40 nm of silver is divided evenly into the number of layers required. An 80 nm proximity result is shown for comparison. (a) presents the result for a Veselago-ratio final spacer thickness, and (b) is for a 10-nm final spacer. The diffraction limit is marked by the vertical dashed line in (a). At this point the fields turn evanescent in the PMMA dielectric.

8.4.2 Graduated-thickness Multi-layer lenses

Figure 8.14 investigates a systems with graduated lens thicknesses. The purpose for investigating different graduation schemes is to attempt to find a lensing stack that can produce the best projected image at a distance away from the final silver layer. We have seen that multiple layers can transmit higher wavenumbers with higher intensity but the question is: can we do better by making certain layers thicker than others?

In Fig. 8.14 a scheme is used where the total silver and dielectric thicknesses remain at 40 nm, but each consecutive silver layer is 3 times thicker than the previous. We will call this a multiple-3-graduated lensing system. Table 8.2 gives the details of the layer thicknesses for the first 3 multi-layer stacks in this scheme. Figure 8.14(a) is for a final separation distance consistent with the Veselago ratio for the final silver layer thickness, while Fig. 8.14(b) is for a final separation of 10 nm.

Table 8.2: Layer thicknesses of multiple-3-graduated lensing systems for 2, 3, and 4 layers of silver. The total silver thickness of each stack adds to 40nm. The silver layers are in bold text.

Multiple-3 stacks	dimensions (nm)								
graduated × 2	5	**10**	20	**30**	15				
graduated × 3	1.5	**3.1**	6.2	**9.2**	16.9	**27.7**	13.8		
graduated × 4	0.5	**1**	2	**3**	5.5	**9**	18	**27**	13.5

By comparing the result for the 4-layer stacks ('graduated × 4' and 'equal 10nm × 4'), we can see that the graduation tends to reduce the bandwidth of the system, but provides stronger amplification at particular frequencies. Bearing this in mind, if patterning of a particular period was required for large area sub-diffraction-limited gratings, a PLL stack could be optimised to maximise transmission of the period of interest. This concept was employed during imaging of 120-nm pitch features by Fang *et al.* [31].

From here we will concentrate on stack optimisation for a final spacer thickness of 10 nm. The chosen value follows from experimental results that produced good quality 10-nm thick SiO_2 films. A thinner layer would affect the integrity of the film, and exponential decay inside the lossy layer means that an increased thickness would reduce the near-field intensity. The next section attempts to find the best transmission possible through a stack configuration with a final spacer layer thickness of 10 nm.

8.4.3 Optimisation for 10-nm Thick Final Spacer

This section explores a number of parameters to find the best configuration to image sub-diffraction-limited features with the constraint of a 10-nm thick final spacer. Often, the transmission co-efficient's dispersion is not flat, so two other transmission curve

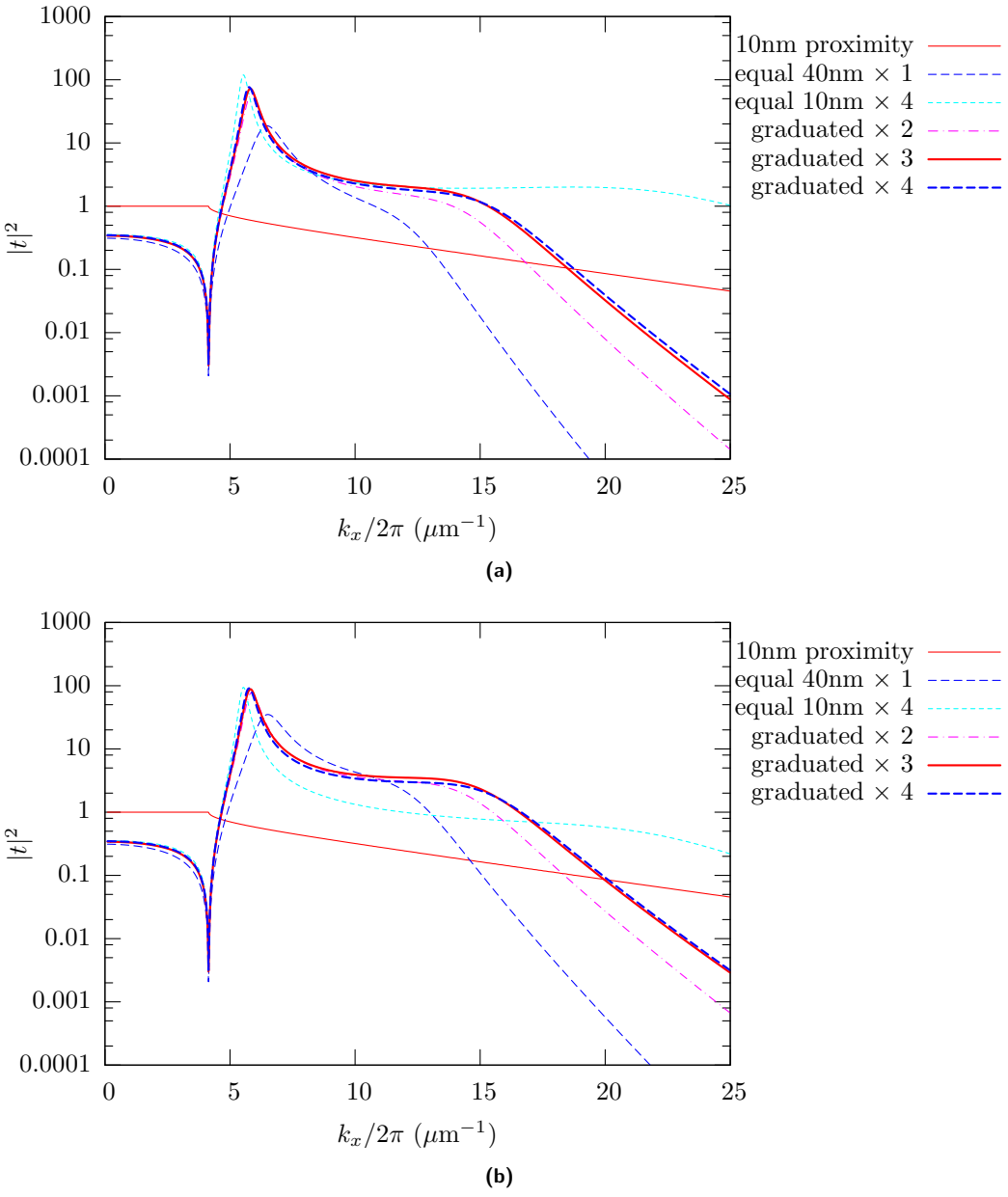

Fig. 8.14: Transmission co-efficients for multiple-3-graduated lensing systems with 2, 3, and 4 layers of silver. Equi-thickness 40nm-single and 10nm-quad lenses, as well as a 10 nm proximity result are shown for comparison. (a) presents the result for a Veselago ratio final spacer thickness, and (b) is for a 10-nm final spacer.

factors are focused on for optimisation, namely; maximum transmission for a 100-nm pitch feature, and above-unity bandwidth.

Transmission coefficient intensity versus total silver thicknesses for single- and double-layer lenses are shown in Fig. 8.15(a) and Fig. 8.16(a) respectively. The ability of the different stacks to transmit the 100-nm pitch feature ($k_x/(2\pi 10^{-6}) = 10$) and above-unity bandwidth is shown in Fig. 8.15(b) and Fig. 8.16(b). The 100-nm pitch intensity is maximised at 40 nm silver thickness for the single lens and at a total thickness of 62 nm (31nm $\times$ 2) for the double-layer stack. The experimental results achieved with 50-nm single-layer and a 30-nm double-layer PLL lensing stacks represent close to the best achievable results for these geometries according to this analysis. Thinning the single-layer lens represents an opportunity to achieve better resolution. The above-unity bandwidth is maximised at around half the peak 100-nm pitch transmission thicknesses in both cases, 18 nm for the single and 32 nm for the double.

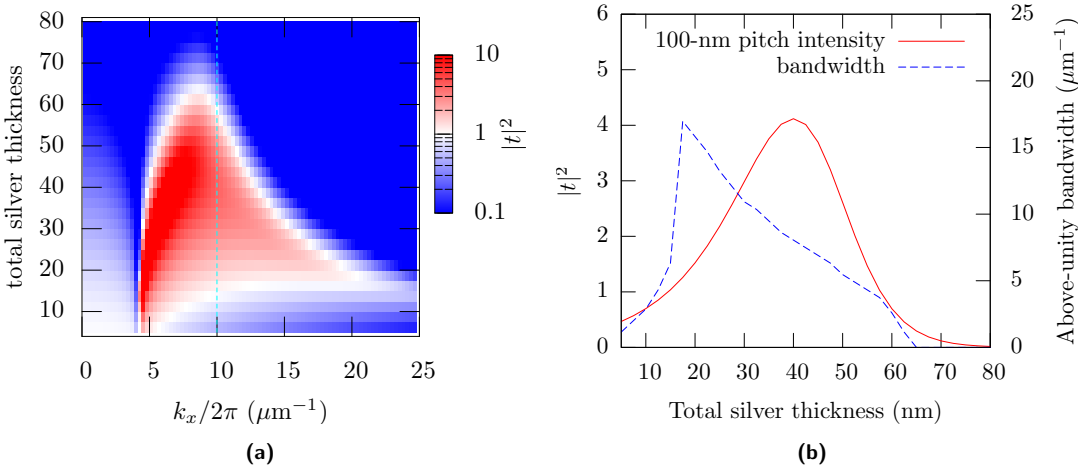

Fig. 8.15: (a) Transmission coefficients for a single-layer lens of varying thicknesses. The first spacer layer is set at the Veselago ratio, while the final spacer is set at 10 nm. (b) shows the transmission intensities for the 100-nm period wavenumber (as marked by the dashed line in (a)) and the above-unity bandwidth variation with respect to the silver thickness.

The multiple-3-graduated system, investigated in the previous section, is just one of a huge range of variations that can be used in a PLL system. The first extension of this model is to investigate a multiple-n-graduated system. In this scheme a multi-layer stack is created where each consecutive layer thickness is n times the previous thickness.

Figure 8.17 shows a 2D plot of transmission for n versus wavenumber. For this simulation a total lens thickness of 62 nm is taken as it corresponds to the maximum transmission of the 100-nm period in Fig. 8.16(b). When n is below 1 this means that the silver layers are getting thinner at that ratio, and above 1 the layers are graduated to become larger.

This result shows that the standard equi-thickness multi-lens is not the most op-

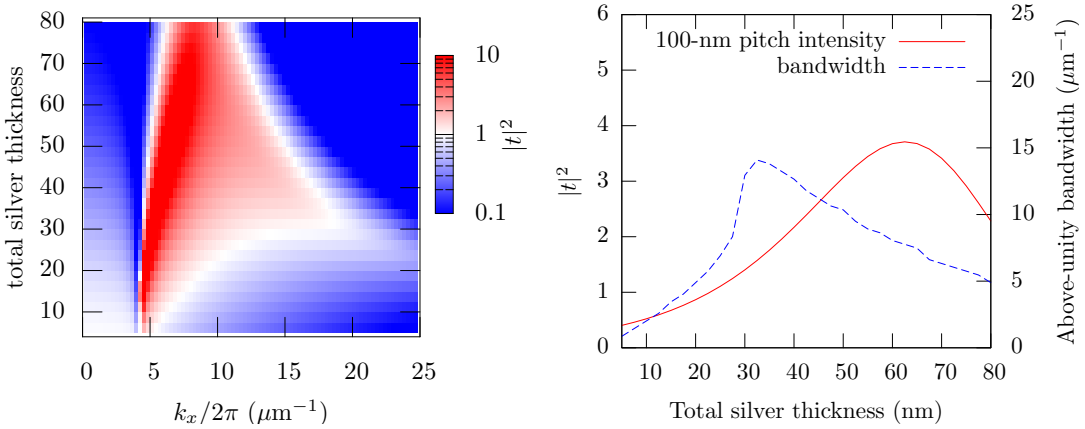

Fig. 8.16: (a) Transmission coefficients for a double-layer lens versus total silver thicknesses. The silver layers have a equal thickness and the final spacer is set at 10 nm. (b) shows the transmission intensities for the 100-nm period wavenumber and the above-unity bandwidth variation with respect to the silver thickness.

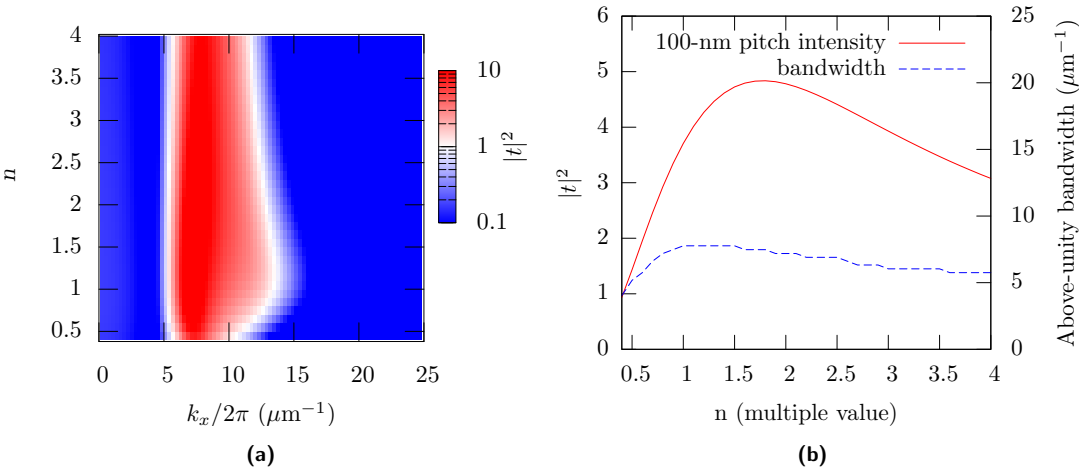

Fig. 8.17: (a) A comparison of transmission coefficients for a range of multiple-*n*-graduated double-layer systems. The total silver thickness for each lens is 62 nm and the final spacer is always set at 10 nm. (b) shows the transmission intensities for the 100-nm period wavenumber and the above-unity bandwidth variation with respect to *n*.

timised geometry for both the 100-nm period and bandwidth factors. At an n=1.8 provides the best transmission for the 100-nm pitch, and the best bandwidth is found at n=1.3 (however, the thickness of silver is not optimised for bandwidth). This results in optimal transmission of the 100-nm period by double-layer stack of 11.1|**22.1**|31|**39.9**|10.

A final type of layer variation investigated was an additive-a-graduated scheme. This scheme calculates a fixed value based on the thickness of the first layer that is then added to each consecutive layer and gives the following calculation for layer thickness

$$D_i = D_1 + (i-1)D_1 a \quad ; \qquad i \geq 1 \tag{8.28}$$

where D_i is the thickness of layer i, D_1 is the thickness of the first layer, and a is the additive ratio to which gives the fixed value to be added. Table 8.3 gives two examples for different a ratios on triple-layer stacks (any less than three layers covers results presented previously).

Table 8.3: Layer thicknesses of two additive-a-graduated lensing systems. There are 3 silver layers for each stack with a total silver thickness of 45 nm. The silver layers are in bold text.

a	added value	dimensions (nm)
0.5	5	5 | **10** | 12.5 | **15** | 17.5 | **20** | 10
2	10	2.5 | **5** | 10 | **15** | 20 | **25** | 12.5

To compare the graduation methods a triple-layer stack is used. Figure 8.18(a) gives the transmission coefficients for equi-thick triple-layer stacks of varying total silver thickness (i.e. no graduation). The maximum amplification for the 100-nm pitch feature now occurs at a total thickness of 80 nm, and the best bandwidth is for a thickness of 42 nm. This is an increase in thickness for both performance indicators from the single- and double-layer result.

We will now attempt to maximise the transmission of a 100-nm pitch feature through a triple-layer stack using an 80-nm total silver thickness (maximum from Fig. 8.18(b)) by calculated coefficients through the two graduation schemes. Figure 8.19 shows the transmission coefficients for both multiple-n- (Fig. 8.19(a)) and additive-a-graduated systems (Fig. 8.19(b)) for triple-layer stacks of total thickness 80-nm. The performance criteria traces for the 100-nm pitch features and the above-unity bandwidth are in Fig. 8.19(c) and (d) for the multiple and additive graduation systems respectively.

There is a subtle variation in performance for both graduation schemes. For the multiple-n-graduated stack the highest amplification of a 100-nm pitch feature occurs at $n = 1.5$, which relates to a 8.4|**16.8**|21|**25.3**|31.6|**37.9**|10 stack. For the additive-a-graduated system it occurs at $a = 0.65$ that relates to a 8.1|**16.2**|21.4|**26.7**|31.9|**37.8**|10 stack. In Fig. 8.20 the optimised triple-layer transmission plots are compared.

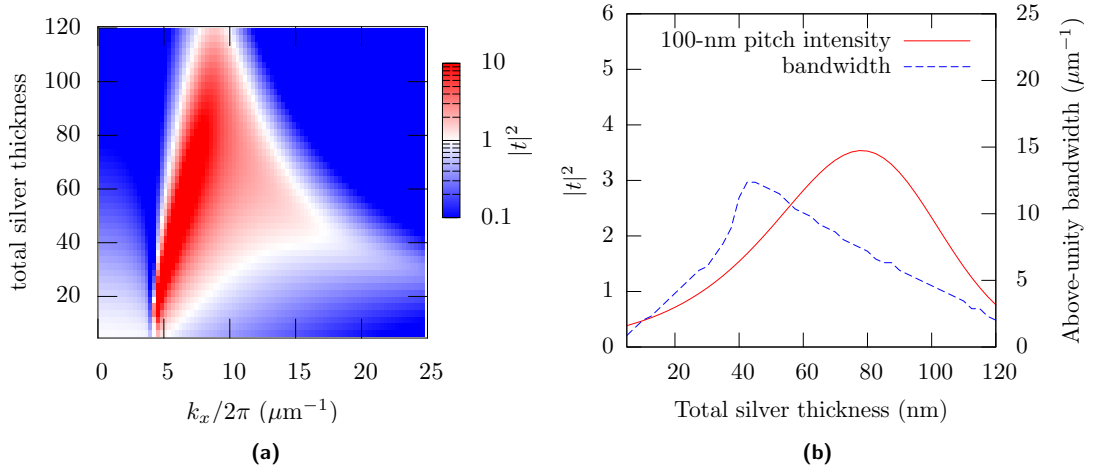

Fig. 8.18: (a) Transmission coefficients for a triple-layer lens versus total thicknesses of silver. The silver layers have a equal thickness and the final spacer is set at 10 nm. (b) shows the transmission intensities for the 100-nm period wavenumber and the above-unity bandwidth variation with respect to the silver thickness.

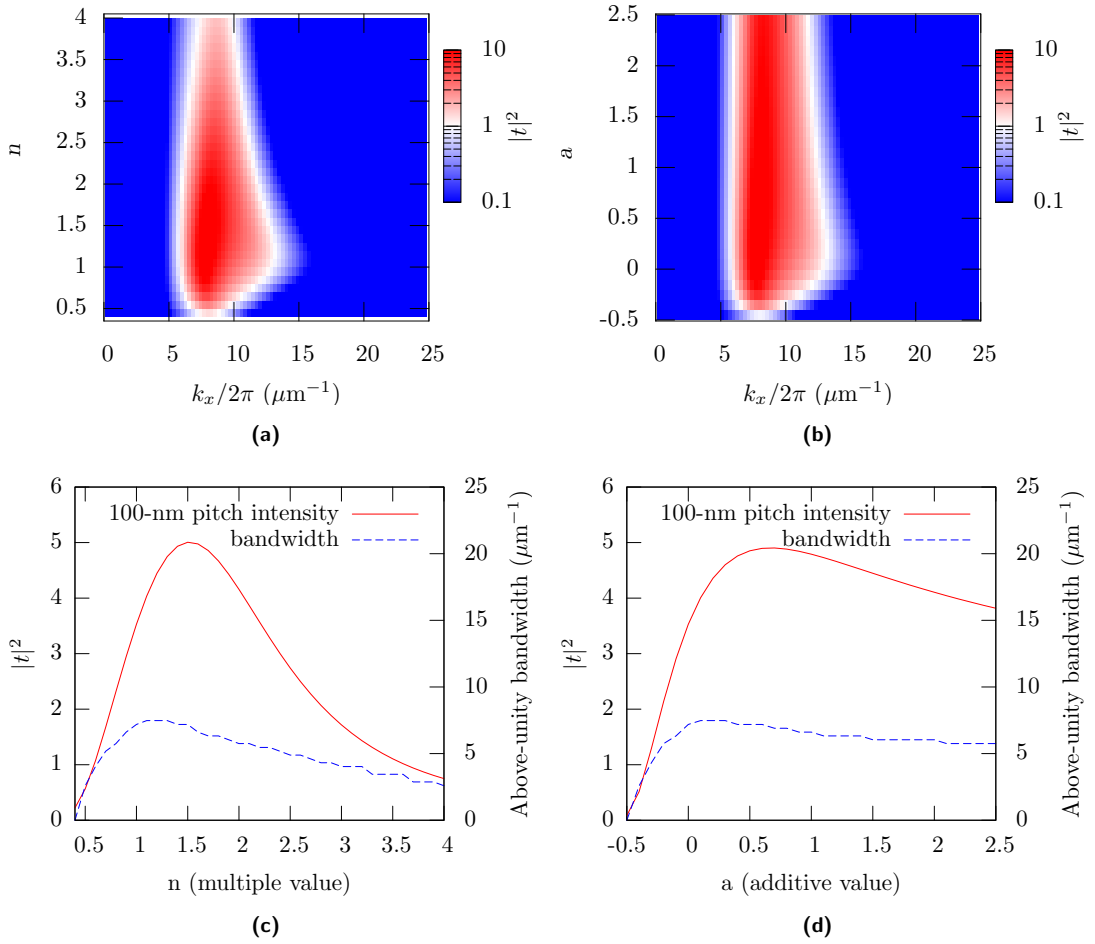

Fig. 8.19: Triple-layer lens transmission coefficients and performance criteria traces for a multiple-*n*- ((a) and (c)) and a additive-*a*- graduation ((b) and (d)). The final spacer is set at 10 nm for all calculations.

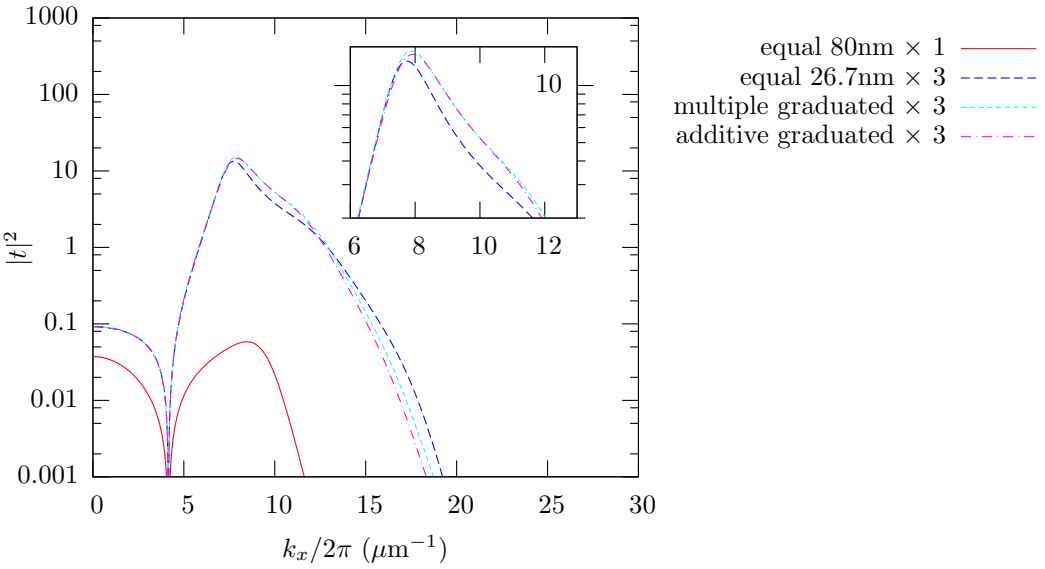

Fig. 8.20: A comparison of transmission coefficients for equi-thick, multiple, and additive silver layer variation on a triple-layer lens stack. The total silver thickness is set at 80 nm. A first spacer layer is set at the Veselago ratio and the final spacer is set at 10 nm.

Due to the closeness of the two graduated system configurations, the similar performance is not a surprise. It is, however, interesting that the equi-thickness triple-layer stack tracks the graduated systems relatively closely. In the end, there is very little difference in performance after the system is optimised in these ways. However, the limited performance variation for a multi-layer graduated lenses indicates that these systems could prove to be robust to relatively large thickness variations.

The greatest performance jump for transmission of sub-diffraction-limited features that can be achieved with Veselago ratio multi-layer lenses and a fixed final spacer layer is by increasing the number of layers.

8.4.4 Phase and Contrast

In a lithography system we are not just interested in maximising transmission, but also image formation. It is the image formation that was the main focus of the FDTD simulations presented earlier (section 8.1). If one can achieve a better image at the cost of reduced transmission it is likely to be a good option, for in a lithography system the final intensity can be increased by simply increasing the illumination intensity. There are two factors when reconstructing an image – amplitude and phase. In this section thus far only amplitude has been investigated. Here, other important factor of phase is studied.

To achieve high contrast in an imaging process we must not only transfer the intensity of the spectral components but also the relative phase. To achieve this a flat phase transfer-function is required. Figure 8.21 is a plot of transmitted phase

for the optimised triple-layer stacks (intensity transmission coefficients were shown in Fig. 8.20).

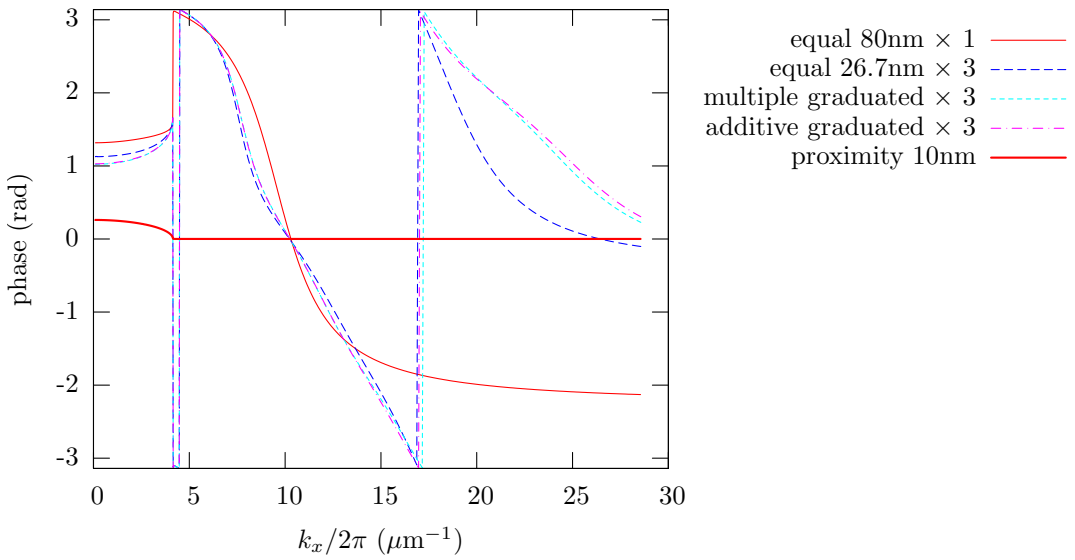

Fig. 8.21: A comparison of transmission phase for equi-thick, multiple, and additive silver layer variation on a triple-layer lens stack. The total silver thickness is set at 80 nm and the final spacer is set at 10 nm. A 10-nm proximity exposure is shown for comparision.

In the sub-diffraction-limited regime ($k_x > 4.12$), the 10-nm proximity stack gives the expected flat phase as the k_z is purely complex leading to only amplitude modulation. However, the phase for the silver stacks is greatly distorted. All the superlens schemes have a range from π to $-\pi$ as the spatial period varies from 240 nm to 60 nm. This phase modulation will cause distortion when forming arbitrary sub-diffraction-limited features.

To study the effect of the phase and amplitude transmission in tandem we will look at the contrast of a reconstructed image from an non-interacting grating (this is unrealistic so results should be interpreted accordingly). The T-matrix derivation limits us to calculations that don't take into account the interaction with the mask. The spatial spectrum components of the grating can be generated by taking calculating the DFT. The DFT generates the relative phase and amplitudes of each wavenumber, which can then be modified by the transmission properties of a stack before an inverse DFT can reconstruct the image at the required location. Figure 8.22 shows the reconstruction of a 100-nm pitch grating for the optimised triple-layer stacks. The raised-cosine grating profile and 10-nm proximity image are plotted for comparison.

The 100-nm period lies at close to zero phase for each of the stacks, thus we should expect good images. The 10-nm proximity case shows excellent contrast, as expected, while the 80-nm thick single layer produces a slightly inverted profile. For the optimised layers the 100-nm pitch features have been transferred too well. As can been seen from the transmission coefficients (Fig. 8.20) the 100-nm wavenumber amplitude exceeds the

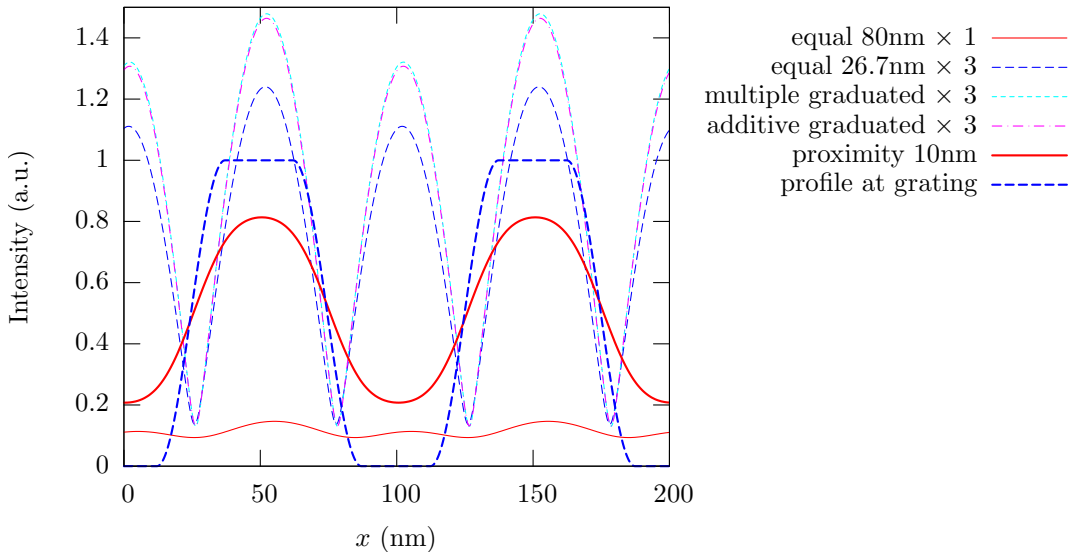

Fig. 8.22: Reconstructed of single-period field profiles for a 100-nm pitch non-reflecting grating feature transfer through a number of different stacks. A 10-nm proximity exposure is shown for comparison.

DC amplitude. Hence, rather than a 100-nm modulation on top of a DC value which gives 100-nm period features, there is rectification of the dominant 100-nm waveform giving 50-nm pitch features, or period halving. This demonstrates the importance of the relationship between the amplitude of DC term and each wavenumber when forming an image. To gain the best imaged formation, a flat dispersion curve with good DC trasnmission is required.

Next, the imaging of 200-nm pitch features through the stacks was studied. For this period there are phase shifts for many of the wavenumbers present in the grating profile. The combination of phase shifts and poor amplitude transmission results in the silver superlens stacks showing very poor imaging. This is consistent with the FDTD simulations where the 200-nm pitch produced poor contrast and FOM for most grating stacks. It is clear that the relationship between phase and amplitude is an important and complicated issue for a superlens, and that optimisation for maximum transmission of intensity does not necessarily provide you with a good imaging system.

Finally, a comparison with the FDTD simulation results was performed to access the impact that the neglect of gratings/lens interaction has on the validity of the analytical calculation. Figure 8.24 shows how the phase performs for different numbers of silver layers when the total thickness remain constant at 40-nm. The improvement over the previous triple-layer lenses is due to the thinning of the lens which reduces the phase shift. For sub-100-nm pitch features the phase flattens for multi-layered lenses. For a single-layer, the phase is highly distorted producing an linear sweep through the sub-diffraction-limited features.

Figure 8.25 is the T-matrix equivalent of the graph produced from FDTD simulation data that is shown in Fig. 8.7(a). Figure 8.25 shows the contrast values ex-

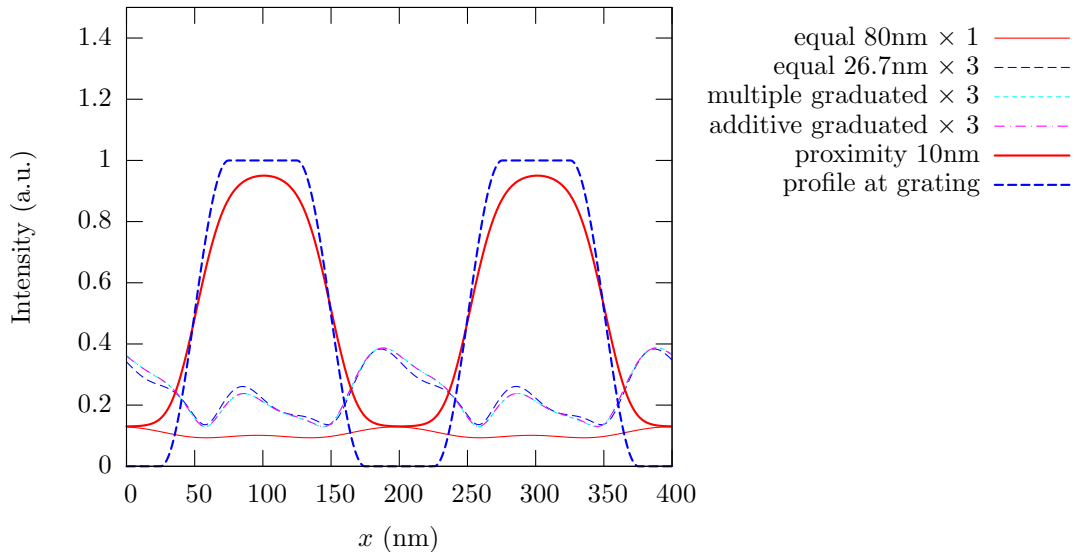

Fig. 8.23: Reconstructed of single-period field profiles for a 200-nm pitch non-reflecting grating feature transfer through a number of different stacks. A 10-nm proximity exposure is shown for comparison.

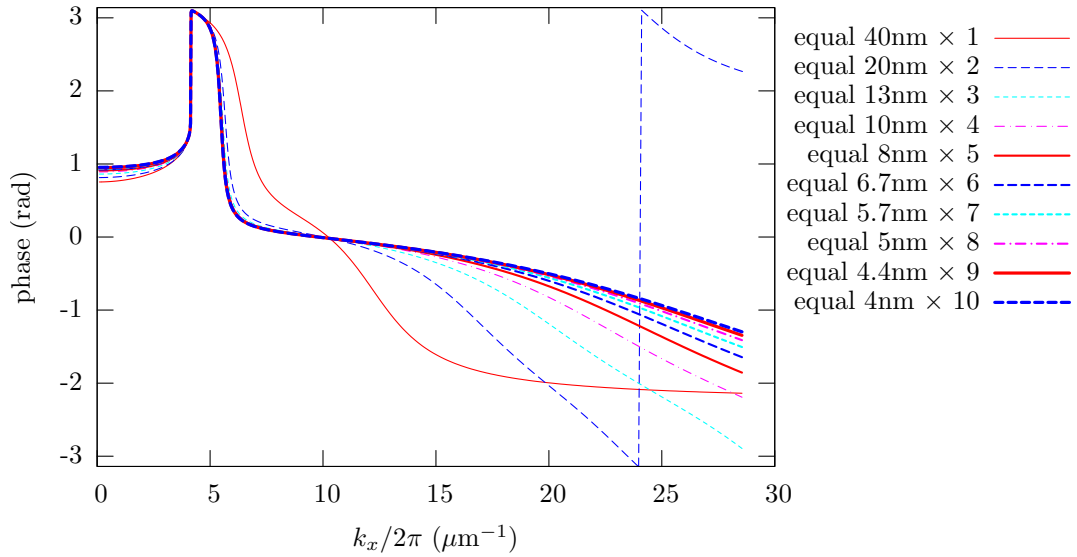

Fig. 8.24: A comparison of transmission phase for equi-thick stacks with different numbers of silver layers. The total silver thickness is set at 40 nm and the final spacer is set at 10 nm.

tracted from reconstructed images of grating profiles (like those shown in Fig. 8.22). Differences between the T-matrix and FDTD data sets are many, but the principal conclusions remain true: the thinner the layers in a multi-layer lens the better contrast is for sub-100-nm features; and, for the lenses with the total thickness of 40 nm the quad-layer beats the triple, which beats the double and all beat the single. The differences between the T-matrix and FDTD methods are mainly due to the inability of the T-matrix technique to simulate mask interaction.

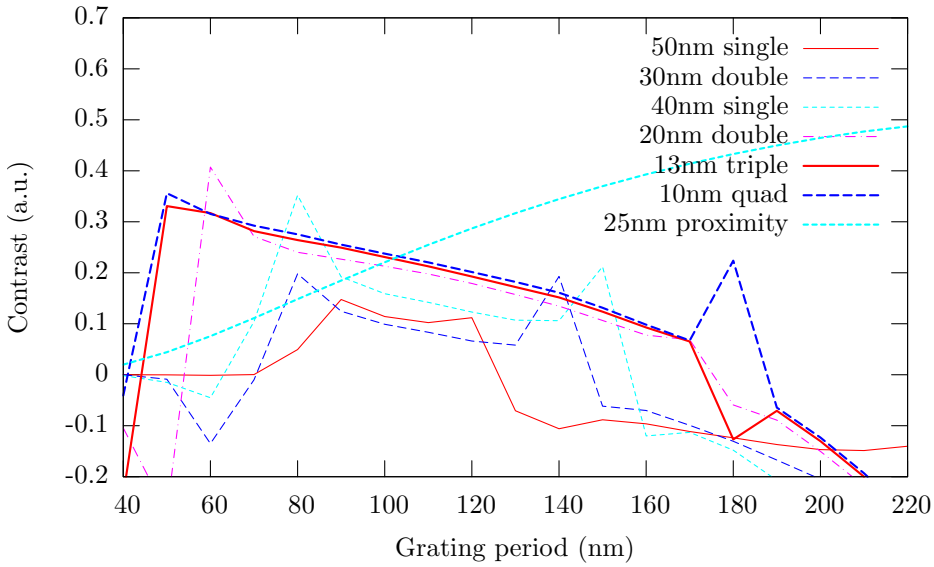

Fig. 8.25: T-matrix calculations for reconstructed images to produce contrast versus grating period data for a number of different silver lenses. All final spacers are set at 10nm.

Investigation of transmission through a superlens by T-matrix calculation has enabled us to see the importance of maintaining both phase and amplitude in the formation of an image. This concept was not covered in previous studies of perfect- and superlenses [18, 26, 163, 164, 171]. For sub-100-nm resolution multi-layer silver lenses out perform single-layer lenses of the same total thickness by providing flatter dispersion curves for both phase and amplitude. In another investigation of multi-layered perfect lenses it was written *"two lenses are better than one but many lenses are best of all."* [26].

8.5 SUMMARY

In this chapter, an in-depth investigation into the performance of the PLL process has been carried out with the use of FDTD numerical simulations and T-matrix analytical modeling. FDTD simulations have been run for different PLL stacks over a range of periods to look at image formation in a resist layer, and analytical modeling has explored the transmission capabilities for different superlens configurations.

A main focus of the simulation work was to investigate multi-layer lenses, as theory promised better performance [26]. It is concluded that multiple layer stacks are indeed a performance enhancement for sub-diffraction-limited imaging. Performance gains were achieved by altering the geometry of the silver layers in multi-layer stacks, however, this performance was only marginally better than a equi-thickness multiple silver-layer.

Optimisations for triple-layer configurations which attempted to find the highest transmission of a sub-diffraction-limited 100-nm pitch feature, but resulted in a poor performing mask. The first reason for this was the discrimination of the DC component. Because the optimised thickness was for an 80 nm total silver layer thickness the transmission of the DC component is orders of magnitude below the 100-nm period component. This causes period halving to occur in the image. The second reason is because of the phase distortion. A 200-nm pitch feature through the optimised stacks failed to produced any clear images. When designing a lensing system phase and relative amplitude transmission must be taken into account.

Chapter 9

CONCLUSIONS AND FUTURE WORK

"Try as I might, I cannot believe I have finished."

- David Melville

In this thesis a novel near-field optical lithographic technique named Planar Lensing Lithography (PLL) was studied. Using this technique the first experimental evidence at optical wavelengths of the Pendry superlens was produced. Pendry surmised that a slab of negative index material could act as a perfect lens, projecting images with resolution detail beyond the limits of conventional lensing systems [18]. A thin silver superlens was his realistic suggestion for a practical near-field perfect lens. This silver superlens concept was employed by the author to image sub-diffraction-limited features using PLL. Amidst a number of other highly publicised experiments relating to the perfect lens and negative refraction, the silver superlens proof was a timely achievement as there was intense academic debate surrounding both theory and experimental proof of these concepts.

The superlens concept was proven by fabricating conformable lithography masks with additional spacer and silver layers to produce an optical lensing system for the near-field. The performance of PLL, intimate contact lithography, and proximity lithography systems was explored for sub-micron, sub-wavelength, and sub-diffraction-limited features under broad- and narrowband UV light illumination.

Simulation and analytical techniques were used to investigate and understand the enhancements and limitations of the PLL technique. A Finite-Difference Time-Domain (FDTD) tool was written to produce full-vector numerical simulations and this provided both broad- and narrowband results, allowing image quality as a function of grating period to be investigated. An analytical T-matrix method was also derived to facilitate computationally-efficient performance analyses for grating transmission through PLL stacks.

The silver superlens utilises plasmonic enhancement, which is an encouraging technique employed in a growing number of research fields. Increased control over excitation, localisation, and amplification of the surface plasmons utilised by PLL will provide

better resolution for applications of lithography and imaging. For the remainder of this final chapter the experimental and simulation results of this thesis are summarised and the author's beliefs about the future of the field presented.

9.1 EXPERIMENTAL

The seminal achievement of this thesis was the attainment of sub-diffraction-limited imaging through a near-field silver superlens. This was achieved after the development of a near-field lithography process which required: membrane photomask fabrication, silver and spacer layer deposition, mask adaption (to allow use in a mask-aligner), and a near-field photoresist expose and develop scheme.

The PLL mask fabrication process research led on from recent Evanescent Near-Field Optical Lithography (ENFOL) research that produced sub-100-nm features using silicon-nitride membrane masks. For PLL, the technique was redesigned to use more robust glass-coverslip masks that allowed flexible integration into research-grade mask-aligner systems. Patterning of tungsten metal absorbers on the glass coverslips was done with Electron Beam Lithography (EBL) in conjunction with a Reactive Ion Etch (RIE) dry etch process to produce sub-100-nm features.

The choice to use tungsten as the metal absorber was driven by the availability of dry etching gases (SF_6) and to avoid lift-off procedures that introduce 'tags' which cause unwanted spacers. However, tungsten's properties at UV wavelengths make it a highly absorbing dielectric rather than a characteristic metal. This leads to increased electric field penetration in the mask and, hence, lower electric field contrast at the mask exit plane. Previous near-field lithography techniques have used nickel-chromium (NiCr) as the absorber, which provides better contrast. For future work the development of a NiCr conformable mask (as in Goodberlet *et al.*'s work [17]) could allow increased performance.

The glass-coverslip conformable mask was first tested as a simple near-field mask, and the demonstration of sub-diffraction-limited 170-nm pitch features in a thin layer of photoresist meant the process had the capability to allow testing for super-resolution through a silver layer.

For PLL, additional spacer and silver layers were added above the membrane mask. A large amount of experimental effort went into making the surfaces of the subsequent layers as planar and as smooth as possible. Planarisation of the tungsten mask by the first spacer layer was of particular importance. A thick layer of PMMA was spun on to the mask, reflowed, and then etched back in a process that was developed to gain a sufficiently flat first spacer with a controllable thickness. After development, the final silver and SiO_2 layers were deposited using thermal evaporation processes. Again, these processes were optimised to produce smooth surfaces.

Initially, sub-micron features were patterned using a broadband Mercury light source and a PLL mask consisting of a 120-nm thick silver lens surrounded by two 60-nm PMMA spacers [23]. Features down to a half-pitch of 350 nm were patterned, but the thickness of the silver limited higher resolution. Advancements to the planarisation process, allowing thinner spacer layers and hence thinner silver layers[1], facilitated the fabrication of 85-nm [152] and 60-nm lenses that produced sub-wavelength 175-nm half-pitch features.

Sub-diffraction-limited features were achieved after further refinement produced a 50-nm thick silver layer, which was part of a 25|50|10 - PMMA|Ag|SiO_2 PLL stack. This system imaged 145-nm pitch, or 77-nm half-pitch, features into a 100-nm thick photoresist on a Bottom Anti-Reflection Coating (BARC). This was to be the best sub-diffraction-limited resolution achieved during experimental testing and the performance is on a par with other near-field lithography techniques [15].

The quality of the features patterned through the 50-nm thick silver lens was improved through the use of optical filters that enabled 365-nm wavelength narrowband exposures to be carried out. The removal of off-resonant wavelengths resulted in higher contrast and lower edge roughness for sub-diffraction-limited results. Isolated line pairs and features were also imaged with the 50-nm lens. Line pairs were imaged with separation distances below both the Rayleigh and Sparrow resolution limits for a lensing system.

A promising extension to the PLL technique is multi-layered PLL, which was experimentally proven by the author. It was proposed that a multi-layered superlens could achieve better resolution than a single layer lens for the same total silver thickness [26]. A PLL mask was created with two 30-nm thick silver layers in a 15|30|30|30|10 - PMMA|Ag|SiO_2|Ag|SiO_2 multiple silver layer mask. A 170-nm pitch sub-diffraction-limited grating was imaged through the double-layer mask, while for a single layer mask with the same total thickness (60 nm) resolution was limited to a 350-nm pitch. The proposed resolution enhancement was verified. However, pattern fidelity was reduced, which was the result of additional spacer roughness.

The future offers many possibilities for improvement to the experimental PLL process. For the mask, improving planarisation and contrast by using embedded amplitude NiCr masks [17] would eliminate the need for the time-consuming first-layer planarisation step. Additionally, processing conformable masks made from coverslips is difficult because of their fragility and their tendency to conform to a wafer spinner's vacuum, leading to non-uniform spun-on layers. Coverslips that are temporarily attached to a more rigid substrate during fabrication could provide a solution to these two issues. A brief investigation into larger diameter coverslips – of up to 50-mm across – found them to have improved conformability, which would also be advantageous.

[1] Enforced by the need to maintain the Veselago ratio of 1:2:1 - spacer:silver:spacer thickness.

Due to time constraints, mask distortion as a result of feature movement during the exposure process was not looked at during this thesis. It is, however, a peripheral concern for conformable mask overlay if distortions across the patterning field are a high proportion of the minimum feature size. Work on conformable masks has shown distortion to be less than 60-nm on average across a 15mm patterned area [66]. This may or may not be acceptable for mask overlay patterning and this is something that warrants future study.

Unfortunately, the reliability of the process is not presently up to a standard that allows repeatable sub-diffraction-limited results. One of the major limitations is the presence of dust. Random dust particles of any size attached to either the mask or substrate will affect the near-field pattern transfer. For research labs the absolute removal of dust is a very difficult task and as such the future of near-field lithography techniques may be limited.

9.2 SIMULATION

PLL's performance has been modelled with both numerical full-vector simulations and an analytical technique. Many groups have studied the perfect and super lenses through basic analytical techniques, but these are limited by the absence of source/system interaction modelling. It is very important when simulating a near-field lithography that the interaction between the source (or the mask) and the system be taken into account. To do this a full-vector simulation program was written based on the FDTD algorithm.

The FDTD simulations have shown that there is a performance advantage for PLL over conventional near-field optical lithography. This advantage comes in the form of greater intensity and penetration depth of the electric field. However, the performance enhances are for features below the diffraction limit, and the enhancement varies greatly with period. The increased depth of field allows for thicker resists to be used experimentally, facilitating increased etch-mask heights.

For PLL, the highest obtainable resolution is achieved by being directly on the lens, but for many sub-diffraction-limited features the point of greatest contrast actually occurs and a separation from the mask. It is this ability to separate the lens from the resist imaging layer that could allow physical separation in a lithography process. This would eliminate mask contamination without compromising image quality. Unfortunately, the separation distances calculated are less than 30 nm, placing very tight criteria on mask-resist alignment control.

Although most analytical tools do not simulate mask interaction, the speed of these techniques makes them useful for quick estimation of a system's performance. An analytical T-matrix method was derived to produce rapid transmission calculations for electric field profiles through arbitrary multi-lens stacks. The technique was used to

optimise the transmission of 100-nm features through multi-layered stacks with different silver-layer graduation schemes. It was concluded that an equi-thickness multi-layer lens was very close to the best possible configuration.

For the graduation schemes the Veselago ratio (1:2:1) was maintained for each silver layer. More work could be done to investigate the performance of when all layer thicknesses are varied independently.

Multi-layered silver lens investigations were a central focus for both the numerical and analytical techniques. From the FDTD simulations the contrast performance for multi-layer lenses was found to be improved over single layers of the same total silver thickness. Contrast, which was calculated with the analytical method, confirmed this and demonstrated that flatter phase and intensity dispersion curves below the diffraction limit were necessary to gain good contrast in the near-field. Simulations predict a resolution enhancement of two-times when comparing a quadruple 10-nm lens and a 40-nm single-layered lens.

There is a huge parameter space to investigate when performing numerical simulations on the PLL technique. Parameters investigated include: silver and spacer layer thickness, spacer layer material, pitch, and exposure wavelength. Others that could be investigated include: mask material, mask thickness, mask duty cycle, illumination angle, lens material (e.g. Gold or Aluminum), and line pairs.

The FDTD simulation tool was also developed for 3D modelling, but due to computational restrictions few of these simulations were run. The analysis of isolated features, such as the imaging of dots, would be a worthwhile study. Preliminary simulation results gathered were promising and sub-wavelength dot structures have been imaged experimentally. Roughness was a limiting factor for resolution through multi-layered lenses and could also be studied through simulation.

Simulation tools played an important role in predicting and supporting experimental results. Future optimisation of the PLL system will benefit from rigorous simulation studies.

9.3 THOUGHTS ON THE FUTURE

Multi-layer PLL is the most encouraging way forward for this process. Initial experimental work on multi-layers has shown performance similar to that of near-field optical lithography and it is clear from simulation work these systems could perform well, providing flatter dispersion and less phase disturbance over a larger bandwidth of sub-diffraction-limited features. The conclusion from simulations is that the thinner and more numerous the layers the better the system performs. However, depositing layers by evaporation or sputtering processes that are thinner than 30-nm and sufficiently smooth is difficult. In the future, more refined deposition techniques could be developed

to grow smooth layers tens of atoms thick to provide high quality multi-layer systems. Molecular beam epitaxy (MBE) is one candidate for high quality film growth. Another prospect is self-assembly of layers though surface fuctionalisation. Self-assembled resonant structures at the nano-scale could also provide a path to negative-index metamaterials operating at visible wavelengths.

The performance of near-field lithography as feature pitches vary is inconsistent, especially for pitches on the order of the wavelength of the exposing light. Once the pitch of the features being imaged is in a certain range above or below the diffraction limit the performance is more consistent. Work could be performed at longer wavelengths, for example infra-red, to place a broader range of accessible pitches below the diffraction limit. Work has already been done using Silicon Carbide to produce super-resolution in the infra-red [106]. Optical lithography at these wavelengths is difficult due to a lack of potential photosensitive resists. However, optical image applications at infra-red wavelengths could provide imaging capabilities for 500-nm pitch features and below.

It is the author's believe that four other plasmon resonance techniques could be combined with PLL and optimised to increase the near-field imaging performance. The first two techniques help by increasing the effectiveness of surface-plasmon coupling through the mask. This is done by placing a thin layer of silver above the mask and has been reported as an enhancement for near-field lithography in Ref. [159]. This scheme uses off-axis illumination to couple into surface plasmon modes. By then combining this with another coupling technique, the requirement for off-axis illumination can be removed. The coupling principle could simply be surface roughness [139,142] or a more elaborate optimised coupling structure [206]. In this manner, rather than the mask converting the propagating fields into the surface plasmons, which leads to a blurring of the features, it is done previously by the layer of silver, and the near-field coupled through this layer is subsequently masked by the metal absorbers.

The third incorporated technique is called Surface Plasmon Enhanced Contact Lithography (SPECL) [200–202]. In the PLL work, reflections from the substrate have been minimised by using a BARC. However, it has been shown that the depth of the electric field in the resist can be increased by going against traditional logic and using a highly reflective substrate. The resonant nature of silver could allow it to be used as a layer in a photoresist scheme that would interact with the PLL mask silver layers to provided the enhancements indicated by SPECL. This would have the added advantage of reducing exposure times. The focus of the author's research was to investigate the quality of the photoresist pattern transfer step, hence no multi-layered resist schemes were investigated. Additional study into multi-layer resist schemes that incorporated silver layers would be beneficial to expand on this current research.

The final potential modification to PLL would be mask pattern optimisation. Sim-

ulation results of the PLL technique demonstrate that certain periods are transferred with better contrast than others. Optical Proximity Correction (OPC) is a common method in industry for optimising pattern transfer quality, and similar methodology could be applied here. An understanding through simulation of what mask features are required to make certain patterns in the resist would be an interesting study. This technique could solve the intensity discrepancy between above- and sub-wavelength features through mask feature and coupling control, making near-field lithography useful over a broader feature range.

Combining the four above mentioned techniques into a modified near-field process, called Optimised Plasmonic Resonance Lithography (OPRL), could provide increased field penetration and better performance.

The future of optical lithography, and semiconductor manufacturing in general, is unclear. For many years, D-day for projection lithography has been looming, but when will its luck run out? And what process will perform well enough to replace it? Could near-field lithography a real contender? A shift in consumer demand could see high-resolution lithography processes take second stage to other concerns such as hardware flexibility, weight, and heat generation. Whatever happens, as was the case for this thesis, a lot of time, money, and effort will be spent on the theory, simulation, and development of next generation lithographies.

Appendix A

FULL DISPERSIVE FDTD EQUATIONS

This appendix contains the equations for the FDTD algorithm. The full equation for the curl is given in appendix section A.5.

A.1 ELECTRIC FIELD EQUATION

$$\begin{aligned}\mathbf{E}|_{i,j,k}^{n+1} &= \mathbf{C_{EH_1}}|_{i,j,k}^{n} \cdot \left(\nabla \times \mathbf{H}|_{i,j,k}^{n+\frac{1}{2}}\right) \\ &+\mathbf{C_{EE_2}}|_{i,j,k}^{n} \cdot \mathbf{E}|_{i,j,k}^{n} + \mathbf{C_{EE_3}}|_{i,j,k}^{n} \cdot \mathbf{E}|_{i,j,k}^{n-1} \\ &+\mathbf{C_{EJ_2}}|_{i,j,k}^{n} \cdot \mathbf{J}|_{i,j,k}^{n} + \mathbf{C_{EJ_3}}|_{i,j,k}^{n} \cdot \mathbf{J}|_{i,j,k}^{n-1} \end{aligned} \tag{A.1}$$

where

$$\begin{aligned}\mathbf{C_{EH_1}}|_{i,j,k}^{n} &= \frac{1}{\frac{\epsilon_0 \mathbf{\Gamma}_e|_{i,j,k}^{n}}{2\cdot(\Delta t)^2\cdot \mathbf{C_E}|_{i,j,k}^{n}} + \frac{\epsilon_0 \mathbf{\Delta}_e|_{i,j,k}^{n}}{2\cdot\Delta t\cdot 2\cdot \mathbf{C_E}} + \frac{\epsilon_0 \boldsymbol{\epsilon}_1|_{i,j,k}^{n}}{\Delta t}} \\ \mathbf{C_{EE_2}}|_{i,j,k}^{n} &= \mathbf{C_{EH_1}}|_{i,j,k}^{n} \cdot \left(\frac{2\epsilon_0 \mathbf{\Gamma}_e|_{i,j,k}^{n}}{(\Delta t)^2 \cdot 2 \cdot \mathbf{C_E}|_{i,j,k}^{n}} + \frac{\epsilon_0 \boldsymbol{\epsilon}_1|_{i,j,k}^{n}}{\Delta t}\right) \\ \mathbf{C_{EE_3}}|_{i,j,k}^{n} &= \mathbf{C_{EH_1}}|_{i,j,k}^{n} \cdot \left(-\frac{\epsilon_0 \mathbf{\Gamma}_e|_{i,j,k}^{n}}{(\Delta t)^2 \cdot 2 \cdot \mathbf{C_E}|_{i,j,k}^{n}} + \frac{\epsilon_0 \mathbf{\Delta}_e|_{i,j,k}^{n}}{2 \cdot \Delta t \cdot 2 \cdot \mathbf{C_E}|_{i,j,k}^{n}}\right) \\ \mathbf{C_{EJ_2}}|_{i,j,k}^{n} &= \mathbf{C_{EH_1}}|_{i,j,k}^{n} \cdot \left(\frac{2\mathbf{A}_e|_{i,j,k}^{n}}{(\Delta t)^2 \cdot 2 \cdot \mathbf{C_E}|_{i,j,k}^{n}} + \frac{\mathbf{C}_e|_{i,j,k}^{n}}{2 \cdot \mathbf{C_E}|_{i,j,k}^{n}} - \frac{1}{2}\right) \\ \mathbf{C_{EJ_3}}|_{i,j,k}^{n} &= \mathbf{C_{EH_1}}|_{i,j,k}^{n} \cdot \left(-\frac{\mathbf{A}_e|_{i,j,k}^{n}}{(\Delta t)^2 \cdot 2 \cdot \mathbf{C_E}|_{i,j,k}^{n}} - \frac{\mathbf{B}_e|_{i,j,k}^{n}}{2 \cdot \Delta t \cdot 2 \cdot \mathbf{C_E}|_{i,j,k}^{n}}\right)\end{aligned}$$

and

$$\mathbf{C_E}|_{i,j,k}^{n} = -\frac{\mathbf{A}_e|_{i,j,k}^{n}}{(\Delta t)^2} + \frac{\mathbf{B}_e}{2\Delta t}$$

A.2 ELECTRIC POLARISATION CURRENT EQUATION

$$\begin{aligned}\mathbf{J}|_{i,j,k}^{n+1} &= \mathbf{C_{JE_1}}|_{i,j,k}^{n} \cdot \mathbf{E}|_{i,j,k}^{n+1} + \mathbf{C_{JE_2}}|_{i,j,k}^{n} \cdot \mathbf{E}|_{i,j,k}^{n} + \mathbf{C_{JE_3}}|_{i,j,k}^{n} \cdot \mathbf{E}|_{i,j,k}^{n-1} \\ &\quad + \mathbf{C_{JJ_2}}|_{i,j,k}^{n} \cdot \mathbf{J}|_{i,j,k}^{n} + \mathbf{C_{JJ_3}}|_{i,j,k}^{n} \cdot \mathbf{J}|_{i,j,k}^{n-1} \end{aligned} \tag{A.2}$$

where

$$\begin{aligned}\mathbf{C_{JE_1}}|_{i,j,k}^{n} &= \mathbf{C_J}|_{i,j,k}^{n} \cdot \left(\frac{\epsilon_0 \boldsymbol{\Gamma}_e|_{i,j,k}^{n}}{(\Delta t)^2} + \frac{\epsilon_0 \boldsymbol{\Delta}_e|_{i,j,k}^{n}}{2\Delta t} \right) \\ \mathbf{C_{JE_2}}|_{i,j,k}^{n} &= -\mathbf{C_J}|_{i,j,k}^{n} \cdot \left(\frac{2\epsilon_0 \boldsymbol{\Gamma}_e|_{i,j,k}^{n}}{(\Delta t)^2} \right) \\ \mathbf{C_{JE_3}}|_{i,j,k}^{n} &= \mathbf{C_J}|_{i,j,k}^{n} \cdot \left(\frac{\epsilon_0 \boldsymbol{\Gamma}_e|_{i,j,k}^{n}}{(\Delta t)^2} - \frac{\epsilon_0 \boldsymbol{\Delta}_e|_{i,j,k}^{n}}{2\Delta t} \right) \\ \mathbf{C_{JJ_2}}|_{i,j,k}^{n} &= -\mathbf{C_J}|_{i,j,k}^{n} \cdot \left(\frac{2\mathbf{A}_e|_{i,j,k}^{n}}{(\Delta t)^2} - \mathbf{C}_e|_{i,j,k}^{n} \right) \\ \mathbf{C_{JJ_3}}|_{i,j,k}^{n} &= \mathbf{C_J}|_{i,j,k}^{n} \cdot \left(\frac{\mathbf{A}_e|_{i,j,k}^{n}}{(\Delta t)^2} + \frac{\mathbf{B}_e|_{i,j,k}^{n}}{2\Delta t} \right) \end{aligned}$$

and

$$\mathbf{C_J} = -\frac{1}{\frac{\mathbf{A}_e|_{i,j,k}^{n}}{(\Delta t)^2} + \frac{\mathbf{B}_e|_{i,j,k}^{n}}{2\Delta t}}$$

A.3 MAGNETIC FIELD EQUATION

$$\begin{aligned}\mathbf{H}|_{i,j,k}^{n+1} &= \mathbf{C_{HE_1}}|_{i,j,k}^{n} \cdot \left(\nabla \times \mathbf{E}|_{i,j,k}^{n+\frac{1}{2}} \right) \\ &\quad + \mathbf{C_{HH_2}}|_{i,j,k}^{n} \cdot \mathbf{H}|_{i,j,k}^{n} + \mathbf{C_{HH_3}}|_{i,j,k}^{n} \cdot \mathbf{H}|_{i,j,k}^{n-1} \\ &\quad + \mathbf{C_{HK_2}}|_{i,j,k}^{n} \cdot \mathbf{K}|_{i,j,k}^{n} + \mathbf{C_{HK_3}}|_{i,j,k}^{n} \cdot \mathbf{K}|_{i,j,k}^{n-1} \end{aligned} \tag{A.3}$$

where

$$\begin{aligned}
\mathbf{C_{HE_1}}|^n_{i,j,k} &= \frac{1}{-\frac{\epsilon_0 \mathbf{\Gamma}_m|^n_{i,j,k}}{2\cdot(\Delta t)^2\cdot \mathbf{C_H}|^n_{i,j,k}} - \frac{\epsilon_0 \mathbf{\Delta}_m|^n_{i,j,k}}{2\cdot\Delta t\cdot 2\cdot \mathbf{C_H}} - \frac{\epsilon_0 \boldsymbol{\epsilon}_1|^n_{i,j,k}}{\Delta t}} \\
\mathbf{C_{HH_2}}|^n_{i,j,k} &= \mathbf{C_{HE_1}}|^n_{i,j,k} \cdot \left(-\frac{2\epsilon_0 \mathbf{\Gamma}_m|^n_{i,j,k}}{(\Delta t)^2 \cdot 2 \cdot \mathbf{C_H}|^n_{i,j,k}} - \frac{\epsilon_0 \boldsymbol{\epsilon}_1|^n_{i,j,k}}{\Delta t} \right) \\
\mathbf{C_{HH_3}}|^n_{i,j,k} &= \mathbf{C_{HE_1}}|^n_{i,j,k} \cdot \left(+\frac{\epsilon_0 \mathbf{\Gamma}_m|^n_{i,j,k}}{(\Delta t)^2 \cdot 2 \cdot \mathbf{C_H}|^n_{i,j,k}} - \frac{\epsilon_0 \mathbf{\Delta}_m|^n_{i,j,k}}{2 \cdot \Delta t \cdot 2 \cdot \mathbf{C_H}|^n_{i,j,k}} \right) \\
\mathbf{C_{HK_2}}|^n_{i,j,k} &= \mathbf{C_{HE_1}}|^n_{i,j,k} \cdot \left(-\frac{2\mathbf{A}_m|^n_{i,j,k}}{(\Delta t)^2 \cdot 2 \cdot \mathbf{C_H}|^n_{i,j,k}} - \frac{\mathbf{C}_m|^n_{i,j,k}}{2 \cdot \mathbf{C_H}|^n_{i,j,k}} + \frac{1}{2} \right) \\
\mathbf{C_{HK_3}}|^n_{i,j,k} &= \mathbf{C_{HE_1}}|^n_{i,j,k} \cdot \left(\frac{\mathbf{A}_m|^n_{i,j,k}}{(\Delta t)^2 \cdot 2 \cdot \mathbf{C_H}|^n_{i,j,k}} + \frac{\mathbf{B}_m|^n_{i,j,k}}{2 \cdot \Delta t \cdot 2 \cdot \mathbf{C_H}|^n_{i,j,k}} \right)
\end{aligned}$$

and

$$\mathbf{C_H}|^n_{i,j,k} = -\frac{\mathbf{A}_m|^n_{i,j,k}}{(\Delta t)^2} + \frac{\mathbf{B}_m}{2\Delta t}$$

A.4 MAGNETIC POLARISATION CURRENT EQUATION

$$\begin{aligned}
\mathbf{K}|^{n+1}_{i,j,k} &= \mathbf{C_{KH_1}}|^n_{i,j,k} \cdot \mathbf{H}|^{n+1}_{i,j,k} + \mathbf{C_{KH_2}}|^n_{i,j,k} \cdot \mathbf{H}|^n_{i,j,k} + \mathbf{C_{KH_3}}|^n_{i,j,k} \cdot \mathbf{H}|^{n-1}_{i,j,k} \\
&\quad + \mathbf{C_{KK_2}}|^n_{i,j,k} \cdot \mathbf{K}|^n_{i,j,k} + \mathbf{C_{KK_3}}|^n_{i,j,k} \cdot \mathbf{K}|^{n-1}_{i,j,k}
\end{aligned} \tag{A.4}$$

where

$$\begin{aligned}
\mathbf{C_{KH_1}}|^n_{i,j,k} &= \mathbf{C_K}|^n_{i,j,k} \cdot \left(\frac{\epsilon_0 \mathbf{\Gamma}_m|^n_{i,j,k}}{(\Delta t)^2} + \frac{\epsilon_0 \mathbf{\Delta}_m|^n_{i,j,k}}{2\Delta t} \right) \\
\mathbf{C_{KH_2}}|^n_{i,j,k} &= -\mathbf{C_K}|^n_{i,j,k} \cdot \left(\frac{2\epsilon_0 \mathbf{\Gamma}_m|^n_{i,j,k}}{(\Delta t)^2} \right) \\
\mathbf{C_{KH_3}}|^n_{i,j,k} &= \mathbf{C_K}|^n_{i,j,k} \cdot \left(\frac{\epsilon_0 \mathbf{\Gamma}_m|^n_{i,j,k}}{(\Delta t)^2} - \frac{\epsilon_0 \mathbf{\Delta}_e|^n_{i,j,k}}{2\Delta t} \right) \\
\mathbf{C_{KK_2}}|^n_{i,j,k} &= -\mathbf{C_K}|^n_{i,j,k} \cdot \left(\frac{2\mathbf{A}_m|^n_{i,j,k}}{(\Delta t)^2} - \mathbf{C}_m|^n_{i,j,k} \right) \\
\mathbf{C_{KK_3}}|^n_{i,j,k} &= \mathbf{C_K}|^n_{i,j,k} \cdot \left(\frac{\mathbf{A}_m|^n_{i,j,k}}{(\Delta t)^2} + \frac{\mathbf{B}_m|^n_{i,j,k}}{2\Delta t} \right)
\end{aligned}$$

and

$$\mathbf{C_K} = -\frac{1}{\frac{\mathbf{A}_m|^n_{i,j,k}}{(\Delta t)^2} + \frac{\mathbf{B}_m|^n_{i,j,k}}{2\Delta t}}$$

A.5 CURL EQUATION

If **A** and **B** are three dimensional vectors offset by half a FDTD cell, then the curl equation,

$$\mathbf{B} = \nabla \times \mathbf{A}$$

on an FDTD grid is given as

$$\begin{aligned}
B_x|_{i,j,k} &= \left(A_z|_{i,j+\frac{1}{2},k} - A_z|_{i,j-\frac{1}{2},k}\right)/\Delta y \\
&\quad - \left(A_y|_{i,j,k+\frac{1}{2}} - A_y|_{i,j,k-\frac{1}{2}}\right)/\Delta z \\
B_y|_{i,j,k} &= \left(A_x|_{i,j,k+\frac{1}{2}} - A_x|_{i,j,k-\frac{1}{2}}\right)/\Delta z \\
&\quad - \left(A_z|_{i+\frac{1}{2},j,k} - A_z|_{i-\frac{1}{2},j,k}\right)/\Delta x \\
B_z|_{i,j,k} &= \left(A_y|_{i+\frac{1}{2},j,k} - A_y|_{i-\frac{1}{2},j,k}\right)/\Delta x \\
&\quad - \left(A_x|_{i,j+\frac{1}{2},k} - A_x|_{i,j-\frac{1}{2},k}\right)/\Delta y
\end{aligned}$$

Appendix B

PERFECTLY MATCHED BOUNDARY DERIVATION

The Perfectly Matched Layer (PML) used in developed Finite-Difference Time-Domain (FDTD) code was implemented as set out in Ref. [182] on pages 286-292. Here, the derivation is reproduced (slightly modified) for completeness. The derivation is provided for the 2D Transverse Electric (TE) case, but can be simply transformed to the Transverse Magnetic (TM) case.

Consider a TE plane wave impinging on the planar interface $x = 0$ of the material half-space Region 2. (subscript 2 is describing Region 2 and subscript 1 is describes Region 1). An incident-wave magnetic field is given by $\breve{H}^{inc} = \hat{z}H_0 e^{-i\beta_{1_x}x - i\beta_{1_y}y}$, giving the total fields in Region 1 as

$$\begin{aligned} \breve{H}_1 &= -\hat{z}H_0\left(1+\Gamma e^{2i\beta_{1_x}x}\right)e^{-i\beta_{1_x}x-i\beta_{1_y}y} \\ \breve{E}_1 &= \left[-\hat{x}\frac{\beta_{1_y}}{\omega\epsilon_1}\left(1+\Gamma e^{2i\beta_{1_x}x}\right)+\hat{y}\frac{\beta_{1_x}}{\omega\epsilon_1}\left(1+\Gamma e^{2i\beta_{1_x}x}\right)\right]H_0 e^{-i\beta_{1_x}x-i\beta_{1_y}y} \end{aligned} \quad \text{(B.1)}$$

The fields transmitted into Region 2 are given by

$$\begin{aligned} \breve{H}_2 &= -\hat{z}H_0\tau e^{-i\beta_{2_x}x-i\beta_{2_y}y} \\ \breve{E}_2 &= \left[-\hat{x}\frac{\beta_{2_y}}{\omega\epsilon_2\left(1+\frac{\sigma}{i\omega\epsilon_2}\right)}+\hat{y}\frac{\beta_{2_x}}{\omega\epsilon_2\left(1+\frac{\sigma}{i\omega\epsilon_2}\right)}\right]H_0\tau e^{-i\beta_{2_x}x-i\beta_{2_y}y} \end{aligned} \quad \text{(B.2)}$$

Γ and τ are the H-field reflection and transmission coefficients, respectively, and

$$\left.\begin{aligned} \beta_{1_x} = k_1\cos\theta; \quad \beta_{1_y} = k_1\sin\theta \end{aligned}\right\} \quad x<0 \quad \text{(B.3a)}$$

$$\left.\begin{aligned} \beta_{2_x} = \sqrt{(k_2)^2\left(1+\frac{\sigma}{i\omega\epsilon_2}\right)\left(1+\frac{\sigma^*}{i\omega\mu_2}\right)-\left(\beta_{2_y}\right)^2} \end{aligned}\right\} \quad x>0 \quad \text{(B.3b)}$$

where $k_j = \omega\sqrt{\mu_j\epsilon_j}$ for $j = 1, 2$. Further, the parameters σ_x and σ_y denote electric conductivities, and the parameters σ_x^* and σ_y^* denote magnetic losses. Enforcing the continuity of the tangential fields across the Region-1/Region-2 interface at $x = 0$ leans

to $\beta_{2_y} = \beta_{1_y} = k_1 \sin\theta$ and

$$\Gamma = \frac{\frac{\beta_{1_x}}{\omega\epsilon_1} - \frac{\beta_{2_x}}{\omega\epsilon_2(1+\sigma/i\omega\epsilon_2)}}{\frac{\beta_{1_x}}{\omega\epsilon_1} + \frac{\beta_{2_x}}{\omega\epsilon_2(1+\sigma/i\omega\epsilon_2)}}; \quad \tau = 1 + \Gamma \tag{B.4}$$

In general, $\Gamma \neq 0$ for arbitrary incidence angle θ. However, for the special case of normal incidence ($\theta = 0$) of the impinging wave we have

$$\Gamma = \frac{\eta_1 - \eta_2}{\eta_1 + \eta_2} \tag{B.5}$$

where the wave impedances in Regions 1 and 2 are given by

$$\eta_1 = \sqrt{\frac{\mu_1}{\epsilon_1}}; \quad \eta_2 = \sqrt{\frac{\mu_2\,(1 + \sigma^*/i\omega\mu_2)}{\epsilon_2\,(1 + \sigma/i\omega\epsilon_2)}} \tag{B.6}$$

Then, if we set $\epsilon_1 = \epsilon_2$ and $\mu_1 = \mu_2$ and further enforce the condition

$$\frac{\sigma^*}{\mu_1} = \frac{\sigma}{\epsilon_1} \quad \rightarrow \quad \sigma^* = \sigma\frac{\mu_1}{\epsilon_1} \tag{B.7}$$

then $k_1 = k_2$ and $\eta_1 = \eta_2$. This yields $\Gamma = 0$, a reflectionless Region-1/Region-2 interface for a normally impinging wave. From Equ. B.3b, we also find for this case that

$$\beta_{2_x} = \left(1 + \frac{\sigma}{i\omega\epsilon_1}\right) k_1 = k_1 - i\sigma\eta_1 \tag{B.8}$$

yielding the transmitted fields in Region 2

$$\breve{H}_2 = -\hat{z}H_0 e^{-ik_1 x} e^{-\sigma\eta_1 x} \tag{B.9a}$$

$$\breve{E}_2 = -\hat{y}\eta_1 H_0 e^{-ik_1 x} e^{-\sigma\eta_1 x} \tag{B.9b}$$

WE observe that, for the normal-incidence case, the transmitted wave in Region 2 attenuates exponentially along the normal direction. Further, despite propagating in a lossy medium, this wave is dispersionless. That is, its wave speed is independent of frequency. Therefore, the material half-space Region 2 having magnetic and electric losses defined by Equ. B.7 is perfectly matched to Region 1 for normally incident waves.

B.1 FIELD-SPLITTING MODIFICATION OF MAXWELL'S EQUATIONS

The previous derivation has been used with only limited success due to the restriction of being perfectly matched for only normal incidence waves. Berenger discovered that a non-physical formulation could be used to produce a matched interface that was

independent of frequency and angle of incidence. His field splitting technique is derived as follows.

Within Region 2, Maxwell's curl equations (Equ's 3.1a and 3.1b) as modified by Berenger are expressed in their time-dependent form as

$$\epsilon_2 \frac{\partial E_x}{\partial t} + \sigma_y E_x = \frac{\partial H_z}{\partial y} \tag{B.10a}$$

$$\epsilon_2 \frac{\partial E_y}{\partial t} + \sigma_x E_y = -\frac{\partial H_z}{\partial x} \tag{B.10b}$$

$$\mu_2 \frac{\partial H_{zx}}{\partial t} + \sigma_x^* H_{zx} = -\frac{\partial E_y}{\partial x} \tag{B.10c}$$

$$\mu_2 \frac{\partial H_{zy}}{\partial t} + \sigma_y^* H_{zy} = -\frac{\partial E_x}{\partial y} \tag{B.10d}$$

Here, H_z is assumed to be split into two additive subcompnents

$$H_z = H_{zx} + H_{zy} \tag{B.11}$$

We see that Berenger's formulation represents a generalisation of normally modeled physical media. If $\sigma_x = \sigma_y = 0$ and $\sigma_x^* = \sigma_y^* = 0$, Equ's B.10a–B.10d reduce to Maxwell's equations in a lossless medium. If $\sigma_x = \sigma_y = \sigma$, $\sigma_x^* = \sigma_y^* = 0$, Equ's B.10a–B.10d describe an electrically conductive medium. And if $\epsilon_2 = \epsilon_1$, $\mu_2 = \mu_1$, $\sigma_x = \sigma_y = \sigma$, $\sigma_x^* = \sigma_y^* = \sigma^*$, and Equ. B.7 is satisfied, then Equ's B.10a–B.10d describe an absorbing medium that is impedance-matched to the Region-1 half-space $x < 0$ for normally incident plane waves.

Additional possibilities present themselves, however. If $\sigma_y = \sigma_y^* = 0$, the medium can absorb a plane wave having field components (E_y,H_{zx}) and (E_x,H_{zy}) if $\sigma_x = \sigma_x^* = 0$. If these properties of particular Berenger media, characterised by the pairwise parameter sets (σ_x,σ_x^*,0,0) and (0,0,σ_y,σ_y^*), satisfy Equ. B.7, then at interfaces normal to x and y, respectively, the Berenger media have zero reflection of electromagnetic waves.

Now consider Equ's B.10a–B.10d expressed in their time-harmonic form in the Berenger medium. Here the hat symbol denotes a phasor quantity, and we have

$$i\omega\epsilon_2 s_y \breve{E}_x = \frac{\partial}{\partial t}\left(\breve{H}_{zx} + \breve{H}_{zy}\right) \tag{B.12a}$$

$$i\omega\epsilon_2 s_x \breve{E}_y = -\frac{\partial}{\partial t}\left(\breve{H}_{zx} + \breve{H}_{zy}\right) \tag{B.12b}$$

$$i\omega\mu_2 s_x \breve{H}_{zx} = -\frac{\partial \breve{E}_y}{\partial x} \tag{B.12c}$$

$$i\omega\mu_2 s_x \breve{H}_{zy} = \frac{\partial \breve{E}_y}{\partial y} \tag{B.12d}$$

where

$$s_w = \left(1 + \frac{\sigma_w}{i\omega\epsilon_2}\right); \quad s_w^* = \left(1 + \frac{\sigma_w^*}{i\omega\mu_2}\right): \quad w = x, y \tag{B.13}$$

B.2 PLANE-WAVE SOLUTION WITHIN THE BERENGER MEDIUM

The next step is to derive the plane-wave solution within the Berenger medium. To this end, Equ. B.12a is differentiated with respect to y and Equ. B.10b with respect to x. Substituting the expressions for $\frac{\partial \breve{E}_y}{\partial x}$ and $\frac{\partial \breve{E}_x}{\partial y}$ from Equ. B.10c and Equ. B.10d leads to

$$-\omega\mu_2\epsilon_2 s_x \breve{H}_{zx} = -\frac{1}{s_x^*}\frac{\partial}{\partial x}\frac{1}{s_x}\frac{\partial}{\partial x}\left(\breve{H}_{zx} + \breve{H}_{zy}\right) \tag{B.14a}$$

$$-\omega\mu_2\epsilon_2 s_x \breve{H}_{zy} = -\frac{1}{s_y^*}\frac{\partial}{\partial y}\frac{1}{s_y}\frac{\partial}{\partial y}\left(\breve{H}_{zx} + \breve{H}_{zy}\right) \tag{B.14b}$$

Adding these together and using Equ. B.11, leads to the representative wave equation

$$\frac{1}{s_x^*}\frac{\partial}{\partial x}\frac{1}{s_x}\frac{\partial}{\partial x}\breve{H}_z + \frac{\partial}{\partial y}\frac{1}{s_y}\frac{\partial}{\partial y}\breve{H}_z + \omega\mu_2\epsilon_2 s_x \breve{H}_z = 0 \tag{B.15}$$

This wave equation supports the solutions

$$\breve{H}_z = H_0 \tau e^{-i\sqrt{s_x s_x^*}\beta_{2_x} x - i\sqrt{s_y s_y^*}\beta_{2_y} y} \tag{B.16}$$

with the dispersion

$$(\beta_{2_x})^2 + \left(\beta_{2_y}\right)^2 = (k_2)^2 \quad \rightarrow \quad \beta_{2_x} = \left[(k_2)^2 - \left(\beta_{2_y}\right)^2\right]^{\frac{1}{2}} \tag{B.17}$$

Then, from Equ's B.12a, B.10b, and B.11, we have

$$\breve{E}_x = -H_0 \tau \frac{\left(\beta_{2_y}\right)^2}{\omega\epsilon_2}\sqrt{\frac{s_y^*}{s_y}} e^{-i\sqrt{s_x s_x^*}\beta_{2_x} x - i\sqrt{s_y s_y^*}\beta_{2_y} y} \tag{B.18a}$$

$$\breve{E}_y = H_0 \tau \frac{\left(\beta_{2_x}\right)^2}{\omega\epsilon_2}\sqrt{\frac{s_x^*}{s_x}} e^{-i\sqrt{s_x s_x^*}\beta_{2_x} x - i\sqrt{s_y s_y^*}\beta_{2_y} y} \tag{B.18b}$$

Despite the field splitting, continuity of the tangential E and H fields must be preserved across the $x = 0$ interface for the fields given by Equ's B.1, B.16, B.18a, and B.18b. To enforce this field continuity, we have $s_y = s_y^* = 1$, or equivalently $\sigma_y = 0 = \sigma_y^*$. this yields the phase-matching condition $\beta_{2_y} = \beta_{1_y} = k_1 \sin\theta$. Further,

we derive the H-field reflection and transmission coefficients

$$\Gamma = \frac{\frac{\beta_{1_x}}{\omega\epsilon_1} - \frac{\beta_{2_x}}{\omega\epsilon_2}\sqrt{\frac{s_x^*}{s_x}}}{\frac{\beta_{1_x}}{\omega\epsilon_1} + \frac{\beta_{2_x}}{\omega\epsilon_2}\sqrt{\frac{s_x^*}{s_x}}}; \quad \tau = 1 + \Gamma \tag{B.19}$$

Now we can determine the reflectionless matching condition. Assume $\epsilon_1 = \epsilon_2$, $\mu_1 = \mu_2$, and $s_x = s_x^*$. This is equvalent to $k_1 = k_2$, $\eta_1 = \sqrt{\mu_1/\epsilon_1} = \sqrt{\mu_2/\epsilon_2}$, and $\sigma_x/\epsilon_1 = \sigma_x^*/\mu_1$ (i.e., σ_x and σ_x^* satisfying Equ. B.7 in a pairwise manner). With $\beta_{2_y} = \beta_{1_y}$, Equ. B.17 now yields $\beta_{2_x} = \beta_{1_x}$. Substituting into Equ. B.19 gives the reflectionless condition $\Gamma = 0$ for *all* incident angles θ. For this case, Equ's B.16, B.18a, and B.18b specify the following transmitted fields within the Berenger medium $x > 0$.

$$\breve{H}_z = H_0 e^{-is_x\beta_{1_x}x - is_y\beta_{1_y}y} = H_0 e^{-i\beta_{1_x}x - i\beta_{1_y}y} e^{-\sigma_x x\eta_1\cos\theta} \tag{B.20a}$$

$$\breve{E}_x = -H_0\eta_1\sin\theta e^{-i\beta_{1_x}x - i\beta_{1_y}y} e^{-\sigma_x x\eta_1\cos\theta} \tag{B.20b}$$

$$\breve{E}_y = H_0\eta_1\sin\theta e^{-i\beta_{1_x}x - i\beta_{1_y}y} e^{-\sigma_x x\eta_1\cos\theta} \tag{B.20c}$$

Within the Berenger medium, the transmitted wave propagates with the same speed and direction as the impinging wave while simultaneously undergoing exponential decay along the x-axis normal to the interface between Regions 1 and 2. The attenuation factor $\sigma_x x\eta_1\cos\theta$ is independent of frequency, and is lossy for all angles.

By using a similar FDTD derivation to that produced in section 3 Equ's B.20a, B.20b, and B.20c can be formed into the time-step algorithm and form a reflectionless boundary in an FDTD simulation.

Appendix C

TM VERSUS TE SIMULATIONS

Results for a number of Transverse Magnetic (TM) and Transverse Electric (TE) simulations are presented to support the polarisation study contained in Section 3.7. Simulations were performed in FEMLAB at both polarisations for 40-nm thick tungsten gratings suspended in free-space at 5-μm, 1-μm, and 170-nm periods (Figures C.1, C.2, and C.4, respectively). At 1-μm, and 170-nm periods simulations were also performed with a 40-nm thick silver layer suspended 20-nm below the mask (Figures C.3 and C.5, respectively).

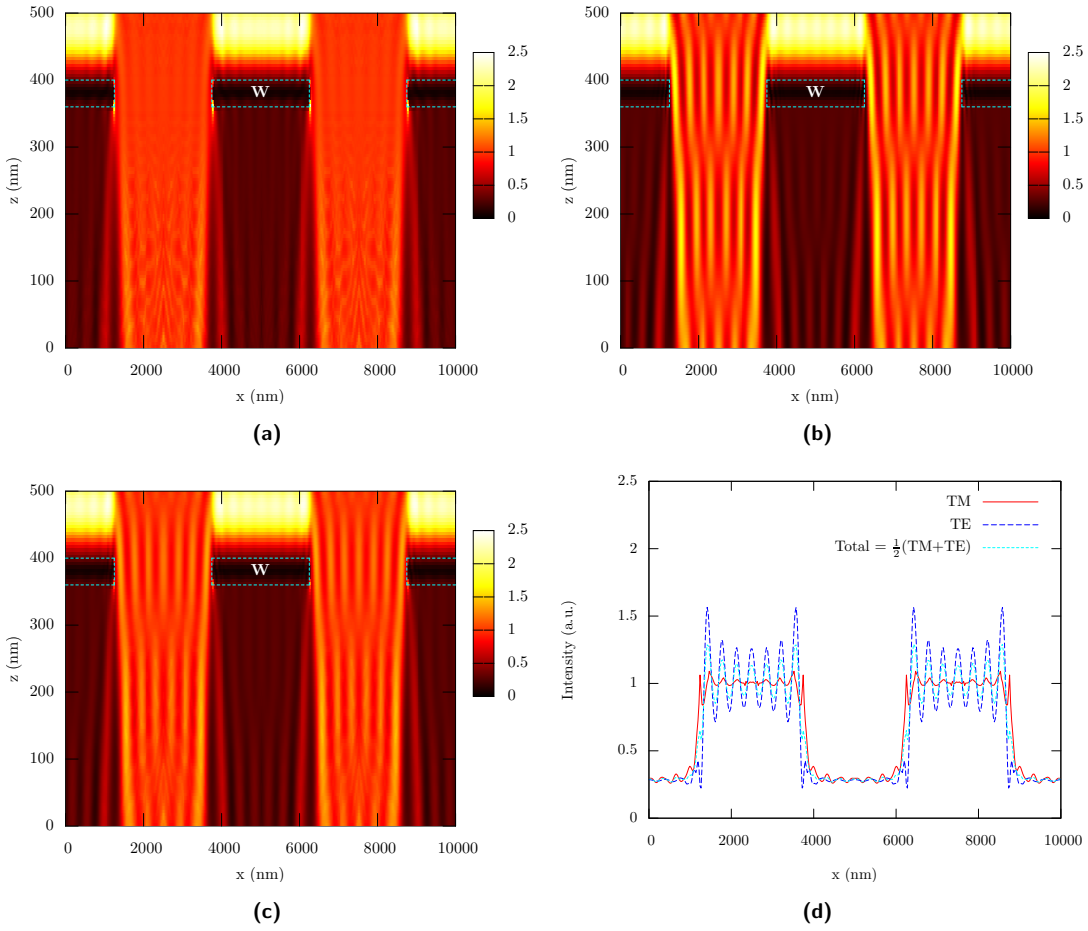

Fig. C.1: Comparison of 2D cross-sections of (a) TM and (b) TE simulations for a 5-μm period, 50% duty-cycle grating produced with FEMLAB. (c) shows the average of the TM and TE simulations giving the total field. (d) shows traces through each cross-section at 340 nm, or 20 nm below the mask.

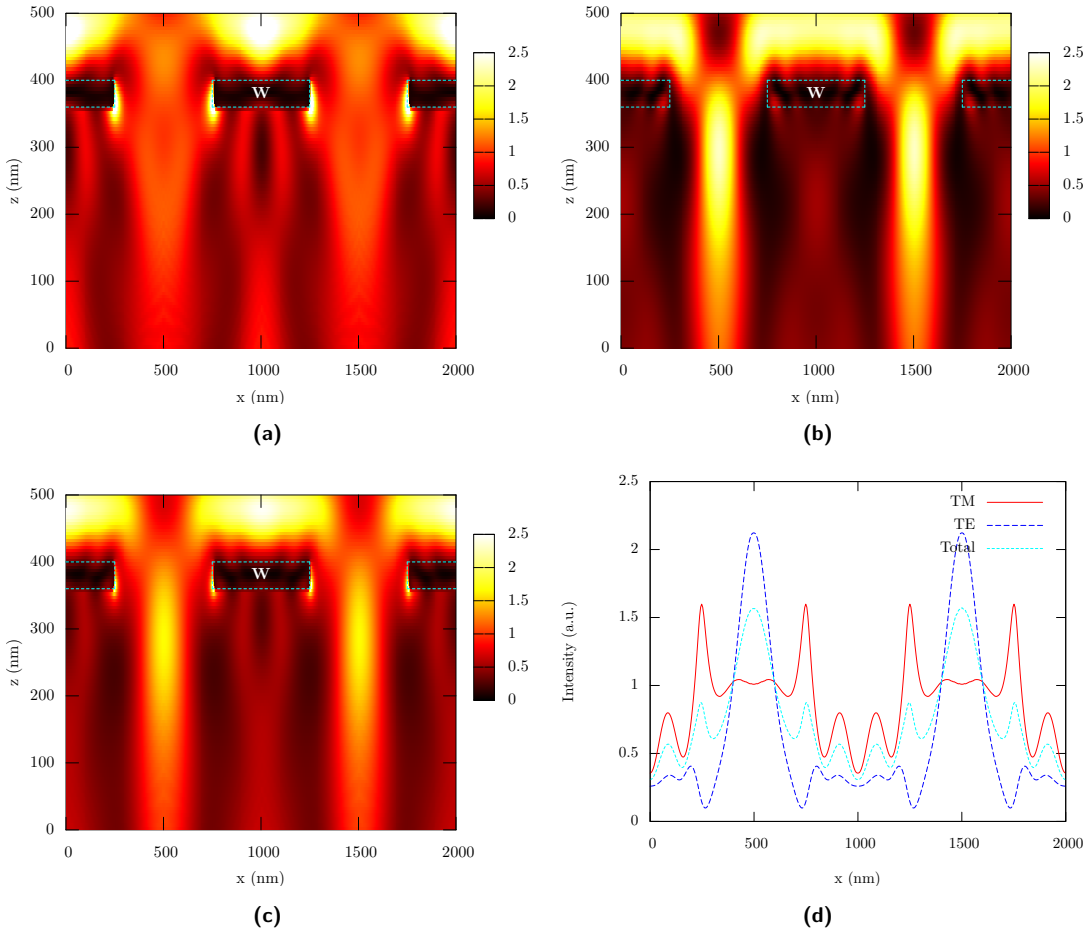

Fig. C.2: Comparison of 2D cross-sections of (a) TM and (b) TE simulations for a 1-μm period, 50% duty-cycle grating produced with FEMLAB. (c) shows the average of the TM and TE simulations giving the total field. (d) shows traces through each cross-section at 340 nm, or 20 nm below the mask.

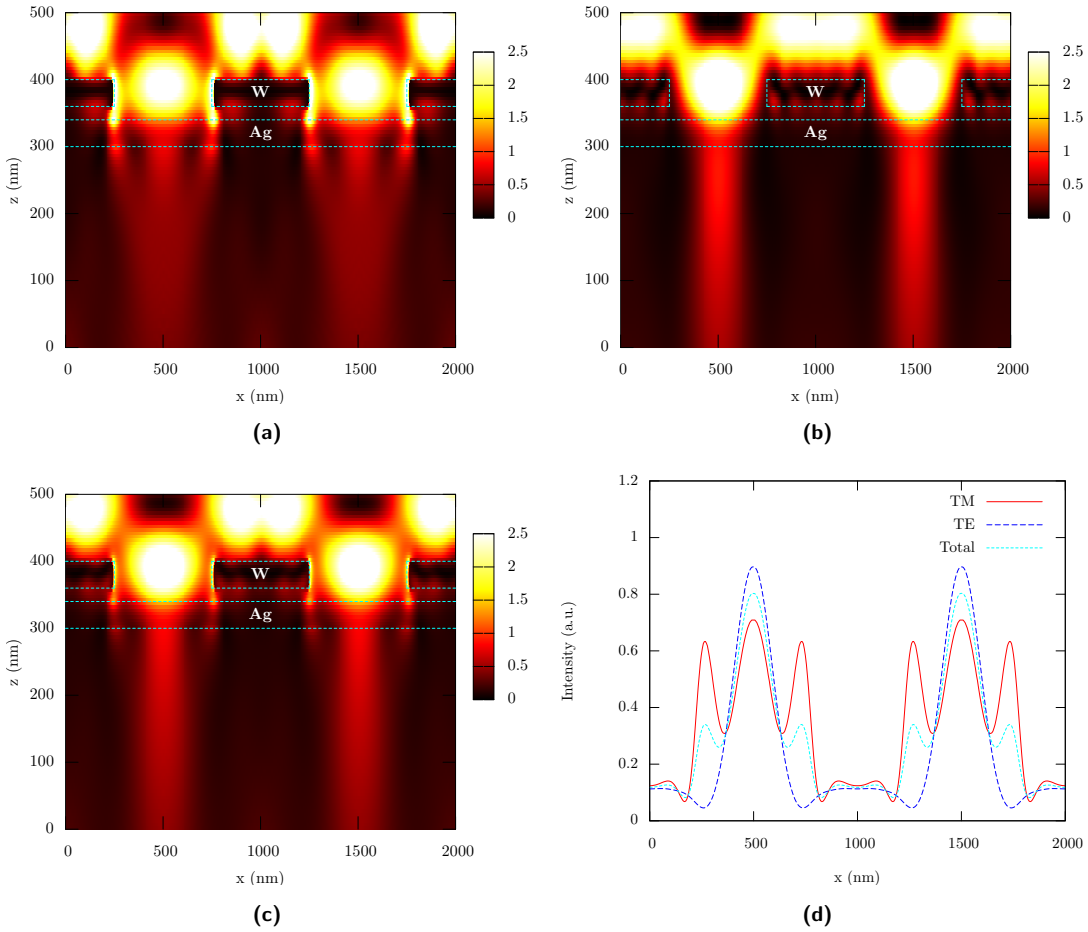

Fig. C.3: Comparison of 2D cross-sections of (a) TM and (b) TE simulations for a 1-μm period, 50% duty-cycle grating above a 40-nm silver later produced with FEMLAB. (c) shows the average of the TM and TE simulations giving the total field. (d) shows traces through each cross-section at 280 nm, or 20 nm below the silver.

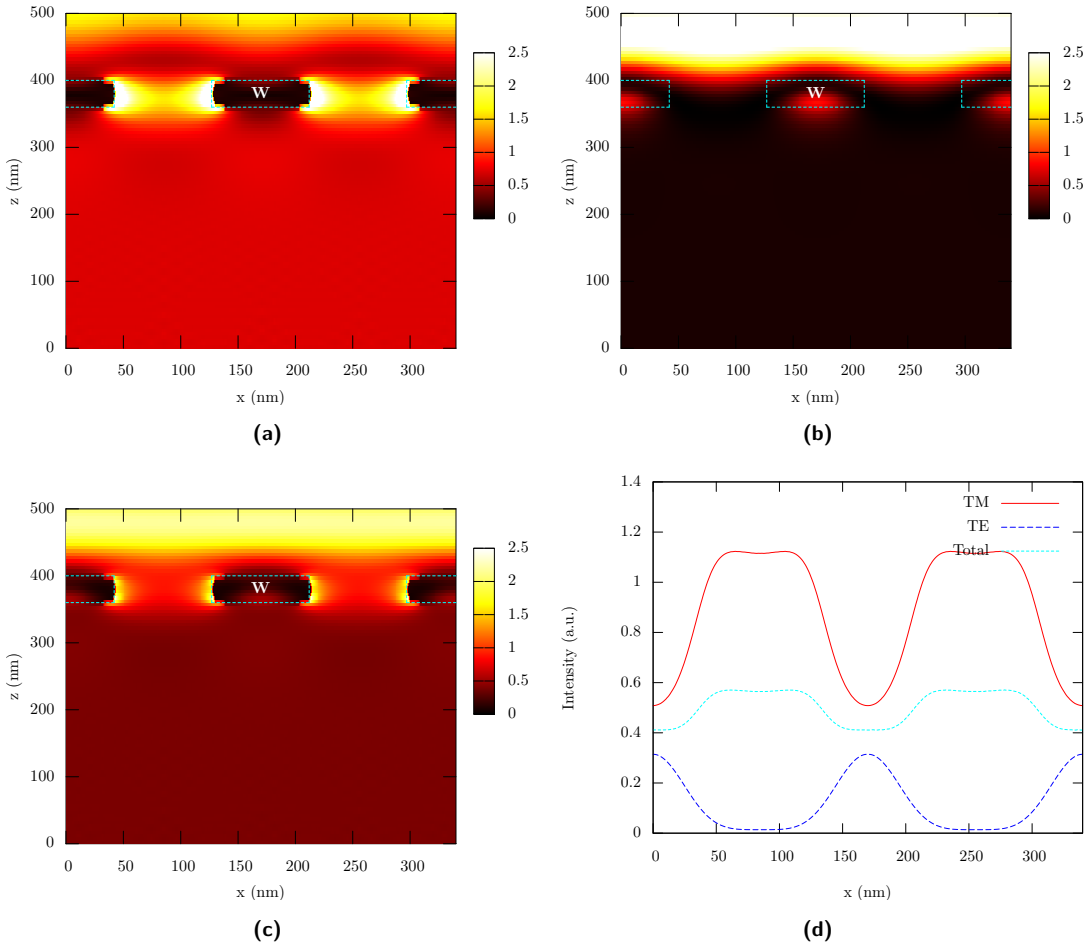

Fig. C.4: Comparison of 2D cross-sections of (a) TM and (b) TE simulations for a 170-nm period, 50% duty-cycle grating produced with FEMLAB. (c) shows the average of the TM and TE simulations giving the total field. (d) shows traces through each cross-section at 340 nm, or 20 nm below the mask.

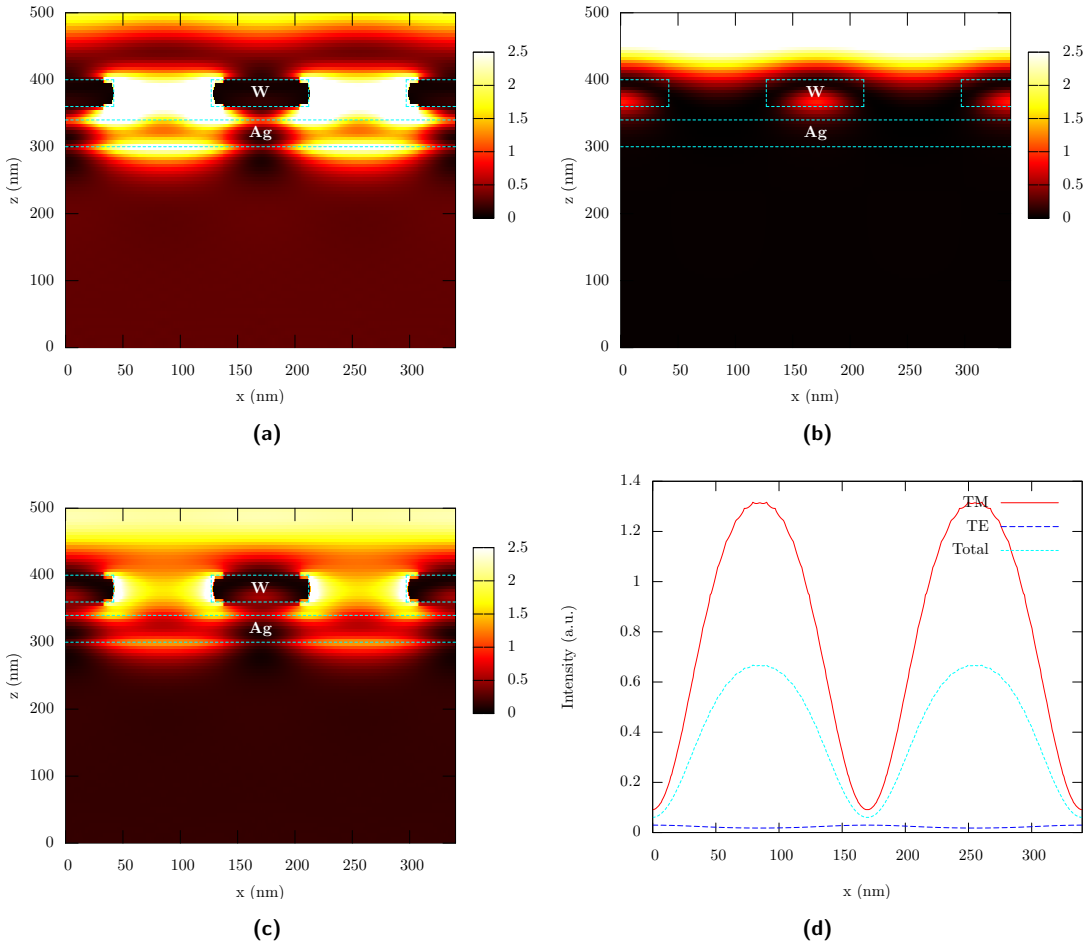

Fig. C.5: Comparison of 2D cross-sections of (a) TM and (b) TE simulations for a 170-nm period, 50% duty-cycle grating above a 40-nm silver later produced with FEMLAB. (c) shows the average of the TM and TE simulations giving the total field. (d) shows traces through each cross-section at 280 nm, or 20 nm below the silver.

Appendix D

ELECTRON BEAM LITHOGRAPHY PATTERN DESIGN

The code used to create the EBL mask patterns is reproduced here for reference. Figure D.1 shows the mask created by the php code published in listings D.1 through D.8 after importing the ASCII file generate from the code into the Raith 150 software.

The code works in a hierarchical manner. First there are basic elements (classes for these are in listing D.5) that describe boxes, lines, dots, and text. The next level up is the 'structure' class. In a structure there can be many other structures and many elements that make it up. A large number of structures are defined in listing D.7. Using this technique arbitrary structures are defined.

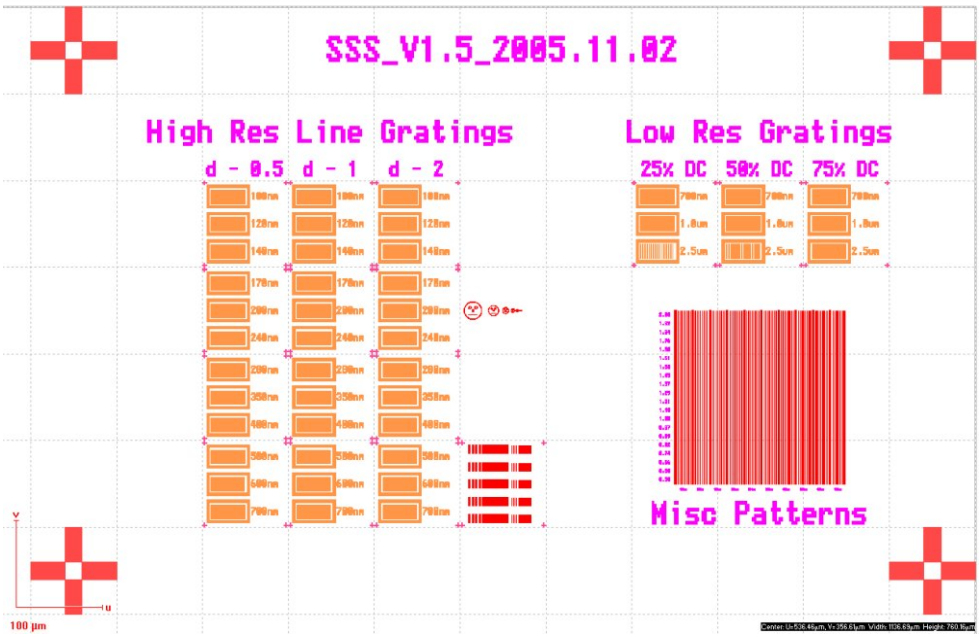

Fig. D.1: Example EBL mask pattern showing gratings from 100-nm to 2.5-μm periods, line pairs with spacing from 50 to 500 nm and varying doses, and arbitrary features.

Listing D.1: SSS.dIC.php

```
<?
 define('MASK', 'SSS');
 define('VERSION', '1.5_'.date('Y.m.d'));

 include_once ('include/init.dIC.php');
?>
<!DOCTYPE HTML PUBLIC "-//W3C//DTD HTML 4.01 Transitional//EN">
<html>
<head>
<title>dIC</title>
<meta http-equiv="Content-Type" content="text/html; charset=iso-8859-1">
</head>
<body>
<?
 include_once ('structures/text.dIC.php');
 include_once ('structures/structures.dIC.php');
 include_once ('structures/SSSStructures.dIC.php');

 $maskInfo = MASK . '_V' . VERSION;
 echo('<h1> creating '.$maskInfo.' structure </h1>'); flush();

 $SSS = new structure ();

 $t = new transform ();
 $SSSTotal_1 = SSSTotal($t);

 echo('<p> adding structure to '.$maskInfo.' structure </p>'); flush();

 $SSS->addStructure($SSSTotal_1);

 echo('<h1> printing ' . MASK . '_V' . VERSION . ' structure </h1>'); flush();
 $SSS->printStructure();

 include_once('include/shutdown.dIC.php');

?>
```

Listing D.2: init.dIC.php

```
<?

 // includes
 include_once ('config.dIC.php');
 include_once ('layers.dIC.php');
 include_once ('functions.dIC.php');
 include_once ('classes.dIC.php');

?>
```

Listing D.3: config.dIC.php

```
<?

 // start session for
 session_start();

 // Setup variables
 $maxExecutionTime = 300;
 define('CONFIG_WRITE_FIELD', 100);
 define('SINGLE_PASS_LINE', 0);
 define('CONFIG_TO_TXT', 1); // where the output will go

 // Set maximum exe time
 set_time_limit ($maxExecutionTime);

 if (CONFIG_TO_TXT) { // if not html echo then write to file
  $_SESSION['filename'] = 'output_'.MASK.'_V'.VERSION.'.asc';
  $_SESSION['fileDir']  = '/davengem/dIC';
  $_SESSION['FILE']     = fopen($_SESSION['filename'], 'w');
 }

?>
```

Listing D.4: functions.dIC.php

```
<?

 function gratingText ($pitch)
 {
  // um or nm
  if ($pitch>=1) {
   return sprintf('%.1f', $pitch) . 'um';
  } else {
    return sprintf('%d', $pitch*1000) . 'nm';
  }
 }

 function elementCode($type)
 {
  switch ($type) {
   case 'BOX':
    return '1';
    break;
   case 'LINE':
    return 'L';
    break;
   case 'POINT':
```

```
23       return 'P';
24       break;
25      case 'CIRCLE':
26       return 'L';
27       break;
28      default:
29       die('!! ERROR - element code not defined.');
30     }
31    }
32
33    function nl()
34    {
35     if(CONFIG_TO_TXT) {
36      return chr(10);
37     } else {
38      return '<br>';
39     }
40    }
41
42   ?>
```

Listing D.5: classes.dIC.php

```
 1   <?
 2
 3    class transform
 4    {
 5     var $x;
 6     var $y;
 7     var $rot;
 8
 9     function transform ($x=0, $y=0, $rot=0)
10     {
11      $this->x = $x;
12      $this->y = $y;
13      $this->rot = $rot;
14     }
15
16     function set ($x, $y, $rot)
17     {
18      $this->x = $x;
19      $this->y = $y;
20      $this->rot = $rot;
21     }
22
23    }
24
25    class aux
26    {
27     var $transform;
28     var $dose;
29     var $layer;
30
31     function aux ($transform, $dose, $layer)
32     {
33      $this->transform  = $transform;
34      $this->dose    = $dose;
35      $this->layer   = $layer;
36     }
37    }
38
39
40    class structure
41    {
42     var $name;
43     var $elements;
44     var $structures;
45
46     function structure ($name='')
47     {
48      $this->name    = $name;
49      $this->elements  = array();
50      $this->structures = array();
51     }
52
53     function addStructure ($struct)
54     {
55      $this->structures[] = $struct;
56     }
57
58     function addElement ($type, $data, $transform, $dose, $layer)
59     {
60      $this->elements[] = new element ($type, $data, $transform, $dose, $layer);
61
62     }
63
64     function transform ($transform)
65     {
66      for ($i=0; $i<count($this->structures); $i++) {
67       $this->structures[$i]->transform($transform);
68      }
69      for ($i=0; $i<count($this->elements); $i++) {
70       $this->elements[$i]->transform($transform);
71      }
72     }
73
74     function printStructure ()
75     {
76      for ($i=0; $i<count($this->structures); $i++) {
77       $this->structures[$i]->printStructure();
78      }
79
80      for ($i=0; $i<count($this->elements); $i++) {
81       $this->elements[$i]->printElement();
```

```
 82      }
 83     }
 84
 85    }
 86
 87
 88    class element
 89    {
 90     var $type;
 91     var $data;
 92     var $dose;
 93     var $layer;
 94
 95     function element ($type, $data, $transform, $dose, $layer)
 96     {
 97      $this->type  = $type;
 98      $this->data  = $data;
 99      $this->dose  = $dose;
100      $this->layer  = $layer;
101      $this->transform ($transform);
102     }
103
104     function transform ($t)
105     {
106      $this->data->transform($t);
107     }
108
109     function printElement ()
110     {
111      if (CONFIG_TO_TXT) {
112       fwrite($_SESSION['FILE'], elementCode($this->type).' ');
113       fwrite($_SESSION['FILE'], $this->dose*100 . ' ');
114       fwrite($_SESSION['FILE'], $this->layer . ' ');
115       $this->data->printData();
116       fwrite($_SESSION['FILE'], '#'.nl());
117      } else {
118       echo(elementCode($this->type).' ');
119       echo($this->dose*100 . ' ');
120       echo($this->layer . ' ');
121       $this->data->printData();
122       echo('#'.nl());
123      }
124     }
125
126
127    }
128
129
130    //
131    // Different data for different types
132    //
133    class point
134    {
135     var $x;
136     var $y;
137
138     function point ($x,$y)
139     {
140      $this->x = $x;
141      $this->y = $y;
142     }
143
144     function transform ($t)
145     {
146      $this->x = $this->x + $t->x;
147      $this->y = $this->y + $t->y;
148     }
149    }
150
151    class boxData
152    {
153     var $BL; // A point
154     var $TR; // A point
155
156     function boxData($BL=0, $TR=0)
157     {
158      $this->BL   = $BL;
159      $this->TR   = $TR;
160     }
161
162     function set($BL, $TR)
163     {
164      $this->BL   = $BL;
165      $this->TR   = $TR;
166     }
167
168     function transform ($t)
169     {
170      $this->BL->transform($t);
171      $this->TR->transform($t);
172     }
173
174     function printData ()
175     {
176      if (CONFIG_TO_TXT) {
177       fwrite($_SESSION['FILE'], nl() ); // newline
178       fwrite($_SESSION['FILE'], sprintf('%.3f %.3f %s', $this->BL->x, $this->BL->y, nl()) );
179       fwrite($_SESSION['FILE'], sprintf('%.3f %.3f %s', $this->TR->x, $this->BL->y, nl()) );
180       fwrite($_SESSION['FILE'], sprintf('%.3f %.3f %s', $this->TR->x, $this->TR->y, nl()) );
181       fwrite($_SESSION['FILE'], sprintf('%.3f %.3f %s', $this->BL->x, $this->TR->y, nl()) );
182      } else {
183       echo( nl() ); // newline
184       echo( sprintf('%.3f %.3f %s', $this->BL->x, $this->BL->y, nl()) );
185       echo( sprintf('%.3f %.3f %s', $this->TR->x, $this->BL->y, nl()) );
186       echo( sprintf('%.3f %.3f %s', $this->TR->x, $this->TR->y, nl()) );
187       echo( sprintf('%.3f %.3f %s', $this->BL->x, $this->TR->y, nl()) );
188      }
```

```
189     }
190
191    }
192
193    //
194    // Line element data
195    //
196    class lineData
197    {
198     var $thickness;
199     var $points; // A point array
200
201     function lineData($thickness=0, $points=0)
202     {
203      $this->thickness  = $thickness;
204      $this->points   = $points;
205     }
206
207     function set($thickness, $points)
208     {
209      $this->thickness  = $thickness;
210      $this->points   = $points;
211     }
212
213     function transform ($t)
214     {
215      for ($i=0; $i<count($this->points); $i++) {
216       $this->points[$i]->transform($t);
217      }
218     }
219
220     function printData ()
221     {
222      if (CONFIG_TO_TXT) {
223       fwrite($_SESSION['FILE'], sprintf('%.3f', $this->thickness) );
224       fwrite($_SESSION['FILE'], nl() ); // newline
225       for ($i=0; $i<count($this->points); $i++) {
226        fwrite($_SESSION['FILE'], sprintf('%.3f %.3f %s', $this->points[$i]->x, $this->points[$i]->y, nl())
               );
227       }
228      } else {
229       echo( sprintf('%.3f', $this->thickness) );
230       echo( nl() ); // newline
231       for ($i=0; $i<count($this->points); $i++) {
232        echo( sprintf('%.3f %.3f %s', $this->points[$i]->x, $this->points[$i]->y, nl()) );
233       }
234      }
235     }
236
237    }
238
239    class dotData
240    {
241     var $centre; // A point
242
243     function dotData($centre=0)
244     {
245      $this->centre = $centre;
246     }
247
248     function set($centre)
249     {
250      $this->centre = $centre;
251     }
252
253     function transform ($t)
254     {
255      $this->centre->transform($t);
256     }
257
258     function printData ()
259     {
260      if (CONFIG_TO_TXT) {
261       fwrite($_SESSION['FILE'], sprintf('%.3f', 0) );
262       fwrite($_SESSION['FILE'], nl() ); // newline
263       fwrite($_SESSION['FILE'], sprintf('%.3f %.3f %s', $this->centre->x, $this->centre->y, nl()) );
264      } else {
265       echo( nl() ); // newline
266       echo( sprintf('%.3f %.3f %s', $this->centre->x, $this->centre->y, nl()) );
267       echo( sprintf('%.3f', $this->thickness) );
268      }
269     }
270
271    }
272
273    //
274    // Circle element data
275    //
276    class circleData
277    {
278     var $thickness;
279     var $centre;
280     var $radius;
281
282     function circleData($centre=0, $radius=0, $thickness=0)
283     {
284      $this->centre   = $centre;
285      $this->raduis   = $radius;
286      $this->thickness  = $thickness;
287     }
288
289     function set($centre, $radius, $thickness)
290     {
291      $this->centre   = $centre;
292      $this->radius   = $radius;
293      $this->thickness  = $thickness;
294     }
```

```
295
296     function transform ($t)
297     {
298      $this->centre->transform($t);
299     }
300
301     function printData ()
302     {
303      $CIRCLE_VERTICIES = 64;
304
305      // Make point array
306      for ($i=0; $i<=$CIRCLE_VERTICIES; $i++) {
307       // start at top and go clockwise
308       $theta = $i*(2*pi()/$CIRCLE_VERTICIES);
309       $x = $this->centre->x + $this->radius*sin($theta);
310       $y = $this->centre->y + $this->radius*cos($theta);
311
312       $points[] = new point($x,$y);
313      }
314
315      // Print
316      if (CONFIG_TO_TXT) {
317       fwrite($_SESSION['FILE'], sprintf('%.3f', $this->thickness) );
318       fwrite($_SESSION['FILE'], nl() ); // newline
319       for ($i=0; $i<count($points); $i++) {
320        fwrite($_SESSION['FILE'], sprintf('%.3f %.3f %s', $points[$i]->x, $points[$i]->y, nl()) );
321       }
322      } else {
323       echo( sprintf('%.3f', $this->thickness) );
324       echo( nl() ); // newline
325       for ($i=0; $i<count($points); $i++) {
326        echo( sprintf('%.3f %.3f %s', $points[$i]->x, $points[$i]->y, nl()) );
327       }
328      }
329     }
330
331    }
332
333    class textData
334    {
335     var $BL;
336     var $height;
337     var $lineWidth;
338     var $text;
339
340     function set($BL, $height, $lineWidth, $text)
341     {
342      $this->BL     = $BL;
343      $this->height   = $height;
344      $this->lineWidth  = $lineWidth;
345      $this->text     = $text;
346     }
347
348     function transform ()
349     {
350
351     }
352
353     function printData ()
354     {
355      if (CONFIG_TO_TXT) {
356       fwrite($_SESSION['FILE'], nl() ); // newline
357       fwrite($_SESSION['FILE'], sprintf('%.3f %.3f %s', $this->BL->x, $this->BL->y, nl()) );
358       fwrite($_SESSION['FILE'], sprintf('%.3f %.3f %s', $this->TR->x, $this->BL->y, nl()) );
359       fwrite($_SESSION['FILE'], sprintf('%.3f %.3f %s', $this->TR->x, $this->TR->y, nl()) );
360       fwrite($_SESSION['FILE'], sprintf('%.3f %.3f %s', $this->BL->x, $this->TR->y, nl()) );
361      } else {
362       echo( nl() ); // newline
363       echo( sprintf('%.3f %.3f %s', $this->BL->x, $this->BL->y, nl()) );
364       echo( sprintf('%.3f %.3f %s', $this->TR->x, $this->BL->y, nl()) );
365       echo( sprintf('%.3f %.3f %s', $this->TR->x, $this->TR->y, nl()) );
366       echo( sprintf('%.3f %.3f %s', $this->BL->x, $this->TR->y, nl()) );
367      }
368
369     }
370    }
371
372   ?>
```

Listing D.6: text.dIC.php

```
1   <?
2
3   function fontBit($x, $y, $nx, $ny, $ascii)
4   {
5    $line = ord($ascii)*$ny + $ny - $y - 1;
6
7    //echo($ascii . ' - ' . $line . ' - ' . $_SESSION['fontData'][$line] . '<br>');
8
9    if ($_SESSION['fontData'][$line] & pow(2,$nx - $x - 1))
10    return true;
11   else
12    return false;
13  }
14
15  function charStructure ($ascii, $height, $width, $transform, $dose, $layer)
16  {
17   $char = new structure ();
18   // font info
19   $nx = 8;
20   $ny = 8;
21
22   $trans = new transform ();
23   $cBoxData = new boxData ();
```

```
   $cBoxData->set(new point(0,0), new point($width/$nx,$height/$ny));

   for ($y=0; $y<$ny; $y++) {
    for ($x=0; $x<$nx; $x++) {
     if ( fontBit($x, $y, $nx, $ny, $ascii) ) {
      $trans->set( $x*($width/$nx), $y*($height/$ny), 0 );
      $char->addElement('BOX', $cBoxData, $trans, $dose, $layer);
     }
    }
   }

   $char->transform ($transform);
   return $char;
  }

  function strStructure($string, $height, $thickness, $align, $transform, $dose, $layer)
  {
   $str = new structure ();

   $width  = 0.6*$height;  // % of height
   $offset = 0.08*$width;  // % of width
   $cTransform = new transform();

   // Align offset setup
   switch($align) {
    case 'l':
     $aOffset = 0;
     break;
    case 'c':
     $aOffset = -(($width+$offset)*strlen($string))/2;
     break;
    case 'r':
     $aOffset = -($width+$offset)*strlen($string);
     break;
    default:
     $aOffset = 0;
     break;
   }

   for ($i=0; $i<strlen($string); $i++) {
    $cTransform->set($aOffset + $i*($width+$offset),0,0);
    $str->addStructure ( charStructure ($string{$i}, $height, $width, $cTransform, $dose, $layer) );
   }

   $str->transform ($transform);
   return $str;
  }

  /* Array of font bitmaps
     Not all letters are present here to minimise space required
     Can be found inside a embedded linux kernal
   */
  $_SESSION['fontData'] = array (

   /* 49 0x31 '1' */
   0x18, /* 00011000 */
   0x78, /* 01111000 */
   0x18, /* 00011000 */
   0x18, /* 00011000 */
   0x18, /* 00011000 */
   0x18, /* 00011000 */
   0x18, /* 00011000 */
   0x00, /* 00000000 */
   /* 50 0x32 '2' */
   0x7c, /* 01111100 */
   0xc6, /* 11000110 */
   0x0c, /* 00001100 */
   0x18, /* 00011000 */
   0x30, /* 00110000 */
   0x60, /* 01100000 */
   0xfe, /* 11111110 */
   0x00, /* 00000000 */
   /* 51 0x33 '3' */
   0x7c, /* 01111100 */
   0xc6, /* 11000110 */
   0x06, /* 00000110 */
   0x1c, /* 00011100 */
   0x06, /* 00000110 */
   0xc6, /* 11000110 */
   0x7c, /* 01111100 */
   0x00, /* 00000000 */
   /* 65 0x41 'A' */
   0x10, /* 00010000 */
   0x38, /* 00111000 */
   0x6c, /* 01101100 */
   0xc6, /* 11000110 */
   0xfe, /* 11111110 */
   0xc6, /* 11000110 */
   0xc6, /* 11000110 */
   0x00, /* 00000000 */
   /* 66 0x42 'B' */
   0xfc, /* 11111100 */
   0xc6, /* 11000110 */
   0xc6, /* 11000110 */
   0xfc, /* 11111100 */
   0xc6, /* 11000110 */
   0xc6, /* 11000110 */
   0xfc, /* 11111100 */
   0x00, /* 00000000 */
   /* 67 0x43 'C' */
   0x7c, /* 01111100 */
   0xc6, /* 11000110 */
   0xc0, /* 11000000 */
   0xc0, /* 11000000 */
   0xc0, /* 11000000 */
   0xc6, /* 11000110 */
   0x7c, /* 01111100 */
```

```
 0x00, /* 00000000 */
);


?>
```

Listing D.7: structures.dIC.php

```
<?

 function boxGrating ($pitch, $dutyCycle, $width, $height, $transform, $dose, $layer)
 {
  $grating = new structure('grating');

  // find number of boxes
  $num    = floor($width/$pitch);
  $boxWidth = $pitch*$dutyCycle/100;
  $data   = new boxData();

  for ($i=0; $i<$num; $i++) {
   $data->set( new point( $i*$pitch, 0 ),
         new point( $i*$pitch + $boxWidth, $height ) );
   $grating->addElement('BOX', $data, new transform(), $dose, $layer);
  }

  $grating->transform($transform);
  return $grating;
 }

 function lineGrating ($pitch, $width, $height, $transform, $dose, $layer)
 {
  $struct = new structure ();

  // find number of line
  $num    = floor($width/$pitch);
  $data   = new lineData();

  for ($i=0; $i<$num; $i++) {
   $data->set(SINGLE_PASS_LINE, array( new point( $i*$pitch, 0 ), new point( $i*$pitch, $height ) ) );
   $struct->addElement('LINE', $data, new transform(), $dose, $layer);
  }

  $struct->transform ($transform);
  return $struct;
 }

 function boarder ( $thickness, $width, $height, $transform, $dose, $layer)
 {
  $boarder = new structure ('boarder');

  $data = new boxData();

  // Bottom boarder
  $data->set( new point( 0, 0 ), new point( $width, $thickness ) );
  $boarder->addElement('BOX', $data, new transform(), $dose, $layer);
  // Left boarder
  $data->set( new point( 0, 0 ), new point( $thickness, $height ) );
  $boarder->addElement('BOX', $data, new transform(), $dose, $layer);
  // Top boarder
  $data->set( new point( 0, $height - $thickness ),
        new point( $width, $height ) );
  $boarder->addElement('BOX', $data, new transform(), $dose, $layer);
  // Right boarder
  $data->set( new point( $width - $thickness, 0 ),
        new point( $width, $height ) );
  $boarder->addElement('BOX', $data, new transform(), $dose, $layer);

  $boarder->transform($transform);
  return $boarder;
 }


 function stdGrating ($type, $pitch, $dutyCycle, $data, $transform, $dose, $layer)
 {
  $stdGrating = new structure('stdGrating');

  // Grating boarder
  $bThickness = $data['bThickness'];
  $bGap     = $data['bGap'];
  $bTransform = new transform (0,0,0);
  $bDose   = 1.0;

  // Grating construction
  $gWidth    = $data['gWidth']; // std grating width
  $gHeight   = $data['gHeight']; // std grating $height
  $gTransform = new transform ($bThickness+$bGap,$bThickness+$bGap,0);

  // Add boarder
  $stdGrating->addStructure (boarder($bThickness,
                    2*$bThickness + 2*$bGap + $gWidth,  // Width
                    2*$bThickness + 2*$bGap + $gHeight, // Height
                    $bTransform, $bDose, $layer));

  // Add appropriate grating
  if ($type=='BOX') {
   // Add box grating
   $stdGrating->addStructure (boxGrating($pitch, $dutyCycle,
                       $gWidth, $gHeight,
                       $gTransform, $dose, $layer));
  } elseif ($type=='LINE') {
   // Add line grating
   $stdGrating->addStructure (lineGrating($pitch,
                        $gWidth, $gHeight,
                        $gTransform, $dose, $layer));
```

```
 97     }
 98
 99
100     // text info
101     // $tData     = new textData();
102     $tHeight    = 10;
103     $tLineWidth  = 1;
104     $tText    = gratingText($pitch);
105     $tTransform  = new transform ( $gWidth + 2*$bThickness + 2*$bGap + 0.5*$bThickness,
106                     ((2*$bThickness + 2*$bGap + $gHeight) - $tHeight)/2, 0 );
107
108     $stdGrating->addStructure ( strStructure($tText, $tHeight, $tLineWidth, 'l', $tTransform, $dose,
            $layer) );
109
110     $stdGrating->transform ($transform);
111     return $stdGrating;
112    }
113
114    function cross ($thickness, $size, $transform, $dose, $layer)
115    {
116     $cross = new structure ();
117
118     $bbl = ($size-$thickness)/2;
119     $bbr = ($size+$thickness)/2;
120     $data = new boxData();
121
122     // Bottom box
123     $data->set( new point( $bbl, 0 ), new point( $bbr, $bbl ) );
124     $cross->addElement('BOX', $data, new transform(), $dose, $layer);
125     // Left box
126     $data->set( new point( 0, $bbl ), new point( $bbl, $bbr ) );
127     $cross->addElement('BOX', $data, new transform(), $dose, $layer);
128     // Top box
129     $data->set( new point( $bbl, $bbr ), new point( $bbr, $size ) );
130     $cross->addElement('BOX', $data, new transform(), $dose, $layer);
131     // Right box
132     $data->set( new point( $bbr, $bbl ), new point( $size, $bbr ) );
133     $cross->addElement('BOX', $data, new transform(), $dose, $layer);
134
135     $cross->transform($transform);
136     return $cross;
137    }
138
139    function writeFieldCell ($transform, $dose, $layer)
140    {
141     $cell = new structure('cell');
142
143     $cThickness = 1;
144     $cSize   = 5;
145     $cTransform = new transform ();
146     $wSize = CONFIG_WRITE_FIELD;
147
148     // BL cross
149     $cTransform->set(0,0,0);
150     $cell->addStructure( cross($cThickness, $cSize, $cTransform, $dose, $layer) );
151     // BR cross
152     $cTransform->set( $wSize - $cSize,0,0);
153     $cell->addStructure( cross($cThickness, $cSize, $cTransform, $dose, $layer) );
154     // TL cross
155     $cTransform->set(0, $wSize - $cSize,0);
156     $cell->addStructure( cross($cThickness, $cSize, $cTransform, $dose, $layer) );
157     // TR cross
158     $cTransform->set($wSize - $cSize, $wSize - $cSize,0);
159     $cell->addStructure( cross($cThickness, $cSize, $cTransform, $dose, $layer) );
160
161     $cell->transform ($transform);
162     return $cell;
163    }
164
165    function stdGratingWF ($type, $pitchArray, $dutyCycle, $transform, $dose )
166    {
167     $struct = new structure ();
168
169     $items = count($pitchArray);
170
171     $cSize        = 5;
172     $gSpacing       = 5;
173     $wSize        = CONFIG_WRITE_FIELD;
174     $gData['bThickness']  = 3;
175     $gData['bGap']     = 2;
176     $gData['gWidth']    = 40; // std grating width
177     $gData['gHeight']    = ((CONFIG_WRITE_FIELD - (2*$cSize + ($items-1)*$gSpacing))/$items)
178                 - (2*$gData['bThickness'] + 2*$gData['bGap']); // std grating $height
179
180     $gT = new transform();
181
182     // make WF
183     $struct->addStructure( writeFieldCell (new transform(), 1.0, LAYER_WF_CELL) );
184
185     // loop on gratings
186     for ($i=0; $i<$items; $i++) {
187      $totalH = 2*$gData['bThickness'] + 2*$gData['bGap'] + $gData['gHeight'];
188      $gY = CONFIG_WRITE_FIELD - ( $cSize + $i*$gSpacing + ($i+1)*$totalH );
189      $gT->set($cSize, $gY ,0 );
190      $struct->addStructure( stdGrating ($type, $pitchArray[$i], $dutyCycle, $gData, $gT, $dose,
            LAYER_GRATING) );
191     }
192
193     $struct->transform ($transform);
194     return $struct;
195    }
196
197    function stdGratingCol ($type, $pitchArray, $maxP, $dutyCycle, $transform, $dose)
198    {
199     $struct = new structure ();
200
201     // loop through all the pitches
```

```
202     $loops  = floor(count($pitchArray) / $maxP);
203     if ( count($pitchArray) % $maxP > 0)
204      $loops++;
205
206     $t = new transform ();
207
208     for ($i=0; $i<$loops; $i++) {
209      $t->set(0,($loops-$i-1)*CONFIG_WRITE_FIELD,0);
210      $struct->addStructure( stdGratingWF ($type, array_slice($pitchArray, $i*$maxP, $maxP), $dutyCycle, $t
           , $dose) );
211     }
212
213     $struct->transform ($transform);
214     return $struct;
215    }
216
217    function testBoxes ($sizeArray, $height, $transform, $dose, $layer)
218    {
219     $struct = new structure ();
220
221     $NOP = 4;
222     $offset = 0;
223     $bData = new boxData();
224     $t = new transform();
225
226     for ($i=0;$i<count($sizeArray);$i++) {
227      for ($j=0; $j<$NOP; $j++) {
228       $bData->set(new point($offset,0),new point($offset+$sizeArray[$i],$height));
229       $struct->addElement ('BOX', $bData, $t, $dose, $layer);
230       $offset = $offset+2*$sizeArray[$i];
231      }
232     }
233
234     $struct->transform ($transform);
235     return $struct;
236
237
238    }
239
240    function testLines ($sizeArray, $height, $transform, $dose, $layer)
241    {
242     $struct = new structure ();
243
244     $NOP = 4;
245     $offset = 0;
246     $lData = new lineData();
247     $t = new transform();
248
249     for ($i=0;$i<count($sizeArray);$i++) {
250      for ($j=0; $j<$NOP; $j++) {
251       $lData->set(SINGLE_PASS_LINE, array(new point($offset,0),new point($offset,$height)) );
252       $struct->addElement ('LINE', $lData, $t, $dose, $layer);
253       $offset = $offset+$sizeArray[$i];
254      }
255     }
256
257     $struct->transform ($transform);
258     return $struct;
259
260
261    }
262
263    function maskTest ($transform)
264    {
265     $struct = new structure ();
266
267     $t = new transform();
268
269     // Boarder
270     $struct->addStructure( writeFieldCell (new transform, 1.0, LAYER_WF_CELL) );
271
272     // Boxes array(0.12,0.145,0.17,0.2,0.25,0.29,0.35,0.42,0.5);
273     $layer  = LAYER_MASK_TEST_BOXES;
274     $height = 10;
275     $sizeArray = array(2, 1, 0.7, 0.5, 0.35, 0.29, 0.25, 0.2, 0.17, 0.145, 0.12);
276     $dose  = 0.5;
277     $t->set(10,5,0);
278     $struct->addStructure( testBoxes ($sizeArray, $height, $t, $dose, $layer) );
279
280     $dose  = 1;
281     $t->set(10,25,0);
282     $struct->addStructure( testBoxes ($sizeArray, $height, $t, $dose, $layer) );
283
284     $dose  = 2;
285     $t->set(10,45,0);
286     $struct->addStructure( testBoxes ($sizeArray, $height, $t, $dose, $layer) );
287
288     $dose  = 3;
289     $t->set(10,65,0);
290     $struct->addStructure( testBoxes ($sizeArray, $height, $t, $dose, $layer) );
291
292     $dose  = 4;
293     $t->set(10,85,0);
294     $struct->addStructure( testBoxes ($sizeArray, $height, $t, $dose, $layer) );
295
296     //
297     $layer  = LAYER_MASK_TEST_LINES;
298     $height = 10;
299     $baseX  = 60;
300     $sizeArray = array(2, 1, 0.7, 0.5, 0.35, 0.29, 0.25, 0.2, 0.17, 0.145, 0.12);
301     $dose  = 0.5;
302     $t->set($baseX,5,0);
303     $struct->addStructure( testLines ($sizeArray, $height, $t, $dose, $layer) );
304
305     $dose  = 1;
306     $t->set($baseX,25,0);
307     $struct->addStructure( testLines ($sizeArray, $height, $t, $dose, $layer) );
```

```
308
309     $dose  = 2;
310     $t->set($baseX,45,0);
311     $struct->addStructure( testLines ($sizeArray, $height, $t, $dose, $layer) );
312
313     $dose  = 3;
314     $t->set($baseX,65,0);
315     $struct->addStructure( testLines ($sizeArray, $height, $t, $dose, $layer) );
316
317     $dose  = 4;
318     $t->set($baseX,85,0);
319     $struct->addStructure( testLines ($sizeArray, $height, $t, $dose, $layer) );
320
321     $struct->transform ($transform);
322     return $struct;
323   }
324
325   function linePair ($lineSpacing, $height, $transform, $dose, $layer)
326   {
327     $struct = new structure ();
328
329     $t = new transform();
330
331     $points = array(new point(0,0), new point(0,$height));
332     $lData  = new lineData(SINGLE_PASS_LINE, $points);
333     $struct->addElement('LINE', $lData, $t, $dose, $layer);
334
335     $points = array(new point($lineSpacing, 0), new point($lineSpacing,$height));
336     $lData  = new lineData(SINGLE_PASS_LINE, $points);
337     $struct->addElement('LINE', $lData, $t, $dose, $layer);
338
339     $struct->transform ($transform);
340     return $struct;
341   }
342
343   function linePairArray ($lineSpacingStart, $lineSpacingEnd, $pitch, $height, $width, $transform, $dose,
          $layer)
344   {
345     $struct = new structure ();
346
347     $lTransform = new transform();
348     $maxPairs  = floor($width/$pitch);
349     $lineSpacingDelta = ($lineSpacingEnd - $lineSpacingStart)/($maxPairs-1);
350     $lineSpacing = $lineSpacingStart;
351
352     for ($i=0; $i<$maxPairs; $i++) {
353       $lTransform->set($i*$pitch,0,0);
354       $struct->addStructure( linePair ($lineSpacing, $height, $lTransform, $dose, $layer) );
355       $lineSpacing = $lineSpacing + $lineSpacingDelta;
356     }
357
358     $struct->transform ($transform);
359     return $struct;
360   }
361
362   function linePairBlock ($lineSpacingStart, $lineSpacingEnd, $bThickness, $pitch, $height, $width,
          $transform, $dose, $layer)
363   {
364     $struct = new structure ();
365
366     $t = new transform();
367
368     // Boarder
369     $bData = new boxData(new point(0, 0), new point($bThickness, $height));
370     $struct->addElement('BOX', $bData, $t, 1, LAYER_LINE_BOARDER );
371
372     // lines
373     $lTransform = new transform();
374     $maxPairs  = floor(($width-2*$bThickness)/$pitch);
375     $lineSpacingDelta = ($lineSpacingEnd - $lineSpacingStart)/($maxPairs-1);
376     $lineSpacing = $lineSpacingStart;
377
378     for ($i=0; $i<$maxPairs; $i++) {
379       $lTransform->set(2*$bThickness + $i*$pitch,0,0); // make room for boarder and previous pairs
380       $struct->addStructure( linePair ($lineSpacing, $height, $lTransform, $dose, $layer) );
381       $lineSpacing = $lineSpacing + $lineSpacingDelta;
382     }
383
384     $struct->transform ($transform);
385     return $struct;
386   }
387
388   function linePairBlockArray ($lineSpacingStart, $lineSpacingEnd, $bThickness, $bRepeatWidth,
389                   $doseStart, $doseEnd, $pitch, $height, $width, $transform, $dose, $layer)
390   {
391     $struct = new structure ();
392
393     $lTransform = new transform();
394
395     $bRepeats     = floor($width/$bRepeatWidth);
396
397     $maxPairs     = floor(($width-$bRepeats*$bThickness)/$pitch);
398     $lineSpacingDelta = ($lineSpacingEnd - $lineSpacingStart)/($maxPairs-1);
399
400     $bMaxPairs      = round($maxPairs/$bRepeats);
401     $blockSpacingDelta  = $lineSpacingDelta*$bMaxPairs;
402     $blockSpacing    = $lineSpacingStart;
403
404     for ($i=0; $i<$bRepeats; $i++) {
405       $lTransform->set($i*$bRepeatWidth,0,0); // make room previous
406       $struct->addStructure( linePairBlock ($blockSpacing, $blockSpacing + $blockSpacingDelta -
            $lineSpacingDelta,
407                       $bThickness, $pitch, $height, $bRepeatWidth, $lTransform, $dose, $layer) );
408       $blockSpacing = $blockSpacing + $blockSpacingDelta;
409     }
410
411     $struct->transform ($transform);
```

```
412     return $struct;
413   }
414
415   function stackedLinePairBlockArray ($lineSpacingStart, $lineSpacingEnd, $bThickness, $bRepeatWidth,
416                       $doseStart, $doseEnd, $totalHeight,
417                       $pitch, $subHeight, $width, $transform, $layer)
418   {
419     $struct = new structure ();
420
421     $aTransform   = new transform();
422     $maxDoseSteps  = floor($totalHeight/$subHeight);
423     $doseDelta    = ($doseEnd - $doseStart)/($maxDoseSteps-1);
424     $dose       = $doseStart;
425     $tTransform   = new transform();
426
427     for ($i=0; $i<$maxDoseSteps; $i++) {
428       $aTransform->set(0,$i*$subHeight,0);
429       $struct->addStructure( linePairBlockArray ($lineSpacingStart, $lineSpacingEnd,
430                           $bThickness, $bRepeatWidth,
431                           $doseStart, $doseEnd,
432                           $pitch, $subHeight, $width, $aTransform, $dose, $layer) );
433       $tTransform->set(-5,($i+0.25)*$subHeight,0);
434       $struct->addStructure( strStructure (sprintf('%.2f', $dose), $subHeight/2, $subHeight/10, 'r',
            $tTransform, 1, LAYER_TEXT) );
435       $dose = $dose + $doseDelta;
436     }
437
438     // At the bottom have the pitches
439     $bRepeats      = floor($width/$bRepeatWidth);
440     $maxPairs      = floor(($width-$bRepeats*$bThickness)/$pitch);
441     $bMaxPairs      = round($maxPairs/$bRepeats);
442     $lineSpacingDelta  = ($lineSpacingEnd - $lineSpacingStart)/($maxPairs-1);
443     $blockSpacingDelta  = $lineSpacingDelta*$bMaxPairs;
444     $blockSpacing    = $lineSpacingStart;
445     $tHeight       = $subHeight/4;
446
447     for ($i=0; $i<$bRepeats; $i++) {
448       $tTransform->set(($i+0.5)*$bRepeatWidth, -5-$tHeight, 0);
449       $struct->addStructure( strStructure ( gratingText ($blockSpacing), $tHeight, $tHeight/10, 'c',
            $tTransform, 1, LAYER_TEXT) );
450       $blockSpacing = $blockSpacing + $blockSpacingDelta;
451     }
452     $struct->transform ($transform);
453     return $struct;
454
455   }
456
457   function smiley ($radius, $aux)
458   {
459     $struct = new structure();
460
461     // Vars
462     $t = new transform();
463     $cData = new circleData();
464     $lData = new lineData();
465     $thickness_1 = $radius/15;
466     $thickness_2 = $thickness_1/2;
467
468     // outer
469     $cData->set(new point(0,0), $radius, $thickness_1);
470     $struct->addElement('CIRCLE', $cData, new transform(), $aux->dose, $aux->layer);
471
472     // Eyes
473     $eye_radius = $radius/7;
474     $cData->set(new point($radius*0.35,$radius*0.35), $eye_radius, $thickness_2);
475     $struct->addElement('CIRCLE', $cData, new transform(), $aux->dose, $aux->layer);
476     $cData->set(new point(-$radius*0.35,$radius*0.35), $eye_radius, $thickness_2);
477     $struct->addElement('CIRCLE', $cData, new transform(), $aux->dose, $aux->layer);
478
479     // nose
480     $nose_radius = $radius/10;
481     $cData->set(new point(0,0), $nose_radius, $thickness_2);
482     $struct->addElement('CIRCLE', $cData, new transform(), $aux->dose, $aux->layer);
483
484     // mouth
485     $points = array(new point(-$radius/2,-$radius/2),
486             new point($radius/2,-$radius/2));
487     $lData->set($thickness_2, $points);
488     $struct->addElement('LINE', $lData, new transform(), $aux->dose, $aux->layer);
489
490     $struct->transform($aux->transform);
491     return $struct;
492
493   }
494
495   function smileyArray ($radius_start, $radius_end, $count, $aux)
496   {
497     $struct = new structure();
498
499     // Vars
500     $t = new transform();
501     $anAux = new aux($t, $aux->dose, $aux->layer);
502     $delta_radius = exp(log($radius_end/$radius_start)/($count-1));
503
504     $x = 0;
505     for ($i=0; $i<$count; $i++) {
506       $radius = $radius_start*(pow($delta_radius,$i));
507       $struct->addStructure(smiley($radius, $anAux));
508       $x += $radius*2*1.2;
509       $anAux->transform->set($x,0,0);
510     }
511
512     $struct->transform($aux->transform);
513     return $struct;
514
515   }
516
```

```
517  ?>
```

Listing D.8: SSSStructures.dIC.php

```
  1  <?
  2   function SSSBox ($nxWF, $nyWF, $transform)
  3   {
  4    $struct = new structure ();
  5
  6    $cThickness = 20;
  7    $cSize   = CONFIG_WRITE_FIELD;
  8    $cTransform = new transform ();
  9    $wSizeX   = $nxWF*CONFIG_WRITE_FIELD;
 10    $wSizeY   = $nyWF*CONFIG_WRITE_FIELD;
 11
 12    $dose    = 1.0;
 13    $layer    = LAYER_WF_BOX;
 14
 15    // BL cross
 16    $cTransform->set(0,0,0);
 17    $struct->addStructure( cross($cThickness, $cSize, $cTransform, $dose, $layer) );
 18    // BR cross
 19    $cTransform->set( $wSizeX - $cSize,0,0);
 20    $struct->addStructure( cross($cThickness, $cSize, $cTransform, $dose, $layer) );
 21    // TL cross
 22    $cTransform->set(0, $wSizeY - $cSize,0);
 23    $struct->addStructure( cross($cThickness, $cSize, $cTransform, $dose, $layer) );
 24    // TR cross
 25    $cTransform->set($wSizeX - $cSize, $wSizeY - $cSize,0);
 26    $struct->addStructure( cross($cThickness, $cSize, $cTransform, $dose, $layer) );
 27
 28    $struct->transform ($transform);
 29    return $struct;
 30   }
 31
 32
 33   function SSSLineGratingCombo ($pitchArray, $gratingsPerWF, $transform, $dose)
 34   {
 35    $struct = new structure ();
 36
 37    $tx = 0.5*CONFIG_WRITE_FIELD;
 38    $ty = ceil(count($pitchArray)/$gratingsPerWF)*CONFIG_WRITE_FIELD + 0.025*CONFIG_WRITE_FIELD;
 39    $tTransform = new transform($tx,$ty,0);
 40
 41    $struct->addStructure( strStructure('d - '.$dose, 20, 5, 'c', $tTransform, $tDose = 1.0, LAYER_TEXT) )
           ;
 42
 43    $gTransform = new transform();
 44    $struct->addStructure( stdGratingCol ('LINE', $pitchArray, $gratingsPerWF, $dutyCycle=0, $gTransform,
           $dose) );
 45
 46    $struct->transform ($transform);
 47    return $struct;
 48   }
 49
 50   function SSSBoxGratingCombo ($pitchArray, $dutyCycle, $gratingsPerWF, $transform, $dose)
 51   {
 52    $struct = new structure ();
 53
 54    $tx = 0.5*CONFIG_WRITE_FIELD;
 55    $ty = ceil(count($pitchArray)/$gratingsPerWF)*CONFIG_WRITE_FIELD + 0.025*CONFIG_WRITE_FIELD;
 56    $tTransform = new transform($tx,$ty,0);
 57
 58    $struct->addStructure( strStructure($dutyCycle.'% DC', 20, 5, 'c', $tTransform, $tDose = 1.0,
           LAYER_TEXT) );
 59
 60    $gTransform = new transform();
 61    $struct->addStructure( stdGratingCol ('BOX', $pitchArray, $gratingsPerWF, $dutyCycle, $gTransform,
           $dose) );
 62
 63    $struct->transform ($transform);
 64    return $struct;
 65   }
 66   /*
 67   function SSSFace ($transform, $dose)
 68   {
 69    $struct = new structure ();
 70
 71
 72
 73    $struct->transform ($transform);
 74    return $struct;
 75   }
 76
 77
 78   function SSSRandom ($transform, $dose)
 79   {
 80    $struct = new structure ();
 81
 82    // A Face
 83
 84
 85    // Word Superlens
 86
 87
 88    // Nano
 89
 90
 91
 92    $struct->transform ($transform);
 93    return $struct;
 94   }
 95
 96   */
```

```
 97
 98   function SSSTotal ($transform)
 99   {
100    $SSS = new structure();
101
102    $maskInfo = MASK . '_V' . VERSION;
103    $dose = 1.0;
104    $t = new transform(0,0,0);
105
106    // outer area
107    $totalSizeX = 11;
108    $totalSizeY = 7;
109    $SSS->addStructure( SSSBox ($totalSizeX,$totalSizeY, new transform(0,0,0)) );
110
111    // TITLE
112    $tSize = CONFIG_WRITE_FIELD/3;
113    $tTransform = new transform( ($totalSizeX/2)*CONFIG_WRITE_FIELD,
114                  $totalSizeY*CONFIG_WRITE_FIELD - ((CONFIG_WRITE_FIELD-$tSize)/2+$tSize), 0 );
115    $SSS->addStructure( strStructure($maskInfo, $tSize, 10, 'c', $tTransform, 1.0, LAYER_TEXT) );
116
117    echo('<p> creating test pattern </p>'); flush();
118    //
119    // test GRATINGS
120    //
121    $baseX = ($totalSizeX/2 - 0.5)*CONFIG_WRITE_FIELD;
122    $baseY = (1)*CONFIG_WRITE_FIELD;
123    $t->set($baseX, $baseY, 0);
124    $SSS->addStructure( maskTest($t) );
125
126    echo('<p> creating line patterns </p>'); flush();
127
128    //
129    // HIGH RES LINE GRATINGS
130    //
131    $baseX = 2*CONFIG_WRITE_FIELD;
132    $baseY = 1*CONFIG_WRITE_FIELD;
133    $pitchArray = array(0.1,0.12,0.14,0.17,0.2,0.24,0.28,0.35,0.4,0.5,0.6,0.7);
134    $gratingsPerWF = 3;
135    // text
136    $tx = $baseX + 1.5*CONFIG_WRITE_FIELD;
137    $ty = $baseY + ceil(count($pitchArray)/$gratingsPerWF)*CONFIG_WRITE_FIELD + 0.4*CONFIG_WRITE_FIELD;
138    $tTransform = new transform ($tx,$ty,0);
139    $SSS->addStructure( strStructure('High Res Line Gratings', 30, 10, 'c', $tTransform, $dose, LAYER_TEXT
         ) );
140    //
141    $dose = 0.5;
142    $t->set($baseX, $baseY, 0);
143    $SSS->addStructure( SSSLineGratingCombo ($pitchArray, $gratingsPerWF, $t, $dose) );
144    //
145    $dose = 1.0;
146    $t->set($baseX + CONFIG_WRITE_FIELD, $baseY, 0);
147    $SSS->addStructure( SSSLineGratingCombo ($pitchArray, $gratingsPerWF, $t, $dose) );
148    //
149    $dose = 2.0;
150    $t->set($baseX + 2*CONFIG_WRITE_FIELD, $baseY, 0);
151    $SSS->addStructure( SSSLineGratingCombo ($pitchArray, $gratingsPerWF, $t, $dose) );
152
153
154    echo('<p> creating misc patterns </p>'); flush();
155    //
156    // MISC
157    //
158    $baseX = 7*CONFIG_WRITE_FIELD;
159    $baseY = 1*CONFIG_WRITE_FIELD;
160    $dose = 1.0;
161    // text
162    $tx = $baseX + 1.5*CONFIG_WRITE_FIELD;
163    $ty = $baseY;
164    $tTransform->set($tx,$ty,0);
165    $SSS->addStructure( strStructure('Misc Patterns', 30, 10, 'c', $tTransform, $dose, LAYER_TEXT) );
166    // paired lines
167    $t->set($baseX + 0.5*CONFIG_WRITE_FIELD, $baseY + 0.5*CONFIG_WRITE_FIELD,0);
168    $SSS->addStructure( stackedLinePairBlockArray (0.1,  0.5, 2, 20,
169                            0.5, 2, 200, //dose start, dose end, total height
170                            2, 10, 200, $t, LAYER_LINES) );
171
172    // Smiley face
173    $start_radius = 10;
174    $baseX = 5*CONFIG_WRITE_FIELD + $start_radius*1.5;
175    $baseY = 3.5*CONFIG_WRITE_FIELD;
176    $dose = 1.0;
177    $tTransform->set($baseX,$baseY,0);
178    $aux = new aux($tTransform, $dose, LAYER_CIRCLES);
179    $SSS->addStructure(smileyArray (10, 0.25, 8, $aux));
180
181
182
183    echo('<p> creating low resolution gratings </p>'); flush();
184    //
185    // LOW RES
186    //
187    $baseX = 7*CONFIG_WRITE_FIELD;
188    $baseY = 4*CONFIG_WRITE_FIELD;
189    $pitchArray = array(0.7,1,2.5);
190    $gratingsPerWF = 3;
191    $dose = 1.0;
192    // text
193    $tx = $baseX + 1.5*CONFIG_WRITE_FIELD;
194    $ty = $baseY + ceil(count($pitchArray)/$gratingsPerWF)*CONFIG_WRITE_FIELD + 0.4*CONFIG_WRITE_FIELD;
195    $tTransform = new transform ($tx,$ty,0);
196    $SSS->addStructure( strStructure('Low Res Gratings', 30, 10, 'c', $tTransform, $dose, LAYER_TEXT) );
197    // 25%
198    $dutyCycle = 25;
199    $t->set($baseX, $baseY, 0);
200    $SSS->addStructure( SSSBoxGratingCombo ($pitchArray, $dutyCycle, $gratingsPerWF, $t, $dose) );
201    //
202    $dutyCycle = 50;
```

```
203     $t->set($baseX + CONFIG_WRITE_FIELD, $baseY, 0);
204     $SSS->addStructure( SSSBoxGratingCombo ($pitchArray, $dutyCycle, $gratingsPerWF, $t, $dose) );
205     //
206     $dutyCycle = 75;
207     $t->set($baseX + 2*CONFIG_WRITE_FIELD, $baseY, 0);
208     $SSS->addStructure( SSSBoxGratingCombo ($pitchArray, $dutyCycle, $gratingsPerWF, $t, $dose) );
209
210
211     //
212     // connecting lines
213     //
214     $bHeight = -750;
215     $bWidth  = 10;
216     // number 1
217     $bx = ($totalSizeX/2)*CONFIG_WRITE_FIELD - ($bWidth/2);
218     $by = (-0.5)*CONFIG_WRITE_FIELD;
219     $bTransform = new transform ($bx,$by,0);
220     $bData   = new boxData();
221     $bData->set( new point(0, 0), new point($bWidth, $bHeight) );
222     $SSS->addElement('BOX', $bData, $bTransform, $dose=1.0, $layer=LAYER_CONNECT_BOX);
223     // number 2
224     $bx = (-0.5)*CONFIG_WRITE_FIELD;
225     $by = ($totalSizeY/2)*CONFIG_WRITE_FIELD - ($bWidth/2);
226     $bTransform = new transform ($bx,$by,0);
227     $bData      = new boxData();
228     $bData->set( new point(0, 0), new point($bHeight, $bWidth) );
229     $SSS->addElement('BOX', $bData, $bTransform, $dose=1.0, $layer=LAYER_CONNECT_BOX);
230
231
232     $SSS->transform($transform);
233     return $SSS;
234    }
235
236   ?>
```

Appendix E

T-MATRIX DERIVATION

To arrive at a transform matrix to describe an interface with incident plane-waves in Transverse Magnetic (TM) polarisation, a domain is setup as shown in Fig. E.1.

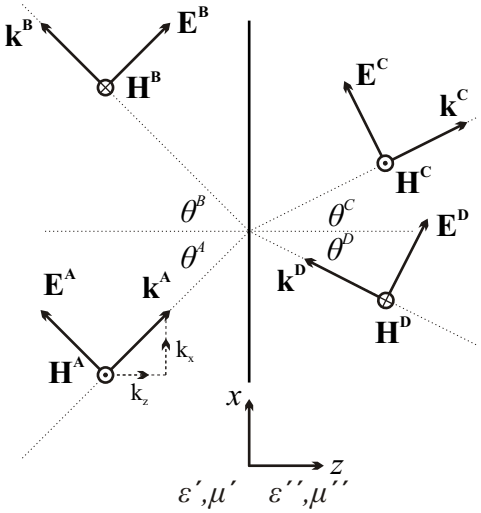

Fig. E.1: Domain setup for two impinging and two reflecting plane waves from a flat interface.

The electric fields on each side of the interface, which are all of the same temporal frequency, can be described by

$$\mathbf{E}(x,z)|_{z<0} = \mathbf{E}^A e^{i(\mathbf{k}^A.\mathbf{r}-\omega t)} + \mathbf{E}^B e^{i(\mathbf{k}^B.\mathbf{r}-\omega t)} \quad \text{(E.1a)}$$

$$\mathbf{E}(x,z)|_{z>0} = \mathbf{E}^C e^{i(\mathbf{k}^C.\mathbf{r}-\omega t)} + \mathbf{E}^D e^{i(\mathbf{k}^D.\mathbf{r}-\omega t)} \quad \text{(E.1b)}$$

where $\mathbf{k}^A$ is the wavenumber for the incident plane wave described by $\mathbf{E}^A$ and $\mathbf{H}^A$, and so on for B, C, and D. From the diagram we can break the wavenumber vector into its x and z components. For plane-wave A the wavenumber can be written

$$\mathbf{k}^A.\mathbf{r} = |\mathbf{k}^A|\sin(\theta^A)\hat{x} + |\mathbf{k}^A|\cos(\theta^A)\hat{z} \quad \text{(E.2)}$$

where θ^A is the angle the plane-wave A makes with the normal. The $\mathbf{k}$-vectors components can then be defined in the x and z directions like so

$$k_x^A = \mathbf{k}^A \sin(\theta^A) \tag{E.3a}$$
$$k_z^A = \mathbf{k}^A \cos(\theta^A) \tag{E.3b}$$

and extended to all wavenumbers in the following manner

$$\mathbf{k}^A.\mathbf{r} = k_x^A \hat{x} + k_z^A \hat{z} \tag{E.4a}$$
$$\mathbf{k}^B.\mathbf{r} = k_x^B \hat{x} - k_z^B \hat{z} \tag{E.4b}$$
$$\mathbf{k}^C.\mathbf{r} = k_x^C \hat{x} + k_z^C \hat{z} \tag{E.4c}$$
$$\mathbf{k}^D.\mathbf{r} = k_x^D \hat{x} - k_z^D \hat{z}. \tag{E.4d}$$

By substituting for all wavenumbers we get

$$\mathbf{E}(x,z)|_{z<0} = \mathbf{E}^A e^{i(k_x^A x + k_z^A z - \omega t)} + \mathbf{E}^B e^{i(k_x^B x - k_z^B z - \omega t)} \tag{E.5a}$$
$$\mathbf{E}(x,z)|_{z>0} = \mathbf{E}^C e^{i(k_x^C x + k_z^C z - \omega t)} + \mathbf{E}^D e^{i(k_x^D x - k_z^D z - \omega t)}. \tag{E.5b}$$

If we now break the electric components into their x and z components, and take the static case where $t = 0$ and ωt can be removed (i.e. steady state), the result is

$$E_x(x,z)|_{z<0} = |\mathbf{E}^A| \cos(\theta^A) e^{i(k_x^A x + k_z^A z)} + |\mathbf{E}^B| \cos(\theta^B) e^{i(k_x^B x - k_z^B z)} \tag{E.6a}$$
$$E_z(x,z)|_{z<0} = -|\mathbf{E}^A| \sin(\theta^A) e^{i(k_x^A x + k_z^A z)} + |\mathbf{E}^B| \sin(\theta^B) e^{i(k_x^B x - k_z^B z)} \tag{E.6b}$$

and

$$E_x(x,z)|_{z>0} = |\mathbf{E}^C| \cos(\theta^C) e^{i(k_x^C x + k_z^C z)} + |\mathbf{E}^D| \cos(\theta^D) e^{i(k_x^D x - k_z^D z)} \tag{E.7a}$$
$$E_z(x,z)|_{z>0} = -|\mathbf{E}^C| \sin(\theta^C) e^{i(k_x^C x + k_z^C z)} + |\mathbf{E}^D| \sin(\theta^D) e^{i(k_x^D x - k_z^D z)} \tag{E.7b}$$

which describes the fields on both sides on the interface.

Through phase matching in the x-direction [207] we necessarily have the angle of incidence equal to the angle of reflection giving

$$\theta^A = \theta^B = \theta' \tag{E.8a}$$
$$\theta^C = \theta^D = \theta'' \tag{E.8b}$$

and as the plane-waves A and B, and C and D are located in the same medium we have

$$k^A = k^B = k' \tag{E.9a}$$
$$k^C = k^D = k''. \tag{E.9b}$$

Now, for each vector we can substitute

$$E_x^A = |\mathbf{E}^A|\cos(\theta^A) \tag{E.10a}$$
$$E_z^A = |\mathbf{E}^A|\sin(\theta^A) \tag{E.10b}$$

arriving at

$$E_x(x,z)|_{z<0} = E_x^A e^{i(k_x^{'}x+k_z^{'}z)} + E_x^B e^{i(k_x^{'}x-k_z^{'}z)} \tag{E.11a}$$
$$E_z(x,z)|_{z<0} = -E_z^A e^{i(k_x^{'}x+k_z^{'}z)} + E_z^B e^{i(k_x^{'}x-k_z^{'}z)} \tag{E.11b}$$

and

$$E_x(x,z)|_{z>0} = E_x^C e^{i(k_x^{''}x+k_z^{''}z)} + E_x^D e^{i(k_x^{''}x-k_z^{''}z)} \tag{E.12a}$$
$$E_z(x,z)|_{z>0} = -E_z^C e^{i(k_x^{''}x+k_z^{''}z)} + E_z^D e^{i(k_x^{''}x-k_z^{''}z)}. \tag{E.12b}$$

At $z = 0$ the equations must equate and we can arbitrarily take the point $x = 0$ to get

$$E_x^A + E_x^B = E_x^C + E_x^D. \tag{E.13}$$

Following the same approach for the magnetic field we get

$$H_y(x,z)|_{z<0} = H_y^A e^{i(k_x^{'}x+k_z^{'}z)} - H_y^B e^{i(k_x^{'}x-k_z^{'}z)} \tag{E.14}$$

and

$$H_y(x,z)|_{z>0} = H_y^C e^{i(k_x^{''}x+k_z^{''}z)} - H_y^D e^{i(k_x^{''}x-k_z^{''}z)}. \tag{E.15}$$

Noting that the second terms are this time subtracted and that in this case

$$H_y^A = |\mathbf{H}^A|. \tag{E.16}$$

By equating at $z = 0$ and $x = 0$ we have

$$H_y^A - H_y^B = H_y^C - H_y^D. \tag{E.17}$$

From Maxwell's equations [207] we can define a plane-wave as impedance for a TM wave as

$$\eta = \frac{\mathbf{E}}{\mathbf{H}} = \frac{k}{\omega\epsilon} \tag{E.18}$$

where ω is the angular velocity. The ratios of the electric and magnetic field components can be expressed as

$$\eta \cos(\theta^{'}) = \frac{|\mathbf{E}^A| \cos(\theta^{'})}{|\mathbf{H}^A|} = \frac{E_x^A}{H_y^A} = \frac{\mathbf{k}^{'} \cos(\theta^{'})}{\omega\epsilon} = \frac{k_z^{'}}{\omega\epsilon} \tag{E.19}$$

and by rearrangement gives

$$H_y^A = \frac{E_x^A \omega\epsilon}{k_z^{'}}. \tag{E.20}$$

This can be substituted into Equ. E.17 to provide us with a second equation linking the electric field components:

$$\frac{\epsilon^{'}}{k_z^{'}} \left(E_x^A - E_x^B\right) = \frac{\epsilon^{''}}{k_z^{''}} \left(E_x^C - E_x^D\right) \tag{E.21}$$

With the two equations E.13 and E.21 we can solve for E_x^C and E_x^D. From Equ. E.13:

$$E_x^D = -E_x^C + E_x^A + E_x^B \tag{E.22}$$

which substitutes into Equ. E.21 to give

$$E_x^C = \frac{1}{2}\frac{k_z^{''}}{\epsilon^{''}} \left(E_x^A \left(\frac{\epsilon^{'}}{k_z^{'}} + \frac{\epsilon^{''}}{k_z^{''}} \right) + E_x^B \left(\frac{\epsilon^{''}}{k_z^{''}} - \frac{\epsilon^{'}}{k_z^{'}} \right) \right). \tag{E.23}$$

This can be then substituted back into E.22 to give E_x^D like so:

$$E_x^D = \frac{1}{2}\frac{k_z^{''}}{\epsilon^{''}} \left(E_x^A \left(\frac{\epsilon^{'}}{k_z^{'}} - \frac{\epsilon^{''}}{k_z^{''}} \right) + E_x^B \left(\frac{\epsilon^{''}}{k_z^{''}} + \frac{\epsilon^{'}}{k_z^{'}} \right) \right). \tag{E.24}$$

These equations can be placed in matrix form to describe the modification of the wave coefficients by through the interface.

$$\begin{bmatrix} E_x^C \\ E_x^D \end{bmatrix} = \frac{1}{2}\frac{k_z^{''}}{\epsilon^{''}} \begin{bmatrix} \frac{\epsilon^{'}}{k_z^{'}} + \frac{\epsilon^{''}}{k_z^{''}} & \frac{\epsilon^{''}}{k_z^{''}} - \frac{\epsilon^{'}}{k_z^{'}} \\ \frac{\epsilon^{''}}{k_z^{''}} - \frac{\epsilon^{'}}{k_z^{'}} & \frac{\epsilon^{''}}{k_z^{''}} + \frac{\epsilon^{'}}{k_z^{'}} \end{bmatrix} \begin{bmatrix} E_x^A \\ E_x^B \end{bmatrix} = T(0) \begin{bmatrix} E_x^A \\ E_x^B \end{bmatrix}. \tag{E.25}$$

The transmission and reflection coefficients of this interface can now be determined.

If we set the incident wave travelling in the positive z-direction to unity and suppose

that there is no incident wave on the other side of the interface we have

$$E_z^A = 1 \tag{E.26a}$$
$$E_z^B = r \tag{E.26b}$$
$$E_z^C = t \tag{E.26c}$$
$$E_z^D = 0 \tag{E.26d}$$

where r and t are the reflection and transmission coefficients, respectively. By substituting this into are arbitrary T-matrix we have

$$\begin{bmatrix} t \\ 0 \end{bmatrix} = \begin{bmatrix} T_{11} & T_{12} \\ T_{21} & T_{22} \end{bmatrix} \begin{bmatrix} 1 \\ r \end{bmatrix}. \tag{E.27}$$

Expanding and solving for r and t gives

$$r = -\frac{T_{21}}{T_{22}} \tag{E.28a}$$
$$t = \frac{T_{11}T_{22} - T_{12}T_{21}}{T_{22}}. \tag{E.28b}$$

From Equ. E.25 the reflection and transmission coefficients for an interface at the origin become

$$r = \frac{\epsilon'' k_z' - \epsilon' k_z''}{\epsilon'' k_z' + \epsilon' k_z''} \tag{E.29a}$$
$$t = \frac{2\epsilon' k_z''}{\epsilon'' k_z' + \epsilon' k_z''}. \tag{E.29b}$$

This formulation describes the 1D nature for one interface at the z-origin. Now, an extension is required to allow the interface to be placed at any point on the z-axis. Once we have done this we will be able to describe to interfaces in space and by equating the fields between them we will have the tools to find the transmission through a slab.

Figure E.2 shows the setup for an interface at the point $z = d$. Here $\mathbf{A}^d$ represents $E_x^{A^d} e^{ik_z' z^d}$, and so on for each component. There equations are formulated in the z^d co-ordinate system and owing that the interface is located at $z^d = 0$ we can use our previous derivation to calculate the T-matrix coefficient translation as

$$\begin{bmatrix} E_x^{C^d} \\ E_x^{D^d} \end{bmatrix} = T^d(0) \begin{bmatrix} E_x^{A^d} \\ E_x^{B^d} \end{bmatrix}. \tag{E.30}$$

However, we want all matrix calculations to occur in the same co-ordinate system so that we can equate coefficients. Given that the co-ordinate translation is $z^d = z + d$,

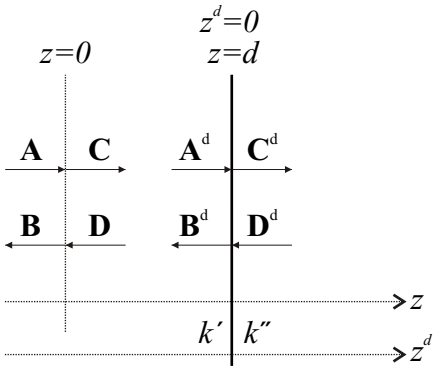

Fig. E.2: Schematic setup for an interface located at $z = d$.

for each component we can translate into the z co-ordinate system like so:

$$E_x^{A^d} e^{ik_z' z^d} = E_x^A e^{ik_z'(z+d)} = E_x^A e^{ik_z' d} e^{ik_z' z}. \tag{E.31}$$

By following through with the other components for both the electric and magnetic fields and then comparing with the previous T-matrix derivation, we have the following T-matrix equation

$$\begin{aligned}
\begin{bmatrix} E_x^C e^{ik_z'' d} \\ E_x^D e^{-ik_z'' d} \end{bmatrix} &= T^d(0) \begin{bmatrix} E_x^A e^{ik_z' d} \\ E_x^B e^{-ik_z' d} \end{bmatrix} \\
\begin{bmatrix} e^{ik_z'' d} & 0 \\ 0 & e^{-ik_z'' d} \end{bmatrix} \begin{bmatrix} E_x^C \\ E_x^D \end{bmatrix} &= T^d(0) \begin{bmatrix} e^{ik_z' d} & 0 \\ 0 & e^{-ik_z' d} \end{bmatrix} \begin{bmatrix} E_x^A \\ E_x^B \end{bmatrix}
\end{aligned} \tag{E.32}$$

which can be rearranged to give

$$\begin{bmatrix} E_x^C \\ E_x^D \end{bmatrix} = \begin{bmatrix} e^{-ik_z'' d} & 0 \\ 0 & e^{ik_z'' d} \end{bmatrix} T^d(0) \begin{bmatrix} e^{ik_z' d} & 0 \\ 0 & e^{-ik_z' d} \end{bmatrix} \begin{bmatrix} E_x^A \\ E_x^B \end{bmatrix}. \tag{E.33}$$

We now have a T-matrix describing an interface at an arbitrary location on the z-axis:

$$T(d) = \begin{bmatrix} e^{-ik_z'' d} & 0 \\ 0 & e^{ik_z'' d} \end{bmatrix} T^d(0) \begin{bmatrix} e^{ik_z' d} & 0 \\ 0 & e^{-ik_z' d} \end{bmatrix} \tag{E.34}$$

which calculates the coefficients in the $z = 0$ plane. By using appropriate phase shifts we can then determine the fields at any point on the z-axis, but care must be taken to ensure the correct wavenumber is used and that the fields of interest are valid at the point of interest. The solution for a Transverse Electric (TE) polarised wave follows

trivially by substituting

$$\frac{k}{\epsilon} = \frac{\mu}{k} \tag{E.35}$$

REFERENCES

[1] Image from wikipedia.org. Lithography print. *Permission not required for reprinting*, 2005.

[2] H. I. Smith. Low cost nanolithography with nanoaccuracy. *Physica E*, 11(2-3):104–109, 2001.

[3] Intel. Moores law timeline. *http://www.Intel.com*, 2005.

[4] T. Ito, M. Ogino, T. Yamada, Y. Inao, T. Yamaguchi, N. Mizutani, and R. Kuroda. Fabrication of sub-100 nm patterns using near-field mask lithography with ultra-thin resist process. *J. Photopolym. Sci. Tec.*, 18(3):435–441, 2005.

[5] J.R. Minkel. Left-handed materials debate heats up. *PhysicsWeb*, 38(8):50–+, 2002.

[6] D.R. Smith, W.J. Padilla, D.C. Vier, S.C. Nemat-Nasser, and S. Schultz. Composite medium with simultaneously negative permeability and permittivity. *Phys. Rev. Lett.*, 84(18):4184–4187, 2000.

[7] R.A. Shelby, D.R. Smith, and S. Schultz. Experimental verification of a negative index of refraction. *Science*, 292(5514):77–79, 2001.

[8] A. N. Lagarkov and V. N. Kissel. Near-perfect imaging in a focusing system based on a left-handed-material plate. *Phys. Rev. Lett.*, 92(7):–, 2004.

[9] A.K. Iyer, P.C. Kremer, and G.V. Eleftheriades. Experimental and theoretical verification of focusing in a large, periodically loaded transmission line negative refractive index metamaterial. *Opt. Express*, 11(7):696–708, 2003.

[10] A. N. Grigorenko, A. K. Geim, H. F. Gleeson, Y. Zhang, A. A. Firsov, I. Y. Khrushchev, and J. Petrovic. Nanofabricated media with negative permeability at visible frequencies. *Nature*, 438(7066):335–338, 2005.

[11] P. B. Johnson and R. W. Christy. Optical constants of the noble metals. *Phys. Rev. B*, 6(12):4370–4379, 2003.

[12] http://www.suss.com. Uv400 lamp specturm. 2006.

[13] E. H. Synge. A suggested method for extending microscopic resolution into the ultra-microscopic region. *Philos Mag*, 6(35):356–362, 1928.

[14] E. Betzig, J. K. Trautman, T. D. Harris, J. S. Weiner, and R. L. Kostelak. Breaking the diffraction barrier - optical microscopy on a nanometric scale. *Science*, 251(5000):1468–1470, 1991.

[15] M. M. Alkaisi, R. J. Blaikie, S. J. McNab, R. Cheung, and D. R. S. Cumming. Sub-diffraction-limited patterning using evanescent near-field optical lithography. *Appl. Phys. Lett.*, 75(22):3560–3562, 1999.

[16] S.J. McNab. *Evanescent Near-Field Optical Lithography Overcoming the Diffraction Limit*. PhD thesis, Electrical and Electronic Engineeing, University of Canterbury, 2001.

[17] J. G. Goodberlet and H. Kavak. Patterning sub-50 nm features with near-field embedded-amplitude masks. *Appl. Phys. Lett.*, 81(7):1315–1317, 2002.

[18] J. B. Pendry. Negative refraction makes a perfect lens. *Phys. Rev. Lett.*, 85(18):3966–3969, 2000.

[19] A. Lakhtakia and M. McCall. Focus on negative refraction. *New J. Phys.*, 7:–, 2005.

[20] S. A. Ramakrishna. Physics of negative refractive index materials. *Rep. Prog. Phys.*, 68(2):449–521, 2005.

[21] V. G. Veselago. The electrodynamics of substances with simultaneously negative values of ϵ and μ. *Sov. Phys. Usp.*, 10(4):509–514, 1968.

[22] R. J. Blaikie and S. J. McNab. Simulation study of 'perfect lenses' for near-field optical nanolithography. *Microelectron. Eng.*, 61-62:97–103, 2002.

[23] D. O. S. Melville, R. J. Blaikie, and C. R. Wolf. Submicron imaging with a planar silver lens. *Appl. Phys. Lett.*, 84(22):4403–4405, 2004.

[24] D. O. S. Melville and R. J. Blaikie. Super-resolution imaging through a planar silver layer. *Opt. Express*, 13(6):2127–2134, 2005.

[25] D. O. S. Melville and R. J. Blaikie. Experimental comparison of resolution and pattern fidelity in single- and double-layer planar lens lithography. *J. Opt. Soc. Am. B*, 23(3):page numbers not available at time of printing, 2006.

[26] S. A. Ramakrishna, J. B. Pendry, M. C. K. Wiltshire, and W. J. Stewart. Imaging the near field. *J. Mod. Opt.*, 50(9):1419–1430, 2003.

[27] H Hogan. Silver superlens enables subdiffraction-limit imaging. *Photon. Spectra*, 39(5):58–+, 2005.

[28] [Anon]. Super-lens brings fine features into focus. *New Scientist*, 186(2497):19, 2005.

[29] J. Wallace. Silver planar lens achieves super-resolution. *Laser Focus World*, 41(6):15–+, 2005.

[30] D. Smith. Superlens breaks optical barrier. *Phys World*, 18(8):23–24, 2005.

[31] N. Fang, H. Lee, C. Sun, and X. Zhang. Sub-diffraction-limited optical imaging with a silver superlens. *Science*, 308(5721):534–537, 2005.

[32] Alois Senefelder. *The invention of lithography*. The Fuchs & Lang Manufacturing Company, New York, 1911.

[33] Stephen A. Campbell. Optical lithography. In *The science and engineering of microelectronic fabrication*, pages 151–182. Oxford University Press, New York, 2nd edition, 2001.

[34] George O. Reynolds and George B. Parrent. *The New physical optics notebook : tutorials in Fourier optics*. Spie Optical Engineering Press ; American Institute of Physics, Bellingham, Wash. New York, N.Y., 1989.

[35] George O. Reynolds and George B. Parrent. Huygen's principle. In *The New physical optics notebook : tutorials in Fourier optics*, pages 1–7. Spie Optical Engineering Press ; American Institute of Physics, Bellingham, Wash. New York, N.Y., 1989.

[36] George O. Reynolds and George B. Parrent. Resolution in terms of impulse response. In *The New physical optics notebook : tutorials in Fourier optics*, pages 38–43. SPIE Optical Engineering Press ; American Institute of Physics, Bellingham, Wash. New York, N.Y., 1989.

[37] H. Kinoshita. History of extreme ultraviolet lithography. *J. Vac. Sci. Technol. B*, 23(6):2584–2588, 2005.

[38] Y. Q. Li and G. S. Huang. Full field analysis of lithography performance for arf immersion lithography. *J. Vac. Sci. Technol. B*, 23(6):2679–2683, 2005.

[39] Q. Leonard, D. Malueg, J. Wallace, J. W. Taylor, S. Dhuey, F. Cerrina, B. Boerger, R. Selzer, M. Yu, Y. Ma, K. Myers, M. Trybendis, E. Moon, and H. I. Smith. Development, installation, and performance of the x-ray stepper jsal 5c. *J. Vac. Sci. Technol. B*, 23(6):2896–2902, 2005.

[40] L. Chen, X. G. Deng, J. Wang, K. Takahashi, and F. Liu. Defect control in nanoimprint lithography. *J. Vac. Sci. Technol. B*, 23(6):2933–2938, 2005.

[41] S. Y. Chou, P. R. Krauss, and P. J. Renstrom. Imprint of sub-25 nm vias and trenches in polymers. *Appl. Phys. Lett.*, 67(21):3114–3116, 1995.

[42] S. Y. Chou, P. R. Krauss, and P. J. Renstrom. Nanoimprint lithography. *J. Vac. Sci. Technol. B*, 14(6):4129–4133, 1996.

[43] S. Y. Chou, P. R. Krauss, W. Zhang, L. J. Guo, and L. Zhuang. Sub-10 nm imprint lithography and applications. *J. Vac. Sci. Technol. B*, 15(6):2897–2904, 1997.

[44] M. Colburn, S. Johnson, M. Stewart, S. Damle, T. Bailey, B. Choi, M. Wedlake, T. Michaelson, S. V. Sreenivasan, J. Ekerdt, and C. G. Willson. Step-and-flash imprint lithography. *Proc. SPIE*, 379, 1999.

[45] M. Colburn, T. Bailey, B. J. Choi, J. G. Ekerdt, S. V. Sreenivasan, and C. G. Willson. Development and advantages of step-and-flash lithography. *Solid State Technol*, 44(7):67–+, 2001.

[46] T. Bailey, B. J. Choi, M. Colburn, M. Meissl, S. Shaya, J. G. Ekerdt, S. V. Sreenivasan, and C. G. Willson. Step and flash imprint lithography: Template surface treatment and defect analysis. *J. Vac. Sci. Technol. B*, 18(6):3572–3577, 2000.

[47] W. J. Dauksher, K. J. Nordquist, N. V. Le, K. A. Gehoski, D. P. Mancini, D. J. Resnick, L. Casoose, R. Bozak, R. White, J. Csuy, and D. Lee. Repair of step and flash imprint lithography templates. *J. Vac. Sci. Technol. B*, 22(6):3306–3311, 2004.

[48] K. Watanabe, K. Kanda, Y. Haruyama, T. Kaito, and S. Matsui. Nanoimprint mold repair by ga+ focused-ion-beam direct etching. *Jpn J. Appl. Phys. 1*, 43(11A):7769–7772, 2004.

[49] A. D. Wilson. X-ray-lithography in IBM, 1980-1992, the development years. *Ibm J Res Dev*, 37(3):299–318, 1993.

[50] S. Hector. Status and future of x-ray lithography. *Microelectron. Eng.*, 42:25–30, 1998.

[51] S. Y. Chou, C. Keimel, and J. Gu. Ultrafast and direct imprint of nanostructures in silicon. *Nature*, 417(6891):835–837, 2002.

[52] H. Tan, A. Gilbertson, and S. Y. Chou. Roller nanoimprint lithography. *J. Vac. Sci. Technol. B*, 16(6):3926–3928, 1998.

[53] H Kawata, J.M. Carter, A. Yen, and Smith H.I. Optical projection lithography using lenses with numerical apertures greater than unity. *Microelectron. Eng.*, 9(1-4):31–36, 1989.

[54] H. Kawata, I. Matsumura, H. Yoshida, and K. Murata. Fabrication of 0.2 μm fine patterns using optical projection lithography with an oil immersion lens. *Jpn J. Appl. Phys. 1*, 31(12B):4174–4177, 1992.

[55] T. A. Brunner. Why optical lithography will live forever. *J. Vac. Sci. Technol. B*, 21(6):2632–2637, 2003.

[56] H. I. Smith. Fabrication techniques for surface-acoustic-wave and thin-film optical devices. *Proc. IEEE*, 62(10):1361–1387, 1974.

[57] H. I. Smith, N. Efremow, and P. L. Kelley. Photolithographic contact printing of 4000a linewidth patterns. *J. Electrochem. Soc.*, 121(11):1503–1506, 1974.

[58] U. C. Fischer and H. P. Zingsheim. Sub-microscopic pattern replication with visible-light. *J. Vac. Sci. & Technol.*, 19(4):881–885, 1981.

[59] R. J. Blaikie, M. M. Alkaisi, S. J. McNab, D. R. S. Cumming, R. Cheung, and D. G. Hasko. Nanolithography using optical contact exposure in the evanescent near field. *Microelectron. Eng.*, 46(1-4):85–88, 1999.

[60] M. M. Alkaisi, R. J. Blaikie, and S. J. McNab. 70 nm features on 140 nm period using evanescent near field optical lithography. *Microelectron. Eng.*, 53(1-4):237–240, 2000.

[61] J. A. Rogers, K. E. Paul, R. J. Jackman, and G. M. Whitesides. Using an elastomeric phase mask for sub-100 nm photolithography in the optical near field. *Appl. Phys. Lett.*, 70(20):2658–2660, 1997.

[62] J. Aizenberg, J. A. Rogers, K. E. Paul, and G. M. Whitesides. Imaging the irradiance distribution in the optical near field. *Appl. Phys. Lett.*, 71(26):3773–3775, 1997.

[63] R. J. Blaikie and S. J. McNab. Evanescent interferometric lithography. *Appl. Opt.*, 40(10):1692–1698, 2001.

[64] H. Schmid, H. Biebuyck, B. Michel, O. J. F. Martin, and N. B. Piller. Light-coupling masks: An alternative, lensless approach to high-resolution optical contact lithography. *J. Vac. Sci. Technol. B*, 16(6):3422–3425, 1998.

[65] H. Schmid, H. Biebuyck, B. Michel, and O. J. F. Martin. Light-coupling masks for lensless, sub-wavelength optical lithography. *Appl. Phys. Lett.*, 72(19):2379–2381, 1998.

[66] J. G. Goodberlet and B. L. Dunn. Deep-ultraviolet contact photolithography. *Microelectron. Eng.*, 53(1-4):95–99, 2000.

[67] M. Naya, I. Tsuruma, T. Tani, A. Mukai, S. Sakaguchi, and S. Yasunami. Near-field optical photolithography for high-aspect-ratio patterning using bilayer resist. *Appl. Phys. Lett.*, 86(20):–, 2005.

[68] Toshiki Ito (PersonalCommunication), 2005.

[69] H. Lamb. On group-velocity. *Proc. London Math. Soc.*, 1:473–479, 1904.

[70] A. Schuster. *An Introduction to the Theory of Optics*. Edward Arnold, London, 1904.

[71] H.C. Pocklington. Growth of a wave-group when the group velocity is negative. *Nature*, 71:607–608, 1905.

[72] L.I. Mandel'shtam. Group velocity in crystalline arrays. *Zh. Eksp. Teor. Fiz.*, 15:475–478, 1945.

[73] A. L. Pokrovsky and A. L. Efros. Lens based on the use of left-handed materials. *Appl. Opt.*, 42(28):5701–5705, 2003.

[74] J.B. Pendry, A.J. Holden, D.J. Robbins, and W.J. Stewart. Magnetism from conductors and enhanced nonlinear phenomena. *IEEE Trans. on Microwave Theory and Techniques*, 47(11):2075–2084, 1999.

[75] G.W. 'tHooft. Comment on "Negative refraction makes a perfect lens". *Phys. Rev. Lett.*, 87(24):art–249701, 2001.

[76] J.M. Williams. Some problems with negative refraction. *Phys. Rev. Lett.*, 8724(24), 2001.

[77] J. Pendry. Comment on “Negative refraction makes a perfect lens” - Reply. *Phys. Rev. Lett.*, 8724(24):art–249702, 2001.

[78] J. Pendry. Some problems with negative refraction - reply. *Phys. Rev. Lett.*, 8724(24), 2001.

[79] P.M. Valanju, R.M. Walser, and A.P. Valanju. Wave refraction in negative-index media: Always positive and very inhomogeneous. *Phys. Rev. Lett.*, 88(18), 2002.

[80] J.B. Pendry and D.R. Smith. Comment on "Wave refraction in negative-index media: Always positive and very inhomogeneous". *Phys. Rev. Lett.*, 90(2), 2003.

[81] P.M. Valanju, R.M. Walser, and A.P. Valanju. Comment on “wave refraction in negative-index media: Always positive and very inhomogeneous” - reply. *Phys. Rev. Lett.*, 90(2), 2003.

[82] S. Foteinopoulou, E.N. Economou, and C.M. Soukoulis. Refraction in media with a negative refractive index. *Phys. Rev. Lett.*, 90(10):107402, 2003.

[83] P. Kolinko and D.R. Smith. Numerical study of electromagnetic waves interacting with negative index materials. *Opt. Express*, 11(7):640–648, 2003.

[84] N. Garcia and M. Nieto-Vesperinas. Left-handed materials do not make a perfect lens. *Phys. Rev. Lett.*, 88(20):207403, 2002.

[85] N. Garcia and M. Nieto-Vesperinas. Is there an experimental verification of a negative index of refraction yet? *Opt. Lett.*, 27(11):885–887, 2002.

[86] A.A. Houck, J.B. Brock, and I.L. Chuang. Experimental observations of a left-handed material that obeys snell's law. *Phys. Rev. Lett.*, 90(13):137401, 2003.

[87] D. Felbacq and A. Moreau. Direct evidence of negative refraction at media with negative epsilon and mu. *J. Opt. A: Pure Appl. Opt.*, 5(3):L9–L11, 2003.

[88] J.B. Pendry. Comment on “Left-handed materials do not make a perfect lens”. *Phys. Rev. Lett.*, 91(9), 2003.

[89] N. Garcia. Comment on “Left-handed materials do not make a perfect lens” - Reply. *Phys. Rev. Lett.*, 91(9), 2003.

[90] R. Marques and D. R. Smith. Comment on "electrodynamics of metallic photonic crystals and the problem of left-handed materials". *Phys. Rev. Lett.*, 92(5):–, 2004.

[91] A. L. Pokrovsky and A. L. Efros. Electrodynamics of metallic photonic crystals and the problem of left-handed materials. *Phys. Rev. Lett.*, 89(9):–, 2002.

[92] A. L. Pokrovsky and A. L. Efros. Comment on "electrodynamics of metallic photonic crystals and the problem of left-handed materials" - reply. *Phys. Rev. Lett.*, 92(11):119401, 2004.

[93] J.B. Pendry, A.J. Holden, W.J. Stewart, and I. Youngs. Extremely low frequency plasmons in metallic mesostructures. *Phys. Rev. Lett.*, 76(25):4773–4776, 1996.

[94] S. A. Cummer and B. I. Popa. Wave fields measured inside a negative refractive index metamaterial. *Appl. Phys. Lett.*, 85(20):4564–4566, 2004.

[95] R.W. Ziolkowski. Design, fabrication, and testing of double negative metamaterials. *Ieee Transactions on Antennas and Propagation*, 51(7):1516–1529, 2003.

[96] Z. L. Lu, S. Y. Shi, C. A. Schuetz, and D. W. Prather. Experimental demonstration of negative refraction imaging in both amplitude and phase. *Opt. Express*, 13(6):2007–2012, 2005.

[97] X. D. Zhang and Z. Y. Liu. Negative refraction of acoustic waves in two-dimensional phononic crystals. *Appl. Phys. Lett.*, 85(2):341–343, 2004.

[98] X. H. Hu and C. T. Chan. Refraction of water waves by periodic cylinder arrays. *Phys. Rev. Lett.*, 95(15):–, 2005.

[99] V. A. Podolskiy and E. E. Narimanov. Near-sighted superlens. *Opt. Lett.*, 30(1):75–77, 2005.

[100] J. Zhou, L. Zhang, G. Tuttle, T. Koschny, and C.M. Soukoulis. Negative index materials using simple short wire pairs. *Phys. Rev. B*, 73:041101, 2006.

[101] G.V. Eleftheriades, A.K. Iyer, and P.C. Kremer. Planar negative refractive index media using periodically l-c loaded transmission lines. *Ieee Transactions on Microwave Theory and Techniques*, 50(12):2702–2712, 2002.

[102] J. D. Joannopoulos, Robert D. Meade, and Joshua N. Winn. *Photonic crystals : molding the flow of light*. Princeton University Press, Princeton, N.J., 1995.

[103] Z.M. Zhang and C.J. Fu. Unusual photon tunneling in the presence of a layer with a negative refractive index. *Appl. Phys. Lett.*, 80(6):1097–1099, 2002.

[104] M.L. Povinelli, S.G. Johnson, J.D. Joannopoulos, and J.B. Pendry. Toward photonic-crystal metamaterials: Creating magnetic emitters in photonic crystals. *Appl. Phys. Lett.*, 82(7):1069–1071, 2003.

[105] L. Wu, S.L. He, and L.F. Shen. Band structure for a one-dimensional photonic crystal containing left-handed materials. *Phys. Rev. B*, 67(23), 2003.

[106] G. Shvets and Y. A. Urzhumov. Engineering the electromagnetic properties of periodic nanostructures using electrostatic resonances. *Phys. Rev. Lett.*, 93(24):–, 2004.

[107] C. Y. Luo, S. G. Johnson, J. D. Joannopoulos, and J. B. Pendry. Subwavelength imaging in photonic crystals. *Phys. Rev. B*, 68(4):–, 2003.

[108] C. Y. Luo, S. G. Johnson, J. D. Joannopoulos, and J. B. Pendry. Negative refraction without negative index in metallic photonic crystals. *Opt. Express*, 11(7):746–754, 2003.

[109] B.C. Gupta and Z. Ye. Disorder effects on the imaging of a negative refractive lens made by arrays of dielectric cylinders. *J. of Appl. Phys.*, 94(4):2173–2176, 2003.

[110] V. M. Shalaev, W. S. Cai, U. K. Chettiar, H. K. Yuan, A. K. Sarychev, V. P. Drachev, and A. V. Kildishev. Negative index of refraction in optical metamaterials. *Opt. Lett.*, 30(24):3356–3358, 2005.

[111] S. Zhang, W. J. Fan, N. C. Panoiu, K. J. Malloy, R. M. Osgood, and S. R. J. Brueck. Experimental demonstration of near-infrared negative-index metamaterials. *Phys. Rev. Lett.*, 95(13):–, 2005.

[112] H. Raether. Surface-plasmons on smooth and rough surfaces and on gratings. *Springer Tr Mod Phys*, 111:1–133, 1988.

[113] P. G. Kik, S. A. Maier, and H. A. Atwater. Image resolution of surface-plasmon-mediated near-field focusing with planar metal films in three dimensions using finite-linewidth dipole sources. *Phys. Rev. B*, 69(4):–, 2004.

[114] T. W. Ebbesen, H. J. Lezec, H. F. Ghaemi, T. Thio, and P. A. Wolff. Extraordinary optical transmission through sub-wavelength hole arrays. *Nature*, 391(6668):667–669, 1998.

[115] R. Zia, M. D. Selker, P. B. Catrysse, and M. L. Brongersma. Geometries and materials for subwavelength surface plasmon modes. *J. Opt. Soc. of Am. A - Optics Image Science and Vision*, 21(12):2442–2446, 2004.

[116] J. R. Krenn and J. C. Weeber. Surface plasmon polaritons in metal stripes and wires. *Philosophical Transactions of the Royal Society of London Series a-Mathematical Physical and Engineering Sciences*, 362(1817):739–756, 2004.

[117] S. A. Maier, M. D. Friedman, P. E. Barclay, and O. Painter. Experimental demonstration of fiber-accessible metal nanoparticle plasmon waveguides for planar energy guiding and sensing. *Appl. Phys. Lett.*, 86(7), 2005.

[118] J. C. Weeber, Y. Lacroute, A. Dereux, E. Devaux, T. Ebbesen, C. Girard, M. U. Gonzalez, and A. L. Baudrion. Near-field characterization of bragg mirrors engraved in surface plasmon waveguides. *Phys. Rev. B*, 70(23), 2004.

[119] M. P. Nezhad, K. Tetz, and Y. Fainman. Gain assisted propagation of surface plasmon polaritons on planar metallic waveguides. *Opt. Express*, 12(17):4072–4079, 2004.

[120] J. A. Dionne, L. A. Sweatlock, H. A. Atwater, and Polman A. Plasmon slot waveguides: Towards chip-scale propagation with subwavelength-scale localization. *Phys. Rev. B*, 73:035407, 2006.

[121] B. Wang and G. P. Wang. Metal heterowaveguides for nanometric focusing of light. *Appl. Phys. Lett.*, 85(16):3599–3601, 2004.

[122] J. R. Krenn, H. Ditlbacher, G. Schider, A. Hohenau, A. Leitner, and F. R. Aussenegg. Surface plasmon micro- and nano-optics. *Journal of Microscopy-Oxford*, 209:167–172, 2003.

[123] H. Ditlbacher, J. R. Krenn, G. Schider, A. Leitner, and F. R. Aussenegg. Two-dimensional optics with surface plasmon polaritons. *Appl. Phys. Lett.*, 81(10):1762–1764, 2002.

[124] A. Drezet, A. L. Stepanov, H. Ditlbacher, A. Hohenau, B. Steinberger, F. R. Aussenegg, A. Leitner, and J. R. Krenn. Surface plasmon propagation in an elliptical corral. *Appl. Phys. Lett.*, 86(7), 2005.

[125] A. Dahlin, M. Zach, T. Rindzevicius, M. Kall, D. S. Sutherland, and F. Hook. Localized surface plasmon resonance sensing of lipid-membrane-mediated biorecognition events. *Journal of the American Chemical Society*, 127(14):5043–5048, 2005.

[126] A. J. Haes and R. P. Van Duyne. A unified view of propagating and localized surface plasmon resonance biosensors. *Analytical and Bioanalytical Chemistry*, 379(7-8):920–930, 2004.

[127] A. J. Haes, S. L. Zou, G. C. Schatz, and R. P. Van Duyne. Nanoscale optical biosensor: Short range distance dependence of the localized surface plasmon resonance of noble metal nanoparticles. *J. Phys. Chem. B*, 108(22):6961–6968, 2004.

[128] E. Hutter and J. H. Fendler. Exploitation of localized surface plasmon resonance. *Advanced Materials*, 16(19):1685–1706, 2004.

[129] R. P. Van Duyne. Molecular plasmonics. *Science*, 306(5698):985–986, 2004.

[130] M. L. Brongersma, J. W. Hartman, and H. A. Atwater. Electromagnetic energy transfer and switching in nanoparticle chain arrays below the diffraction limit. *Phys. Rev. B*, 62(24):R16356–R16359, 2000.

[131] M. Salerno, J. R. Krenn, B. Lamprecht, G. Schider, H. Ditlbacher, N. Felidj, A. Leitner, and F. R. Aussenegg. Plasmon polaritons in metal nanostructures: the optoelectronic route to nanotechnology. *Opto-Electronics Review*, 10(3):217–224, 2002.

[132] W. L. Barnes, A. Dereux, and T. W. Ebbesen. Surface plasmon subwavelength optics. *Nature*, 424(6950):824–830, 2003.

[133] I. I. Smolyaninov, J. Elliott, A. V. Zayats, and C. C. Davis. Far-field optical microscopy with a nanometer-scale resolution based on the in-plane image magnification by surface plasmon polaritons. *Phys. Rev. Lett.*, 94(5):–, 2005.

[134] J. Hashizume and F. Koyama. Plasmon enhanced optical near-field probing of metal nanoaperture surface emitting laser. *Opt. Express*, 12(25):6391–6396, 2004.

[135] S. Maslovski, S. Tretyakov, and P. Alitalo. Near-field enhancement and imaging in double planar polariton-resonant structures. *J. of Appl. Phys.*, 96(3):1293–1300, 2004.

[136] W. X. Sun and Z. X. Shen. Optimizing the near field around silver tips. *J. Opt. Soc. of Am. A - Optics Image Science and Vision*, 20(12):2254–2259, 2003.

[137] A. S. Barker. Direct optical coupling to surface excitations. *Phys. Rev. Lett.*, 28(14):892–+, 1972.

[138] S.N. Jasperso and S.E. Schnatte. Photon-surface-plasmon coupling in thick Ag foils. *Phys. Rev.*, 188(2):759–+, 1969.

[139] N. Fang, Z.W. Liu, T.J. Yen, and X. Zhang. Regenerating evanescent waves from a silver superlens. *Opt. Express*, 11(7):682–687, 2003.

[140] P. Andrew and W. L. Barnes. Energy transfer across a metal film mediated by surface plasmon polaritons. *Science*, 306(5698):1002–1005, 2004.

[141] J. Seidel, F. I. Baida, L. Bischoff, B. Guizal, S. Grafstrom, D. Van Labeke, and L. M. Eng. Coupling between surface plasmon modes on metal films. *Phys. Rev. B*, 69(12):–, 2004.

[142] Z. W. Liu, N. Fang, T. J. Yen, and X. Zhang. Rapid growth of evanescent wave by a silver superlens. *Appl. Phys. Lett.*, 83(25):5184–5186, 2003.

[143] H. Lee, Y. Xiong, N. Fang, W. Srituravanich, S. Durant, M. Ambati, C. Sun, and X. Zhang. Realization of optical superlens imaging below the diffraction limit. *New J. Phys.*, 7:–, 2005.

[144] A. Ono, J. Kato, and S. Kawata. Subwavelength optical imaging through a metallic nanorod array. *Phys. Rev. Lett.*, 95:267407, 2005.

[145] Z. W. Liu, J. M. Steele, W. Srituravanich, Y. Pikus, C. Sun, and X. Zhang. Focusing surface plasmons with a plasmonic lens. *Nano Lett.*, 5(9):1726–1729, 2005.

[146] X. H. Hu and C. T. Chan. Photonic crystals with silver nanowires as a near-infrared superlens. *Appl. Phys. Lett.*, 85(9):1520–1522, 2004.

[147] X. Wang and K. Kempa. Effects of disorder on subwavelength lensing in two-dimensional photonic crystal slabs. *Phys. Rev. B*, 71(8):–, 2005.

[148] D. Korobkin, Y. A. Urzhumov, C. Zorman, and G. Shivets. Far-field detection of the super-lensing effect in the mid-infrared: theory and experiment. *J. Mod. Opt.*, 52(16):2351–2364, 2005.

[149] J. G. Goodberlet. Patterning 100 nm features using deep-ultraviolet contact photolithography. *Appl. Phys. Lett.*, 76(6):667–669, 2000.

[150] S. Durant, N. Fang, and X. Zhang. Comment on "Submicron imaging with a planar silver lens" [Appl. Phys. Lett. 84, 4403 (2004)]. *Appl. Phys. Lett.*, 86(12):–, 2005.

[151] D. O. S. Melville and R. J. Blaikie. Response to "comment on 'Submicron imaging with a planar silver lens' " [Appl. Phys. Lett. 86, 126101 (2005)]. *Appl. Phys. Lett.*, 86(12):126102, 2005.

[152] D. O. S. Melville and R. J. Blaikie. Near-field optical lithography using a planar silver lens. *J. Vac. Sci. Technol. B*, 22(6):3470–3474, 2004.

[153] R. J. Blaikie and D. O. S. Melville. Imaging through planar silver lenses in the optical near field. *J. Opt. A: Pure Appl. Opt.*, 7(2):S176–S183, 2005.

[154] D. O. S. Melville and R. J. Blaikie. Improvement to silver superlens performance through narrowband exposure. *Proc. SPIE*, 5928:18–26, 2005.

[155] D. S. Burgess. Silver slab promises subwavelength imaging. *Photon. Spectra*, 38(7):24–+, 2004.

[156] X. G. Luo and T. Ishihara. Surface plasmon resonant interference nanolithography technique. *Appl. Phys. Lett.*, 84(23):4780–4782, 2004.

[157] X. G. Luo and T. Ishihara. Sub-100-nm photolithography based on plasmon resonance. *Jpn J. Appl. Phys. 1*, 43(6B):4017–4021, 2004.

[158] W. Srituravanich, N. Fang, S. Durant, M. Ambati, C. Sun, and X. Zhang. Sub-100 nm lithography using ultrashort wavelength of surface plasmons. *J. Vac. Sci. Technol. B*, 22(6):3475–3478, 2004.

[159] O. J. F. Martin. Surface plasmon illumination scheme for contact lithography beyond the diffraction limit. *Microelectron. Eng.*, 67-8:24–30, 2003.

[160] J. Aizpurua, P. Hanarp, D.S. Sutherland, M. Kall, G.W. Bryant, and F.J.G. de Abajo. Optical properties of gold nanorings. *Phys. Rev. Lett.*, 90(5), 2003.

[161] S.M. Huang, M.H. Hong, B.S. Lukyanchuk, and T.C. Chong. Direct and subdiffraction-limit laser nanofabrication in silicon. *Appl. Phys. Lett.*, 82(26):4809–4811, 2003.

[162] M. D. Malinsky, K. L. Kelly, G. C. Schatz, and R. P. Van Duyne. Nanosphere lithography: Effect of substrate on the localized surface plasmon resonance spectrum of silver nanoparticles. *J. Phys. Chem. B*, 105(12):2343–2350, 2001.

[163] N. Fang and X. Zhang. Imaging properties of a metamaterial superlens. *Appl. Phys. Lett.*, 82(2):161–163, 2003.

[164] D.R. Smith, D. Schurig, M. Rosenbluth, S. Schultz, S.A. Ramakrishna, and J.B. Pendry. Limitations on subdiffraction imaging with a negative refractive index slab. *Appl. Phys. Lett.*, 82(10):1506–1508, 2003.

[165] C. Hafner and R. Ballisti. The multiple multipole method (MMP). *Compel - Int. J. Comp. & Math. in Elec. & Electron. Eng.*, 2(1):1–7, 1983.

[166] S. J. McNab, R. J. Blaikie, and M. M. Alkaisi. Analytic study of gratings patterned by evanescent near field optical lithography. *J. Vac. Sci. Technol. B*, 18(6):2900–2904, 2000.

[167] S.J. McNab and R.J. Blaikie. Contrast in the evanescent near field of $\lambda/20$ period gratings for photolithography. *Appl. Opt.*, 39(1):20–25, 2000.

[168] S. H. Jiang and R. Pike. A full electromagnetic simulation study of near-field imaging using silver films. *New J. Phys.*, 7:–, 2005.

[169] R.W. Ziolkowski and E. Heyman. Wave propagation in media having negative permittivity and permeability. *Phys. Rev. E*, 6405(5):056625, 2001.

[170] S.A. Cummer. Simulated causal subwavelength focusing by a negative refractive index slab. *Appl. Phys. Lett.*, 82(10):1503–1505, 2003.

[171] X.S. Rao and C.K. Ong. Subwavelength imaging by a left-handed material superlens. *Phys. Rev. E*, 68(6):067601, 2003.

[172] M. W. Feise, J. B. Schneider, and P. J. Bevelacqua. Finite-difference and pseudospectral time-domain methods applied to backward-wave metamaterials. *Ieee Transactions on Antennas and Propagation*, 52(11):2955–2962, 2004.

[173] R. W. Ziolkowski. Pulsed and cw gaussian beam interactions with double negative metamaterial slabs. *Opt. Express*, 11(7):662–681, 2003.

[174] K.S. Yee. Numerical solution of initial boundary value problems involving maxwell's equations in iostropic media. *Ieee Transactions on Antennas and Propagation*, 14:302–307, 1966.

[175] S. Ramo, J.R. Whinnery, and T. Van Duzer. *Fields and Waves in Communication Electronics*. John Wiley & Sons, Inc., 3rd edition, 1994.

[176] R.W. Ziolkowski. Time-derivative lorentz material model-based absorbing boundary condition. *Ieee Transactions on Antennas and Propagation*, 45(10):1530–1535, 1997.

[177] J.P. Berenger. A perfectly matched layer for the absorption of electromagnetic waves. *Journal of Computational Physics*, 114:185–200, 1996.

[178] W.C. Chew and W.H. Weedon. A 3-d pefectly matched medium from modified maxwell's equations with stretched coordinates. *Microwave Optics Technology Letters*, 7(13):599–604, 1994.

[179] Z.S. Sacks, D.M. Kingsland, R. Lee, and J.F. Lee. A perfectly matched anisotropic absorber for use as an absorbing boundary condition. *Ieee Transactions on Antennas and Propagation*, 43(12):1460–1463, 1995.

[180] R.W. Ziolkowski. The design of maxwellian absorbers for numerical boundary conditions and for practical applications using engineered artificial materials. *Ieee Transactions on Antennas and Propagation*, 45(4):656–671, 1997.

[181] D.C. Wittwer and R.W. Ziolkowski. Two time-derivative lorentz material (2tdlm) formulation of a maxwellian absorbing layer matched to a lossy medium. *Ieee Transactions on Antennas and Propagation*, 48(2):192–199, 2000.

[182] A. Taflove and S.C. Hagness. *Computational Electrodynamics: The Finite-Difference Time-Domain Method*. Artech House, 2nd edition, 2000.

[183] J. B. J. Chen, T. M. Grzegorczyk, B. I. Wu, and J. A. Kong. Limitation of fdtd in simulation of a perfect lens imaging system. *Opt. Express*, 13(26):10840–10845, 2005.

[184] J. Carper. The CRC handbook of chemistry and physics. *Libr J*, 124(10):192–+, 1999.

[185] http://www.comsol.com. Femlab. 2006.

[186] L. A. Vainshtein. *The theory of diffraction and the factorization method (generalized Wiener-Hopf technique)*. Golem Press, Boulder, Colorado, 1969.

[187] G.L. Baldwin. On the diffraction of a plane wave by an infinite plane grating. *Math. Scand.*, 2:103–118, 1954.

[188] Nathan Marcuvitz. *Waveguide handbook*. McGraw-Hill, New York,, 1st edition, 1951.

[189] J. P. Auton. Infrared transmission polarizers by photolithography. *Appl. Opt.*, 6(6):1023, 1967.

[190] Stephen A. Campbell. *The science and engineering of microelectronic fabrication*. Oxford University Press, New York, 2nd edition, 2001.

[191] Simon S. Haykin. *Communication systems*. Wiley, New York, 4th edition, 2001.

[192] D. Schurig. *Indefinite Focusing*. Phd thesis, University of California, San Diego, 2002.

[193] J. G. Goodberlet, J. T. Hastings, and H. I. Smith. Performance of the raith 150 electron-beam lithography system. *J. Vac. Sci. Technol. B*, 19(6):2499–2503, 2001.

[194] MikroMasch. Sting - DP15/STING/AIBS. *http://www.mikromasch.com, Tallinn, Estonia*, 2005.

[195] MikroMasch. Ultrasharp salibration gratings - set TGS02. *http://www.spmtips.com, Tallinn, Estonia*, 2005.

[196] K. R. Williams and R. S. Muller. Etch rates for micromachining processing. *J. Microelectromech. Syst.*, 5(4):256–269, 1996.

[197] E. Devaux, T. W. Ebbesen, J. C. Weeber, and A. Dereux. Launching and decoupling surface plasmons via micro-gratings. *Appl. Phys. Lett.*, 83(24):4936–4938, 2003.

[198] V. A. Podolskiy, N. A. Kuhta, and G. W. Milton. Optimizing the superlens: Manipulating geometry to enhance the resolution. *Appl. Phys. Lett.*, 87(23):–, 2005.

[199] H. F. Talbot. Facts relating to optical science. *Phil. Mag.*, 9:401–407, 1836.

[200] R. J. Blaikie and S. J. McNab. Surface-plasmon-mediated lensing and resolution enhancements for near-field photolithography. *Association of Asia Pacific Physical Societies Bulletin*, 11(3):15–20, 2002.

[201] D. B. Shao and S. C. Chen. Surface-plasmon-assisted nanoscale photolithography by polarized light. *Appl. Phys. Lett.*, 86(25):–, 2005.

[202] D. B. Shao and S. C. Chen. Numerical simulation of surface-plasmon-assisted nanolithography. *Opt. Express*, 13(18):6964–6973, 2005.

[203] R. J. Blaikie, D. O. S. Melville, and M. M. Alkaisi. Super-resolution near-field lithography using planar silver lenses: a review of recent developments. *Microelectron. Eng.*, To be published, 2006.

[204] J. H. Davies. *The physics of low-dimensional semiconductors : an introduction*. Cambridge University Press, Cambridge, U.K. ; New York, NY, USA, 1998.

[205] O. S. Heavens. *Optical properties of thin solid films*. Butterworths Scientific Publications, London,, 1955.

[206] R. A. Linke H. J. Lezec Tineke Thio, K. M. Pellerin and T. W. Ebbesen. Enhanced light transmission through a single subwavelength aperture. *Opt. Lett.*, (26):1972–1974, 2001.

[207] S. Ramo, J.R. Whinnery, and T. Van Duzer. Plane-wave propagation and reflection. In *Fields and Waves in Communication Electronics*, pages 300–309. John Wiley & Sons, Inc., 3rd edition, 1994.